Dynamics and Limiting Mechanisms of Self-Aligned Carbon Nanotube Growth

by

Eric Ryan Meshot

A dissertation submitted in partial fulfillment
of the requirements for the degree of
Doctor of Philosophy
(Mechanical Engineering)
in The University of Michigan
2012

Doctoral Committee:

Assistant Professor Anastasios John Hart, Chair
Professor Michael D. Thouless
Associate Professor Krishnakumar R. Garikipati
Associate Professor Suljo Linic
Assistant Professor Desirée L. Plata, Duke University

To Carter, Caleb, and Noelle

ACKNOWLEDGEMENTS

Of course, there are many events and people that seemingly conspired together to arrive me at Michigan. I am from California, if you have not heard. Although I will not list those events and people here, I am grateful for them.

I would like to express my appreciation and respect to my advisor Professor John Hart. The first time I spoke with John on the phone to discuss my joining his lab, I had suffered a head injury the day prior, and my scalp was boasting a respectable four staples. It was under these concussed circumstances that we began the brainstorming and hypothesizing that has resulted in this thesis—it promises to be a fantastic read. Working with John has offered many unique experiences, including building a laboratory from a humble, empty room and actually working *with* John. It is my impression that not every graduate student has this rich opportunity of working side-by-side with his advisor in the lab, and thus I count myself fortunate. Directly from John, I learned valuable skills from many a nanotube growth experiment and many a late night at the G1 hutch. His enthusiasm for discovery is truly motivating, and he taught me a tremendous amount about scientific communication—and indeed "our writing styles [have] converged." His availability via email is remarkable, and my success is partially attributed to the fact that I can get feedback and have a scientific discussion with him at quite literally any hour of the day. Dedication.

I thank Professors Michael Thouless, Krishna Garikipati, Suljo Linic, and Desirée Plata for their time and service on my dissertation committee. Your support and valuable discussions are greatly appreciated. Desirée's mentorship has been particularly enlightening and heartening. I learned by her example what it means to be a conscientious scientist, and her selflessness is inspiring. Laughing with her eases the acute pain of mass spec data, and although the laughter at times may have been 1,3-butadiene-induced, the fun was always 100% real.

To the Mechanosynthesizers, my fellow men and women in the nanotube trenches: thank you honestly for challenging me to be a better researcher. Although some of you have never actually seen me in the lab, I promise I did all of my experiments before you got there—the data is real. I especially thank the undergraduate students who contributed to my research: Jeremy Ng, Kevin Lyons, and Keval Patel. Other highly honorable mentions include Eric Verploegen, Arthur Woll, Sol Gruner's group, EMAL, Kotov's lab, CHESS, and the owl operator. Also, the Fatties Intramural softball squad, and the Fall 2011 Co-Rec League Champions, have taught me about discipline, teamwork, and true sportsmanship. I would also like to thank Tracie Straub, Amanda Gaytan, Cynthia Quann-White, and other ME staff for their availability and assistance. All other project-specific acknowledgements can be found at the end of each chapter.

Thank you to my friends that exist outside of the basement lab for providing me some semblance of life. My deepest appreciation to Frank Kava for keeping us warm with his fires and for letting me beat him at racquetball, over and over, and over, again. Thank you to Josh Horwitz, inventor of the Horwitz Ham-O-Rama, for bringing to my attention the potential risk of nanobabies and nanobaby-related phenomena. Johnny Apricot, the Amazing Wizard, and Richard are beautiful and dear to me. I give my affection and appreciation to Yessa Villarreal, Jebidiah Long, Daniel Sinnott, Leto Rankine, Shane Smith, Jim Montgomery, Meishia Kernahan, Anne Henningfeld, Kelli Conroy, Emily Chapple, Margaret Grady, my Friday night crew, my Saturday morning crew, and the Russell Street Collective.

My family's unconditional support and even more unconditional huggings have sustained me through this endeavor. Thank you to Mom, Dad, Megan, Adam, Rhiannon, and Carter for the gifts we share, so special and unique with each of you. The army of aunts, uncles, cousins, and angels did not go unnoticed—every chance I get to see your faces or hear your voices fills me with love, rejuvenates me.

TABLE OF CONTENTS

LIST OF FIGURES

x

ABSTRACT

Carbon nanotubes (CNTs) are long, cylindrical molecules, which boast exceptional tensile strength and large thermal and electrical conductivities. Vertically aligned CNT "forests" have promising potential uses, including dry adhesives, electrical interconnects, light emitters, thermal interface materials, gas and liquid filters, composite reinforcements, and photonic crystals. They can also be transformed into macroscale yarns and sheets by drawing and spinning techniques. Manufacturing indefinitely long CNTs may realize dreams of CNT-based cables and wires having stiffness, strength, and transport properties exceeding today's best metal alloys and advanced fibers. However, the functional properties of CNT ensembles (such as forests and cables) have so far fallen short of those of individual CNTs. This is largely due to their low packing fraction, polydisperse diameters, and relatively short lengths.

Toward the eventual goal of bridging this structure-property relationship, my dissertation presents a novel set of *in situ* and *ex situ* characterization tools for CNT forest growth by chemical vapor deposition (CVD), as well as the use of these tools to investigate the limiting mechanisms thereof. *In situ* X-ray scattering reveals the dynamics of catalyst thin film dewetting into nanoparticle growth sites, the initial self-organization of the CNT forest, and the abrupt self-termination of growth. Quantification of catalyst and CNT sizes show that they are inevitably polydisperse, regardless of synthesis conditions. To overcome this, a novel method is introduced for templated

dewetting of the catalyst film toward the formation of ordered, monodisperse particles using nanoporous anodic alumina. Further, a map of thermal conditions is explored by independently tuning the temperatures of the catalyst and gaseous precursors, thereby establishing a set of rules for engineering crucial characteristics of forest growth, including CNT diameter, structural quality, vertical alignment, as well as rate and lifetime of the reaction. Finally, aligned CNT ensembles are used as templates to direct the self-assembly of fullerene C_{60}, creating hybrid films with high photoconductive gain, thereby demonstrating an immediate application of this exciting material.

These studies represent many new insights into the so-called "birth, life, and death" of CNT growth, and they have important implications for future work in synthesis of advanced materials, including CNTs, graphene, and undiscovered carbon allotropes. Meanwhile, these results have immediate applicability to efficient CNT manufacturing, improved characterization, and new hybrid materials for energy conversion.

Chapter 1
Introduction and scope

1.1 Motivation

A carbon nanotube (CNT) is a high-aspect-ratio molecule with a cylindrical form factor composed purely of carbon atoms—their sp^2-hybridized bonding configuration results in a hexagonal lattice within the shell of the cylinder.[1-3] *Conceptually*, a CNT is formed by rolling a monolayer (for single-wall) or multilayer (for multi-wall) sheet of graphene and stitching the edges together to form a seamless cylindrical structure (**Figure 1.1**). *Practically*, CNTs are synthetically manufactured in different ways, which are detailed in Chapter 2, and the most typical method is by chemical vapor deposition (CVD). The strong carbon-carbon bonding in a CNT results in tensile strength exceeding that of steel at one fourth of the density[4] and thermal conductivity (up to 10^4 W m^{-1} K^{-1})[5-8] greater than diamond. Intriguingly, a CNT's electronic properties (*i.e.*, metallic versus semiconducting) are determined by its diameter and the orientation of the hexagonal lattice with respect to its longitudinal axis, which is referred to as its chirality.[9] Electronic resistance through a metallic CNT is lower than through copper at micron length scales,[10] and CNTs are less susceptible to electromigration, which is important for advancing electronics to smaller dimensions.[11, 12]

Despite the outstanding properties of an individual CNT, practical use of CNTs often involves combining a large number of CNTs with some degree of order[13]—ranging from low order in dispersions and networks to high order in self-organized arrays and regular, horizontal grids for memory devices.[14] The integration of many CNTs (of any ordering) into bulk form, while maintaining their exceptional properties, is challenging

graphene   **carbon nanotube**   **C$_{60}$ fullerene**
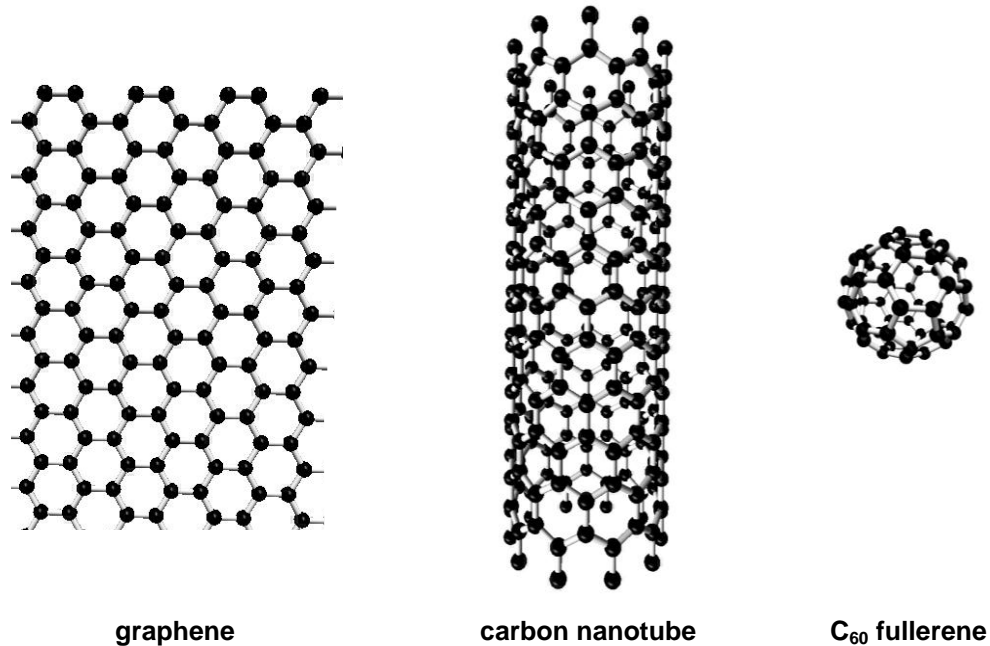
Figure 1.1 Molecular structures of a select set of carbon allotropes having sp^2-hybridized bonding: monolayer graphene, carbon nanotube (may have a single wall or multiple concentric walls), and C$_{60}$ fullerene (aka "bucky ball"). Drawings by Desirée Plata.

and largely has not yet been realized. For instance, despite their high thermal conductivity, dense tangled CNT networks have low thermal conductivity (lower than polymers) because CNT-CNT contacts cause phonon scattering.[15] Mechanical properties of bulk CNT materials also do not exhibit classically predicted properties due to agglomeration and issues in load transfer between adjacent CNTs. A promising approach is to spin CNTs directly into yarns, but there is still a large compromise compared to continuous CNTs that can distribute and translate a load along their lengths effectively.[16] Thus, developing new materials and processes to overcome these challenges is vital in order to realize the rare properties of individual CNTs.

Therefore, to harness the attractive properties of CNTs at larger scales, it is desirable to organize the CNTs during synthesis, which avoids costly and complicated port-processing. One attractive configuration results from the ensemble of vertically self-aligned CNTs. These arrays are affectionately referred to as "forests"[17] because of the extremely high aspect ratio of the constituent CNTs (up to 10^7), their relatively sparse

2
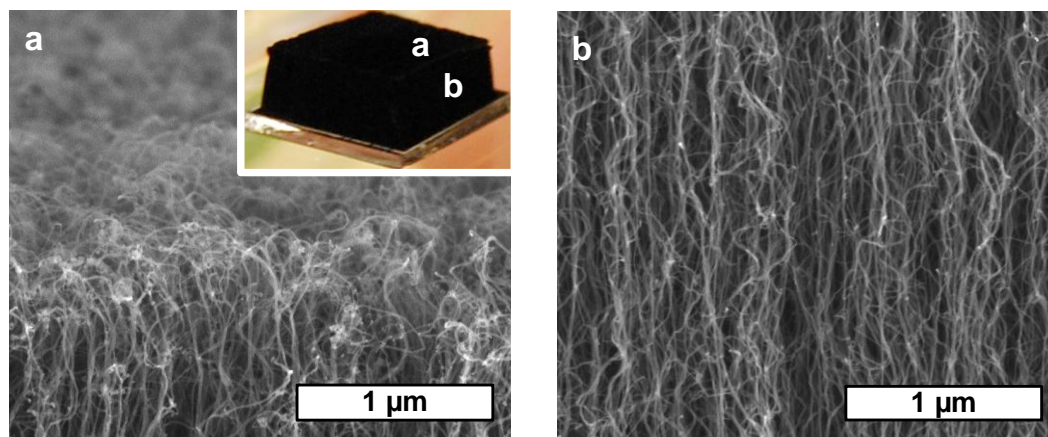
Figure 1.2 Example of tortuous morphologies in a vertically aligned CNT forest. SEM images of the (a) top and (b) sidewall of a forest, as indicated in the inset digital photograph in (a).

coverage over an area (CNT-CNT spacing on the order of 10^2 nm)], and their tortuous and interconnected morphology (**Figure 1.2**). A CNT forest even has a characteristic "canopy" structure at the top (representing the beginning of growth; see Chapter 4).[18] The distinctive self-organization of an aligned CNT forest is governed by physical interactions among large numbers of CNTs growing at microscopically fantastic speeds (up to 2 mm in 5 min).[17, 19] Due to their anisotropy, CNT forests are uniquely configured for many potential uses, including dry adhesives,[20-22] electrical interconnects,[23-27] light emitters,[28-30] thermal interface materials,[31, 32] gas and liquid filters,[33, 34] composite reinforcements,[35, 36] photonic crystals,[37, 38] and can be transformed into macroscale yarns and sheets by drawing and spinning techniques.[39, 40] Furthermore, manufacturing an infinite cable of *continuous* CNTs would possibly realize dreams of CNT-based cables and wires having stiffness, strength, and transport properties exceeding today's best metal alloys and advanced fibers. Advances in understanding CNT forest growth can lead to broader improvements to the manufacture of CNT powders and composites.

1.2 Thesis scope and outline

Ultimately, CNT ensembles have fallen short of realizing the rare properties of individual CNTs because of their low packing fraction, polydisperse diameters, and

relatively short lengths. In order to overcome these shortcomings in CNT forest processing, we need techniques that enable real-time investigations of synthesis, as well as mapping of the forest characteristics for large sample sizes and populations. To this end, the goal of my dissertation is to **develop a novel set of *in situ* and *ex situ* characterization tools to elucidate the mechanisms of CNT forest growth from both conventional and new approaches to synthesis.**

The dissertation is organized into chapters as follows:

Chapter 2 summarizes the current understanding of limiting mechanisms of aligned CNT growth. I discuss the state of the art in synthesis of CNT forests as well as the governing factors for engineering the properties of CNT forests.

Chapter 3 studies the dynamics of catalyst film dewetting into nanoparticle growth sites and subsequent CNT nucleation. Initial results are presented from a new approach to direct film dewetting using a nanoporous substrate as a template.

Chapter 4 discusses the origin and evolution of the characteristic aligned morphology in CNT forest during growth. I combine *ex situ* and *in situ* X-ray scattering techniques to quantify the self-organization stage, as well as abrupt self-termination of growth. A unique method is introduced for correcting forest height kinetics to reveal the true lengthening rate of CNTs.

Chapter 5 presents how the characteristics of CNT forests can be engineered by decoupled thermal treatment of the Fe catalyst from that of the gaseous carbon precursor. I thus establish a set of rules for engineering the crucial aspects of forest growth, including CNT diameter, structural quality, vertical alignment, as well as rate and lifetime of the reaction.

Chapter 6 demonstrates an application of aligned CNTs as a template to direct the self-assembly of C_{60}. Crystalline C_{60} rods synthesized by this method are aligned to the direction of CNTs within microfabricated, multidirectional films. The chapter includes

detailed characterization of the hierarchical structure as well as initial photoconductivity measurements, which demonstrate the utility of these hybrid films as UV sensors.

Chapter 7 summarizes the contributions of this dissertation and provides an outlook for future developments.

1.3 References

1.   Dresselhaus, M. S.; Dresselhaus, G.; Avouris, P., *Carbon nanotubes : synthesis, structure, properties, and applications*. Springer: Berlin ; New York, 2001; 447 p.

2.   Graham, A. P.; Duesberg, G. S.; Hoenlein, W.; Kreupl, F.; Liebau, M.; Martin, R.; Rajasekharan, B.; Pamler, W.; Seidel, R.; Steinhoegl, W.; Unger, E., How do carbon nanotubes fit into the semiconductor roadmap? *Applied Physics A: Materials Science & Processing* 2005, *80* (6), 1141-1151.

3.   Hirsch, A., The era of carbon allotropes. *Nature Materials* 2010, *9* (11), 868-871.

4.   Lu, J. P., Elastic properties of carbon nanotubes and nanoropes. *Physical Review Letters* 1997, *79* (7), 1297-1300.

5.   Yu, C.; Shi, L.; Yao, Z.; Li, D.; Majumdar, A., Thermal conductance and thermopower of an individual single-wall carbon nanotube. *Nano Letters* 2005, *5* (9), 1842-1846.

6.   Kim, P.; Shi, L.; Majumdar, A.; McEuen, P. L., Thermal transport measurements of individual multiwalled nanotubes. *Physical Review Letters* 2001, *87*, 215502.

7.   Choi, T.; Poulikakos, D.; Tharian, J.; Sennhauser, U., Measurement of thermal conductivity of individual multiwalled carbon nanotubes by the 3-omega method. *Applied Physics Letters* 2005.

8.   Choi, T.; Poulikakos, D.; Tharian, J.; Sennhauser, U., Measurement of the thermal conductivity of individual carbon nanotubes by the four-point three-omega method. *Nano Letters* 2006, 1589-1593.

9.   Jorio, A.; Saito, R.; Hafner, J. H.; Lieber, C. M.; Hunter, M.; McClure, T.; Dresselhaus, G.; Dresselhaus, M. S., Structural (*n, m*) Determination of isolated single-wall carbon nanotubes by resonant raman scattering. *Physical Review Letters* 2001, *86* (6), 1118.

10.   Baughman, R. H.; Zakhidov, A. A.; de Heer, W. A., Carbon nanotubes - the route toward applications. *Science* 2002, *297* (5582), 787-792.

11.   Avouris, P.; Appenzeller, J.; Martel, R.; Wind, S. J., Carbon nanotube electronics. *Proceedings of the IEEE* 2003, *91* (11), 13.

12.   Javey, A.; Guo, J.; Farmer, D. B.; Wang, Q.; Yenilmez, E.; Gordon, R. G.; Lundstrom, M.; Dai, H., Self-aligned ballistic molecular transistors and electrically parallel nanotube arrays. *Nano Letters* 2004, *4* (7), 1319-1322.

13. Hart, A. J. Chemical, mechanical, and thermal control of substrate-bound carbon nanotube growth. Massachusetts Institute of Technology, 2006.

14. Rueckes, T.; Kim, K.; Joselevich, E.; Tseng, G. Y.; Cheung, C.-L.; Lieber, C. M., Carbon nanotube-based nonvolatile random access memory for molecular computing. *Science* 2000, *289* (5476), 94-97.

15. Prasher, R. S.; Hu, X. J.; Chalopin, Y.; Mingo, N.; Lofgreen, K.; Volz, S.; Cleri, F.; Keblinski, P., Turning carbon nanotubes from exceptional heat conductors into insulators. *Physical Review Letters* 2009, *102*, 105901.

16. Espinosa, H. D.; Yong, Z.; Moldovan, N., Design and operation of a mems-based material testing system for nanomechanical characterization. *Journal of Microelectromechanical Systems,* 2007, *16* (5), 1219-1231.

17. Fan, S. S.; Chapline, M. G.; Franklin, N. R.; Tombler, T. W.; Cassell, A. M.; Dai, H. J., Self-oriented regular arrays of carbon nanotubes and their field emission properties. *Science* 1999, *283* (5401), 512-514.

18. Zhang, L.; Li, Z.; Tan, Y.; Lolli, G.; Sakulchaicharoen, N.; Requejo, F.; Mun, B.; Resasco, D., Influence of a top crust of entangled nanotubes on the structure of vertically aligned forests of single-walled carbon nanotubes. *Chemistry of Materials* 2006, *18* (23), 5624-5629.

19. Meshot, E.; Plata, D.; Tawfick, S.; Zhang, Y.; Verploegen, E.; Hart, A., Engineering vertically aligned carbon nanotube growth by decoupled thermal treatment of precursor and catalyst. *ACS Nano* 2009, *3* (9), 2477-2486.

20. Ge, L.; Sethi, S.; Ci, L.; Ajayan, P. M.; Dhinojwala, A., Carbon nanotube-based synthetic gecko tapes. *Proceedings of the National Academy of Sciences* 2007, *104* (26), 10792-10795.

21. Qu, L.; Dai, L.; Stone, M.; Xia, Z.; Wang, Z., Carbon nanotube arrays with strong shear binding-on and easy normal lifting-off. *Science* 2008, *322* (5899), 238-242.

22. Sethi, S.; Ge, L.; Ci, L.; Ajayan, P. M.; Dhinojwala, A., Gecko-inspired carbon nanotube-based self-cleaning adhesives. *Nano Letters* 2008, *8* (3), 822-825.

23. Nihei, M.; Horibe, M.; Kawabata, A.; Awano, Y., Simultaneous formation of multiwall carbon nanotubes and their end-bonded ohmic contacts to Ti electrodes for future ULSI interconnects. *Japanese Journal of Applied Physics, Part 1* 2004, *43* (4B), 1856-9.

24. Horibe, M.; Nihei, M.; Kondo, D.; Kawabata, A.; Awano, Y., Carbon nanotube growth technologies using tantalum barrier layer for future ULSIs with Cu/low-k interconnect processes. *Japanese Journal of Applied Physics, Part 1* 2005, *44* (7A), 5309-5312.

25. Nihei, M.; Kawabata, A.; Kondo, D.; Horibe, M.; Sato, S.; Awano, Y., Electrical properties of carbon nanotube bundles for future via interconnects. *Japanese Journal of Applied Physics, Part 1* 2005, *44* (4A), 1626-1628.

26. Kreupl, F.; Graham, A. P.; Duesberg, G. S.; Steinhogl, W.; Liebau, M.; Unger, E.; Honlein, W., Carbon nanotubes in interconnect applications. *Microelectronic Engineering* 2002, *64* (1-4), 399-408.

27. Chiodarelli, N.; Li, Y.; Cott, D. J.; Mertens, S.; Perys, N.; Heyns, M.; De Gendt, S.; Groeseneken, G.; Vereecken, P. M., Integration and electrical characterization of carbon nanotube via interconnects. *Microelectronic Engineering* 2010.

28. Zhu, L. B.; Sun, Y. Y.; Hess, D. W.; Wong, C. P., Well-aligned open-ended carbon nanotube architectures: An approach for device assembly. *Nano Letters* 2006, *6* (2), 243-247.

29. Sohn, J.; Lee, S.; Song, Y.; Choi, S.; Cho, K.; Nam, K., Patterned selective growth of carbon nanotubes and large field emission from vertically well-aligned carbon nanotube field emitter arrays. *Applied Physics Letters* 2001, *78* (7), 901-903.

30. Pan, Z. W.; Au, F. C. K.; Lai, H. L.; Zhou, W. Y.; Sun, L. F.; Liu, Z. Q.; Tang, D. S.; Lee, C. S.; Lee, S. T.; Xie, S. S., Very low-field emission from aligned and opened carbon nanotube arrays. *Journal of Physical Chemistry B* 2001, *105* (8), 1519-1522.

31. Huang, H.; Liu, C. H.; Wu, Y.; Fan, S. S., Aligned carbon nanotube composite films for thermal management. *Advanced Materials* 2005, *17* (13), 1652.

32. Tong, T.; Zhao, Y.; Delzeit, L.; Kashani, A.; Meyyappan, M.; Majumdar, A., Dense, vertically aligned multiwalled carbon nanotube arrays as thermal interface materials. *IEEE Transactions on Components and Packaging Technologies* 2007, *30* (1), 92-100.

33. Holt, J.; Park, H.; Wang, Y.; Stadermann, M.; Artyukhin, A.; Grigoropoulos, C.; Noy, A.; Bakajin, O., Fast mass transport through sub-2-nanometer carbon nanotubes. *Science* 2006, *312* (5776), 1034-1037.

34. Hinds, B.; Chopra, N.; Rantell, T.; Andrews, R.; Gavalas, V.; Bachas, L., Aligned multiwalled carbon nanotube membranes. *Science* 2004, *303* (5654), 62-65.

35.   Garcia, E. J.; Wardle, B. L.; Hart, A. J., Joining prepreg composite interfaces with aligned carbon nanotubes. *Composites Part A-Applied Science and Manufacturing* 2008, *39* (6), 1065-1070.

36.   De Volder, M.; Tawfick, S. H.; Park, S. J.; Copic, D.; Zhao, Z.; Lu, W.; Hart, A. J., Diverse 3D Microarchitectures Made by Capillary Forming of Carbon Nanotubes. *Advanced Materials* 2010, *22* (39), 4384-4389.

37.   Kempa, K.; Kimball, B.; Rybczynski, J.; Huang, Z. P.; Wu, P. F.; Steeves, D.; Sennett, M.; Giersig, M.; Rao, D. V. G. L. N.; Carnahan, D. L.; Wang, D. Z.; Lao, J. Y.; Li, W. Z.; Ren, Z. F., Photonic crystals based on periodic arrays of aligned carbon nanotubes. *Nano Letters* 2002, *3* (1), 13-18.

38.   Lidorikis, E.; Ferrari, A. C., Photonics with multiwall carbon nanotube arrays. *ACS Nano* 2009, *3* (5), 1238-1248.

39.   Zhang, M.; Fang, S.; Zakhidov, A. A.; Lee, S. B.; Aliev, A. E.; Williams, C. D.; Atkinson, K. R.; Baughman, R. H., Strong, transparent, multifunctional, carbon nanotube sheets. *Science* 2005, *309* (5738), 1215-1219.

40.   Jiang, K.; Wang, J.; Li, Q.; Liu, L.; Liu, C.; Fan, S., Superaligned carbon nanotube arrays, films, and yarns: a road to applications. *Advanced Materials* 2011, *23* (9), 1154-1161.

Chapter 2
Perspective on limiting mechanisms of
CNT forest growth by CVD

This chapter provides a perspective on the current understanding of important growth and termination mechanisms of carbon nanotube (CNT) forests. I briefly introduce the various synthesis methods for making carbon nanotubes (CNTs) followed by a discussion focused specifically on forest growth by chemical vapor deposition (CVD). I identify the ultimate goals for manufacturing CNT forests and discuss the critical challenges in achieving these goals.

2.1   Introduction

2.1.1   Methods of CNT synthesis

CNTs have been made by many synthetic means, including CVD,[1, 2] laser ablation,[3] flame synthesis,[4, 5] and arc discharge.[6, 7] The latter method is responsible for generating the CNTs first observed by Iijima in TEM,[6] where he described the well-defined core and concentric walls of 0.34-nm spacing. Variations of CVD reactors include plasma-enhanced,[8] laser-assisted,[9] and fluidized-bed;[2] different catalyst or substrate configurations include aerosol,[10, 11] floating catalyst,[12, 13] as well as horizontally aligned.[14, 15] CNT synthesis from supercritical toluene[16] has also been demonstrated, and carbon "nanohoops"[17] synthesized in solution may be CNT building blocks in the future. It would be highly attractive to make CNTs at low synthesis temperatures in fluids, which essentially highlights the inherent the inverse relationship between temperature and pressure in CVD, where typical ranges are 500-1200 °C and 10^0-10^2 torr, respectively.
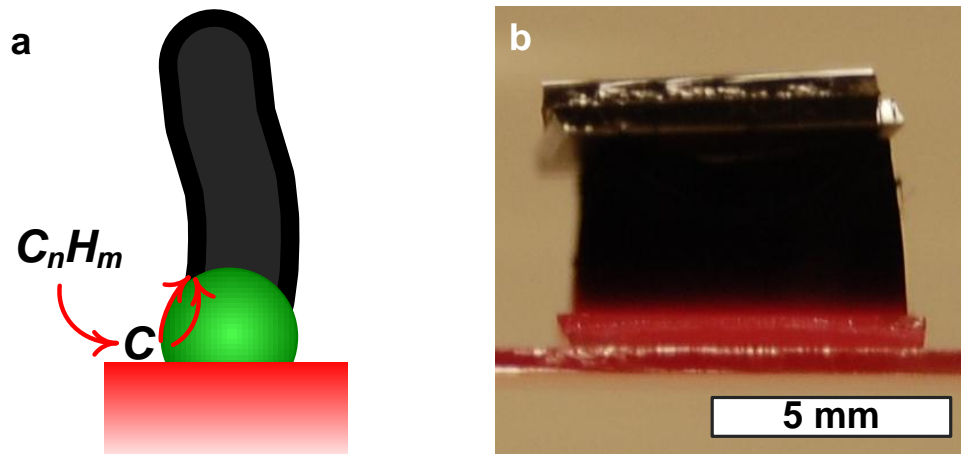
Figure 2.1 Depictions of substrate-bound CNT growth. (a) Schematic shows a catalyst nanoparticle (green) attached to a substrate (*e.g.*, a metal-oxide). C_nH_m represents a generic gaseous hydrocarbon that dissociates at the catalyst's surface and diffuses to and incorporates into the growing lattice. (b) Digital photograph showing 1 billion vertically aligned CNTs (typical forest) fixed on a locally heated platform during CVD.

2.1.2 Collective mechanism of self-aligned CNT forest growth

CVD synthesis is essentially a thermal dehydrogenation reaction whereby a catalyst nanoparticle is believed to lower the temperature required in order to dissociate a gaseous hydrocarbon precursor molecule into carbon and hydrogen (**Figure 2.1**).[2] Carbon diffuses on and/or in the catalyst particle, which enables the graphitic network to precipitate, starting with the "cap" of the CNT. Growth of a substrate-bound, self-aligned forest results when this reaction is performed synchronously over many catalysts that are arranged at sufficiently high density.[18] The general process of collective CNT forest growth[19] is shown in **Figure 2.2**. Briefly, catalyst nanoparticles are fixed on a flat substrate (*e.g.*, Si wafer) either by dewetting a thin film (where surface tension drives the formation of islands)[20] or by casting predefined nanoparticles.[21, 22] The catalyst is often first reduced (*i.e.*, by exposure to H_2), and it is then exposed to hydrocarbon precursors (*e.g*, C_2H_4, C_2H_2) to initiate nucleation and growth of individual CNTs. As growth proceeds, the initially tangled network of CNTs self-orient as they reach some critical length and density (Chapter 4). Then, vertical growth continues steadily for some time until the number density (packing fraction) of CNTs decays until

11
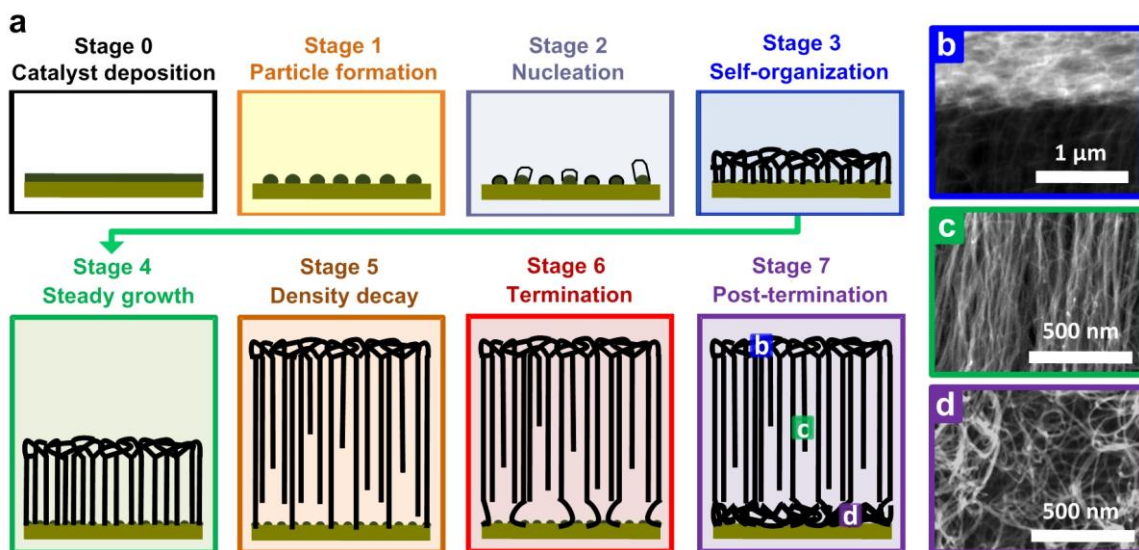
Figure 2.2 Collective growth mechanism of a CNT forest: (a) schematic of growth stages and (b-d) accompanying SEM images of various locations in the forest, labeled accordingly in "Stage 7". Adapted with permission from *Journal of Physical Chemistry C* 2009, 113, 20576-20582. Copyright © 2009 American Chemical Society.

collective growth terminates abruptly. For this discussion, I mainly consider the "base growth" mechanism whereby the catalyst particle remains fixed to the substrate and catalyst addition occurs at the base of the forest, but "tip growth" can also occur when the catalyst adheres weakly to the substrate.

The critical CNT characteristics for applications of CNT forests (Chapter 1) are CNT diameter and chirality, packing density, and the length of a constituent CNT. I consider the length of individual CNTs separately from the length of an ensemble of CNTs) because this *collective* length is the result of several competing mechanisms, including but not limited to packing density and interactions of the CNTs, as well as differences in growth rate among neighboring CNTs.

Table 2.1 Characteristics of CNT forests and their determining factors

Characteristic	*Determing factor(s)*	*State of the art*
diameter and chirality	particle geometry (size, shape, contact angle with support, crystal orientation)	-diameter tuning from single thickness of catalyst thin film (by temperature/annealing conditions)[41] -block-copolymer patterning of particles[20,21] -selelctive growth of metallic CNTs by manipulation of catalyt crystallography[50] -selective growth of (6,5) CNTs
packing fraction	particle spacing, catalyst chemical/physical stability	-multiple catalyst film depositions yields 10^{13} cm^{-2} (after capillary densification)[59] -block-copolymer patterning of particles controls CNT density[21] -CNTs initially crowd then order-of-magnitude density decays[22,82]
length (individual)	catalyst chemical/physical stability, gas chemistry	-longest CNT is 18.5 cm from horizontally aligned growth on quartz[139]
length (ensemble)	CNT packing fraction, force coupling, tortuosity	-tallest forest is 18 mm by water-assisted CVD (slow)[32,138] -2 mm forest in 5 min by decoupled CVD (fast)[41]

2.2   Discussion of important governing factors

Table 2.1 shows a summary of the discussion that follows, where I introduce components or mechanisms of the synthesis process that determine each critical forest characteristic as well as the state of the art, with a focus on the current limiting factors.

2.2.1   Diameter and density benchmarks

The diameter of a CNT is important for many applications and typically range from 1-100 nm at densities of 10^9-10^{13} cm^{-2}, and for a single-wall (SW) CNT, the diameter and chirality are related. The chirality of a CNT dictates its electrical properties (metallic or semiconducting). Therefore, chirality-selective CNT growth is perhaps the grand challenge for CNT synthesis research,[23] having significant implications for advancing nanoscale electronic and optoelectronic devices.[24] Although multi-wall (MW) CNTs are strictly metallic regardless of diameter, controlling diameter still has interesting

applications toward filtration,[25, 26] photonics,[27, 28] and conductance properties.[29-36] Precedence in literature suggests that size of the catalyst nanoparticle dictates the diameter of the CNT,[11, 37-44] where the particle templates growth of the graphitic carbon lattice (**Figure 2.3**).[45-47] It is not as well understood precisely what dictates CNT chirality;[48, 49] however, it is likely related to the conditions of CNT nucleation, including the size,[48, 50] structure,[49] and elemental composition[51, 52] of the catalyst, as well as the reaction temperature.[53] Researchers have recently improved techniques for achieving selectivity,[49, 54, 55] with increasing evidence suggesting that crystal facets of the catalyst particle play a role in determining chirality. Nevertheless, control of chirality within CNT forests has not been achieved.

The packing density of CNTs in a forest is also influenced by the catalyst particle—or, more precisely, by the arrangement and spacing of many particles, as well as by the CNT diameter. Conceptually increasing CNT diameter at constant number density results in a higher packing fraction. However, the challenge of achieving high density (or tuning of density) is two-tiered: (1) one must achieve desired number density of catalysts, and then (2) activate catalyst particles and grow CNTs. Researchers have templated the catalyst using block-copolymer chemistry to achieve prescribed areal density of catalyst particles, which controls the packing fraction (and morphology) of CNT forests.[22] Other techniques of manipulating the density of catalyst particles via catalyst deposition technique[56-58] and/or annealing[59-61] have resulted in dense forests up to 1.1×10^{13} cm^{-2},[a] but typically densities are lower.

2.2.2 The catalyst nanoparticle

Given the prominent influence the catalyst particle has on the resultant CNT structure (diameter and chirality) and packing (number density), I must understand how the catalyst behaves during synthesis. Researchers have invested significant effort in understanding the physical and chemical state of the particle during synthesis because these influences whether or not the catalyst grows a CNT, as well as how the CNT grows (*e.g.*, rate, structure).

---

[a] Number represents packing density after capillary densification by exposure to liquid.[58]
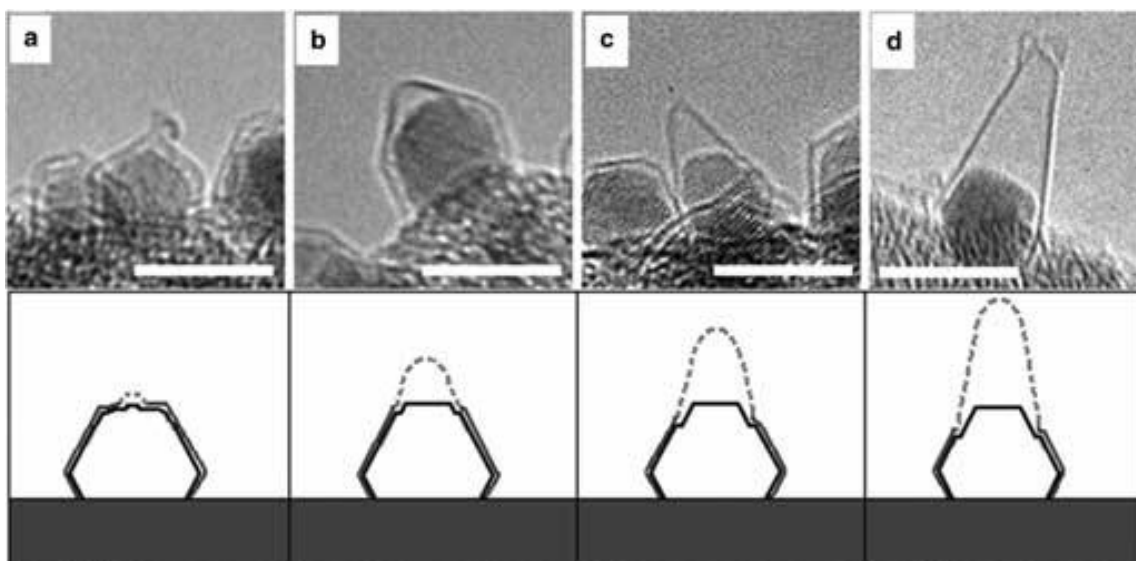
Figure 2.3 CNTs at different phases during early nucleation and growth. (a) Formation of the CNT "cap" structure and (b) initial lift off demonstrates how the catalyst particle size and possibly its facets can determine CNT diameter as growth proceeds (c-d). Adapted with permission from *Small* 2005, 1, 1180-1183. Copyright © 2005 John Wiley & Sons, Inc.

The primary role of the catalyst is to dissociate carbon-containing molecules from the gas phase by adsorption. It also enables incorporation of carbon atoms at the growing CNT lattice via various diffusion pathways (*i.e.*, surface,[62] bulk[63]; **Figure 2.1**). Principally, a material's ability to react with the carbon precursor without binding carbon irreversibly dictates its utility as a CNT catalyst, and researchers have demonstrated the use of a wide range of elements and materials,[15, 64-68] including oxides[69] and semiconductors.[70] Using nanoscale catalysts[71, 72] with a metal-oxide support[73, 74] provides selective surface sites, which presumably enables use of materials that otherwise are not particularly reactive. It should noted that transmission metals having high carbon solubility (*i.e.*, Fe, Ni, Co) have been proven to be most effective, which suggests that some form of dissolution-precipitation occurs during CNT growth analogous to the vapor-liquid-solid (VLS) model for growth of Si nanowires.[75] On the other hand, the fact that metal-oxides and semiconductors having effectively no carbon solubility can grow CNTs indicates that VLS does not strictly govern growth and that surface processes are also important. The metal-oxide support layer serves to physically stabilize the particle,[76-79] and it can also induce reactive sites at the boundary with the metal catalyst.[73]
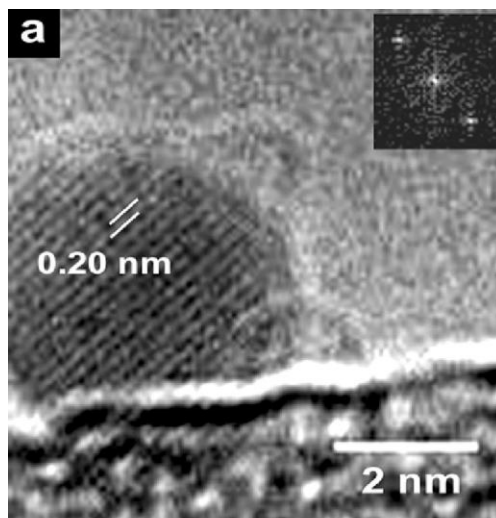
Figure 2.4 *In situ* environmental TEM imaging of CNT growth on Ni catalysts. (a-b) TEM images recorded at 615 °C during low-pressure growth with C_2H_2. The crystal structure is apparent in both cases, with clear, regular spacing, as confirmed by the inset FFTs. Adapted with permission from *Nano Letters* 2007, 7, 602-608. Copyright © 2007 American Chemical Society.

Despite the variety of elements and combinations proven, the traditional combination of Fe on an alumina support (various stoichiometries[80]) has emerged as conventional practice particularly in CVD growth of CNT forests.[58, 80-84] Alumina may also aid in the oxidation-reduction cycle of the catalyst by donating electrons as a Lewis acid.[85]

What, then, is the chemical state of the catalyst during CNT synthesis? Observations by *in situ* XPS[86, 87] and XRD[88] show that Fe is reduced upon exposure to the CNT growth gases and exists as a carbide during growth. However, a separate XPS study suggests that CNTs grow more efficiently from iron oxide.[89] Nonetheless, given the chemical stability of iron carbide, there may be a critical balance between the metallic and carbide phases, and perhaps the oxide phase as well. A pure carbide phase is not necessarily preferred for CNT growth. For instance, adding Mo to a Fe catalyst showed an enhancement in CNT growth, which was explained by the formation of Mo_2C resulting in a larger percentage of metallic Fe.[67]

As mentioned earlier, nanoscale effects can increase the reactivity of a catalyst by revealing more selective sites. In addition, surfaces and interfaces begin to dominate other properties of the particle, including the melting point and solubility.[87, 90-92] This is especially important considering the high temperatures that are typical for thermal CVD,
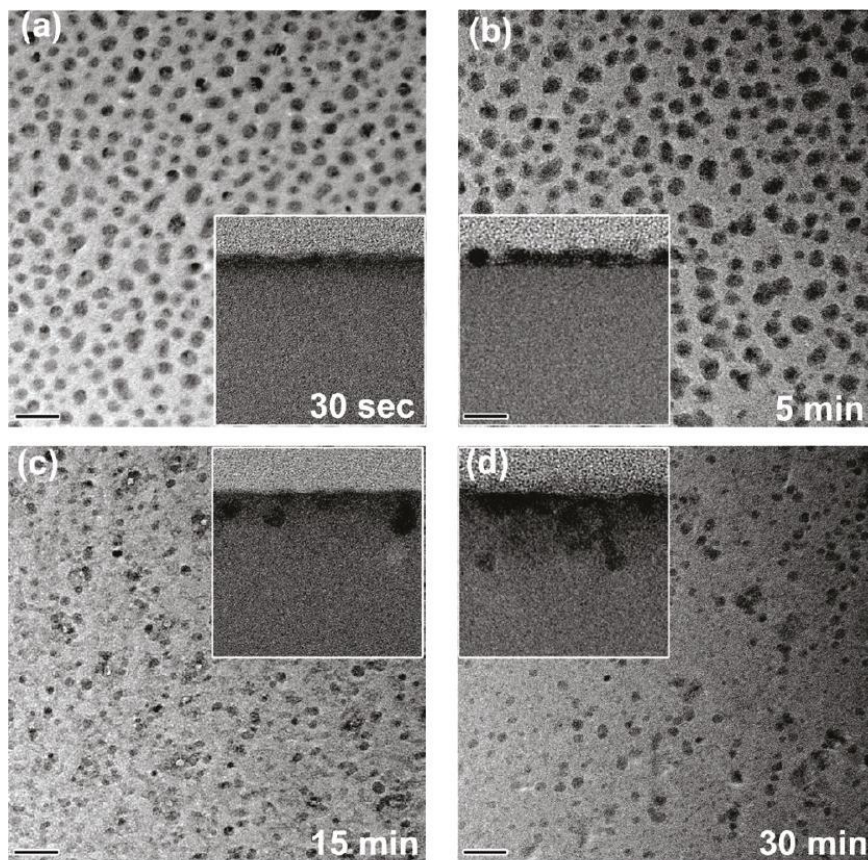
Figure 2.5 Catalyst migration during annealing in H_2/H_2O. Plan-view TEM images of annealed Fe/Al_2O_3 catalyst layers at 750 °C for various labeled times for (a) 30 s, (b) 5 min, (c) 15 min, and (d) 30 min. Insets are cross-sectional views demonstrating subsurface diffusion of Fe into the Al_2O_3 layer. Scale bar: 20 nm (10 nm for insets). Adapted with permission from *Journal of Physical Chemistry Letters* 2010, 1, 918-922. Copyright © 2010 American Chemical Society.

and to this end, a key question is whether the catalyst particle is a solid or liquid during synthesis. *In situ* environmental TEM observations show metal catalyst particles with distinct crystal structure as CNTs grow (**Figure 2.4**),[45, 87, 93] but atoms of the catalyst and carbon atoms both exhibit high mobility, which enables rapid restructuring and/or migration.[46] Inducing changes to the crystal facets of the particle has been shown as a mechanism toward selective growth of chiral SWCNTs having metallic properties.[49] Considering the low temperatures used in these *in situ* studies (430-580 °C), it is plausible that the catalyst may behave differently at elevated temperatures. Other studies suggest that CNT synthesis from a liquid metal catalyst is possible,[66] and that the liquid phase may be a necessary condition for effective CNT growth.[94]

Given the high mobility of the catalyst atoms at the high temperatures of CVD, migration of catalyst atoms becomes a major governing factor of CNT growth, whether by general ripening mechanisms or by diffusion into the support layer (**Figure 2.5**),[95, 96] although it is not clear how these effects scale for larger particles. Regardless, the loss of catalyst material from the support layer has been corroborated by TEM,[95] XPS,[82] and Rutherford backscattering spectroscopy studies,[b] and the precedence for decaying forest growth rates observed in experimental data may be explained in part due to the deactivation of particles as their morphologies evolve.

Despite catalyst evolution, it appears that the diameter of an individual CNT is quite stable during growth. This means that changes in the mean CNT diameter during growth[82] are the result of a shift in the population of diameters as growth of individual CNTs terminates, rather than alterations of the CNT structure during growth. Notably, in another study, Raman spectroscopy of a 6 mm long SWNT showed no chirality change during growth,[97] suggesting that there is a certain energetic barrier[c] to a change in chirality or diameter despite the small differences in energies between different chiralities.[98-100]

In general, understanding how to activate and maintain a large percentage of catalysts is crucial. The evolution of catalyst morphology has a significant impact on the CNT packing fraction because the number of active catalysts decreases with growth time,[19, 82] leading to variations in the forest density of up to an order of magnitude.

2.2.3 Gas-phase precursor chemistry

The gas chemistry is highly influential to CNT growth,[40, 84, 101-103] and nearly any small hydrocarbon—with and without oxygen—can be used. In Section 2.2.2, I discussed how the number of particles evolves with growth time, naturally leading to variations in CNT packing. The packing fraction of CNTs can vary depending on the precursor gases, even for the same areal density of catalyst particles. For instance,

---

[b] Unpublished data.
[c] In the simple case of a SWCNT, for instance, creation of a heptagon of carbon atoms instead of a hexagon can lead to an increase the CNT diameter, which computations suggest costs ≤ 1.2 eV.[98] Alternatively, a single C-C bond rotation creates the Stone-Wales (5-7-7-5) arrangement, which has formation energy of ~ 5 eV.[99,100]

increases in CNT packing are observed in the beginning of growth, approximately corresponding to an incubation period during which the critical gas species reach sufficient concentration;[82] autocatalytic reactions can also lead to this increasing activity with growth time.[104] Furthermore, the mean CNT packing can be increased by altering the precursor chemistry,[101] again without altering the areal density of catalysts. The density of CNTs depends on the partial pressure of active gaseous precursors over the whole reactor as well as locally at the catalyst.[105] Only ~0.01 atm of the input gas mixture is consumed during synthesis,[106] so the CNT yield, and thus possibly the density, will be quite sensitive to even small changes in precursor chemistry. Interestingly, changes in precursor chemistry, either by temperature[40] or by injection of different trace hydrocarbons,[101] do not alter the CNT diameter. This suggests the catalyst particle governs the diameter of the CNT, irrespective of available gas precursors.

The carbon precursor feeds the reaction, but excessive decomposition and/or poisonous deposition on the catalyst can inhibit growth. Thus, precursor chemistry naturally also determines the length of the CNT by governing the reaction rate (*i.e.*, lengthening rate) and influencing catalyst lifetime. Identifying precisely which compounds contribute to CNT growth is challenging, given the plurality of gas compounds generated during thermal CVD,[106] but it is clear that the gas composition affects the rate and lifetime of the reaction.[40, 84, 101] Acetylene (C_2H_2) has been identified as a key precursor[107-110] due to the reactive nature of its triple bond — the universality of which has been demonstrated by Plata *et al.*,[101] who proved the efficiency of several different triple-bonded carbon compounds (alkynes). Additives to the gas atmosphere (beside hydrocarbons) can enhance growth by extending the lifetime of the catalyst. Several oxygen-containing species have been demonstrated as "growth enhancers", including O_2,[111] H_2O,[81, 112, 113] C_2H_5OH,[114-116] CO_2,[117, 118] while sulfur has also been used.[12, 13, 119, 120] The extension of catalyst lifetime by addition of H_2O in the growth atmosphere[112] has inspired appreciable research activity, and subsequent publications have proposed that oxygen keeps the selective sites of the catalyst available for adsorption by reacting with carbonaceous deposits (other than graphitic carbon).[113, 121-123] Water was also shown to extend reaction lifetime by inhibiting Ostwald ripening of the catalysts.[96] However, other studies contrarily found particle coarsening to be unaffected
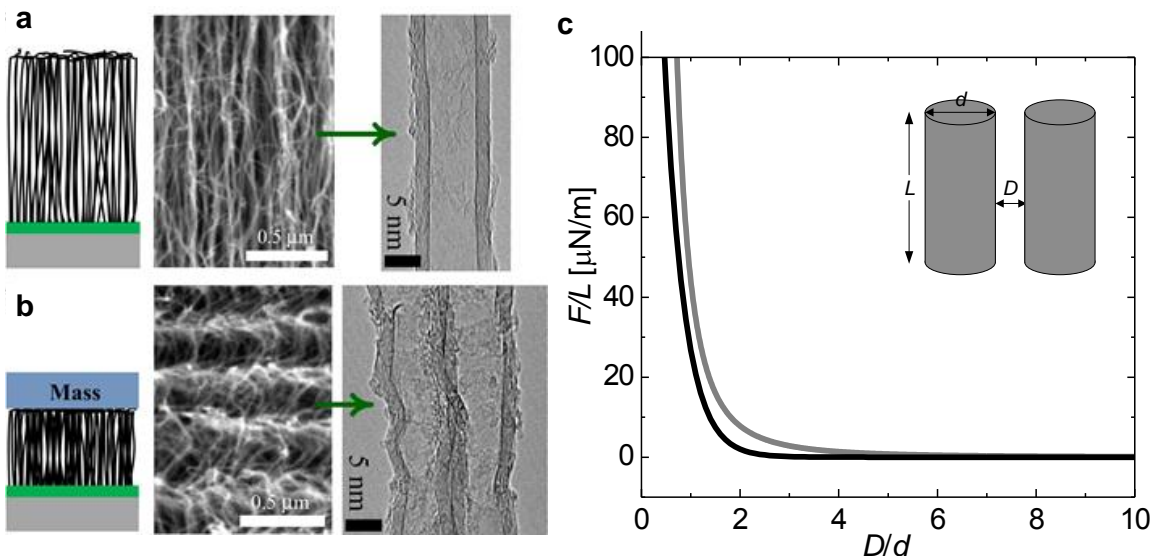
Figure 2.6 Effect of mechanical forces on CNT ensembles. CNT forests grown (a) without and (b) with an applied static compressive force, demonstrating that mechanical forces cause significant defects in the CNTs during growth. Adapted with permission from *Nano Letters* 2006, 6, 1254-1260. Copyright © 2006 American Chemical Society. (c) Model of van der Waals attraction between a pair of parallel CNTs (10 nm diameter, gray) and a pair of CNT bundles (10 µm diameter, black curve). Force per unit length is calculated for a range of *D* values, normalized by *d*, for each case. Reprinted with permission from *Microelectronic Engineering* 2010, 1233-1238. Copyright © 2010 Elsevier.

by the presence of H_2O,[81] which may be attributed to different concentrations of H_2O used and warrants further investigation because arresting coarsening is important for prolonging growth and achieving uniform CNT packing.

As alluded to earlier, deleterious carbon species are generated in concert with desirable precursors, and this results in competing pathways between accumulation of "good" and "bad" carbon.[124] For instance, thermal decomposition and rearrangement of C_2H_4 and H_2 leads to the generation of polycyclic aromatic hydrocarbons (PAHs) in the parts per billion range.[106] Despite suggestions that select PAHs (*i.e.*, fluoranthene) may be associated with formation of the CNT "cap" during nucleation,[109] PAHs are generally considered not helpful for CNT growth because of their tendency to either physisorb to surfaces (*e.g.*, catalyst) and/or lead to formation of soot.[63, 106, 125] The connection between precursor chemistry and carbonaceous impurities is highlighted by experimental results showing increased accumulation of amorphous carbon with both gas temperature[40] and growth time.[125]

In order to describe CNT growth, models for an individual CNT have been developed in order to describe several of the competing mechanisms, including gas dissociation, atomic diffusion over the catalyst, and accumulation of impurities.[63, 104, 121, 123, 126-128] Some models have captured important characteristic features of CNT growth kinetics curves, such as the initial acceleration[104] (bottom of S-shape) and abrupt termination (top of S-shape),[123] and notably, Puretzky, *et al.* adapted their model to reveal diameter-dependent kinetics.[83] Chirality-dependent growth rates have also been reported elsewhere both theoretically[129] and experimentally.[130]

2.2.4 Collective growth and physical interactions

Despite many promising insights derived from models of individual CNT growth, they fail to accurately describe the dynamics of CNT *populations* that are inherent in forest growth.[19, 82] That is, forest growth results from the collective behavior of many CNTs, which have a distribution of diameters and thus growth rates.[83] The proximity of CNTs within a forest allows for interactions among neighboring CNTs and along their lengths. For instance, my calculations in **Figure 2.6** show that van der Waals forces are sufficient at short distances to induce bending and maintain coupling between CNTs and CNT bundles (**Figure 2.6**),[131, 132] which partially explains the ubiquitously tortuous morphology of CNT forests and demonstrates that mechanical forces can inhibit growth.[d] Externally applied forces can induce micro- and nanoscale morphological perturbations in CNTs,[133] which highlights the importance of mechanical forces and furthers the notion that coupling among CNTs may frustrate growth of individual CNTs. Han *et al.* proposed that CNT-CNT coupling within a forest can cause termination,[134] which is supported by phenomenological observations that slow-growing or terminated CNTs could influence adjacent CNTs.[135] Here, they model force coupling as a network of springs, and termination occurs in one CNT when the mechanical energy from neighboring springs becomes greater than the input chemical energy at the catalyst, and thus termination propagates throughout the forest thereafter. Initial *ex situ* observations

---

[d] For instance, when CNTs are in contact ($D/d \approx 0.02$)[120] the coupling force due to van der Waals can be as much as 80 nN for a contact length L of 100 nm. This may easily constrain a growing CNT since this far exceeds the mechanical force output measured from a single CNT (0.16 nN).[133]
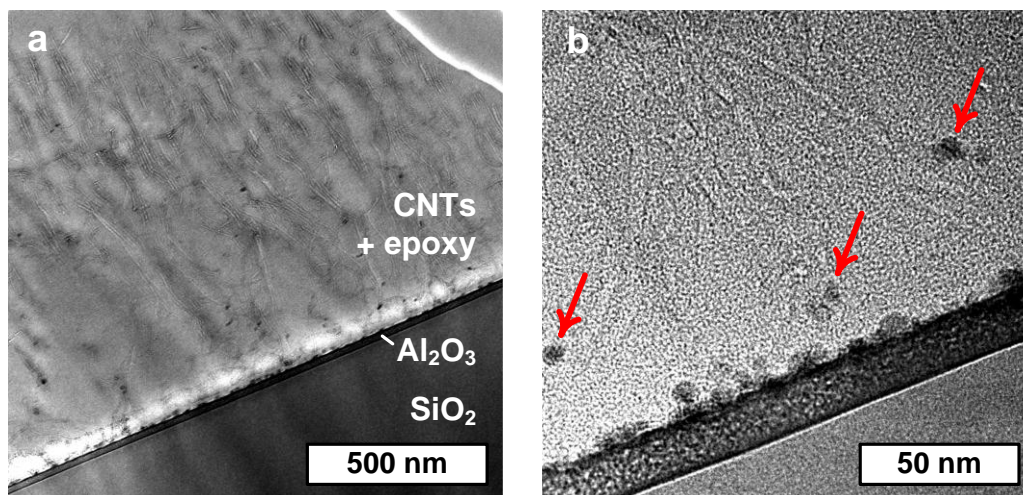
Figure 2.7 Cross-sectional view of CNT forest 5 min growth in C_2H_4/H_2. (a-b) Cross-sectional TEM of CNTs at different magnifications, which were embedded in an epoxy matrix after growth. Many catalyst particles appear to have detached from the Al_2O_3 support as the result of coupling between CNTs. (Specimen prepared by E. Meshot and TEM imaging was performed by Jiaming Zhang.)

by cross-sectional TEM (**Figure 2.7**) also show that CNTs and catalysts may detach from the substrate during growth, which may be due to these force-coupling mechanisms discussed.

The ensemble length of CNTs is inevitably governed by these interactions, and the height of the forest is not only an underestimation of the real length of the CNTs,[136] but due to these collective effects, many CNTs do not even span the entire forest height; the height has been found to continue increasing during growth as CNT number density decays.[19] Understanding these effects is critical to engineering uniformly long CNT forests. To my knowledge, the largest ensemble length (*i.e.*, height) of a CNT forest has been recorded at 18 mm;[122, 137] however, the longest recorded freestanding CNT is 18.5 cm.[138] It is not a coincidence that the longest CNTs are made by a horizontally aligned CVD method that the typically low densities found in horizontal growth. This process involves CNTs growing perpendicularly to a raised line of catalyst on a substrate, horizontally grown aligned CNTs have been found to grow by the so-called "kite mechanism", whereby the catalyst floats and is carried in the direction of gas flow as the CNT grows.[139] All of these features of horizontal growth results in significantly fewer
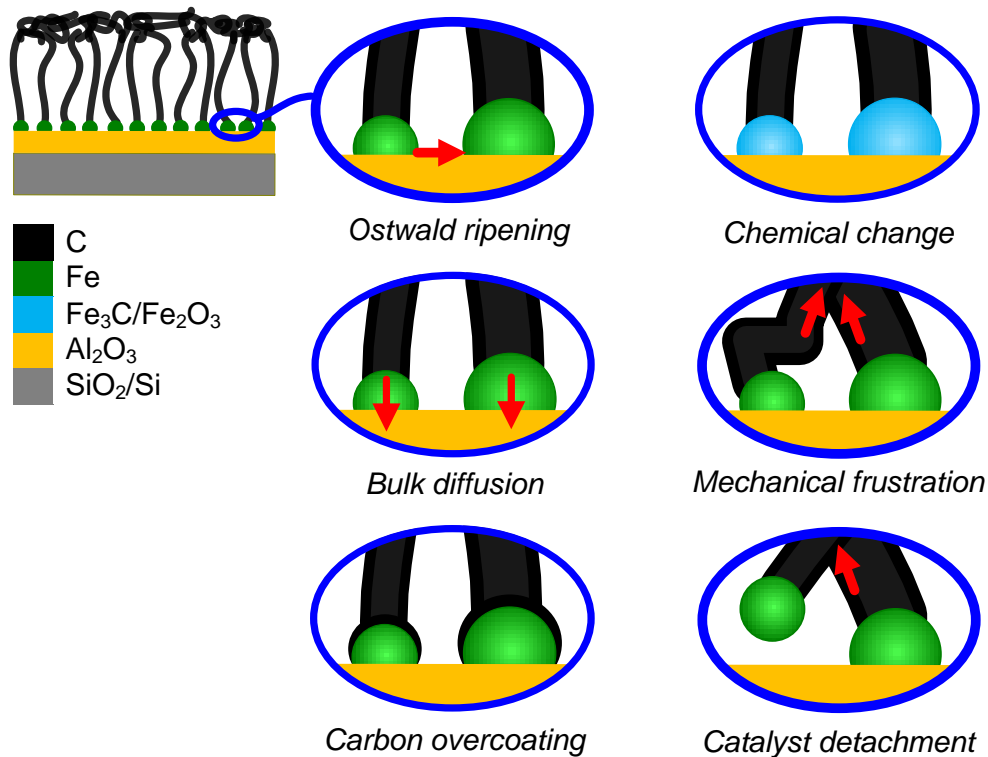
Figure 2.8 Proposed mechanisms of CNT growth termination. Schematics showing the interaction of adjacent Fe catalyst particles adhered to an Al_2O_3 support layer each with an attached CNT.

interactions between neighboring CNTs and with the substrate, so the CNTs experience fewer mechanical constraints, which allows growth of ultra long CNTs.

2.2.5 Mechanisms of growth termination

Understanding exactly how each factor contributes to growth is vital for controlling growth and overcoming self-termination, the latter of which has not yet been accomplished. In **Figure 2.8**, I summarize the current understanding of the possible mechanisms governing growth termination, as discussed in previous sections. Several of the proposed mechanisms likely act in concert to slow or cease growth, which makes diagnosing growth termination a challenging problem.

2.3 Conclusions

CNT forest growth is a multi-stage process, involving formation of catalyst particles, nucleation and self-organization of CNTs, followed by steady growth and eventually density begins to decay until growth terminates. I have discussed several factors that govern each of these stages and the resultant properties of the forest. To engineer the functional properties of CNT materials such as forests, I must develop reaction processes that not only treat the stages of forest growth independently, but that are also accompanied by characterization techniques that enable mapping of the forest characteristics for large sample sizes and populations. In the following chapters, I employ unique synthesis approaches and multi-dimensional characterization to reveal the governing chemical and physical phenomena of CNT forest growth.

2.4 References

1. Nessim, G. D., Properties, synthesis, and growth mechanisms of carbon nanotubes with special focus on thermal chemical vapor deposition. *Nanoscale* 2010, 2, 1306-1323.

2. See, C. H.; Harris, A. T., A review of carbon nanotube synthesis via fluidized-bed chemical vapor deposition. *Industrial & Engineering Chemistry Research* 2007, 46, 997-1012.

3. Puretzky, A. A.; Geohegan, D. B.; Fan, X.; Pennycook, S. J., In situ imaging and spectroscopy of single-wall carbon nanotube synthesis by laser vaporization. *Applied Physics Letters* 2000, 76, 182-184.

4. Yuan, L.; Saito, K.; Hu, W.; Chen, Z., Ethylene flame synthesis of well-aligned multi-walled carbon nanotubes. *Chemical Physics Letters* 2001, 346, 23-28.

5. Zhou, Q.; Li, C.; Gu, F.; Du, H. L., Flame synthesis of carbon nanotubes with high density on stainless steel mesh. *Journal of Alloys and Compounds* 2008, 463, 317-322.

6. Iijima, S., Helical microtubules of graphitic carbon. *Nature* 1991, 354, 56-58.
7. Ebbesen, T. W.; Ajayan, P. M., Large-scale synthesis of carbon nanotubes. *Nature* 1992, 358, 220-222.

8. Meyyappan, M.; Delzeit, L.; Cassell, A.; Hash, D. Carbon nanotube growth by PECVD: a review. *Plasma Sources Science and Technology* 2003, 12, 205.

9. Bondi, S. N.; Lackey, W. J.; Johnson, R. W.; Wang, X.; Wang, Z. L., Laser assisted chemical vapor deposition synthesis of carbon nanotubes and their characterization. *Carbon* 2006, 44, 1393-1403.

10. Moisala, A.; Nasibulin, A.; Kauppinen, E., The role of metal nanoparticles in the catalytic production of single-walled carbon nanotubes - a review. *Journal Of Physics-Condensed Matter* 2003, 15, S3011-S3035.

11. Nasibulin, A.; Pikhitsa, P.; Jiang, H.; Kauppinen, E., Correlation between catalyst particle and single-walled carbon nanotube diameters. *Carbon* 2005, 43, 2251-2257.

12. Li, Y.-L.; Kinloch, I. A.; Windle, A. H., Direct spinning of carbon nanotube fibers from chemical vapor deposition synthesis. *Science* 2004, 304, 276-278.

13.   Zhu, H. W.; Xu, C. L.; Wu, D. H.; Wei, B. Q.; Vajtai, R.; Ajayan, P. M., Direct synthesis of long single-walled carbon nanotube strands. *Science* 2002, 296, 884-886.

14.   Zheng, L. X.; O'Connell, M. J.; Doorn, S. K.; Liao, X. Z.; Zhao, Y. H.; Akhadov, E. A.; Hoffbauer, M. A.; Roop, B. J.; Jia, Q. X.; Dye, R. C.; Peterson, D. E.; Huang, S. M.; Liu, J.; Zhu, Y. T., Ultralong single-wall carbon nanotubes. *Nature Materials* 2004, 3, 673-676.

15.   Yuan, D.; Ding, L.; Chu, H.; Feng, Y.; McNicholas, T. P.; Liu, J., Horizontally aligned single-walled carbon nanotube on quartz from a large variety of metal catalysts. *Nano Letters* 2008, 8, 2576-2579.

16.   Lee, D. C.; Mikulec, F. V.; Korgel, B. A., Carbon nanotube synthesis in supercritical toluene. *Journal of the American Chemical Society* 2004, 126, 4951-4957.

17.   Jasti, R.; Bhattacharjee, J.; Neaton, J. B.; Bertozzi, C. R., Synthesis, characterization, and theory of [9]-, [12]-, and [18]cycloparaphenylene: carbon nanohoop structures. *Journal of the American Chemical Society* 2008, 130, 17646-17647.

18.   Fan, S. S.; Chapline, M. G.; Franklin, N. R.; Tombler, T. W.; Cassell, A. M.; Dai, H. J., Self-oriented regular arrays of carbon nanotubes and their field emission properties. *Science* 1999, 283, 512-514.

19.   Bedewy, M.; Meshot, E.; Guo, H.; Verploegen, E.; Lu, W.; Hart, A., Collective Mechanism for the Evolution and Self-Termination of Vertically Aligned Carbon Nanotube Growth. *Journal of Physical Chemistry C* 2009, 113, 20576-20582.

20.   Hart, A.; Slocum, A., Rapid growth and flow-mediated nucleation of millimeter-scale aligned carbon nanotube structures from a thin-film catalyst. *Journal of Physical Chemistry B* 2006, 110, 8250-8257.

21.   Lee, D. H.; Shin, D. O.; Lee, W. J.; Kim, S. O., Hierarchically Organized Carbon Nanotube Arrays from Self-Assembled Block Copolymer Nanotemplates. *Advanced Materials* 2008, 20, 2480-2485.

22.   Bennett, R. D.; Hart, A. J.; Cohen, R. E., Controlling the morphology of carbon nanotnbe films by varying the areal density of catalyst nanoclusters using block-copolymer micellar thin films. *Advanced Materials* 2006, 18, 2274.

23.   Hersam, M. C., Progress towards monodisperse single-walled carbon nanotubes. *Nature Nanotechnology* 2008, 3, 387-394.

24.   Cao, Q.; Rogers, J. A., Ultrathin films of single-walled carbon nanotubes for electronics and sensors: a review of fundamental and applied aspects. *Advanced Materials* 2009, 21, 29-53.

25.   Holt, J.; Park, H.; Wang, Y.; Stadermann, M.; Artyukhin, A.; Grigoropoulos, C.; Noy, A.; Bakajin, O., Fast mass transport through sub-2-nanometer carbon nanotubes. *Science* 2006, 312, 1034-1037.

26.   Hinds, B.; Chopra, N.; Rantell, T.; Andrews, R.; Gavalas, V.; Bachas, L., Aligned multiwalled carbon nanotube membranes. *Science* 2004, 303, 62-65.

27.   Kempa, K.; Kimball, B.; Rybczynski, J.; Huang, Z. P.; Wu, P. F.; Steeves, D.; Sennett, M.; Giersig, M.; Rao, D. V. G. L. N.; Carnahan, D. L.; Wang, D. Z.; Lao, J. Y.; Li, W. Z.; Ren, Z. F., Photonic crystals based on periodic arrays of aligned carbon nanotubes. *Nano Letters* 2002, 3, 13-18.

28.   Lidorikis, E.; Ferrari, A. C., Photonics with multiwall carbon nanotube arrays. *ACS Nano* 2009, 3, 1238-1248.

29.   Huang, H.; Liu, C. H.; Wu, Y.; Fan, S. S., Aligned carbon nanotube composite films for thermal management. *Advanced Materials* 2005, 17, 1652.

30.   Tong, T.; Zhao, Y.; Delzeit, L.; Kashani, A.; Meyyappan, M.; Majumdar, A., Dense, vertically aligned multiwalled carbon nanotube arrays as thermal interface materials. *IEEE Transactions on Components and Packaging Technologies* 2007, 30, 92-100.

31.   Jakubinek, M. B.; White, M. A.; Li, G.; Jayasinghe, C.; Cho, W.; Schulz, M. J.; Shanov, V., Thermal and electrical conductivity of tall, vertically aligned carbon nanotube arrays. *Carbon* 2010, 48, 3947-3952.

32.   Nihei, M.; Horibe, M.; Kawabata, A.; Awano, Y., Simultaneous formation of multiwall carbon nanotubes and their end-bonded ohmic contacts to Ti electrodes for future ULSI interconnects. *Japanese Journal of Applied Physics, Part 1* 2004, 43, 1856-9.

33.   Horibe, M.; Nihei, M.; Kondo, D.; Kawabata, A.; Awano, Y., Carbon nanotube growth technologies using tantalum barrier layer for future ULSIs with Cu/low-k interconnect processes. *Japanese Journal of Applied Physics, Part 1* 2005, 44, 5309-5312.

34.   Nihei, M.; Kawabata, A.; Kondo, D.; Horibe, M.; Sato, S.; Awano, Y., Electrical properties of carbon nanotube bundles for future via interconnects. *Japanese Journal of Applied Physics, Part 1* 2005, 44, 1626-1628.

35.   Kreupl, F.; Graham, A. P.; Duesberg, G. S.; Steinhogl, W.; Liebau, M.; Unger, E.; Honlein, W., Carbon nanotubes in interconnect applications. *Microelectronic Engineering* 2002, 64, 399-408.

36.   Chiodarelli, N.; Li, Y.; Cott, D. J.; Mertens, S.; Perys, N.; Heyns, M.; De Gendt, S.; Groeseneken, G.; Vereecken, P. M., Integration and electrical characterization of carbon nanotube via interconnects. *Microelectronic Engineering* 2010.

37.   Wei, Y.; Eres, G.; Merkulov, V.; Lowndes, D., Effect of catalyst film thickness on carbon nanotube growth by selective area chemical vapor deposition. *Applied Physics Letters* 2001, 78, 1394-1396.

38.   Zhao, B.; Futaba, D. N.; Yasuda, S.; Akoshima, M.; Yamada, T.; Hata, K., Exploring advantages of diverse carbon nanotube forests with tailored structures synthesized by supergrowth from engineered catalysts. *ACS Nano* 2009, 3, 108-114.

39.   Chen, Y.; Zhang, J., Diameter controlled growth of single-walled carbon nanotubes from SiO_2 nanoparticles. *Carbon* 2011, 49, 3316-3324.

40.   Meshot, E.; Plata, D.; Tawfick, S.; Zhang, Y.; Verploegen, E.; Hart, A., Engineering vertically aligned carbon nanotube growth by decoupled thermal treatment of precursor and catalyst. *ACS Nano* 2009, 3, 2477-2486.

41.   Nessim, G. D.; Hart, A. J.; Kim, J. S.; Acquaviva, D.; Oh, J.; Morgan, C. D.; Seita, M.; Leib, J. S.; Thompson, C. V., Tuning of vertically-aligned carbon nanotube diameter and areal density through catalyst pre-treatment. *Nano Letters* 2008, 8, 3587-3593.

42.   Ishida, M.; Hongo, H.; Nihey, F.; Ochiai, Y., Diameter-controlled carbon nanotubes grown from lithographically defined nanoparticles. *Japanese Journal of Applied Physics, Part 2* 2004, 43, L1356-L1358.

43.   Nerushev, O. A.; Dittmar, S.; Morjan, R. E.; Rohmund, F.; Campbell, E. E. B., Particle size dependence and model for iron-catalyzed growth of carbon nanotubes by thermal chemical vapor deposition. *Journal of Applied Physics* 2003, 93, 4185-4190.

44.   Rümmeli, M. H.; Schäffel, F.; Kramberger, C.; Gemming, T.; Bachmatiuk, A.; Kalenczuk, R. J.; Rellinghaus, B.; Büchner, B.; Pichler, T., Oxide-driven carbon nanotube growth in supported catalyst CVD. *Journal of the American Chemical Society* 2007, 129, 15772-15773.

45.   Hofmann, S.; Sharma, R.; Ducati, C.; Du, G.; Mattevi, C.; Cepek, C.; Cantoro, M.; Pisana, S.; Parvez, A.; Cervantes-Sodi, F.; Ferrari, A. C.; Dunin-Borkowski, R.; Lizzit, S.; Petaccia, L.; Goldoni, A.; Robertson, J., In situ observations of catalyst

dynamics during surface-bound carbon nanotube nucleation. *Nano Letters* 2007, 7, 602-608.

46. Helveg, S.; Lopez-Cartes, C.; Sehested, J.; Hansen, P. L.; Clausen, B. S.; Rostrup-Nielsen, J. R.; Abild-Pedersen, F.; Norskov, J. K., Atomic-scale imaging of carbon nanofibre growth. *Nature* 2004, 427, 426-429.

47. Zhu, H.; Suenaga, K.; Hashimoto, A.; Urita, K.; Hata, K.; Iijima, S., Atomic-resolution imaging of the nucleation points of single-walled carbon nanotubes. *Small* 2005, 1, 1180-1183.

48. Reich, S.; Li, L.; Robertson, J., Control the chirality of carbon nanotubes by epitaxial growth. *Chemical Physics Letters* 2006, 421, 469-472.

49. Harutyunyan, A. R.; Chen, G.; Paronyan, T. M.; Pigos, E. M.; Kuznetsov, O. A.; Hewaparakrama, K.; Kim, S. M.; Zakharov, D.; Stach, E. A.; Sumanasekera, G. U., Preferential growth of single-walled carbon nanotubes with metallic conductivity. *Science* 2009, 326, 116-120.

50. Reich, S.; Li, L.; Robertson, J., Structure and formation energy of carbon nanotube caps. *Physical Review B* 2005, 72.

51. Chiang, W.-H.; Mohan Sankaran, R., Linking catalyst composition to chirality distributions of as-grown single-walled carbon nanotubes by tuning NixFe1-x nanoparticles. *Nature Materials* 2009, 8, 882-886.

52. Chiang, W.-H.; Sakr, M.; Gao, X. P. A.; Sankaran, R. M., Nanoengineering NixFe1−x catalysts for gas-phase, selective synthesis of semiconducting single-walled carbon nanotubes. *ACS Nano* 2009.

53. Ishigami, N.; Ago, H.; Imamoto, K.; Tsuji, M.; Iakoubovskii, K.; Minami, N., Crystal plane dependent growth of aligned single-walled carbon nanotubes on sapphire. *Journal of the American Chemical Society* 2008, 130, 9918-9924.

54. Bachilo, S. M.; Balzano, L.; Herrera, J. E.; Pompeo, F.; Resasco, D. E.; Weisman, R. B., Narrow (n,m)-distribution of single-walled carbon nanotubes grown using a solid supported catalyst. *Journal of the American Chemical Society* 2003, 125, 11186-11187.

55. Ding, L.; Tselev, A.; Wang, J.; Yuan, D.; Chu, H.; McNicholas, T. P.; Li, Y.; Liu, J., Selective growth of well-aligned semiconducting single-walled carbon nanotubes. *Nano Letters* 2009, 9, 800-805.

56. Bennett, R. D.; Xiong, G. Y.; Ren, Z. F.; Cohen, R. E., Using block copolymer micellar thin films as templates for the production of catalysts for carbon nanotube growth. *Chemistry of Materials* 2004, 16, 5589-5595.

57. Lee, D. H.; Lee, W. J.; Kim, S. O., Vertical single-walled carbon nanotube arrays via block copolymer lithography. *Chemistry of Materials* 2009, 21, 1368-1374.

58. Esconjauregui, S.; Fouquet, M.; Bayer, B.; Ducati, C.; Smajda, R.; Hofmann, S.; Robertson, J., Growth of ultrahigh density vertically aligned carbon nanotube forests for interconnects. *ACS Nano* 2010, 4, 7431-7436.

59. Esconjauregui, S.; Fouquet, M.; Bayer, B.; Eslava, S.; Khachadorian, S.; Hofmann, S.; Robertson, J., Manipulation of the catalyst-support interactions for inducing nanotube forest growth. *Journal of Applied Physics* 2011, 109.

60. Esconjauregui, S.; Bayer, B.; Fouquet, M.; Wirth, C.; Yan, F.; Xie, R.; Ducati, C.; Baehtz, C.; Castellarin-Cudia, C.; Bhardwaj, S.; Cepek, C.; Hofmann, S.; Robertson, J., Use of plasma treatment to grow carbon nanotube forests on TiN substrate. *Journal of Applied Physics* 2011, 109.

61. Yoshihara, K.; Honda, S.; Lee, J.; Mori, H.; Oura, K.; Katayama, M., High-density growth of vertically aligned carbon nanotubes with high linearity by catalyst preheating in acetylene atmosphere. *Japanese Journal of Applied Physics* 2008, 47, 1941-1943.

62. Hofmann, S.; Csanyi, G.; Ferrari, A. C.; Payne, M. C.; Robertson, J., Surface diffusion: the low activation energy path for nanotube growth. *Physical Review Letters* 2005, 95, 036101-4.

63. Puretzky, A.; Geohegan, D.; Jesse, S.; Ivanov, I.; Eres, G., In situ measurements and modeling of carbon nanotube array growth kinetics during chemical vapor deposition. *Applied Physics A-Materials Science & Processing* 2005, 81, 223-240.

64. Takagi, D.; Homma, Y.; Hibino, H.; Suzuki, S.; Kobayashi, Y., Single-walled carbon nanotube growth from highly activated metal nanoparticles. *Nano Letters* 2006, 6, 2642-2645.

65. Noda, S.; Sugime, H.; Osawa, T.; Tsuji, Y.; Chiashi, S.; Murakami, Y.; Maruyama, S., A simple combinatorial method to discover Co–Mo binary catalysts that grow vertically aligned single-walled carbon nanotubes. *Carbon* 2006, 44, 1414-1419.

66. Rao, R.; Eyink, K. G.; Maruyama, B., Single-walled carbon nanotube growth from liquid gallium and indium. *Carbon* 2010, 48, 3971-3973.

67. Curtarolo, S.; Awasthi, N.; Setyawan, W.; Jiang, A.; Bolton, K.; Tokune, T.; Harutyunyan, A. R., Influence of Mo on the Fe:Mo:C nanocatalyst thermodynamics for single-walled carbon nanotube growth. *Physical Review B* 2008, 78, 054105.

68.   Ritschel, M.; Leonhardt, A.; Elefant, D.; Oswald, S.; Büchner, B., Rhenium-catalyzed growth carbon nanotubes. *Journal of Physical Chemistry C* 2007, 111, 8414-8417.

69.   Steiner, S. A.; Baumann, T. F.; Bayer, B. C.; Blume, R.; Worsley, M. A.; MoberlyChan, W. J.; Shaw, E. L.; Schlögl, R.; Hart, A. J.; Hofmann, S.; Wardle, B. L., Nanoscale zirconia as a nonmetallic catalyst for graphitization of carbon and growth of single- and multiwall carbon nanotubes. *Journal of the American Chemical Society* 2009, 131, 12144-12154.

70.   Takagi, D.; Hibino, H.; Suzuki, S.; Kobayashi, Y.; Homma, Y., Carbon nanotube growth from semiconductor nanoparticles. *Nano Letters* 2007, 7, 2272-2275.

71.   Christensen, C. H.; Norskov, J. K., A molecular view of heterogeneous catalysis. *Journal of Chemical Physics* 2008, 128, 182503-8.

72.   Hammer, B., Special sites at noble and late transition metal catalysts. *Topics in Catalysis* 2006, 37, 3-16.

73.   Valden, M.; Lai, X.; Goodman, D. W., Onset of catalytic activity of gold clusters on titania with the appearance of nonmetallic properties. *Science* 1998, 281, 1647-1650.

74.   Hans-Joachim, F., Clusters and islands on oxides: from catalysis via electronics and magnetism to optics. *Surface Science* 2002, 500, 271-299.

75.   Wagner, R.; Ellis, W., Vapor-liquid-solid mechanism of crystal growth. *Journal of Metals* 1964, 16, 761-&.

76.   Sushumna, I.; Ruckenstein, E., Role of physical and chemical interactions in the behavior of supported metal catalysts: iron on alumina - a case study. *Journal of Catalysis* 94, 239-288.

77.   Haller, G. L.; Resasco, D. E., Metal-support interaction: group VIII metals and reducible oxides. In *Advances in Catalysis*. Academic Press: 1989; Vol. Volume 36, pp 173-235.

78.   Anderson, P.; Rodriguez, N., Influence of the support on the structural characteristics of carbon nanofibers produced from the metal-catalyzed decomposition of ethylene. *Chemistry of Materials* 2000, 12, 823-830.

79.   Tauster, S. J., Strong metal-support interactions. *Accounts of Chemical Research* 2002, 20, 389-394.

80. Amama, P. B.; Pint, C. L.; Kim, S. M.; McJilton, L.; Eyink, K. G.; Stach, E. A.; Hauge, R. H.; Maruyama, B., Influence of alumina type on the evolution and activity of alumina-supported Fe catalysts in single-walled carbon nanotube carpet growth. *ACS Nano* 2010, 4, 895-904.

81. Hasegawa, K.; Noda, S., Millimeter-tall single-walled carbon nanotubes rapidly grown with and without water. *ACS Nano* 2011, 5, 975-984.

82. Bedewy, M.; Meshot, E. R.; Reinker, M. J.; Hart, A. J., Population growth dynamics of carbon nanotubes. *ACS Nano* 2011, 5, 8974-8989.

83. Geohegan, D. B.; Puretzky, A. A.; Jackson, J. J.; Rouleau, C. M.; Eres, G.; More, K. L., Flux-dependent growth kinetics and diameter selectivity in single-wall carbon nanotube arrays. *ACS Nano* 2011, 5, 8311-8321.

84. Yasuda, S.; Futaba, D. N.; Yamada, T.; Yumura, M.; Hata, K., Gas dwell time control for rapid and long lifetime growth of single-walled carbon nanotube forests. *Nano Letters* 2011.

85. Boffa, A. B.; Lin, C.; Bell, A. T.; Somorjai, G. A., Lewis acidity as an explanation for oxide promotion of metals: implications of its importance and limits for catalytic reactions. *Catalysis Letters* 27, 243-249.

86. Mattevi, C.; Wirth, C. T.; Hofmann, S.; Blume, R.; Cantoro, M.; Ducati, C.; Cepek, C.; Knop-Gericke, A.; Milne, S.; Castellarin-Cudia, C.; Dolafi, S.; Goldoni, A.; Schloegl, R.; Robertson, J., In-situ X-ray photoelectron spectroscopy study of catalyst-support interactions and growth of carbon nanotube forests. *Journal of Physical Chemistry C* 2008, 112, 12207-12213.

87. Hofmann, S.; Blume, R.; Wirth, C. T.; Cantoro, M.; Sharma, R.; Ducati, C.; Havecker, M.; Zafeiratos, S.; Schnoerch, P.; Oestereich, A.; Teschner, D.; Albrecht, M.; Knop-Gericke, A.; Schlogl, R.; Robertson, J., State of transition metal catalysts during carbon nanotube growth. *Journal of Physical Chemistry C* 2009, 113, 1648-1656.

88. Nishimura, K.; Okazaki, N.; Pan, L.; Nakayama, Y., *In situ* study of iron catalysts for carbon nanotube growth using x-ray diffraction analysis. *Japanese Journal of Applied Physics* 2004, 43, 4.

89. de los Arcos, T.; Oelhafen, P.; Thommen, V.; Mathys, D., The influence of catalyst's oxidation degree on carbon nanotube growth as a substrate-independent parameter. *Journal of Physical Chemistry C* 2007, 111, 16392-16396.

90. Forrest, G. A.; Alexander, A. J., Quantitative inhibiting effect of Group I-III cations on the growth of carbon nanotubes. *Carbon* 2008, 46, 818-821.

91. Duan, H.; Ding, F.; Rosén, A.; Harutyunyan, A. R.; Curtarolo, S.; Bolton, K., Size dependent melting mechanisms of iron nanoclusters. *Chemical Physics* 2007, 333, 57-62.

92. Ding, F.; Rosen, A.; Curtarolo, S.; Bolton, K., Modeling the melting of supported clusters. *Applied Physics Letters* 2006, 88, 133110-3.

93. Sharma, R.; Moore, E.; Rez, P.; Treacy, M. M. J., Site-specific fabrication of fe particles for carbon nanotube growth. *Nano Letters* 2009, 9, 689-694.

94. Harutyunyan, A. R.; Tokune, T.; Mora, E., Liquid as a required catalyst phase for carbon single-walled nanotube growth. *Applied Physics Letters* 2005, 87, 051919-3.

95. Kim, S. M.; Pint, C. L.; Amama, P. B.; Zakharov, D. N.; Hauge, R. H.; Maruyama, B.; Stach, E. A., Evolution in catalyst morphology leads to carbon nanotube growth termination. *Journal of Physical Chemistry Letters* 2010, 1, 918-922.

96. Amama, P.; Pint, C.; McJilton, L.; Kim, S.; Stach, E.; Murray, P.; Hauge, R.; Maruyama, B., Role of water in super growth of single-walled carbon nanotube carpets. *Nano Letters* 2009, 9, 44-49.

97. Yao, Y.; Li, Q.; Zhang, J.; Liu, R.; Jiao, L.; Zhu, Y. T.; Liu, Z., Temperature-mediated growth of single-walled carbon-nanotube intramolecular junctions. *Nature Materials* 2007, 6, 283-286.

98. Zhu, W.; Rosen, A.; Bolton, K., Changes in single-walled carbon nanotube chirality during growth and regrowth. *Journal of Chemical Physics* 2008, 128, 124708-6.

99. Ma, J.; Alfe, D.; Michaelides, A.; Wang, E., Stone-Wales defects in graphene and other planar sp^2-bonded materials. *Physical Review B* 2009, 80, 033407-4.

100. Marcos, P. A.; López, M. J.; Rubio, A.; Alonso, J. A., Thermal road for fullerene annealing. *Chemical Physics Letters* 1997, 273, 367-370.

101. Plata, D.; Meshot, E.; Reddy, C.; Hart, A.; Gschwend, P., Multiple alkynes react with ethylene to enhance carbon nanotube synthesis, suggesting a polymerization-like formation mechanism. *ACS Nano* 2010, 4, 7185-7192.

102. Nessim, G.; Seita, M.; Plata, D.; O'Brien, K.; Hart, A.; Meshot, E.; Reddy, C.; Gschwend, P.; Thompson, C., Precursor gas chemistry determines the crystallinity of carbon nanotubes synthesized at low temperature. *Carbon* 2011, 49, 804-810.

103. Nessim, G. D.; Seita, M.; O'Brien, K. P.; Hart, A. J.; Bonaparte, R. K.; Mitchell, R. R.; Thompson, C. V., Low temperature synthesis of vertically aligned carbon nanotubes with electrical contact to metallic substrates enabled by thermal decomposition of the carbon feedstock. *Nano Letters* 2009, 9, 3398-3405.

104. Latorre, N.; Romeo, E.; Cazaña, F.; Ubieto, T.; Royo, C.; Villacampa, J. I.; Monzón, A., Carbon nanotube growth by catalytic chemical vapor deposition: a phenomenological kinetic model. *Journal of Physical Chemistry C* 2010, 114, 4773-4782.

105. Jeong, G.-H.; Olofsson, N.; Falk, L. K. L.; Campbell, E. E. B., Effect of catalyst pattern geometry on the growth of vertically aligned carbon nanotube arrays. *Carbon* 2009, 47, 696-704.

106. Plata, D. e. L.; Hart, A. J.; Reddy, C. M.; Gschwend, P. M., Early evaluation of potential environmental impacts of carbon nanotube synthesis by chemical vapor deposition. *Environmental Science & Technology* 2009, 43, 8367-8373.

107. Zhong, G.; Hofmann, S.; Yan, F.; Telg, H.; Warner, J. H.; Eder, D.; Thomsen, C.; Milne, W. I.; Robertson, J., Acetylene: a key growth precursor for single-walled carbon nanotube forests. *Journal of Physical Chemistry C* 2009, 113, 17321-17325.

108. Eres, G.; Rouleau, C. M.; Yoon, M.; Puretzky, A. A.; Jackson, J. J.; Geohegan, D. B., Model for self-assembly of carbon nanotubes from acetylene based on real-time studies of vertically aligned growth kinetics. *Journal of Physical Chemistry C* 2009, 113, 15484-15491.

109. Eres, G.; Kinkhabwala, A. A.; Cui, H.; Geohegan, D. B.; Puretzky, A. A.; Lowndes, D. H., Molecular beam-controlled nucleation and growth of vertically aligned single-wall carbon nanotube arrays. *Journal of Physical Chemistry B* 2005, 109, 16684-16694.

110. Xiang, R.; Einarsson, E.; Okawa, J.; Miyauchi, Y.; Maruyama, S., Acetylene-accelerated alcohol catalytic chemical vapor deposition growth of vertically aligned single-walled carbon nanotubes. *Journal of Physical Chemistry C* 2009, 113, 7511-7515.

111. Zhang, G. Y.; Mann, D.; Zhang, L.; Javey, A.; Li, Y. M.; Yenilmez, E.; Wang, Q.; McVittie, J. P.; Nishi, Y.; Gibbons, J.; Dai, H. J., Ultra-high-yield growth of vertical single-walled carbon nanotubes: hidden roles of hydrogen and oxygen. *Proceedings of the National Academy of Sciences of the United States of America* 2005, 102, 16141-16145.

112. Hata, K.; Futaba, D. N.; Mizuno, K.; Namai, T.; Yumura, M.; Iijima, S., Water-assisted highly efficient synthesis of impurity-free single-waited carbon nanotubes. *Science* 2004, 306, 1362-1364.

113. Yamada, T.; Maigne, A.; Yudasaka, M.; Mizuno, K.; Futaba, D. N.; Yumura, M.; Iijima, S.; Hata, K., Revealing the secret of water-assisted carbon nanotube synthesis by microscopic observation of the interaction of water on the catalysts. *Nano Letters* 2008, 8, 4288-4292.

114. Zhang, Y. Y.; Gregoire, J. M.; van Dover, R. B.; Hart, A. J., Ethanol-promoted high-yield growth of few-walled carbon nanotubes. *Journal of Physical Chemistry C* 2010, 114, 6389-6395.

115. Einarsson, E.; Murakami, Y.; Kadowaki, M.; Maruyama, S., Growth dynamics of vertically aligned single-walled carbon nanotubes from in situ measurements. *Carbon* 2008, 46, 923-930.

116. Maruyama, S.; Einarsson, E.; Murakami, Y.; Edamura, T., Growth process of vertically aligned single-walled carbon nanotubes. *Chemical Physics Letters* 2005, 403, 320-323.

117. Magrez, A.; Seo, J.; Kuznetsov, V.; Forro, L., Evidence of an equimolar C_2H_2-CO_2 reaction in the synthesis of carbon nanotubes. *Angewandte Chemie-International Edition* 2007, 46, 441-444.

118. Magrez, A.; Seo, J. W.; Smajda, R.; Korbely, B.; Andresen, J. C.; Mionić, M.; Casimirius, S. P.; Forró, L. S., Low-temperature, highly efficient growth of carbon nanotubes on functional materials by an oxidative dehydrogenation reaction. *ACS Nano* 2010, 4, 3702–3708.

119. Rao, R.; Pierce, N.; Zhang, X.; Wheeler, R.; Maruyama, B.; Talapatra, S., Understanding the role of sulfur in tuning the diameter and morphology in the chemical vapor deposition growth of carbon nanotubes. *Materials Express* 2011, 1, 7.

120. Barreiro, A.; Kramberger, C.; Rümmeli, M. H.; Grüneis, A.; Grimm, D.; Hampel, S.; Gemming, T.; Büchner, B.; Bachtold, A.; Pichler, T., Control of the single-wall carbon nanotube mean diameter in sulphur promoted aerosol-assisted chemical vapour deposition. *Carbon* 2007, 45, 55-61.

121. Futaba, D.; Hata, K.; Yamada, T.; Mizuno, K.; Yumura, M.; Iijima, S., Kinetics of water-assisted single-walled carbon nanotube synthesis revealed by a time-evolution analysis. *Physical Review Letters* 2005, 95, -.

122. Yun, Y.; Shanov, V.; Tu, Y.; Subramaniam, S.; Schulz, M. J., Growth mechanism of long aligned multiwall carbon nanotube arrays by water-assisted chemical vapor deposition. *Journal of Physical Chemistry B* 2006, 110, 23920-23925.

123. Stadermann, M.; Sherlock, S. P.; In, J.-B.; Fornasiero, F.; Park, H. G.; Artyukhin, A. B.; Wang, Y.; De Yoreo, J. J.; Grigoropoulos, C. P.; Bakajin, O.; Chernov, A. A.; Noy, A., Mechanism and kinetics of growth termination in controlled chemical vapor deposition growth of multiwall carbon nanotube arrays. *Nano Letters* 2009, 9, 738-744.

124. Lacava, A. I.; Bernardo, C. A.; Trimm, D. L., Studies of deactivation of metals by carbon deposition. *Carbon* 1982, 20, 219-223.

125. Yasuda, S.; Hiraoka, T.; Futaba, D. N.; Yamada, T.; Yumura, M.; Hata, K., Existence and kinetics of graphitic carbonaceous impurities in carbon nanotube forests to assess the absolute purity. *Nano Letters* 2009, 9, 769-773.

126. Tibbetts, G. G.; Devour, M. G.; Rodda, E. J., An adsorption-diffusion isotherm and its application to the growth of carbon filaments on iron catalyst particles. *Carbon* 1987, 25, 367-375.

127. Louchev, O.; Laude, T.; Sato, Y.; Kanda, H., Diffusion-controlled kinetics of carbon nanotube forest growth by chemical vapor deposition. *Journal of Chemical Physics* 2003, 118, 7622-7634.

128. Xiang, R.; Yang, Z.; Zhang, Q.; Luo, G.; Qian, W.; Wei, F.; Kadowaki, M.; Einarsson, E.; Maruyama, S., Growth deceleration of vertically aligned carbon nanotube arrays: catalyst deactivation or feedstock diffusion controlled? *Journal of Physical Chemistry C* 2008, 112, 4892-4896.

129. Dumlich, H.; Reich, S., Chirality-dependent growth rate of carbon nanotubes: a theoretical study. *Physical Review B* 2010, 82, 085421.

130. Rao, R.; Maruyama, B. In *Chirality-dependent rates in single-wall carbon nanotube growth*, The Fifth Rice University, Air Force Research Laboratory, and NASA Workshop on Nucleation and Growth Mechanisms of Single Wall Carbon Nanotubes, Bandera, TX USA, 2011.

131. De Volder, M.; Vidaud, D.; Meshot, E.; Tawfick, S.; Hart, A., Self-similar organization of arrays of individual carbon nanotubes and carbon nanotube micropillars. *Microelectronic Engineering* 2010, 1233-1238.

132. Israelachvili, J. N., *Intermolecular and Surface Forces*. 2 ed.; Academic Press: 1992.

133. Hart, A.; Slocum, A., Force output, control of film structure, and microscale shape transfer by carbon nanotube growth under mechanical pressure. *Nano Letters* 2006, 6, 1254-1260.

134. Han, J. H.; Graff, R. A.; Welch, B.; Marsh, C. P.; Franks, R.; Strano, M. S., A mechanochemical model of growth termination in vertical carbon nanotube forests. *ACS Nano* 2008, 2, 53-60.

135. Zhang, Q.; Zhou, W.; Qian, W.; Xiang, R.; Huang, J.; Wang, D.; Wei, F., Synchronous growth of vertically aligned carbon nanotubes with pristine stress in the heterogeneous catalysis process. *Journal of Physical Chemistry C* 2007, 111, 14638-14643.

136. Meshot, E.; Bedewy, M.; Lyons, K.; Woll, A.; Juggernauth, K.; Tawfick, S.; Hart, A., Measuring the lengthening kinetics of aligned nanostructures by spatiotemporal correlation of height and orientation. *Nanoscale* 2010, 896-900.

137. Shanov, V. N.; Gorton, A.; Yun, Y.-H.; Schultz, M. J. Composite catalyst and method for manufacturing carbon nanostructured materials. US Patent Application 2008/095695.

138. Wang, X.; Li, Q.; Xie, J.; Jin, Z.; Wang, J.; Li, Y.; Jiang, K.; Fan, S., Fabrication of ultralong and electrically uniform single-walled carbon nanotubes on clean substrates. *Nano Letters* 2009, 9, 3137-3141.

139. Huang, S.; Woodson, M.; Smalley, R.; Liu, J., Growth mechanism of oriented long single walled carbon nanotubes using "fast-heating" chemical vapor deposition process. *Nano Letters* 2004, 4, 1025-1028.

Chapter 3
Dynamics of catalyst film dewetting
and CNT nucleation

There remains a void in understanding the dynamics of catalyst nanoparticle formation and how this process influences the nucleation and growth of CNTs. In order to manufacture forests with uniform attributes (*e.g.,* diameter, alignment density) it is necessary to understand the temporal and spatial variations in the size and shape of the catalyst particles and CNTs. To this end, I combine *in situ* grazing incidence small-angle X-ray scattering (GISAXS) with complementary *ex situ* AFM analyses to elucidate the rapid dynamics of catalyst particle formation and early stages of forest growth. My findings reveal low-temperature limits for particle formation and CNT nucleation under particular process conditions, and show that significant CNT diameter changes can occur quickly during nucleation and self-organization of CNT forests. Knowledge of these intrinsically rapid processes is vital to improve precision in control of CNT structure (chirality, number of walls), and to synthesis of high-density arrays of long, straight CNTs. Finally, I introduce a novel approach to influence the catalyst dewetting process using ordered nanoporous alumina substrates, and I show initial characterization and CNT growth results from this material system.

3.1   Introduction

Previous studies show evidence of significant evolution during forest growth,[1-6] yet the dynamics of catalyst formation and subsequent CNT nucleation and growth are

largely unknown. Understanding these various processes fundamentally is vital for controlling the resultant properties of CNT forests. Many studies point to correlation in size between catalysts and CNTs,[7-9] and Harutyunyan and coworkers clearly demonstrate the important role of catalyst shape and evolution in influencing the chirality of single-wall (SW) CNTs.[10] In practice, knowing how to control the dewetting of thin films into small particles with low polydispersity is necessary to achieve highly uniform multi-wall (MW) and SWCNT forests as well as other 1-D nanostructures such as semiconductor nanowires.

AFM and TEM are preferred methods for directly imaging and measuring particles, but their typical incompatibility with the high temperatures (500-900 °C) required to anneal thin-film metals and grow CNTs restricts their use to *ex situ* observations or requires special sample preparation. The morphology of the catalyst may be altered in the process of cooling or in the presence of CNT growth, so not only is *ex situ* investigation a misrepresentation of the catalyst during both annealing and CNT growth, but the dynamics of these process are too rapid to be accurately captured *ex situ*. Thus, *in situ* techniques are necessary in order to reveal the rapid dynamics and authentic state of the catalyst. In response to this need, researchers have developed *in situ* methods for studying CNT synthesis such as laser vaporization and absorption spectroscopy,[11] environmental TEM,[3, 4, 10, 12] XPS,[12-14] and Raman spectroscopy;[15] however, many of these require low pressures that are not typical for CVD of CNTs, or do not sample statistically significant numbers of structures (*i.e.*, catalysts or CNTs), or are not suitable for growing forests.

In situ small-angle X-ray scattering (SAXS) has been previously used to probe the synthesis of other nanomaterials, including substrate-bound nanoparticles,[16-18] nanoparticles in solution,[19, 20] and pyrolytic powders.[21-23] In this chapter, I present the first use of grazing incidence small-angle X-ray scattering (GISAXS) for real-time investigation of the dynamics of thin film dewetting and subsequent nucleation and growth of CNTs. This work also includes the first *in situ* scattering studies of the self-organization of CNT forests, which is discussed in Section 4.2.1 of Chapter 4. Combining synchrotron radiation and the use of a high-speed pixel array detector (PAD), I resolve the dynamics of catalyst formation from a thin film, stability of catalyst

39

morphology, nucleation of early CNTs, as well as prolonged CNT growth/evolution. I uniquely quantify *populations* and correlate catalyst size with CNT diameter and alignment at a time resolution of 10 msec. This non-destructive technique allows sampling of statistically significant populations of nanostructures (10^9) at atmospheric pressure without subjecting the material to damaging, high-energy electron beams, such as in TEM and or low pressure, such as in XPS.

3.2   Results and discussion

3.2.1   Experimental setup in G1 Station at CHESS

I study the synthesis of CNT forests from C_2H_4/H_2 precursors, which are first passed through a "pre-heater" ($\approx$ 1040-1070 °C) upstream of the reactor in order to thermally generate the suite of gas compounds necessary for accelerated CNT growth to millimeter heights.[24, 25] I use a bilayer thin-film catalyst, 1-nm Fe film on top of a 10-nm Al_2O_3 support, sequentially deposited by electron-beam evaporation onto (100) Si wafers coated with 100 nm of thermally grown SiO_2.[26] The CVD apparatus is mounted as shown in **Figure 3.1**, directly in the X-ray beampath at the G1 station of the Cornell High-Energy Synchrotron Source (CHESS). A beam energy of 10 ± 0.1 keV is selected with synthetic multilayer optics (W/B4C, 27.1 Å *d*-spacing), and I use a 2-D pixel array detector (PAD)[27, 28] for X-ray imaging at a frame rate of 100 Hz. The PAD was designed, validated, and operated during these experiments by Sol Gruner and colleagues from CHESS. The incident collimated X-ray beam has a height of 100 µm as controlled by slits upstream of the CNT reactor. The catalyst substrate is tilted into the X-ray beam at an angle $\alpha_i = 0.15°$ for grazing incidence, which is near the substrate critical angle for total external reflection.[29] The cold-wall reactor features a resistively heated Si platform upon which the catalyst substrate rests. This enables local heating, rapid temperature control of the catalyst,[30, 31] and modification of the quartz tube with thin polyimide (Kapton) windows that are highly X-ray transmissive (**Figure 3.1b**). Therefore, incident
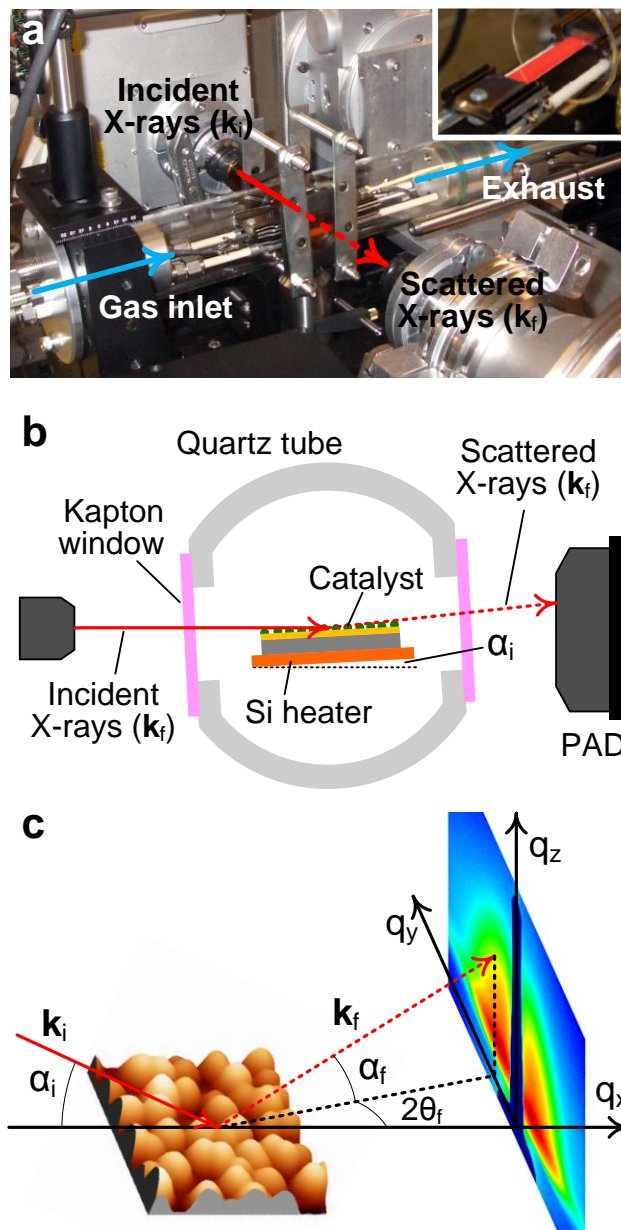
Figure 3.1 Experimental setup and GISAXS configuration. (a) Setup with cold-wall CVD apparatus mounted in the path of the X-ray beam (illustrated by red lines) on 4-axis (x-y-z-α) stage. The quartz tube is modified with Kapton windows. (b) and (c) show the side view geometry of the reactor with respect to the beam, where the sample is positioned at an angle α_i with respect to the incoming X-ray beam ($\mathbf{k}_i$) by rotating the reactor stage, and scattered X-rays ($\mathbf{k}_f$) at an exit angle α_f are collected by a 2-D pixel array detector (PAD).
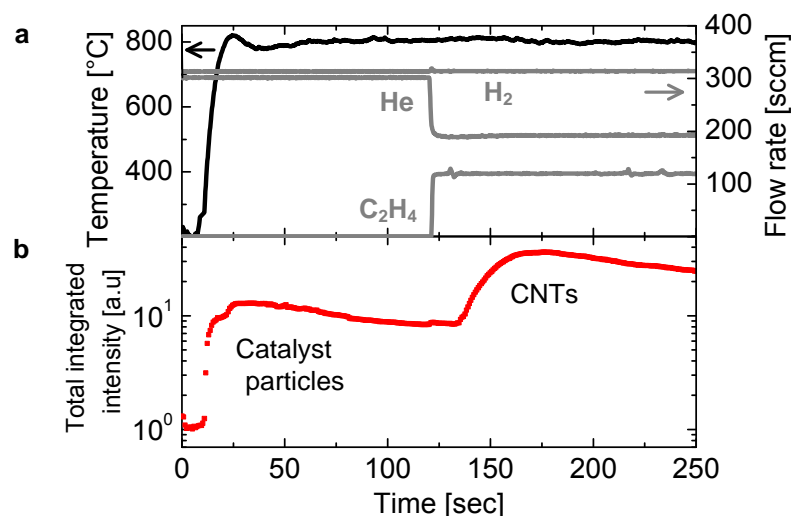
Figure 3.2 CNT synthesis conditions and total scattering intensity. (a) Temperature and gas flow conditions during a representative CNT growth experiment with (b) total integrated scattering intensity showing the onset of particle formation followed by CNT nucleation.

and scattered X-rays pass through the enclosed reactor with minimal parasitic scattering.[32]

The synthesis conditions for a typical experiment are shown in **Figure 3.2**, with total integrated scattering intensity collected by the PAD in **Figure 3.2b**. This demonstrates the ability of this technique to track rapid processes, and generally I observe significant changes in scattering signal upon the initial temperature increase (catalyst particle formation) and then again upon the introduction of hydrocarbon precursors (CNT nucleation). While total intensity gives an indication of the relevant timescales of these processes, I can extract further information about the nanostructure geometry and distribution of sizes from the *shape* of the scattering pattern. The stages of the synthesis process for CNT forests are schematically represented in **Figure 3.3**, along with corresponding *in situ* GISAXS images. This figure provides an overview of the dynamics and their relationship to the scattering patterns, and more in depth discussion of the dynamics follows later. The plots beneath each image show 1-D intensity profiles, $I(q_y)$, that are extracted from the 2-D images and used for fitting of the mathematical scattering model described later. The GISAXS patterns are symmetric about the X-ray beam because the form factor of the catalysts, CNTs, and their organization in the x-y
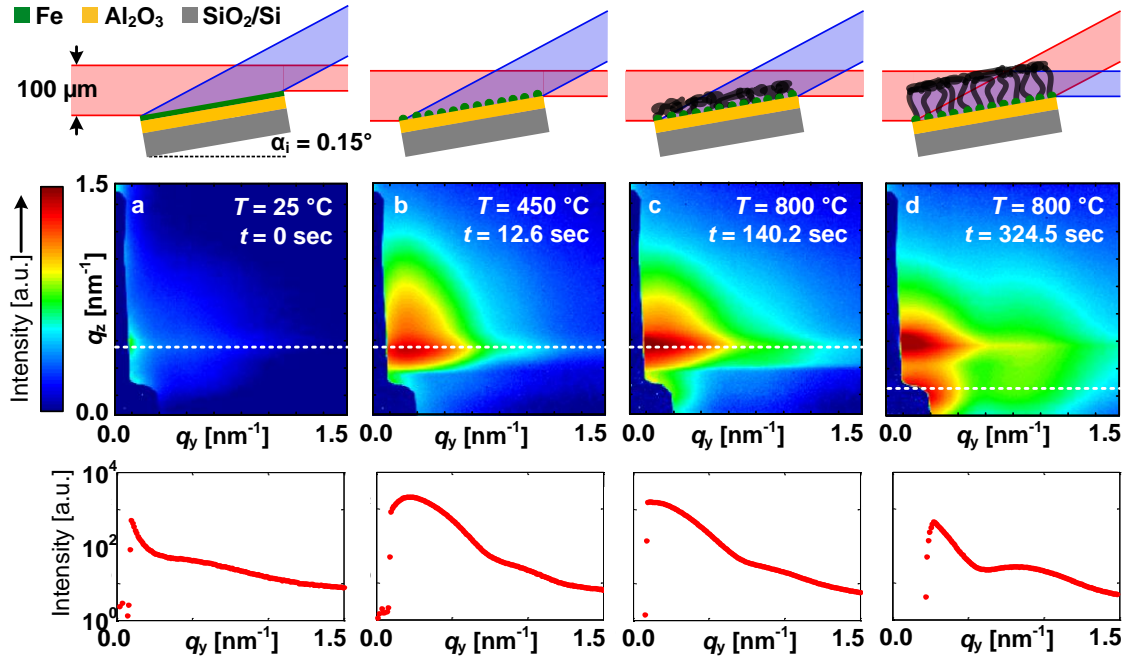
Figure 3.3 GISAXS images of four different stages of the CNT synthesis process: (a) as-deposited Fe/Al_2O_3 film before heating; (b) during rapid heating (Fe particles); (c) nucleation of CNTs (CNTs and Fe particles); and (d) CNT growth (only CNTs observed with transmitted beam). Each 2-D SAXS image corresponds to the schematic of scattering geometry above, and the plot of $I(q_y)$ along the dashed line in the SAXS image. According to the top row schematics, the blue shaded portion of the scattered X-ray beam is used for analysis; for example in d), the transmitted beam corresponds to the white dashed line at a lower position on the detector compared to when the grazing incidence scattering is analyzed (a-c).

plane (substrate) are all isotropic; therefore, only one half of the GISAXS image is required for the analysis in this study. I hereafter refer to q_y as simply q because I only consider this parallel scattering in this work.

To initiate CNT formation, the substrate is first annealed in H_2/He by rapidly heating to 800 °C and holding for 2 min. It is well known that this step causes the Fe film to dewet into particles, which determine the CNT diameter; however, the dynamics of film dewetting and particle size evolution were not previously known. During heating, I observe a distinct and rapid transition from diffuse scattering from the as-deposited Fe/Al_2O_3 film (**Figure 3.3a**) to coherent scattering from well-defined particles (**Figure 3.3b**). After the film dewets, the scattering pattern remains constant for the 2-min annealing step, indicating that particles are quite stable and do not undergo significant coarsening in this timeframe. This is discussed quantitatively in Section 3.2.5.

After CNT growth starts I monitor the transmission beam, but after introduction of C_2H_4 flow and before detecting transmission SAXS, I observe changes in the GISAXS pattern and a significant increase in the total scattered intensity (**Figure 3.3c**), which I attribute to the nucleation of CNTs by deposition of carbon at the Fe catalyst. The time delay between when C_2H_4 is added and the onset of CNT scattering is an apparent induction period during which the concentration of hydrocarbon is transient (*i.e.*, $C_2H=$ is mixing into the reactor with H_2/He), and surpasses the partial pressure sufficient for nucleating CNTs. By real-time monitoring using a quadrapole mass spectrometer (QMS), I estimate the partial pressure of C_2H_4 is 10^{-2} atm after 18 sec, and it takes ~100 sec for the C_2H_4 concentration to reach 90% of its steady state value (0.2 atm) (See **Figure 4.10** in Chapter 4). It is not surprising that nucleation occurs before the steady state partial pressure of C_2H_4 is reached because I have previously shown that only trace amounts (0.01 atm) of alkynes in concert with C_2H_4 are needed for efficient forest growth.[33] For a 100-µm X-ray beam impinging on the 1x1 cm catalyst substrate at $\alpha_i = 0.15°$, I estimate that, before CNT growth, 75 µm of the beam passes over the downstream edge of the substrate without scattering. This portion of the beam is entirely blocked by the lead beamstop and not visible on the detector until the height of the CNT forest increases such that it scatters these X-rays onto a visible area of the detector below the GISAXS features. I use this transmission scattering to monitor and quantify prolonged, vertically aligned CNT growth (**Figure 3.3d**).

3.2.2   Modeling GISAXS of substrate-bound particles

I use the GISAXS data to fit a mathematical model of the particle size and spacing. I adapt the approach of Renaud and coworkers[34] to model the scattering cross section of an arrangement of truncated spheres (particles) on a flat substrate (schematic representation in **Figure 3.4a**). The GISAXS intensity collected from the catalyst particles is proportional to the modulus of the form factor squared $|F(q)|^2$ multiplied by the interference function $S(q)$. That is,

$$I(q) = A|F(q)|^2 S(q). \hspace{4cm} \text{Eq. 1}$$
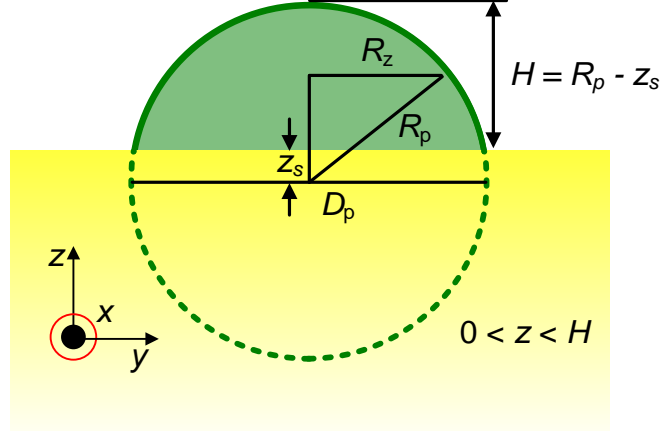
Figure 3.4 Truncated sphere form factor model. Assumes infinitely flat substrate, and height is given by the degree of truncation (H/D_p).

$F(q)$ and $S(q)$ are the Fourier transforms of the catalyst shape and the particle-particle pair correlation function (*i.e.*, spacing), respectively.[17, 29, 35] The overall form factor is

$$|F(q)|^2 = \frac{\int_0^\infty P(R_p){f_p}^2 dR_p}{\int_0^\infty P(R_p) dR_p},$$

Eq. 2

where A is an adjustable constant, R_p is the radius of a sphere (particle) with variance ${\sigma_{R_p}}^2$, and H (height) is the distance from the substrate to the top of a sphere. $P(R_p)$ is the probability density function (PDF) for the population of particle radii, which accounts for the polydispersity in particle size; and f_p is the form factor of the individual scattering body (truncated sphere). There is precedence in literature to suggest that the particles formed by dewetting of a thin film on a flat substrate have a lognormal size distribution,[36, 37] analogous to the size distribution of grain growth;[38] as a result, $P(R_p)$ is assigned a lognormal distribution. I also find that the logarithm of particle height, as measured by AFM in Section 3.2.3, passes a test one-sample Kolmogorov-Smirnov test (99% confidence). Accordingly,

$$P(R_p) = \frac{1}{R_p \sigma_{R_p} \sqrt{2\pi}} \exp\left[\frac{-\left(\ln R_p - \langle R_p \rangle\right)^2}{2{\sigma_{R_p}}^2}\right]$$

Eq. 3

and

$$f_{\mathrm{p}}(q, R_{\mathrm{z}}, H) = \int_0^H 2\pi R_{\mathrm{z}}^2 \frac{J_1(qR_{\mathrm{z}})}{qR_{\mathrm{z}}} \, dz \qquad \text{Eq. 4}$$

In the latter equation, $R_{\mathrm{z}} = (R_{\mathrm{p}}^2 - z^2)^{1/2}$, z is the vertical coordinate and J_1 is a Bessel function of the first kind.

The structure factor represents particle-particle scattering, and I use the structure factor for a 1-D paracrystal, which is locally ordered but lacks long-range order. This is

$$S(q) = \frac{1 - e^{-q^2 \sigma_\delta^2}}{1 + e^{-q^2 \sigma_\delta^2} - 2e^{-\frac{q^2 \sigma_\delta^2}{2}} \cos(q\delta)}, \qquad \text{Eq. 5}$$

where δ is the mean particle spacing with variance σ_δ^2.

According to this model, the spatial distribution of scattered intensity depends on the following parameters of the particles: diameter D_{p} ($2 \times R_{\mathrm{p}}$) and its variance ($\sigma_{D_{\mathrm{p}}}^2$), spacing δ and its variance (σ_δ^2), and height H. Thus, fitting Eq. 1 to linescans, $I(q_{\mathrm{y}})$, from the GISAXS data enables us to extract quantitative, statistical information about the population of metal nanoparticles created by dewetting of the Fe film. Fitting is performed by least-squares error minimization using custom code and the MATLAB curve fitting toolbox.

3.2.3 Quantitative analysis of particles with AFM

In order to validate the GISAXS measurement technique, I compare the fitting results to quantitative analysis of *ex situ* AFM images, which is a standard means of analysis nanoparticles on a substrate. For reference, I prepare a set of samples by annealing Fe/Al_2O_3 at different temperatures and durations, and I probe the catalyst morphology by both GISAXS and AFM for each sample. In the AFM image processing (**Figure 3.5**), I first identify the positions of all local maxima within each image and

46
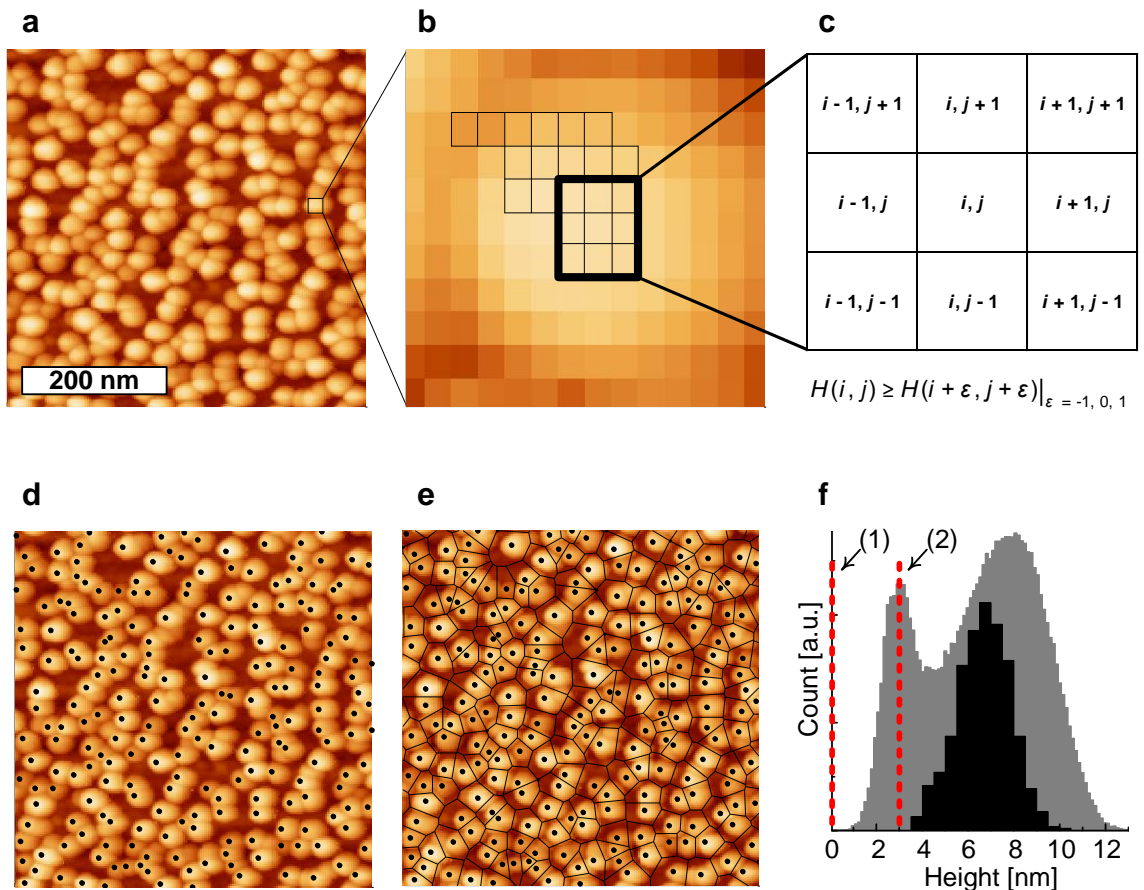
Figure 3.5 Example AFM images of Fe on Al_2O_3 and processing methodology. (a) Fe particles after 2-min annealing in H_2/He at 825 °C with (b) an exploded view of a single particle and (c) schematic of particle-peak finding algorithm. Automated processing (d) finds particle locations based on local maxima and (e) decomposes image into Voronoi cells. (f) Overlaid histograms demonstrate the difference between recorded height of each pixel (grey) versus particle height (black). Particle height is reference from the roughness (mean height) of the alumina support denoted by (2).

decompose the image by Voronoi tessellation. A 2-D Voronoi cell is a convex polygon whose segments are all the points in the line that are equidistant to the two nearest maxima and whose vertices are the points equidistant to three maxima (**Figure 3.5e**). Thus, the Voronoi cell size, defined as the square root of the polygon's area, is a measure of particle-particle nearest-neighbor spacing δ. This type of spatial decomposition is traditionally used to analyze paracrystals, and it applies to substrate bound nanoparticles because they exhibit only short-range order arising from steric effects and local

coarsening. Further, the particle-particle spacing in the GISAXS model has previously been associated with a distribution of Voronoi cell sizes.[18]

Using AFM images, I determine the height H of each particle by the subtracting its maximum from the mean roughness of the Al_2O_3, which ranges from 3-5 nm depending on annealing conditions (**Figure 3.5f**). I consider peak height to be a reliable metric from AFM imaging, because the shape and diameter of a particle is affected by the tip geometry (which changes with time due to wear) and the tip-sample convolution. As a result, recording the peak height of each particle most accurately captures the distribution of sizes, as opposed to tallying every pixel or measuring the curvature of the peaks. In the latter case, larger particles are unfairly weighted because they occupy more pixels than smaller particles.

The summarized results in **Figure 3.6c** and **Figure 3.6d** show that both AFM and GISAXS provide consistent quantitative measures of the mean particle height H and spacing δ, for a variety of annealing conditions that change the film morphology I attribute the discrepancy of H to the Decoupling Approximation (DA) used in the model,[18] which neglects all correlations between size of scattering bodies and their relative position and thus essentially assumes the catalysts have no spatial correlation. While DA is typically only used for diffuse systems because it allows for overlapping of the structures, integrating size-space correlations is challenging for large numbers of images.[34] The GISAXS model also assumes the particles are supported on a flat substrate, whereas the Al_2O_3 support is in fact rough. Nevertheless, my approach that includes these simplifying assumptions yields good agreement with AFM, thus enabling *in situ* measurement of the film and particle dynamics. I also quantify the roughness of the as-deposited Fe film using my GISAXS and AFM analyses in **Figure 3.7**, which again show good agreement and gives an initial roughness of 1.1 nm.

3.2.4   Modeling SAXS of CNTs

The scattering of CNTs (similar to Eq. 1) is described as a population of hollow cylinders with lognormally distributed outer diameters.[24, 39]
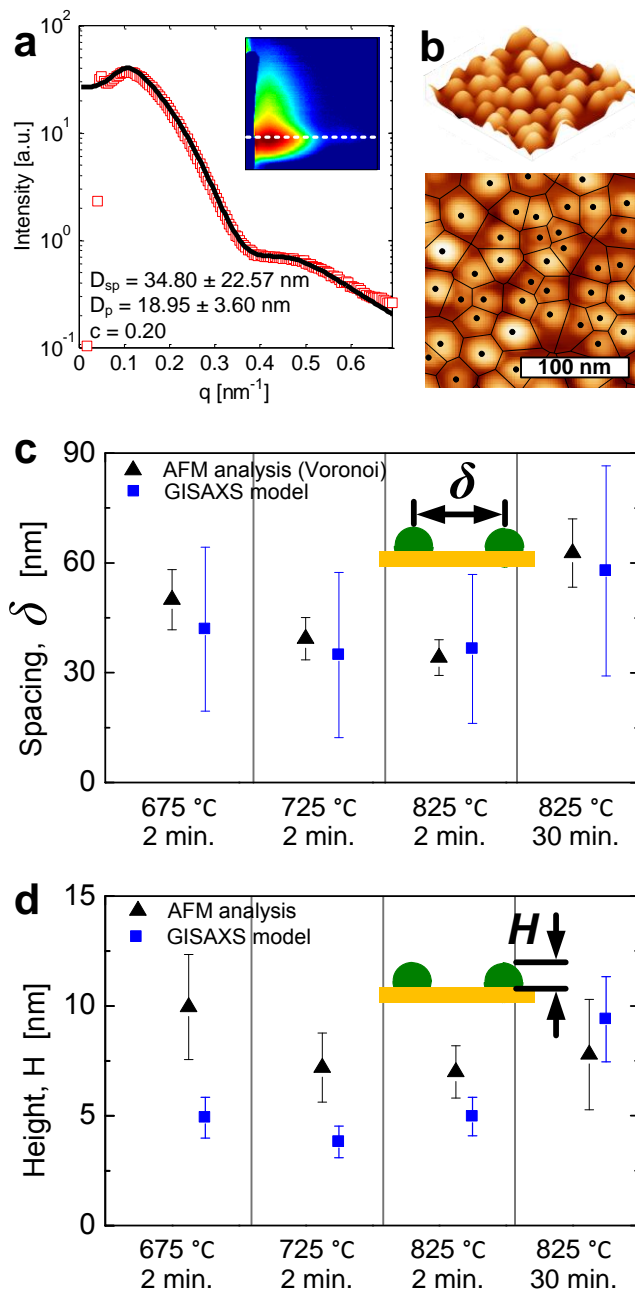
Figure 3.6 Comparison of GISAXS model with AFM image analysis. (a) *Ex situ* GISAXS data and model fitting of Fe particles formed by rapid heating and 2 min annealing in H_2/He at 725 °C. The fit parameters are listed on the plot and the corresponding 2-D image is inset. (b) Top and isometric views of an AFM image of the same sample, with particle peak with particle peak heights (black circles) and Voronoi tessellation (black lines) indicated. Comparison of GISAXS fit results with AFM analysis for (c) particle spacing and (d) particle height. Marker and error bar represent population mean and +/- standard deviation, respectively.
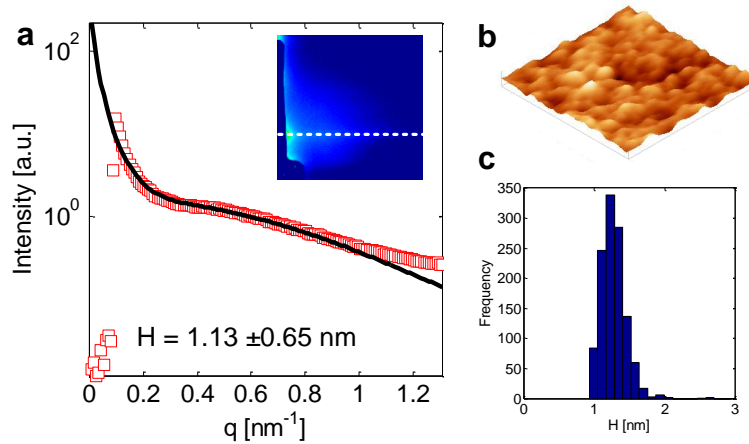
Figure 3.7 GISAXS and AFM analysis of Fe film as-deposited. (a) GISAXS data and fitting shows the mean roughness of the film is comparable to that measured by AFM (b-c).

$$F(q) = \frac{L\pi}{q} \frac{\int_0^\infty P(R_c) f_c^2 \, dR_c}{\int_0^\infty P(R_c) \, dR_c},$$
Eq. 6

where L is the length of a CNT, R_c is the radius of a CNT, and $P(R_c)$ is the lognormal PDF of CNT radii, having the same form as Eq. 3. Additionally,

$$f_c(q, R_c, \xi) = \Delta\rho \frac{2[J_1(R_c q) - \xi J_1(\xi R_c q)]}{q R_c (1 - \xi^2)},$$
Eq. 7

where ξ is the ratio of inner to outer CNT radii, $\Delta\rho$ is the difference in scattering density distribution, and J_1 is the spherical Bessel function of the first kind. Here, the fitting parameters are the outer diameter, D_c ($2 \times R_c$), its variance ($\sigma_{D_c}^2$), and ξ, while prefactors L and $\Delta\rho$ are absorbed by a normalization constant, A, as in Eq. 1. For CNTs, I set $S(q) = 1$ because I do not observe structure factor scattering for this q range; CNT-CNT spacing is ≈100 nm ($q \approx 10^{-2}$ nm^{-1}) and therefore is visible only by ultra-small-angle X-ray scattering (USAXS).[40] **Figure 3.8** shows a schematic of the CNT form factor model and an example of Eq. 6 fit to a single frame of the *in situ* SAXS data.

To fit the CNT scattering data, I use transmission SAXS data from the portion of the X-ray beam that passes over the substrate as illustrated in **Figure 3.3** (instead of
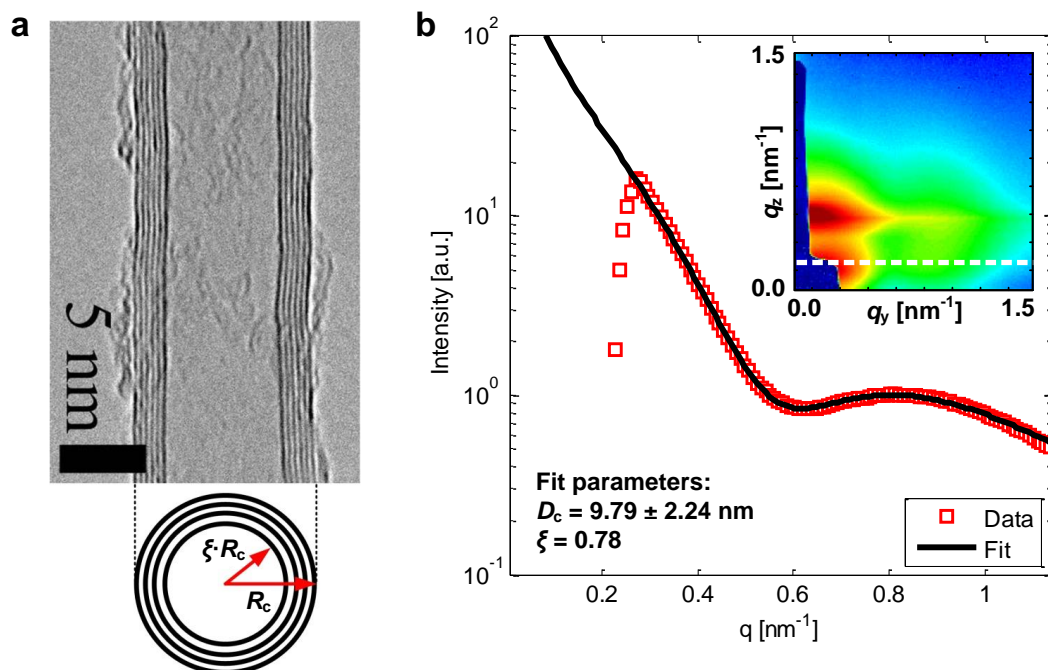
Figure 3.8 SAXS form factor model for CNTs. (a) TEM and schematic show the important geometrical parameters used in this core-shell model, where Rc is the outer radius of the cylinder (CNT) and ξ is the ratio of inner to outer radii. (b) Example of SAXS fitting for data taken *in situ*. Note, CNT data is monitored from transmission SAXS, which appears at a q_z indicated by the white dashed line on the inset SAXS image. Resultant fitting parameters are also labeled on the plot. TEM provided by A. J. Hart.

impinging at the angle α_i). Once CNTs begin growing, the specular beam contains scattering information for both Fe particles and CNTs; therefore, I use a q_z value corresponding to the transmitted SAXS, which is purely from CNTs. Before self-orienting perpendicular to the substrate, the CNTs comprise a thin, tangled film (Section 4.2.1 in Chapter 4), such that GISAXS carries information from both pure Fe particles (without CNTs) as well as from short CNTs emerging from the Fe particles. This arrangement of catalysts and CNTs within the same plane is different than a previous *ex situ* study that treated GISAXS from catalyst particles and aligned CNTs as a multilayer GISAXS problem.[41] Even as growth proceeds and the CNT density increases, the percentage of active catalysts is less than 10% (thus the porosity of forest is approximately 99%),[6] so X-rays still penetrate through the forest to scatter from both active and inactive particles on the Al_2O_3 support.
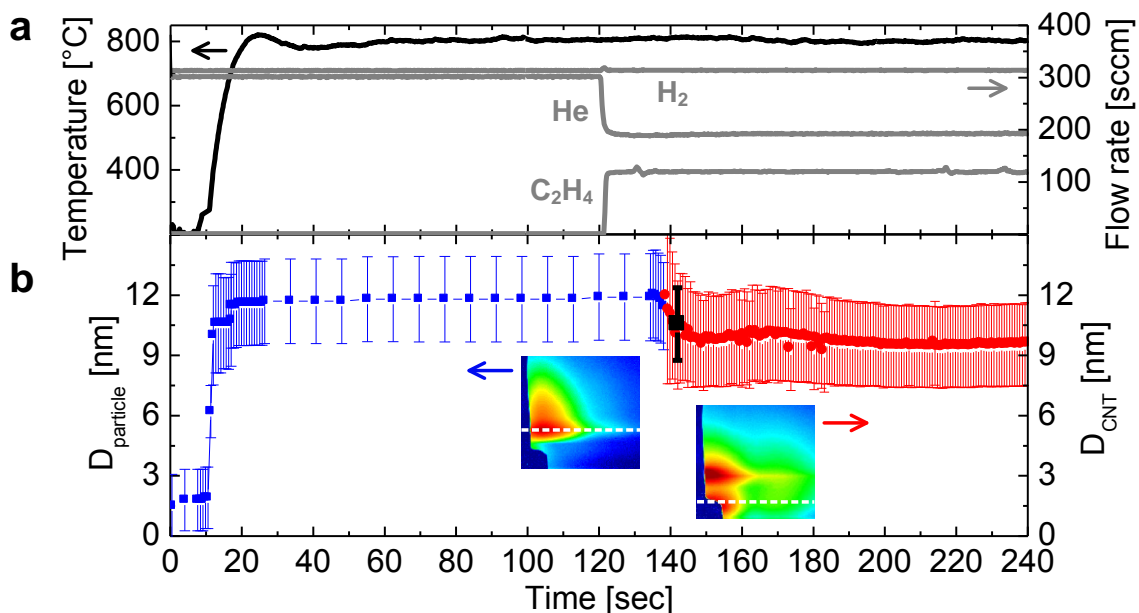
Figure 3.9 Dynamics of catalyst dewetting and CNT growth for rapid heating (33 °C sec^{-1}) in H$_2$/He. (a) Synthesis conditions (*i.e.*, temperature, gas flow) versus time (setpoint value 800 °C). Zero indicates when the substrate heater is turned on. (b) Fitting results of real-time GISAXS image sequences for particles and CNTs. Time evolution of particle diameter (blue, left axis) and CNT diameter (red, right axis), with inset GISAXS images that show the position on the PAD where the linescan (white dashed line) is taken for data analysis. The black square near t = 140 sec denotes the mean CNT diameter as measured in SEM (see **Figure3.10**). Marker and error bar represent population mean and +/- standard deviation, respectively.

3.2.5 Catalyst particle and CNT dynamics

By separately fitting the GI scattering during heating and annealing (before CNT nucleation), and the transmission scattering after CNT nucleation, I quantify the dynamics of both catalyst particle formation and CNT growth for a series of thermal and chemical conditions. This enables direct investigation of how the CNT population relates to a population of catalyst particles of known geometry. First, I study the dynamics when the substrate is rapidly heated (33 °C sec^{-1}) to 800 °C in H$_2$/He (**Figure 3.9**). The film dewets and forms particles rapidly, starting when the substrate is below 400 C. At this instant, D_p and σ_{D_p} both rapidly increase and saturate at 17 sec, approximately 6 sec after dewetting begins. The particle size distribution remains constant at $D_p = 11.7 \pm 2.1$ nm for the rest of the 2-minute annealing step,. The diameter of CNTs at the start of growth ($D_c = 12.0 \pm 4.3$ nm) is, within error of the fitting procedure, identical to the steady-state particle size distribution. However, within 10 sec after nucleation, the CNT diameter
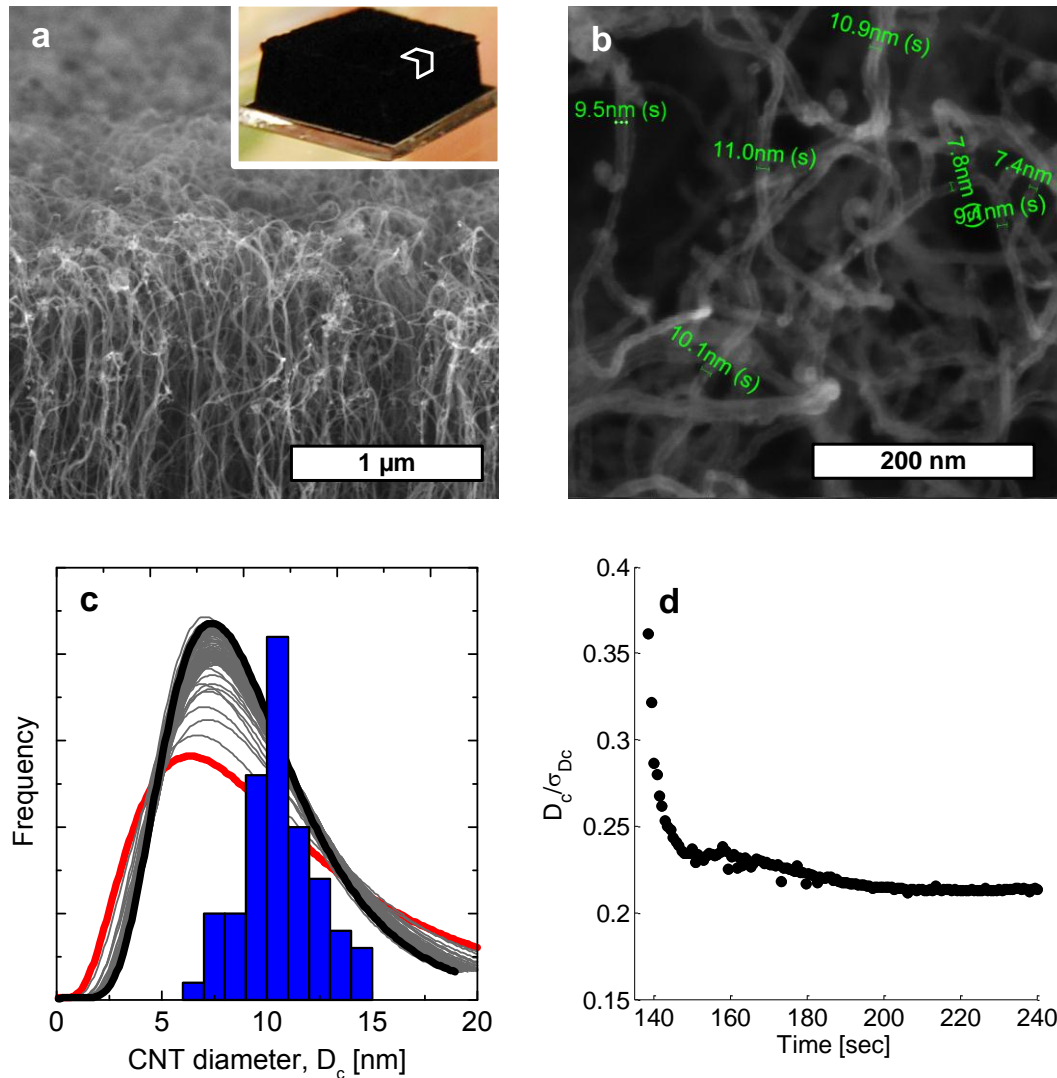
Figure3.10 High-resolution SEM imaging and analysis of CNT dynamics. (a) Side view of the top of the CNT forest (*i.e.*, beginning of growth) synthesis in the experiment described in **Figure 3.9** with inset digital photograph of the forest on 675-µm Si wafer. (b) Magnified top view of forest with CNT diameter measurements displayed. (c) Tabulated diameter measurements (blue bars) with overlaid PDFs calculated from fitting data (**Figure 3.9**), where the distribution evolves from $t = 139$ sec (red) to 231 sec (black). (d) Evolution of CNT population represented by the coefficient of variation (diameter divided by standard deviation) versus time.

distribution rapidly shifts downward, and the distribution (σ_{D_c}) narrows, reaching 2.6 nm.

High-resolution SEM imaging of the top of the forest (**Figure3.10**), representing the

beginning of growth gives a measure of D_c (10.6 ± 1.8nm), confirming the SAXS

technique accurately measures CNTs that begin to grow first. This value is shown as the
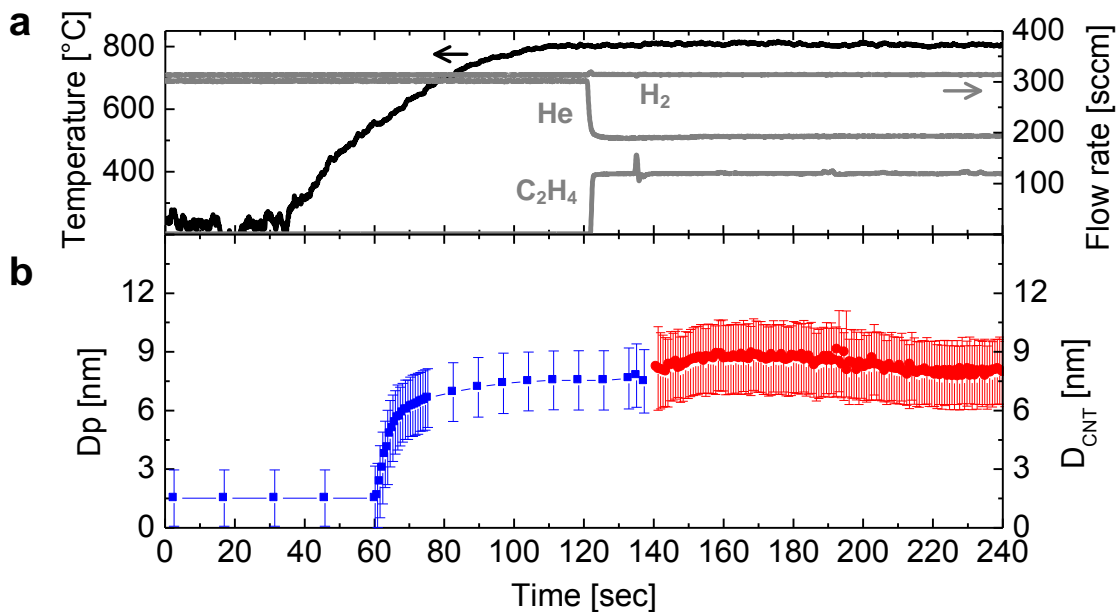
Figure 3.11 Dynamics of catalyst dewetting and CNT growth for slow heating (10 °C sec^{-1}) in H_2/He. (a) Synthesis conditions (*i.e.*, temperature, gas flow) versus time (setpoint value 800 °C). Zero indicates when the substrate heater is turned on. (b) Fitting results of real-time GISAXS image sequences for particles and CNTs. Time evolution of particle diameter (blue, left axis) and CNT diameter (red, right axis). Marker and error bar represent population mean and +/- standard deviation, respectively.

black data point superimposed in **Figure 3.9**. The downward shifts in D_c and σ_{D_c} in my measurements suggest that newly nucleating CNTs overwhelm the existing population with time, and the diameter of individual CNTs does not change. This is consistent with our recent observations that density increases 5-10 times during the initial stages of CNT forest growth.[6] Indeed, previous studies of isolated, millimeter-long CNTs have shown that diameter and chirality changes typically do not occur during growth,[6] unless a process variable such as temperature[42, 43] is varied.

Under relatively slow heating (10 °C sec^{-1}) in H_2/He, the film dewets at approximately 550 °C, and the subsequent increase of D_p (**Figure 3.11**) is more gradual and reaches a smaller final value compared to the rapid heating experiment (100 °C sec^{-1}). Further, D_p reaches steady state more slowly, as it continues to evolve until CNTs nucleate (past which accurate quantification of particles is difficult). While the early D_c
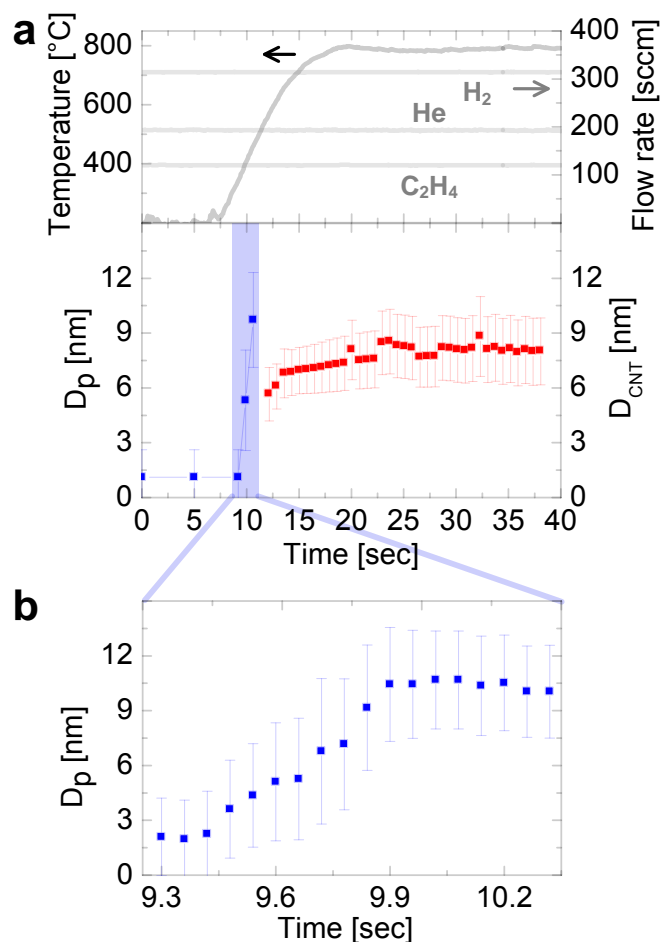
Figure 3.12 Dynamics of catalyst dewetting and CNT growth for rapid heating (100 °C sec⁻¹) in C₂H₄/H₂/He. (a) Synthesis conditions (*i.e.*, temperature, gas flow) versus time (setpoint value 800 °C). Zero indicates when the substrate heater is turned on. (b) Fitting results of real-time GISAXS image sequences for particles and CNTs. Time evolution of particle diameter (blue, left axis) and CNT diameter (red, right axis). (c) Expanded timescale corresponding to the shaded blue region in a), which shows ability to quantify film dynamics with a time resolution of 60 msec. Under thesis conditions, the film dewets in approximately 0.5 sec. Marker and error bar represent population mean and +/- standard deviation, respectively.

mean for this case is also dynamic, σ_{D_c} remains comparatively more stable and smaller overall. Thus, the heating rate influences the size and monodispersity of the particles and resultant CNTs, and in these experiments a slower heating rate in H₂/He results in smaller and more monodisperse CNTs.

While I find that particles can form very rapidly at a critical temperature in H₂/He, previous studies have suggested that continued exposure to H₂/He causes coarsening of

the catalyst size distribution.[4, 44] As a result, an increasingly common practice for CNT synthesis is to rapidly heat the catalyst to form particles in the presence of both hydrocarbon and H_2 precursors in order to achieve small CNTs.[45, 46] **Figure 3.12a** shows results where the substrate was heated rapidly (100 °C sec^{-1}) in $C_2H_4/H_2/He$, and accompanying SAXS results, and the exploded view of the time axis in **Figure 3.12b** illustrates the time resolution of my technique. I clearly resolve the particle scattering signature before CNT scattering appears, thus confirming that dewetting of the film into approximately hemispherical islands is a distinct step of the process, even in the presence of hydrocarbon. Here, the film begins to dewet at approximately 375 °C, and the particle diameter (D_p = 10.4 ± 2.7 nm) is close to the value obtained by rapid heating in H_2/He. However, the first CNTs observed in transmission scattering are much smaller (D_c = 5.7 ± 1.5 nm) than after initial heating in H_2/He. Interestingly, the initial CNTs are smaller than the mean diameter of the particles. This suggests that heating the catalyst film in the presence of active carbon precursors creates a subpopulation of catalysts of small diameters. However, as time proceeds, the CNT population evolves to D_c = 9.2 ± 2.1 nm, which is closer to the initial size of the catalysts. Thus, the smaller subpopulation either is not stable to support prolonged CNT growth, or is overwhelmed by the main population of larger particles and corresponding larger CNTs that dominates the eventual film.

In all experiments, I observe that the Fe film dewets rapidly and is followed by relatively slow coarsening of the particles. This complements recent studies that show that populations of much smaller catalyst particles can coarsen significantly during annealing.[3, 4] However, the particles in those studies are smaller than those reported in my work, which makes them more susceptible to ripening through surface diffusion. Although I observe that the Fe particles remain relatively stable over the 2-minute annealing step, my AFM data and additional *in situ* GISAXS studies clearly show morphological evolution occurs beyond 2 minutes while annealing in H_2/He, as particle size and spacing increase (**Figure 3.13**).

During the initial heating, the Fe film (natively oxide) reduces to its metallic state,[12] dewets, and forms stable islands. When the substrate is heated in an inert atmosphere (*i.e.*, He) I do not observe dewetting. Thus, a reducing environment is
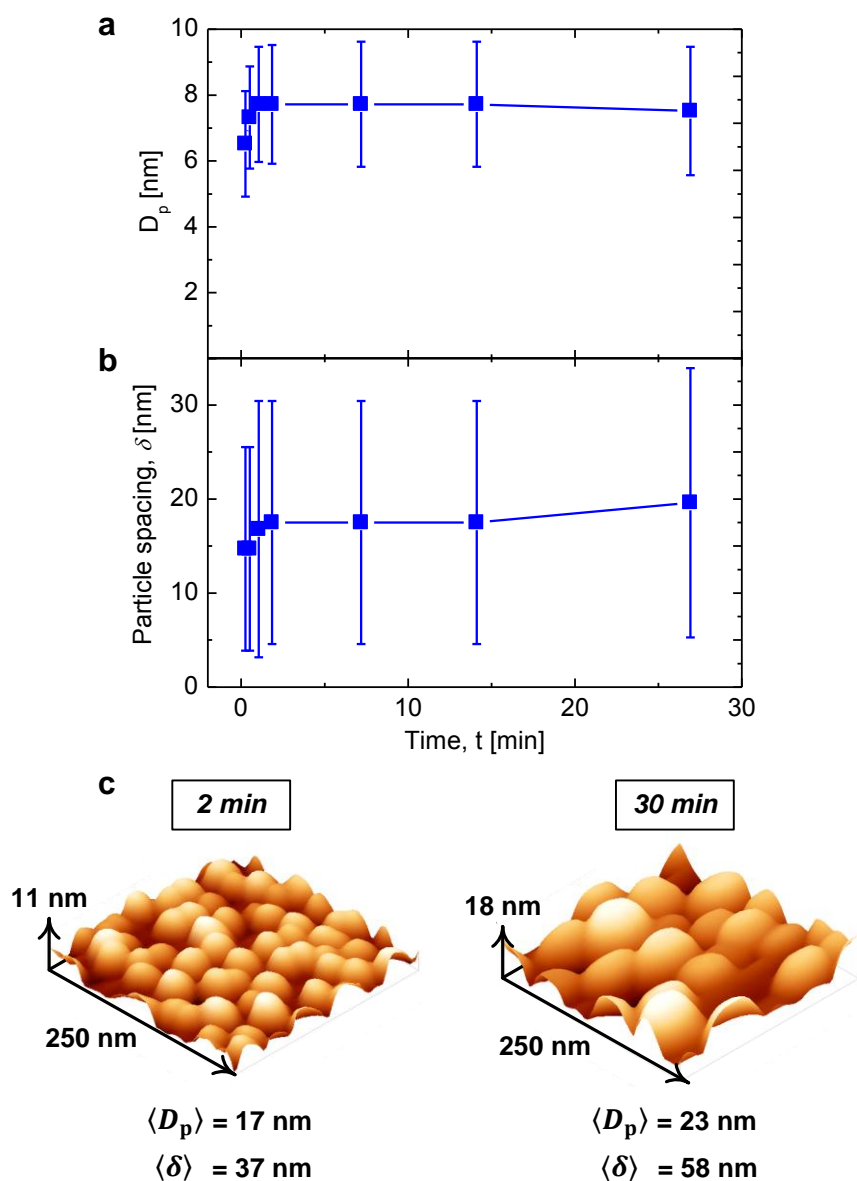
Figure 3.13 Dynamics of catalyst dewetting and particle coarsening for long annealing time in H$_2$/He. Fitting results of real-time GISAXS image sequences for particles, showing (a) particle diameter and (b) spacing versus time (setpoint value 825 °C). Zero indicates when the substrate heater is turned on. (c) AFM images and analysis results for mean diameter and spacing of particles for 2 and 30 min (825 °C).

important for transforming a thin film into particles. Overall, the dewetting of the Fe film is driven by instability induced by thermal stress, arising from mismatch in coefficients of thermal expansion between the film and its support.[47-51] There is a net decrease in free energy when the film restructures into hemispherical particles by surface diffusion of Fe. The subsequent rate of particle growth is expected to decay exponentially[48, 50] as the system tends toward equilibrium. The equilibrium size and shape (*i.e*., contact angle) of the catalyst particles are related to the free energy balance of the lower-energy surface of the Al_2O_3 support with that of the Fe,[52] and here I show that the heating rate also influences the resultant particle geometry.

3.2.6   Templated catalyst film dewetting on porous alumina

The *in situ* SAXS studies in the previous section demonstrate that the thermal and chemical conditions during annealing and growth influence dewetting of the catalyst film, and the resultant particle size distribution influences the CNT diameter distribution. However, regardless of how I control these conditions to influence dewetting on a flat substrate, the size and spacing will always be polydisperse, so investigating alternative methods of control is important. In this section, I present a new approach to engineering the catalyst particle size and spacing, whereby the catalyst is prepared by sputtering Fe onto an anodic aluminum oxide (AAO) substrate (Synkera Technologies, Inc.; **Figure 3.14)**. AAO is a nanostructured material with cylindrical pores that are regularly spaced at high densities. Recent technological advances in controlling the pore size and density make this material potentially attractive for directing the catalyst dewetting process. Previous reports show that CNT diameter can be templated by growing inside the AAO pores,[53, 54] but to my knowledge, AAO has not been used to template catalysts using the *positive space*.

In **Figure 3.15**, I present the concept of this approach, where Fe is first sputtered on top of heat-treated AAO (γ-alumina), on the area surrounding pores (pore diameter is 18 nm). Fe is limited to this top surface principally because sputtering is a line-of-sight deposition technique. Then, upon annealing in H_2/He, I expect the local curvature of the pores and the restricted amount of top surface area to drive dewetting such that isolated particles form between pores. Theoretical modeling has previously described the
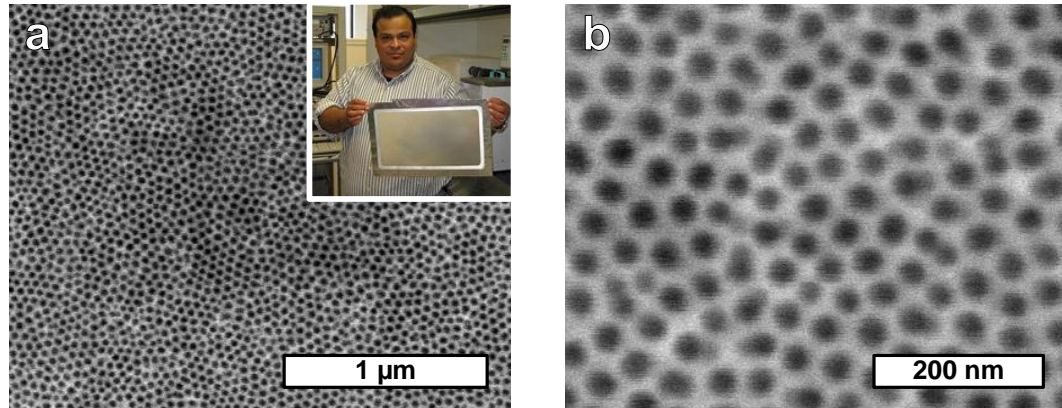
Figure 3.14 SEM imaging of AAO top surface. (a) Low- and (b) high-magnification images showing ordered, porous structure. Digital photograph inset (a) features 11" x 18" AAO membrane produced by Synkera Technologies, Inc.
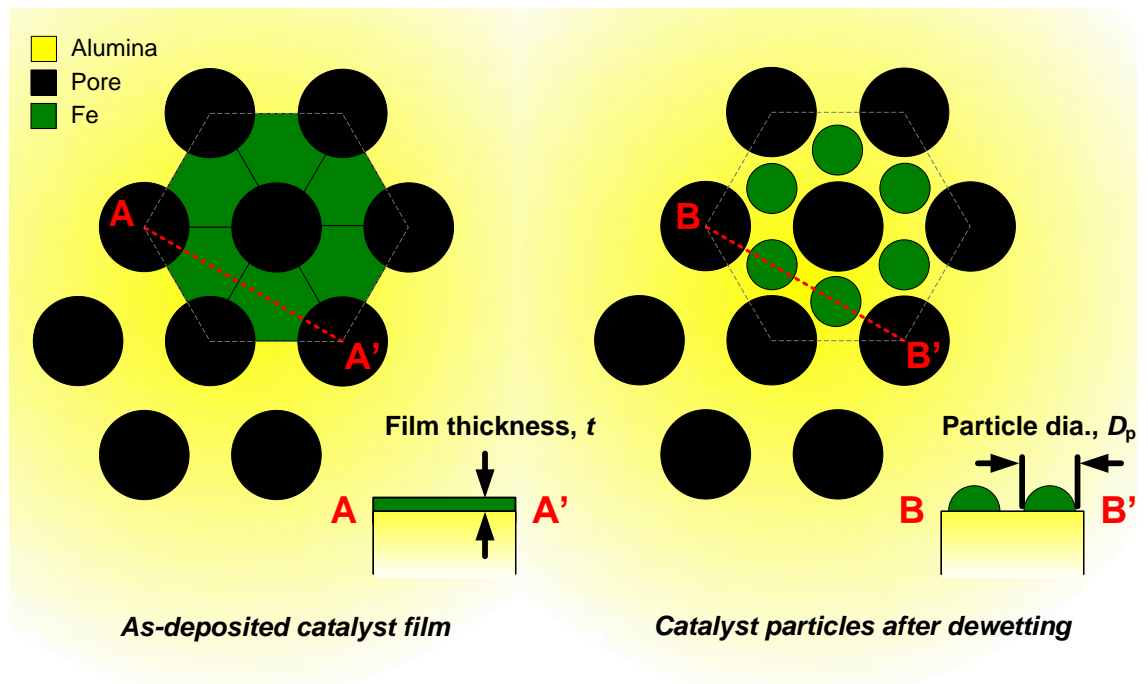
Figure 3.15 Model of templated dewetting of Fe on AAO. Schematic shows how a thin film deposited in the area between pores (black) forms particles, assuming conservation of mass.

1 nm Fe (e-beam)   **1 nm Fe (sputter)**
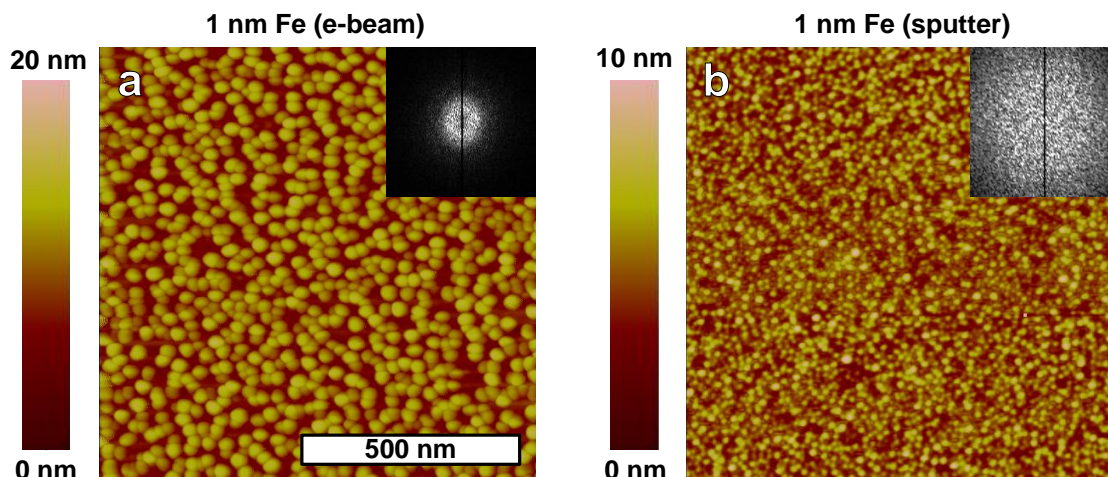
Figure 0.16 AFM and FFT analysis of control Fe films on flat alumina. Results for two different control cases: (a) Fe film deposited by electron-beam evaporation, annealed in H_2/He at 825 °C for 2 min; and (b) Fe film deposited by sputtering, annealed in H_2/He at 775 °C for 10 min.

instability in a thin film as caused by growth of holes due to surface tension, and this leads to dewetting.[48, 50, 55] In my experiments, I use AAO to template holes of prescribed size and spacing order to influence surface-tension-driven dewetting. Note, in the idealized case illustrated in **Figure 3.15**, I expect the number of particles to be twice the number of AAO pores.

I first emphasize that in a control experiment on flat alumina, the Fe film dewets to form isolated particles, without order. This is confirmed by AFM imaging and analysis by fast Fourier transforms (FFT) of the images. The FFT converts the image to the frequency domain and gives an indication of spatial order by characteristic features in the image. The diffuse FFT patterns in **Figure 0.16** indicate a lack of order for Fe particles that are formed by annealing films deposited by both electron-beam evaporation and sputtering (both with electron-beam-evaporated alumina on SiO_2/Si). On the other hand, I confirm that the AAO substrate is well ordered as expected (as indicated by the "diffraction ring" in the FFT), and Fe particles formed by dewetting on AAO are also ordered (**Figure 3.17**). I investigate particles formed from 1, 2, and 5 nm Fe films, and I show that particles from 1 and 2 nm are well ordered, but when the film is too thick (*i.e*, 5 nm), resultant particles are large and spatial order is lost (**Figure 3.17d**). This could be due to excessive coating of the inside rim of the AAO pores, such that the film no longer
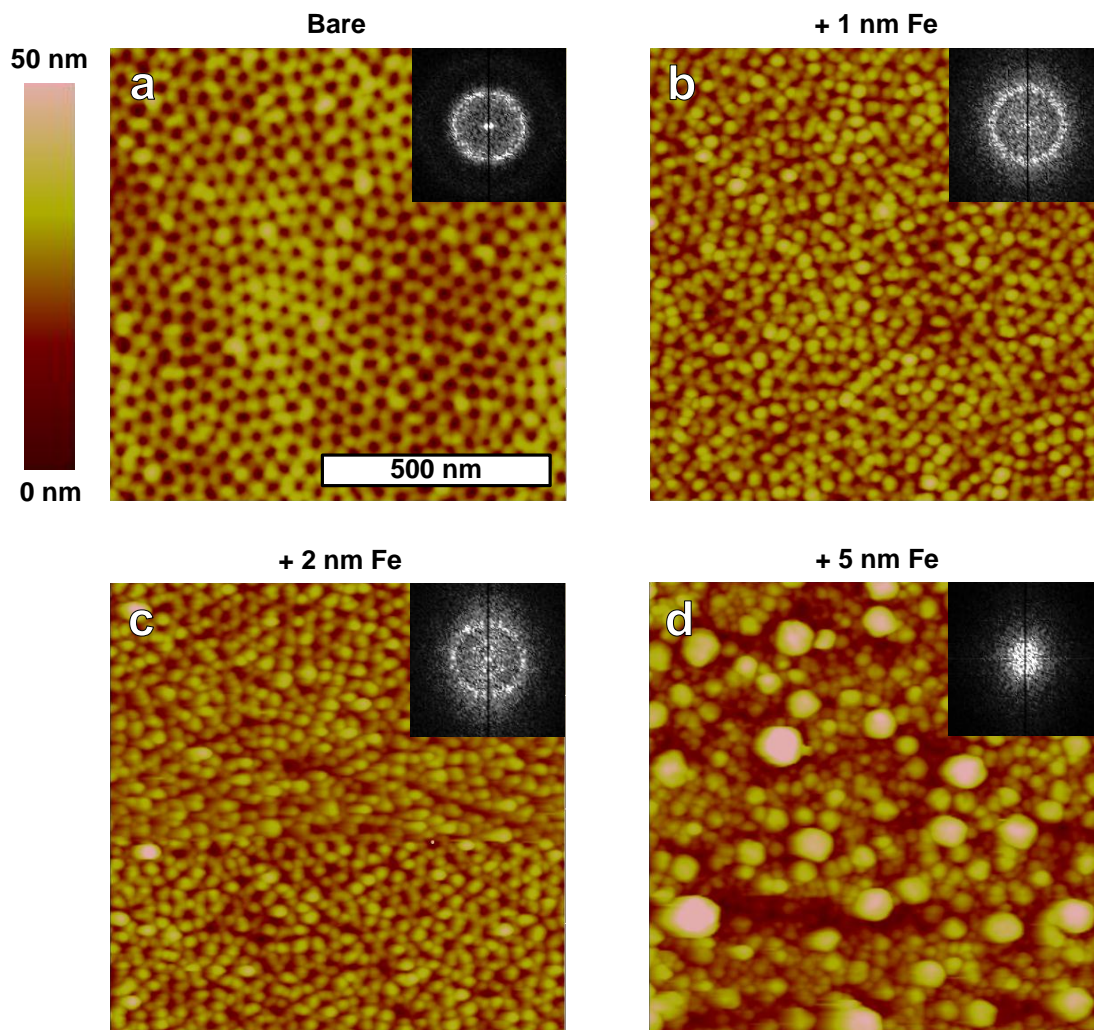
Figure 3.17 AFM and FFT analysis for series of Fe films on AAO. Results for four different cases of AAO: (a) without Fe deposition; (b) 1 nm Fe; (c) 2 nm Fe; and (d) 5 nm Fe. All films deposited by sputtering before annealing in H_2/He at 775 °C for 10 minutes.

dewets according to the isolated areas between pores because it is continuous across the pores.

Magnified views compare Fe particles from 1- and 2-nm films, confirms that the short-range order of bare AAO translates to particles formed on AAO (**Figure 3.18**). The six-fold symmetry of the hexagonally arranged AAO pores is captured by the FFT pattern. Interestingly, the FFT pattern is blurred for 1 nm, while it has clear diffraction spots for 2 nm, similar to bare AAO. The fact that the hexagonal symmetry emerges for 2 nm but is lost for 5 nm suggests that there may be an optimal window of film thickness
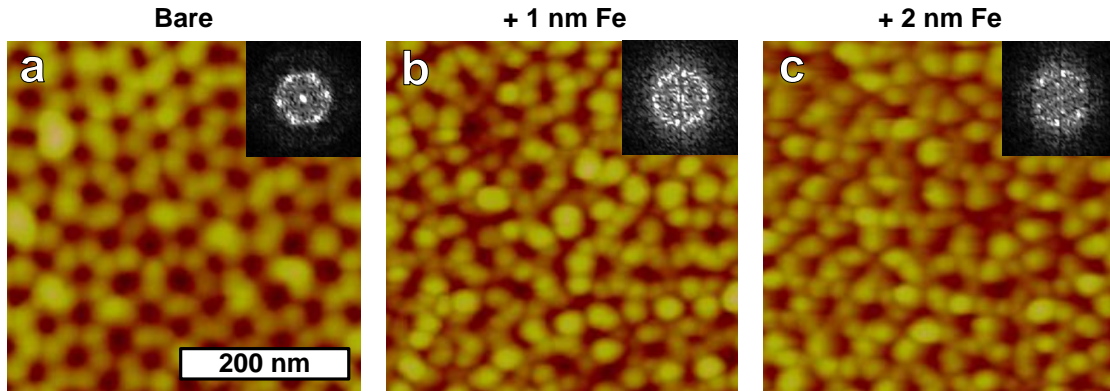
Figure 3.18 High-resolution AFM and FFT analysis for series of Fe films on AAO. Magnified views for three cases shown in Figure. 17a-c: (a) without Fe deposition; (b) 1 nm Fe; and (c) 2 nm Fe. All films deposited by sputtering before annealing in H_2/He at 775 °C for 10 minutes.

over which templated dewetting and ordering of Fe particles is effective. It is plausible that Fe is lost in the pores during annealing, but my images appear to have particles present on the AAO surface, which is corroborated by an increase in surface roughness as quantified by the root mean square (RMS). For instance, I observe an increased roughness after Fe deposition and annealing, with RMS = 4.7 nm for bare AAO versus 5.6 nm for 1 nm Fe.

Using the custom AFM image processing described in Section 3.2.3, I quantify the areal density of both pores on bare AAO and particles after dewetting on AAO. I quantitatively compare the spacing of the pores to the spacing of the particles (1 nm Fe) using Voronoi tessellation (**Figure 3.19**). I confirm the pore spacing of the as-received, bare AAO (45.6 nm), and I observe that the mean spacing of the particles (37.0 nm) is smaller, which agrees with my model in **Figure 3.15**. Furthermore, I find that the ratio of the number of particles to the number of pores is 1.6, which is less than the ideal ratio of 2, but it is a promising outcome. From this initial ratio, I estimate that the probability of isolating one particle between three pores is approximately 0.8, although more than one particle may sit in these interstitial sites due to the tendency for Fe particles to agglomerate. I anticipate that by varying the Fe thickness and annealing conditions, the number of particles per pore could approach 2.
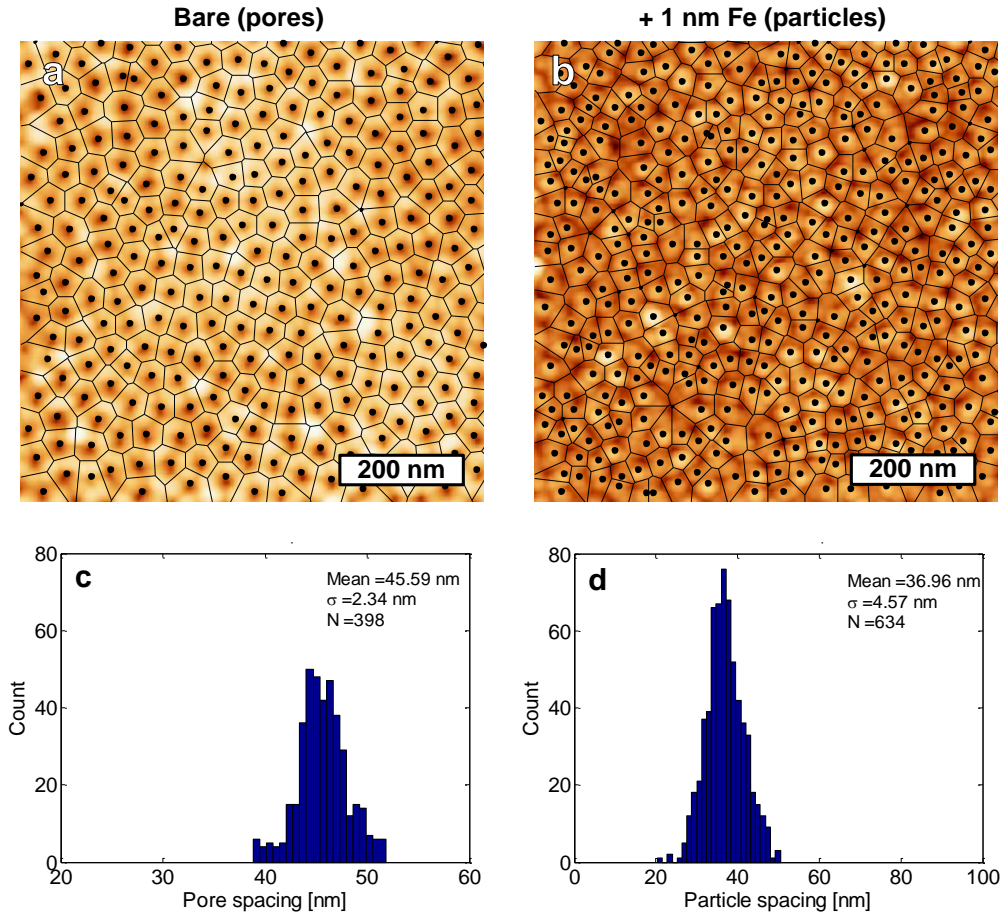
Figure 3.19 AFM and Voronoi decomposition analysis of AAO with and without Fe particles. (a) Bare AAO showing Voronoi tessellation according to location of the pores with the distribution of *pore* spacing in (c). (b) Particles on AAO from 1 nm Fe showing Voronoi tessellation according to location of particles with the distribution of *particle* spacing in (d).

I also characterize the AAO and Fe/AAO substrates using *ex situ* GISAXS (as described in 3.2.1) in **Figure 3.20**. Bare AAO exhibits a strong correlation peak at about $q = 0.2$ nm^{-1}, corresponding to the spacing of the pores. GISAXS of AAO with Fe particles shows a slight upward shift in q of the correlation peak as well as the emergence of a second peak at $q = 0.39$ nm^{-1}. Without modeling the porous structure of the AAO, I can approximate the characteristic feature size as $d = 2\pi/q$; this indicates that the Fe particles are about 16 nm with an average spacing of 30 nm (**Figure 3.20d**), which is near the value measured by AFM (37 nm) (**Figure 3.19d**).

Initial results in **Figure 3.21** from CNT growth experiments show that particles from 1 nm Fe on AAO yield a uniform, tangled CNT film. The AAO pore density

$(5 \times 10^{10}$ cm$^{-2})$ ideally relates to the particle areal density (by factor of 2), and on a flat substrate <10% of catalyst particles are active for CNT growth.[6] Given that ~10^9 CNTs cm^{-2} is required for the self-oriented, vertical structure in a forest, I expect that the particle density from 1 nm Fe on this substrate (at this pore density) is not sufficient to form a vertically aligned forest. However, by optimizing annealing and growth conditions for this new material as well as Fe thickness, growth of CNTs forests with prescribed densities may be possible by this templating method.
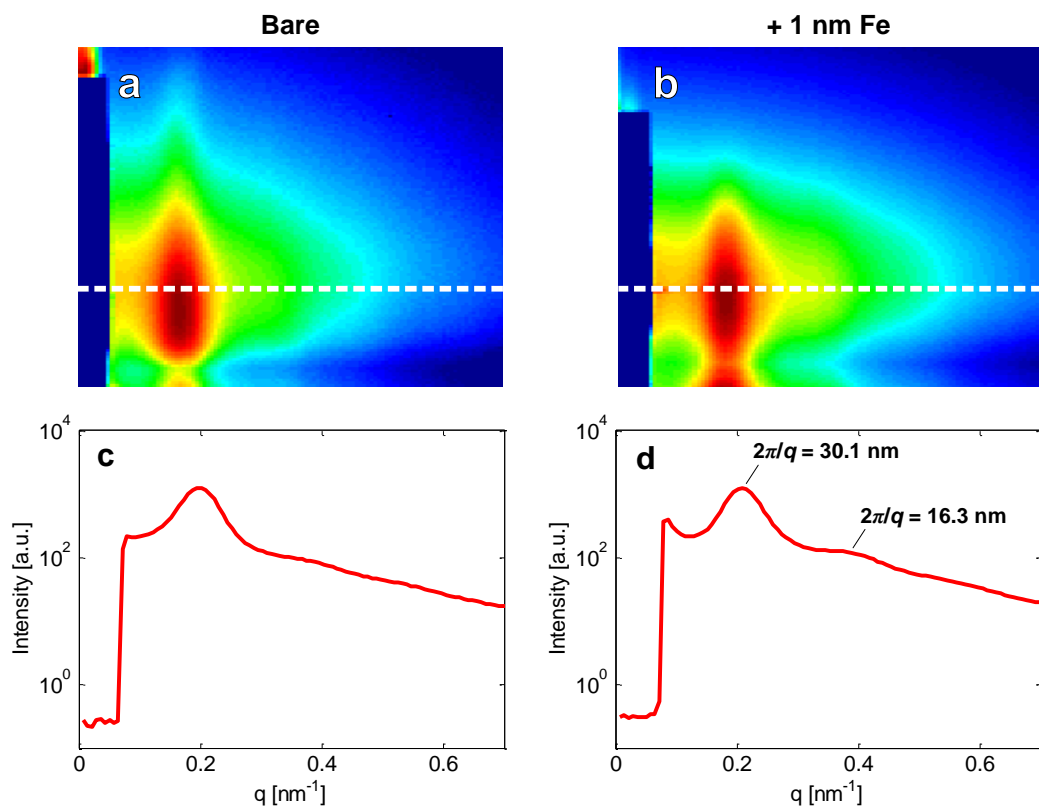
Figure 3.20 GISAXS analysis of AAO with and without Fe particles. 2-D GISAXS images of (a) bare AAO and (b) particles on AAO from 1 nm Fe, with corresponding 1-D intensity profiles in (c) and (d) respectively. Intensity scans are taken according to the white dashed lines in the GISAXS images. Particles formed by annealing in H$_2$/He at 775 °C for 10 minutes (same samples as in **Figure 3.18** and **Figure 3.19**.
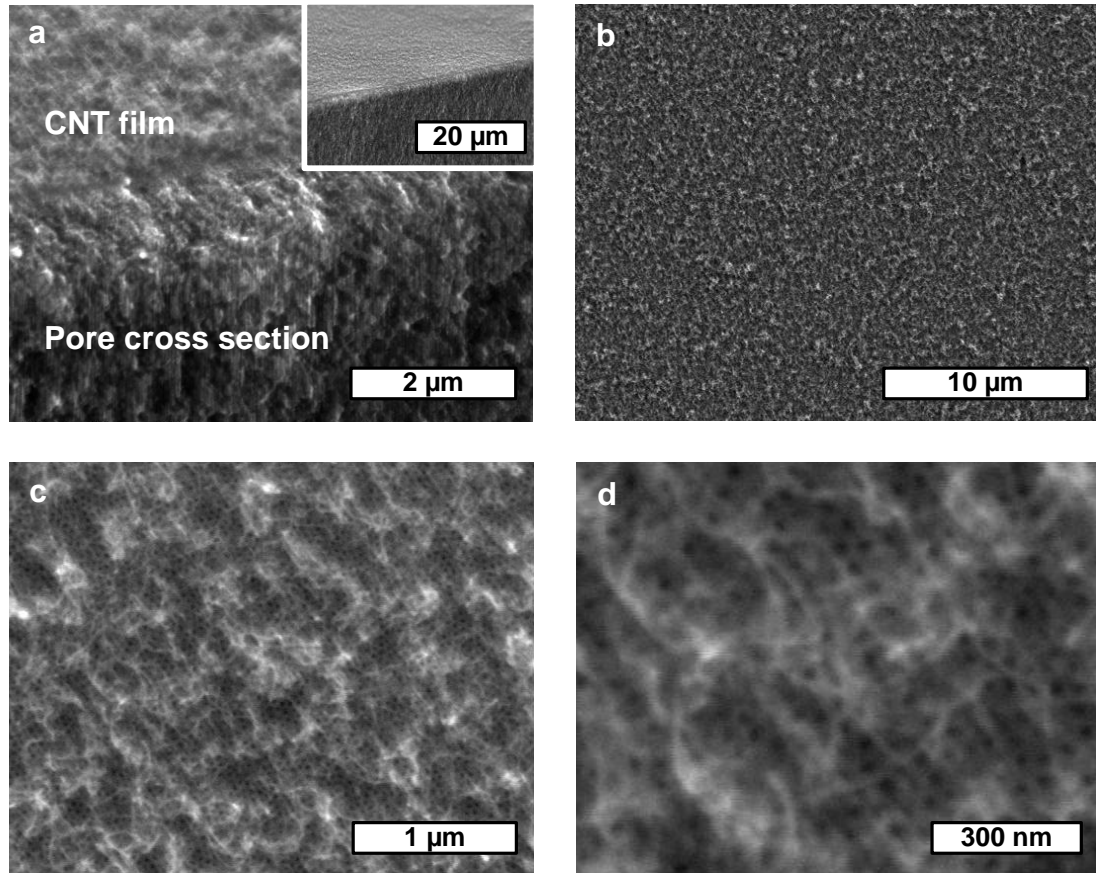
Figure 3.21 SEM imaging of CNT growth results from 1 nm Fe on AAO. (a) Side view (72 ° tilt) showing thickness of CNT film and corrugated, porous structure of the AAO. (b-d) Top view of CNT film at various magnifications.

3.3   Conclusions

I show that in situ X-ray scattering enables non-destructive analysis of the populations of catalyst particles formed from a thin film. The CNT diameters that first emerge match the distribution of catalyst sizes but the population evolves rapidly as new CNTs begin growing. CNT forest growth is a multi-stage process; parameters in each stage critically determine the forest characteristics and lead to structural variations in the forest which determine suitability for many prospective applications. By *in situ* GISAXS I reveal limiting dynamics of the growth process and find that the catalyst film dewets nearly instantaneously and heating rate determinates the resultant particles size. This nondestructive technique enables sampling of large numbers of nanostructures, giving insight into rapidly evolving populations. Revealing the timescales for the pertinent process throughout forest growth enables better understanding and thus an opportunity to tune these processes. The use of synchrotron light and a high-speed array detector is a powerful diagnostic tool for nanomaterials production, and it will be useful to devise a next generation feedback control scheme to optimizing synthesis. Finally, I apply a set of complementary characterization techniques to a new catalyst system in order to probe the effects of templating catalyst films with a porous support layer. Initial results show that the AAO support induces spatial order in the arrangement of particles, and CNT films are achieved. This is promising technique for directing dewetting of films for a variety of applications and materials.

3.4 References

1.   Bedewy, M.; Meshot, E.; Guo, H.; Verploegen, E.; Lu, W.; Hart, A., Collective mechanism for the evolution and self-termination of vertically aligned carbon nanotube growth. *Journal of Physical Chemistry C* 2009, 113, 20576-20582.

2.   Meshot, E.; Bedewy, M.; Lyons, K.; Woll, A.; Juggernauth, K.; Tawfick, S.; Hart, A., Measuring the lengthening kinetics of aligned nanostructures by spatiotemporal correlation of height and orientation. *Nanoscale* 2010, 896-900.

3.   Amama, P.; Pint, C.; McJilton, L.; Kim, S.; Stach, E.; Murray, P.; Hauge, R.; Maruyama, B., Role of water in super growth of single-walled carbon nanotube carpets. *Nano Letters* 2009, 9, 44-49.

4.   Kim, S. M.; Pint, C. L.; Amama, P. B.; Zakharov, D. N.; Hauge, R. H.; Maruyama, B.; Stach, E. A., Evolution in catalyst morphology leads to carbon nanotube growth termination. *Journal of Physical Chemistry Letters* 2010, 1, 918-922.

5.   Hasegawa, K.; Noda, S., Millimeter-tall single-walled carbon nanotubes rapidly grown with and without water. *ACS Nano* 2011, 5, 975-984.

6.   Bedewy, M.; Meshot, E. R.; Reinker, M. J.; Hart, A. J., Population growth dynamics of carbon nanotubes. *ACS Nano* 2011, 5, 8974-8989.

7.   Kukovitsky, E. F.; L'Vov, S. G.; Sainov, N. A.; Shustov, V. A.; Chernozatonskii, L. A., Correlation between metal catalyst particle size and carbon nanotube growth. 2002, 355, 497-503.

8.   Nerushev, O. A.; Dittmar, S.; Morjan, R. E.; Rohmund, F.; Campbell, E. E. B., Particle size dependence and model for iron-catalyzed growth of carbon nanotubes by thermal chemical vapor deposition. *Journal of Applied Physics* 2003, 93, 4185-4190.

9.   Lin, M.; Tan, J. P. Y.; Boothroyd, C.; Loh, K. P.; Tok, E. S.; Foo, Y. L., Direct observation of single-walled carbon nanotube growth at the atomistic scale. *Nano Letters* 2006, 6, 449-452.

10.   Harutyunyan, A. R.; Chen, G.; Paronyan, T. M.; Pigos, E. M.; Kuznetsov, O. A.; Hewaparakrama, K.; Kim, S. M.; Zakharov, D.; Stach, E. A.; Sumanasekera, G. U., Preferential growth of single-walled carbon nanotubes with metallic conductivity. *Science* 2009, 326, 116-120.

11.   Puretzky, A. A.; Geohegan, D. B.; Schittenhelm, H.; Fan, X.; Guillorn, M. A., Time-resolved diagnostics of single wall carbon nanotube synthesis by laser vaporization. *Applied Surface Science* 2002, 197-198, 552-562.

12.   Hofmann, S.; Blume, R.; Wirth, C. T.; Cantoro, M.; Sharma, R.; Ducati, C.; Havecker, M.; Zafeiratos, S.; Schnoerch, P.; Oestereich, A.; Teschner, D.; Albrecht, M.; Knop-Gericke, A.; Schlogl, R.; Robertson, J., State of transition metal catalysts during carbon nanotube growth. *Journal of Physical Chemistry C* 2009, 113, 1648-1656.

13.   Mattevi, C.; Wirth, C. T.; Hofmann, S.; Blume, R.; Cantoro, M.; Ducati, C.; Cepek, C.; Knop-Gericke, A.; Milne, S.; Castellarin-Cudia, C.; Dolafi, S.; Goldoni, A.; Schloegl, R.; Robertson, J., In-situ X-ray photoelectron spectroscopy study of catalyst-support interactions and growth of carbon nanotube forests. *Journal of Physical Chemistry C* 2008, 112, 12207-12213.

14.   Hofmann, S.; Sharma, R.; Ducati, C.; Du, G.; Mattevi, C.; Cepek, C.; Cantoro, M.; Pisana, S.; Parvez, A.; Cervantes-Sodi, F.; Ferrari, A. C.; Dunin-Borkowski, R.; Lizzit, S.; Petaccia, L.; Goldoni, A.; Robertson, J., In situ observations of catalyst dynamics during surface-bound carbon nanotube nucleation. *Nano Letters* 2007, 7, 602-608.

15.   Picher, M.; Anglaret, E.; Arenal, R.; Jourdain, V., Self-deactivation of single-walled carbon nanotube growth studied by in situ raman measurements. *NANO Letters* 2009, 9, 542-547.

16.   Revenant, C.; Leroy, F.; Lazzari, R.; Renaud, G.; Henry, C. R., Quantitative analysis of grazing incidence small-angle x-ray scattering: Pd/MgO(001) growth. *Physical Review B* 2004, 69, 035411.

17.   Renaud, G.; Lazzari, R.; Revenant, C.; Barbier, A.; Noblet, M.; Ulrich, O.; Leroy, F.; Jupille, J.; Borensztein, Y.; Henry, C. R.; Deville, J.-P.; Scheurer, F.; Mane-Mane, J.; Fruchart, O., Real-time monitoring of growing nanoparticles. *Science* 2003, 300, 1416-1419.

18.   Lazzari, R.; eacute; mi; Renaud, G.; Jupille, J.; Leroy, F.; ric, Self-similarity during growth of the Au/TiO$_2$ (110) model catalyst as seen by the scattering of X-rays at grazing-angle incidence. *Physical Review B* 2007, 76, 125412.

19.   Abecassis, B.; Testard, F.; Spalla, O.; Barboux, P., Probing in situ the nucleation and growth of gold nanoparticles by small-angle X-ray scattering. *Nano Letters* 2007, 7, 1723-1727.

20.   Ab; eacute; cassis, B.; Testard, F.; Spalla, O., Gold nanoparticle superlattice crystallization probed in situ. *Physical Review Letters* 2008, 100, 115504.

21.   Beaucage, G.; Kammler, H. K.; Pratsinis, S. E., Particle size distributions from small-angle scattering using global scattering functions. *Journal of Applied Crystallography* 2004, 37, 523-535.

22.   Beaucage, G.; Kammler, H. K.; Mueller, R.; Strobel, R.; Agashe, N.; Pratsinis, S. E.; Narayanan, T., Probing the dynamics of nanoparticle growth in a flame using synchrotron radiation. *Nature Materials* 2004, 3, 370-373.

23.   Sztucki, M.; Narayanana, T.; Beaucage, G., In situ study of aggregation of soot particles in an acetylene flame by small-angle X-ray scattering. *Journal of Applied Physics* 2007, 101.

24.   Meshot, E.; Plata, D.; Tawfick, S.; Zhang, Y.; Verploegen, E.; Hart, A., Engineering vertically aligned carbon nanotube growth by decoupled thermal treatment of precursor and catalyst. *ACS Nano* 2009, 3, 2477-2486.

25.   Plata, D. e. L.; Hart, A. J.; Reddy, C. M.; Gschwend, P. M., Early evaluation of potential environmental impacts of carbon nanotube synthesis by chemical vapor deposition. *Environmental Science & Technology* 2009, 43, 8367-8373.

26.   Hart, A.; Slocum, A., Rapid growth and flow-mediated nucleation of millimeter-scale aligned carbon nanotube structures from a thin-film catalyst. *Journal of Physical Chemistry B* 2006, 110, 8250-8257.

27.   Koerner, L. J.; et al., X-ray tests of a pixel array detector for coherent x-ray imaging at the linac coherent light source. *Journal of Instrumentation* 2009, 4, P03001.

28.   Philipp, H.; Koerner, L.; Hromalik, M.; Tate, M.; Gruner, S., Femtosecond radiation experiment detector for x-ray free-electron laser (XFEL) coherent X-ray imaging. *IEEE Transactions on Nuclear Science* 2010, 57, 3795-3799.

29.   Levine, J. R.; Cohen, J. B.; Chung, Y. W.; Georgopoulos, P., Grazing-incidence small-angle X-ray scattering: new tool for studying thin film growth. *Journal of Applied Crystallography* 1989, 22, 528-532.

30.   van Laake, L.; Hart, A. J.; Slocum, A. H., Suspended heated silicon platform for rapid thermal control of surface reactions with application to carbon nanotube synthesis. *Review of Scientific Instruments* 2007, 78.

31.   Meshot, E.; Hart, A., Abrupt self-termination of vertically aligned carbon nanotube growth. *Applied Physics Letters* 2008, *92* (11), 113107.

32.   Henderson, S., Comparison of parasitic scattering from window materials used for small-angle X-ray scattering: a better beryllium window. *Journal of Applied Crystallography* 1995, 28, 820-826.

33.   Plata, D.; Meshot, E.; Reddy, C.; Hart, A.; Gschwend, P., Multiple alkynes react with ethylene to enhance carbon nanotube synthesis, suggesting a polymerization-like formation mechanism. *ACS Nano* 2010, 4, 7185-7192.

34.   Renaud, G.; Lazzari, R.; Leroy, F., Probing surface and interface morphology with grazing incidence small angle X-ray scattering. *Surface Science Reports* 2009, 64, 255-380.

35.   Rauscher, M.; Paniago, R.; Metzger, H.; Kovats, Z.; Domke, J.; Peisl, J.; Pfannes, H.; Schulze, J.; Eisele, I., Grazing incidence small angle X-ray scattering from free-standing nanostructures. *Journal of Applied Physics* 1999, 86, 6763-6769.

36.   Söderlund, J.; Kiss, L. B.; Niklasson, G. A.; Granqvist, C. G., Lognormal size distributions in particle growth processes without coagulation. *Physical Review Letters* 1998, 80, 2386-2388.

37.   Granqvist, L. B. K. a. J. S. a. G. A. N. a. C. G., New approach to the origin of lognormal size distributions of nanoparticles. *Nanotechnology* 1999, 10, 25.

38.   Thompson, C. V., Coarsening of particles on a planar substrate - interface energy anisotropy and application to grain-growth in thin films. *Acta Metallurgica* 1988, 36, 2929-2934.

39.   Wang, B.; Bennett, R.; Verploegen, E.; Hart, A.; Cohen, R., Quantitative characterization of the morphology of multiwall carbon nanotube films by small-angle X-ray scattering. *Journal of Physical Chemistry C* 2007, 111, 5859-5865.

40.   Verploegen, E.; Hart, A.; De Volder, M.; Tawfick, S.; Chia, K.; Cohen, R., Non-destructive characterization of structural hierarchy within aligned carbon nanotube assemblies. *Journal of Applied Physics* 2011, 109, 094316.

41.   Mane Mane, J.; Cojocaru, C. S.; Barbier, A.; Deville, J. P.; Thiodjio Sendja, B.; Le Normand, F., GISAXS study of the alignment of oriented carbon nanotubes grown on plain SiO_2/Si(100) substrates by a catalytically enhanced CVD process. *Physica Status Solidi A* 2007, 204, 4209-4229.

42.   Doorn, S. K.; Zheng, L.; O'Connell, M. J.; Zhu, Y.; Huang, S.; Liu, J., Raman spectroscopy and imaging of ultralong carbon nanotubes. *Journal of Physical Chemistry B* 2005, 109, 3751-3758.

43.   Anderson, N.; Hartschuh, A.; Novotny, L., Chirality changes in carbon nanotubes studied with near-field raman spectroscopy. *Nano Letters* 2007, 7, 577-582.

44.   Sugime, H.; Noda, S.; Maruyama, S.; Yamaguchi, Y., Multiple "optimum" conditions for Co–Mo catalyzed growth of vertically aligned single-walled carbon nanotube forests. *Carbon* 2009, 47, 234-241.

45.   Pint, C. L.; Pheasant, S. T.; Parra-Vasquez, A. N. G.; Horton, C.; Xu, Y.; Hauge, R. H., Investigation of optimal parameters for oxide-assisted growth of vertically aligned single-walled carbon nanotubes. *Journal of Physical Chemistry C* 2009, 113, 4125-4133.

46.   Zhang, Y. Y.; Gregoire, J. M.; van Dover, R. B.; Hart, A. J., Ethanol-promoted high-yield growth of few-walled carbon nanotubes. *Journal of Physical Chemistry C* 2010, 114, 6389-6395.

47.   Seemann, R.; Herminghaus, S.; Jacobs, K., Dewetting patterns and molecular forces: a reconciliation. *Physical Review Letters* 2001, 86, 5534.

48.   Jiran, E.; Thompson, C. V., Capillary instabilities in thin, continuous films. *Thin Solid Films* 1992, 208, 23-28.

49.   Thompson, C. V.; Carel, R., Stress and grain growth in thin films. *Journal of the Mechanics and Physics of Solids* 1996, 44, 657-673.

50.   Srolovitz, D.; Safran, S., Capillary instabilities in thin-films 2. Kinetics. *Journal of Applied Physics* 1986, 60, 255-260.

51.   Srolovitz, D. J., On the stability of surfaces of stressed solids. *Acta Metallurgica* 1989, 37, 621-625.

52.   Danielson, D. T., Surface-energy-driven dewetting theory of silicon-on-insulator agglomeration. *Journal of Applied Physics* 2006, 100, 083507.

53.   Yuan, Z.; Huang, H.; Liu, L.; Fan, S., Controlled growth of carbon nanotubes in diameter and shape using template-synthesis method. *Chemical Physics Letters* 2001, 345, 39-43.

54.   Kaatz, F.; Siegal, M.; Overmyer, D.; Provencio, P.; Jackson, J., Diameter control and emission properties of carbon nanotubes grown using chemical vapor deposition. *Materials Science & Engineering C-Biomimetic and Supramolecular Systems* 2003, 23, 141-144.

55.   Srolovitz, D.; Safran, S., Capillary instabilities in thin-films 1. Energetics. *Journal of Applied Physics* 1986, 60, 247-254.

Chapter 4
Morphological evolution in CNT forest growth

In the chapter, I identify and discuss four distinct stages of morphological evolution during the CNT forest formation process. This is enabled by combining electron microscopy and X-ray scattering studies with real-time forest height measurements during synthesis. I observe the *in situ* formation of the ubiquitous tangled "crust" from an initial discontinuous film (Stage 1), and I reveal the kinetics of self-organization (Stage 2), which I corroborate with the initial acceleration in forest height. CNTs remain well aligned during steady growth (constant rate; Stage 3), but I identify a distinct loss of order at the end of growth that coincides with abrupt self-termination in height kinetics (Stage 4). Correcting the height kinetics for the varying CNT tortuosity during synthesis allows for new interpretation of reaction kinetics based on the true lengthening rates of CNTs. Portions of this chapter originally appeared in various journal publications and are reproduced here with permission from the respective publishers. The current presentation of the work herein represents my contributions, principally.

4.1   Introduction

Synthesis of CNT forests involves the collective self-organization and upward growth of billions of CNTs per square centimeter[2]. Thus, forests are very porous, comprising typically no less than 95% air by volume.[1, 2] A CNT can have an exceptionally large aspect ratio (*i.e.*, length-to-diameter ratio; $\approx 10^5$ in a millimeter-tall forest), with a reported persistence length on the order of 100s of nm for multi-wall CNTs.[3] This low number density and the mechanical compliance of individual CNTs, in concert with a propensity for physical interaction among neighboring CNTs (primarily
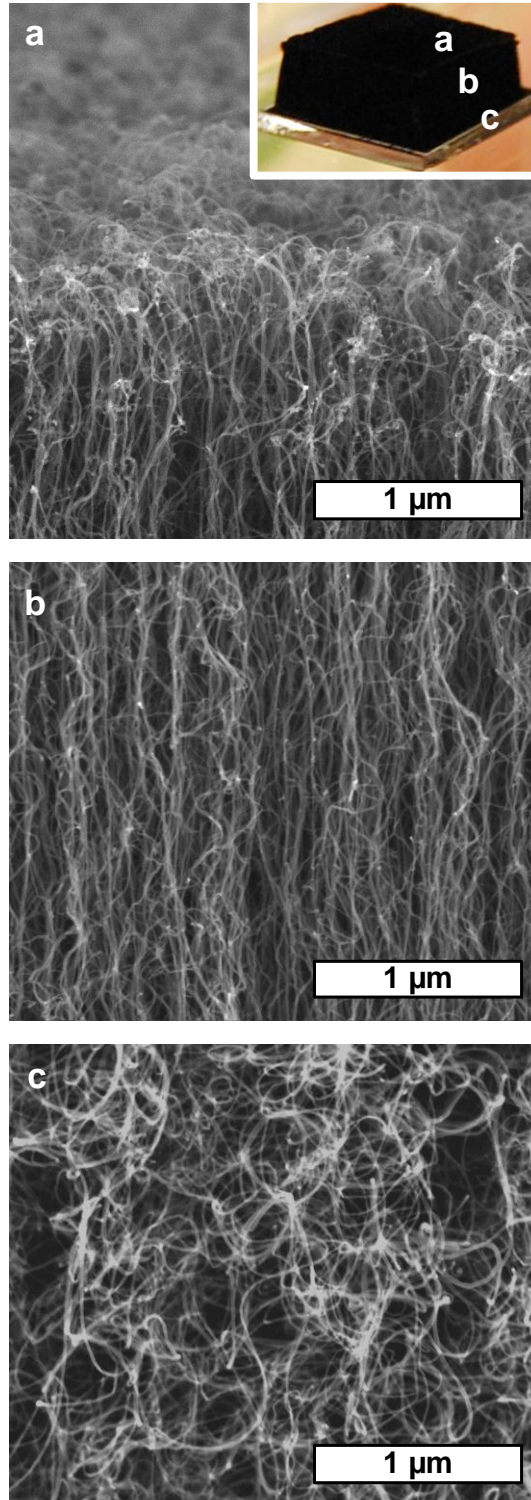
Figure 4.1 Morphology along the height of a typical CNT forest. SEM images of forest sidewall (at 52° tilt): (a) top, (b) middle, and (c) base of the forest correspond to beginning, middle and end of growth (for base- growth mechanism). Inset photograph of 3-mm-tall CNT forest on Si. (T_s/T_p = 800/1040 °C).

due to van der Waals attraction), results in a tortuous morphology as shown in **Figure 4.1**.

Indeed, mechanical coupling among CNTs and CNT bundles has been highlighted as an important factor in self-organized CNT growth,[4, 5] and when the spacing is sufficiently large to reduce these interactions, the forest loses its self-aligned structure.[2] The general observation that denser forests have less tortuous CNTs[6] also underscores the importance of physical interactions among CNTs and implies an inverse relationship between density and tortuosity. Externally applied forces can even frustrate growth and induce morphological changes.[7] Despite these key findings, the evolution in forest morphology during synthesis and its relationship to governing mechanical and/or chemical mechanisms is poorly understood. Unfortunately, the electrical and thermal transport properties of CNT forests continue to be limited by defects either caused by or associated with CNT tortuosity.[8-11] This inhibits the practical use of CNT forests as thermal and electrical interface materials.[12-15] Therefore, tools and methods for diagnosing CNT forest growth will not only enable improvement of forest properties, but elucidating morphological signatures conveys vital information about the synthesis process.

I combine electron microscopy and X-ray scattering studies with real-time forest height measurements during synthesis to identify and quantify four pertinent stages of CNT forest evolution: self-organization, steady growth, density decay, and self-termination. Example morphologies in **Figure 4.1** demonstrate the evolution of CNT morphology approximately according to these different stages (*i.e.*, beginning, middle, and end of growth). I reveal the kinetics of self-organization and use forest height measurements to corroborate the onset of CNT alignment with the initial acceleration in height. CNTs remain well aligned during steady growth, but I identify a distinct loss of order at the end of growth and correlate it with abrupt self-termination in height kinetics. Correcting the height kinetics for the non-constant CNT tortuosity during synthesis allows new interpretation of reaction kinetics based on the true lengthening rates of CNTs.

4.1.1   Quantifying CNT alignment with X-rays

The morphology within a CNT forest evolves during the growth process, and thus it varies with height as well.[2, 16-18] The SEM images in **Figure 4.1** demonstrate variation in alignment along the height of a typical CNT forest, with an initially tangled morphology in the top crust followed by well aligned CNTs.
I find that CNTs tend toward randomly oriented configurations at the base (*i.e.*, end of growth), which was a novel finding at the time of our original finding[18] and has since been corroborated by others.[19-24] I discuss abrupt termination and loss of CNT alignment further in Section 4.2.2.

I quantify CNT alignment by analyzing small-angle X-ray scattering (SAXS) images. Using synchrotron radiation ensures a large signal-to-noise ratio and enables rapid collection times for *in situ* measurements of forest growth and high-resolution spatial mapping of forests. Our typical experimental setup is depicted in **Figure 4.2a**, where the source X-ray beam is focused through optics upstream of the specimen, and scattered X-rays are collected on a detector at a specified distance for SAXS ($\approx 10^2\text{-}10^3$ cm). I then calculate the orientation parameter (*f*), which was originally developed by Hermans and colleagues for measuring polymer chain alignment[25] and is often used to evaluate order in liquid crystals.[26] This parameter quantifies the average orientation of the ensemble of individual CNTs within the X-ray beam path, in relation to a reference direction (*i.e.*, z-axis). Hence, *f* is a measure for the mean square cosine of the angle between the CNT direction and the reference direction (ϕ),

$$f = \frac{1}{2}\left(3\langle\cos^2\phi\rangle - 1\right)$$

Eq. 4.1

The average angle of alignment (ϕ) is calculated by integrating the corresponding intensity distribution $I(\phi)$ of the SAXS pattern about the beam's axis,[17, 27, 28]
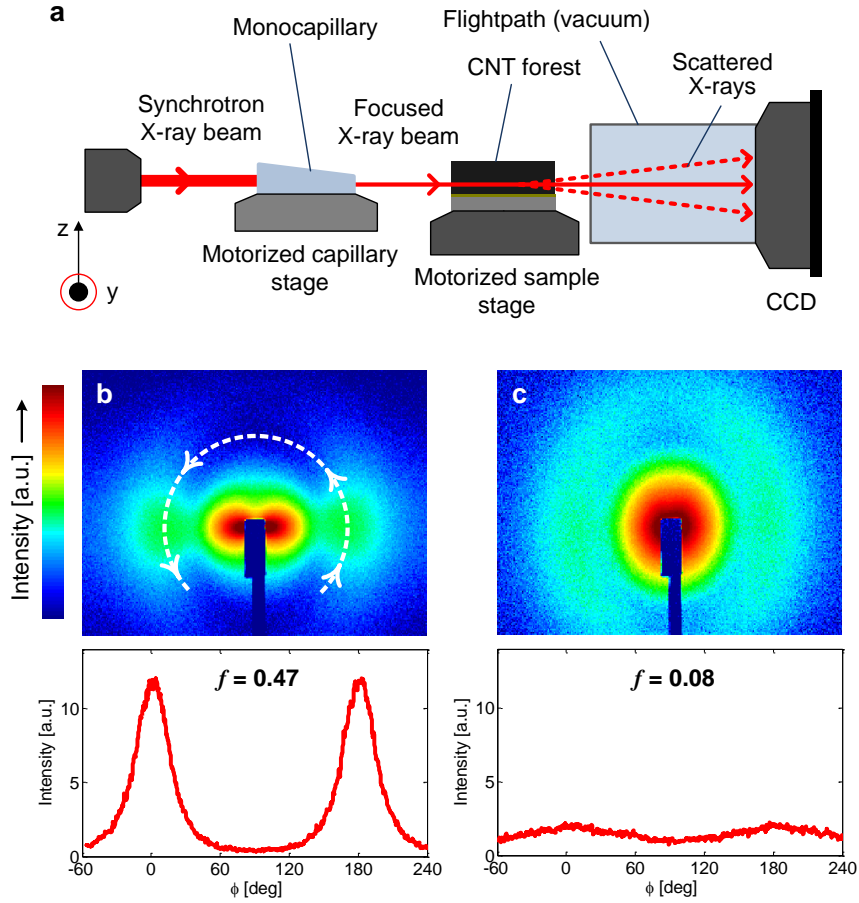
Figure 4.2 SAXS mapping of CNT forests with monocapillary optics for optional focusing of the beam down to 40 μm at the specimen. (a) Schematic of setup and sample SAXS patterns taken at the (b) middle and (c) base of a CNT forest with accompanying azimuthal intensity scans below each image (with calculated order parameter *f*). These data clearly illustrate the different between anisotropic (aligned CNTs) and isotropic (disordered CNTs) scattering.

$$\left\langle \cos^2 \phi \right\rangle = \frac{\int_0^{\frac{\pi}{2}} \left(I(\phi) \sin \phi \cos^2 \phi \right) d\phi}{\int_0^{\frac{\pi}{2}} \left(I(\phi) \sin \phi \right) d\phi} \;.$$

Eq. 4.2

Thus, the distribution of intensity, $I(\phi)$, about the azimuthal angle ϕ is a direct indication of the average CNT orientation within the scattering cross section. Note, this azimuthal scan is executed at a specified radius in *q*, the value of which is determined by

the location of the CNT signature peak ($q \approx$ 0.5-1.5 nm^{-1}). Here, q is the scattering vector that describes momentum transfer and is equal to $\frac{4\pi}{\lambda}\sin(\theta)$, where 2θ is the conventional diffraction angle. Critical values of f are -0.5, 0 and 1, corresponding to perfectly horizontal, disordered, and perfectly vertical orientations, respectively. I therefore assign a value of f to each time step and/or height interval in order quantify the evolution of alignment in CNT forest growth.

Example SAXS patterns of aligned ($f = 0.47$) and disordered ($f = 0.08$) CNTs are shown in **Figure 4.2b** and **Figure 4.2c**, respectively. Notably, these images are taken within the same forest but at different positions along the height (*e.g.*, **Figure 4.1b** and **Figure 4.1c**, respectively), which demonstrates the wide variation in order that occurs during synthesis. The distribution of scattering intensity $I(\phi)$ is also shown below the SAXS patterns in **Figure 4.2**, which clearly illustrates that isotropic scattering results from disordered, unaligned CNTs.

4.2 Results and discussion

4.2.1 Self-organization of CNTs in early forest growth

I synthesize multi-wall (MW) CNTs by CVD from a catalyst thin film of 1nm Fe on 10 nm Al$_2$O$_3$ deposited by electron-beam evaporation on a (100) Si wafer coated with 300 nm of thermally grown oxide. I first anneal the thin film in H$_2$/He at 775 °C in a tube furnace, causing the film to dewet into nanoparticles, and I grow CNTs by subsequent exposure of the catalyst to C$_2$H$_4$/H$_2$/He. Growth is intentionally ceased by rapidly cooling the system by removing the reactor tube from the furnace while maintaining the C$_2$H$_4$/H$_2$/He environment, which is why there is some growth for the "0 sec" case. **Figure 4.3** shows the evolution of forest growth under these synthesis conditions, with a clear transition from disordered CNTs to an aligned forest with increasing process time.

As mentioned in the introduction, the self-aligned morphology relies on physical interactions among neighboring CNTs.[29] Thus, the criteria for initiating alignment are related to the number density and length of CNTs,[30] both of which are dynamic and are
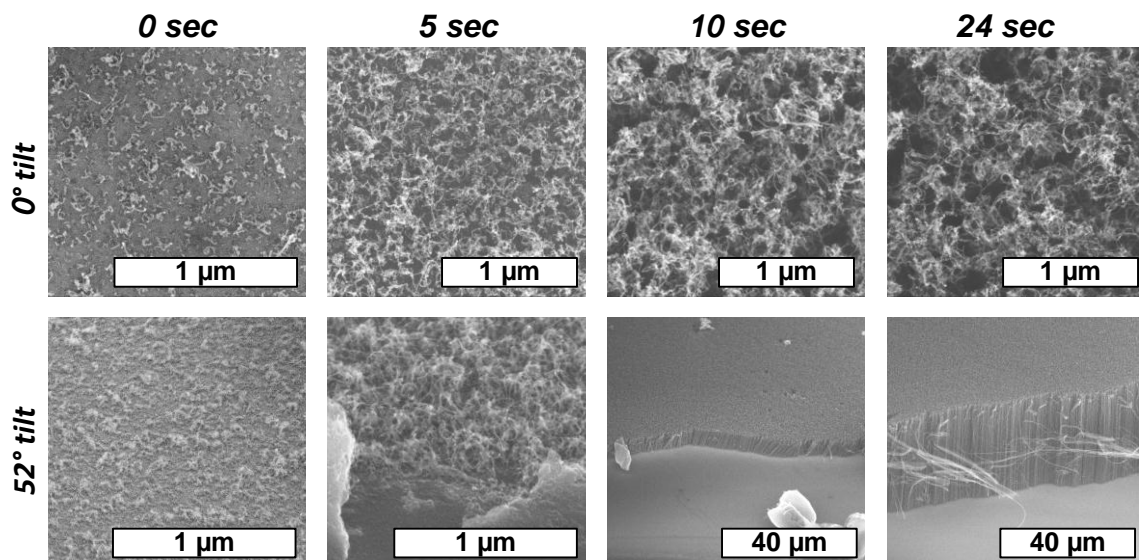
Figure 4.3 SEM images of CNT growth time series, representing the early stages of forest growth, with images corresponding to (a) 0 sec, (b) 5 sec, (c) 10 sec, and (d) 24 sec after C_2H_4 is introduced to the reactor. At the specified time, the reactor is rapidly cooled in the growth gases, so the carbon deposits on the Fe catalyst in all cases, including the "0 sec" case. Note, the onset of CNT alignment at 10 sec. In all cases, CNTs are synthesized in a hot-wall reactor at 775 °C.
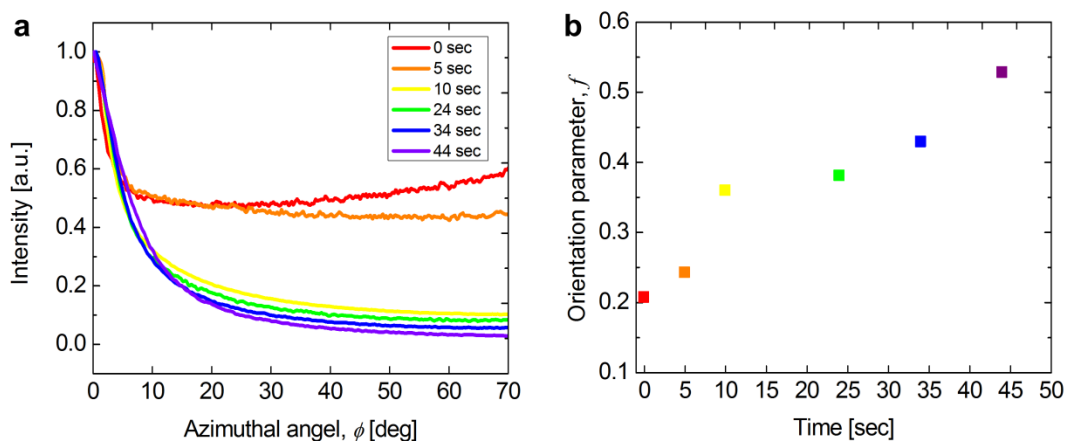
Figure 4.4 CNT alignment during forest self-organization as measured by GISAXS. (a) Azimuthal intensity scans taken from GISAXS of same CNTs shown in **Figure 4.3**, which show trend toward higher anisotropy with time, as quantified in (b) with the orientation parameter f

assumed to be generally increasing with time shortly after the hydrocarbon is introduced. When individual CNTs begin to grow, they are separated by large distances, as approximately determined by the spacing of catalyst particles, which I found in Section 3.2.3 to be ≈ 2-6 times the CNT diameter (**Figure 3.6**). In fact, the separation distances are even larger than this particle spacing because the initial catalyst activity is about 1%.[1] Therefore, the initial CNTs (*i.e.*, at "0 sec") begin as a discontinuous tangled film, where the CNT orientation is subject to random fluctuations due to thermal energy[31] and can also be influenced by surface forces exerted by the Al_2O_3 support layer. As the synthesis process proceeds, CNTs continue to elongate by the addition of carbon at the catalyst-CNT interface, and by 5 sec, neighboring CNTs contact one another to form a continuous network. At this time, the substrate is still visible between the voids in the network (in contrast with those after 5 sec), and the tilted view reveals that there is no vertical alignment beneath the network.

I observe the onset of self-alignment at 10 sec, where the existing tangled network reaches a critical density, which provides a mechanical support. Previous work has shown that by controllably increasing the areal density of catalyst particles, the morphology of resultant CNTs tends toward vertically aligned forests, with a critical threshold density between $2.5\text{-}6 \times 10^{10}$ cm^{-2}.[32] Interestingly, this also agrees with our previous experimental and simulation results[2] showing that the CNT self-aligned morphology may be lost when the CNT number density decays to $0.8\text{-}2 \times 10^9$ cm^{-2} (or $\times 10^{10}$ cm^{-2} catalyst particle density, assuming 10% activity[1]). The onset of order may be aided by configurational entropy,[33] commonly observed in polymeric systems and ligands in self-assembled monolayers (SAMs).[34] In this mechanism, as empty volume decreases and the propensity of steric hindrances increases, the system tends toward more order to minimize energy, as described by the Onsager hard-rod model.[35] CNTs are rods of practically infinite aspect ratio,[36] so they pack in bundles to maximize contact area and minimize entropy; however, this transition likely costs elastic energy to deform the CNTs. After 10 sec, the forest height increases as expected, and importantly, the morphology of the top crust does not evolve since Fe catalysts remain fixed on the Al_2O_3 support.

The transition from tangled to alignment morphologies was previously captured for single-wall (SW) CNTs,[37] but the transition is more rapid in my system because the growth rate is much faster for our synthesis conditions. I quantify the morphological transition using SAXS. Using a setup similar to the one shown in **Figure 4.1**, I tilt the specimen into the X-ray beam at an angle near the critical angle for total external reflection of the film. This enables probing of the surface at a grazing incidence with SAXS, or *i.e*, GISAXS (as described in Chapter 3).[38] Using GISAXS to analyze CNT forests has been reported by one other group,[39] but the method I employ of taking azimuthal scans to calculate an order parameter reduces error because it does not require modeling or simulations of the GISAXS. Further, this method is quantitative and can decipher degrees of alignment within a specimen.

Azimuthal intensity scans and corresponding orientation parameter values (*f*) (**Figure 4.4**) are extracted from GISAXS images of the samples shown in **Figure 4.3**. GISAXS data confirms observations from SEM, where the organization of the CNTs evolves from a disordered to a self-aligned state with growth time. The azimuthal scan is executed at a radius in q corresponding to the location of the CNT signature peak. This is important so as not to confuse the catalyst scattering with that of the CNTs, since for a period, there are contributions from both nanostructures in the GISAXS images. For instance, for 0 sec and 5 sec, CNTs sparsely cover the substrate, so GISAXS images contain Fe scattering as well, but beyond 5 sec, CNT scattering dominates. There is inherent anisotropy in GISAXS patterns because of the multiple scattering phenomena that occur near the critical angle for total external reflection (*i.e.*, near or along the horizon in the GISAXS image).[40] This may lead to slightly skewed measurements of *f*, and for instance, the disordered film at 5 sec produces $f > 0.2$ rather than a value concurrent with isotropic scattering ($f = 0$). However, *f* still servers as an ordinal measure of alignment as I still decipher a measureable difference between unaligned and aligned morphologies as well as degrees of alignment (**Figure 4.4b**), which makes this technique uniquely valuable for capturing CNT self-organization.

I also perform i*n situ* GISAXS studies of CNT self-organization to complement the *ex situ* results. I mount a cold-wall reactor in the X-ray beampath with X-ray-transparent windows made of polyimide (Kapton) as described in Figure 3.1 in
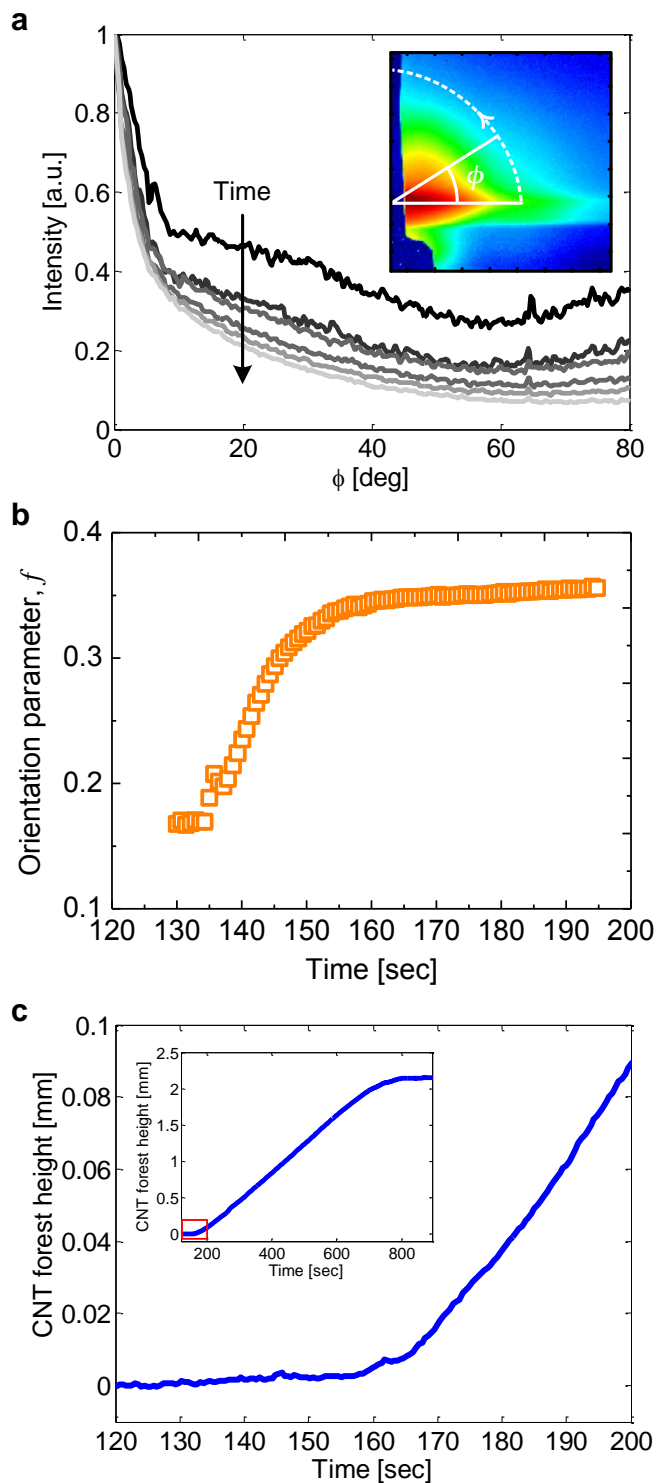
Figure 4.5 CNT alignment during forest self-organization as measured in real time by GISAXS. (a) Azimuthal intensity scans from *in situ* GISAXS measurements taken during CNT synthesis (ANN1), with inset example GISAXS image. (b) Corresponding evolution of orientation parameter with growth time (C_2H_4 introduced at 120 sec), which is corroborated by (c) real-time height measurements of a CNT forest growth under similar conditions ($T_s/T_p = 775/1050$ °C).

81
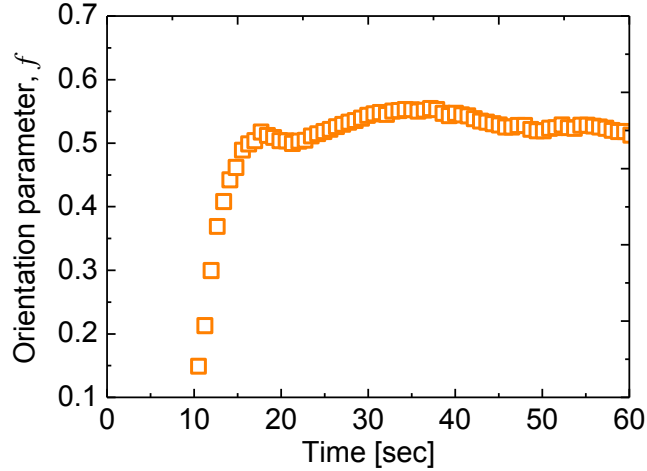
Figure 4.6 Evolution of orientation parameter f for CNT synthesis where the catalyst is rapidly heated in $C_2H_4/H_2/He$ (ANN2), where time = 0 corresponds to when the heater turns on. (T_s/T_p = 800/1070 °C).
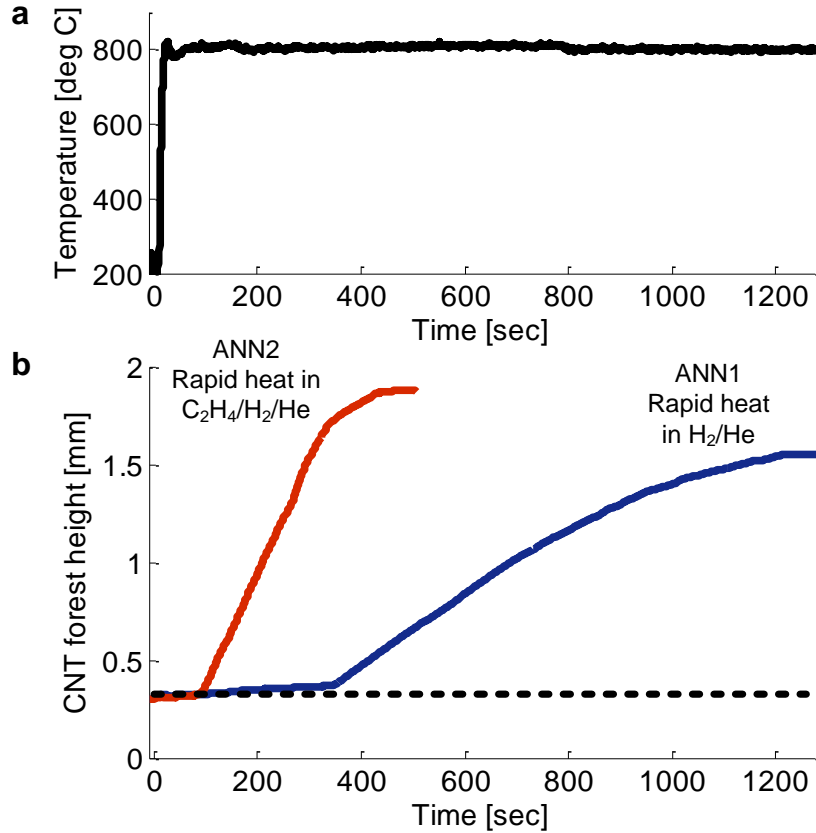
Figure 4.7 Temperature and height profiles for synthesis with rapid heating in either H_2 or C_2H_4/H_2. (a) Temperature profile and (b) CNT height kinetics for two annealing cases discussed in section on *in situ* self-organization measurements. Note, C_2H_4 is not introduced for ANN1 until 120 sec. Laser sensor measurement begins at 300 μm to allow for a gap through which the X-ray beam can pass (marked by black dashed line). Note, C_2H_4 is not introduced to the reactor until 120 sec for ANN1, which explains the apparent lag between "lift off" in forest growth.

Section 3.2.1. Use of a high-rate detector[41] enables a 100 Hz frame rate during acquisition for capture of rapid dynamics during growth for two different experiments for comparison. In the sample preparation method "ANN1", the catalyst is annealed by rapid heating to 800 °C in H_2/He and conditions are held for 2 min before C_2H_4 is added to the reactor (through a preheating). In the method "ANN2", the temperature conditions are the same, but the catalyst is instead heated in the growth gases (C_2H_4/H_2/He) without pre-annealing, so CNTs begin growing nearly instantaneously (see Figure 3.12 in Section 3.2.5).

The azimuthal intensity scans in **Figure 4.5a** are from GISAXS images of ANN1 immediately before and after CNTs begin growing (0.72-sec time steps) along with calculated values of the orientation parameter f plotted versus time in **Figure 4.5b** (where zero corresponds to when the substrate heater turns on). I identify two regimes in this alignment evolution curve. The first is an initial monotonic increase in the orientation parameter, representing the transition from a disordered, tangled film toward a vertically aligned morphology. This transition is induced by an increasing number density of CNTs that I have previously quantified[1], combined with the elongation of existing CNTs. I expect that there is some critical density beyond which the transition occurs, similar to the critical density below which the self-aligned morphology terminates at the end of growth.[2] The transient increase in alignment is sublinear with growth time and is followed by a second regime characterized by saturation of f with time, which is concomitant with the beginning of upward forest growth (**Figure 4.5c**). Thus, a critical degree of alignment is required to produce vertical growth in CNT forests.

In the other experiment (ANN2), I heat the catalyst in the growth gases, which effectively eliminates the transient gas mixing that occurs when the processes of catalyst annealing and introduction of C_2H_4 are otherwise decoupled (ANN1). Incidentally, I observe an enhanced rate of forest formation and transition to the aligned morphology ($\approx$ 3x) (**Figure 4.6**), when comparing ANN2 to ANN1. CNTs likely begin growing simultaneously in this case compared to ANN1 because there is no shortage of active hydrocarbon precursors, which means the number density of CNTs is comparatively less dynamic in this early phase. If the transition from disorder to order in forest growth is governed by number density and lengthening rate of CNTs, then in ANN2, the transition
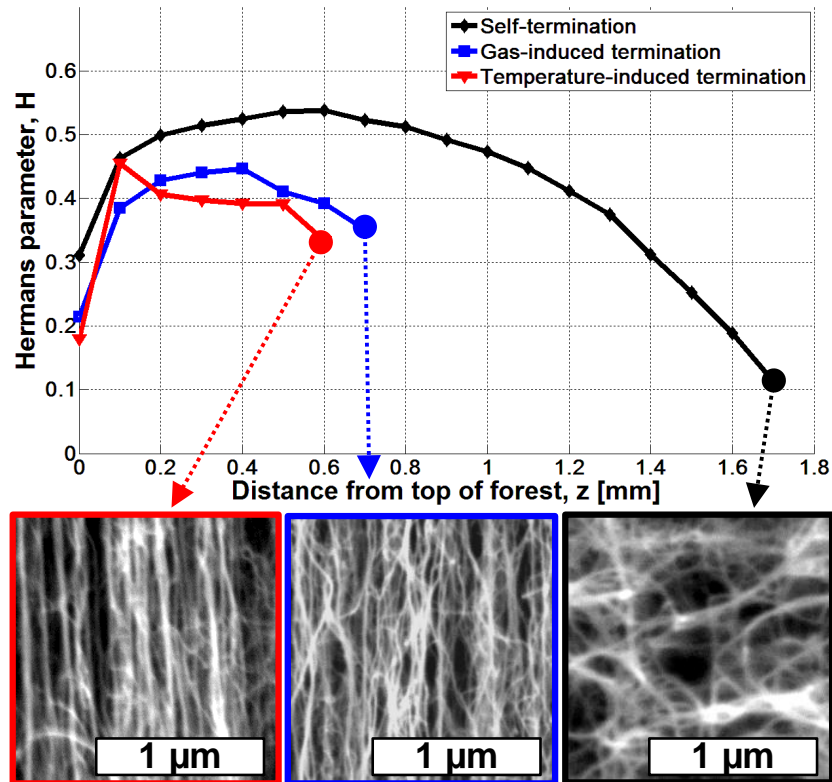
Figure 4.8 Analysis of CNT alignment derived from SAXS mapping along the height of forests that are grown to different termination conditions, per the legend: (1) self-termination, and termination induced by (2) cessation of feedstock supply and (3) rapidly cooling the reactor. Corresponding SEM images taken at the base of each forest show that alignment is lost only in the self-terminated case. In all cases $T_s/T_p = 825/1040$ °C. Adapted with permission from *Journal of Physical Chemistry C* 2009, 113, 20576-20582. Copyright © 2009 American Chemical Society.

is faster because the critical density is achieved sooner. Thus, the transition is likely driven primarily by CNT lengthening if the density is in fact less dynamic for these synthesis conditions. Further, it is also interesting that the rate at which the transition occurs appears to correlate with the average growth rate, r_{avg}, of the forest, where $r_{avg} = 1.7 \ \mu m \ sec^{-1}$ for ANN1 and $5.6 \ \mu m \ sec^{-1}$ for ANN2 (**Figure 4.7**).
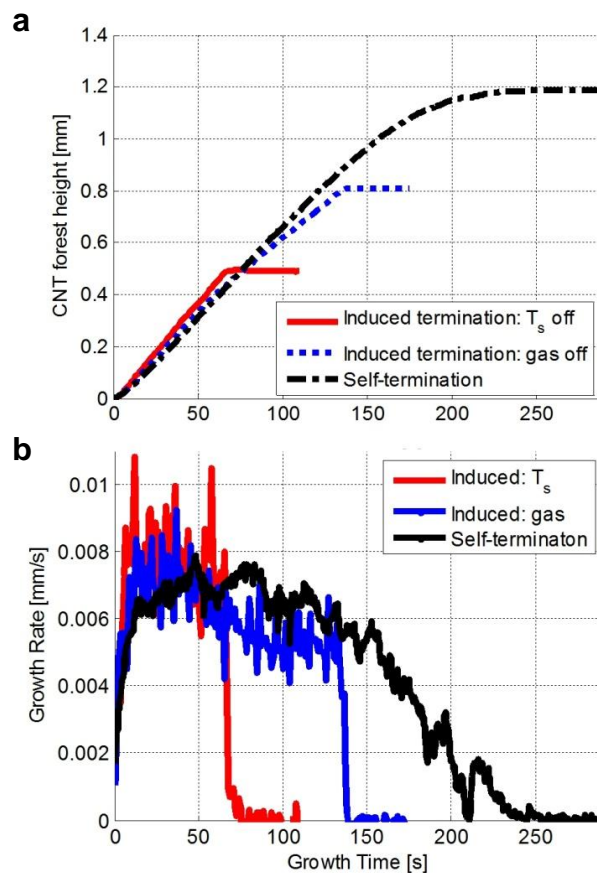
Figure 4.9 CNT forest height kinetics showing abrupt termination. (a) Height kinetics for same CNT forests analyzed in Figure 7 with (b) accompanying rates versus time. ($T_s/T_p = 825/1040$ °C). Adapted with permission from *Journal of Physical Chemistry C* 2009, 113, 20576-20582. Copyright © 2009 American Chemical Society.
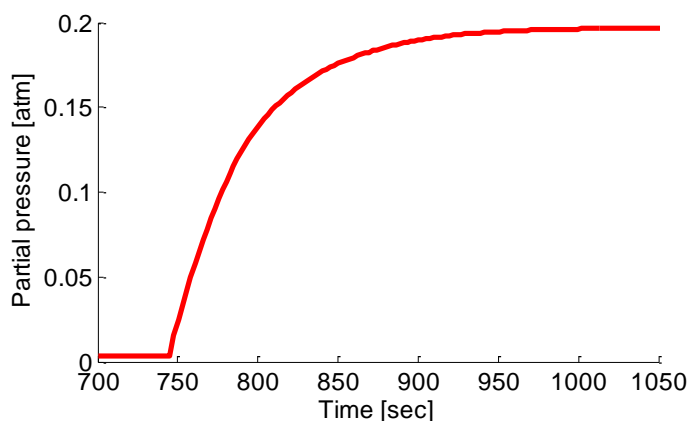
Figure 4.10 Partial pressure of C_2H_4 in the cold-wall reactor as measured by online quadrapole mass spectrometry. Transient behavior is the result of mass flow controller beginning to flow C_2H_4 into an established mixture of H_2/He ($\approx 0.5/0.5$ atm), and the system tends to steady state partial pressures of $C_2H_4/H_2/He \approx 0.2/0.5/0.3$.

85

4.2.2 Abrupt self-termination of CNT forest growth

In separate work,[2] we have identified the stages of growth, including self-organization, steady growth, density decay, and abrupt self-termination, the latter of which I was the first to identify.[18] Recently, we identified an additional "crowding" phase that occurs coincidentally with self-organization;[1] in this phase, we observe an increasing CNT number density with growth time. After the initial transient in the evolution of CNT alignment, the alignment remains fairly constant thereafter, through the steady growth (constant rate) regime before it decays toward self-termination.[2, 18] At this point f drops near zero, representing a distinct loss of order (**Figure 4.8**). Intentional stoppage of growth by discontinuing the supply of the hydrocarbon feedstock or reducing to steady state partial pressures of $C_2H_4/H_2/He \approx 0.2/0.5/0.3$. The temperature of the catalyst also gives abrupt termination, yet in these cases the CNTs remain aligned at the bottom of the forest. Accompanying height kinetics (**Figure 4.9**) for these experiments show that growth terminates abruptly in all of the cases tested, but the loss of alignment is a signature of growth *self*-termination only and is not caused by cooling the reactor or by starving the catalyst of hydrocarbon precursors.

Upon introduction of C_2H_4, it takes approximately 15 seconds for the growth rate to reach a maximum as the gas mixes to a steady composition in the chamber, and then the growth rate decreases before the termination event. This time delay is an apparent induction period during which the incoming gas mixture (including the hydrocarbon precursors) is transient, and surpasses the partial pressure sufficient for nucleating CNTs. I estimate the partial pressure of C_2H_4 is 10^{-2} atm after 18 sec, and it takes ~100 sec for C_2H_4 to reach 90% of its steady state value (0.2 atm) (as analyzed by nass spectrometry in **Figure 4.10**). It is not surprising that nucleation occurs before the steady state partial pressure of C_2H_4 is reached because we have previously shown that only trace amounts (0.01 atm) of alkynes in concert with C_2H_4 are needed for effective forest growth.[42] The growth kinetics in my system exhibit a nearly constant yet gradually decreasing growth rate, followed by abrupt termination at which time the growth rate drops to zero (*e.g.*, **Figure 4.9b**).[18] The terminal height of the forest is limited to several millimeters, and current kinetics model fail to capture the observed kinetics.
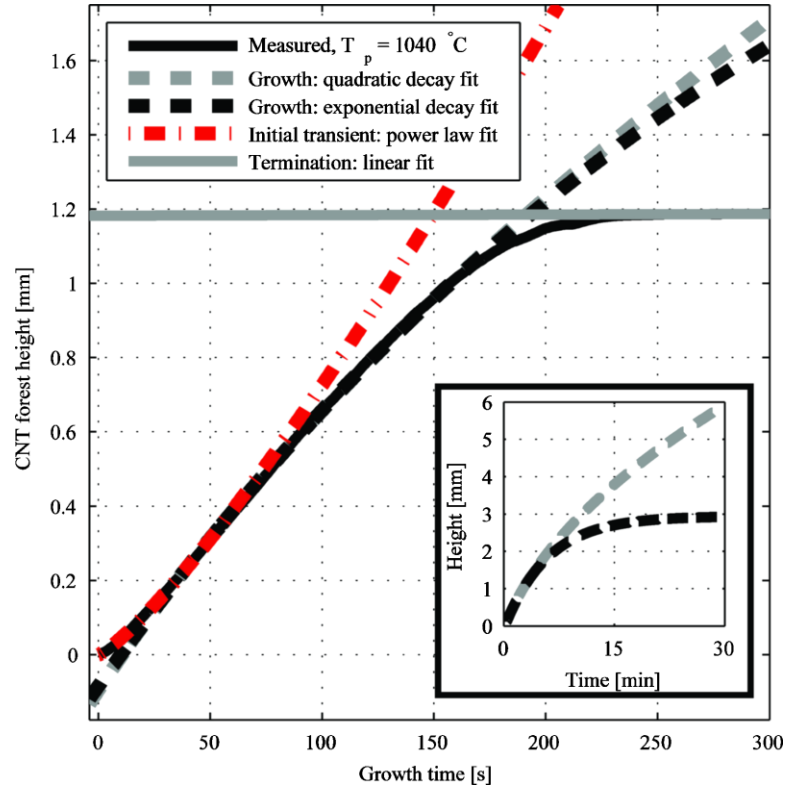
Figure 4.11 Curve fits to CNT forest growth kinetics (self-terminated case in **Figure 4.8** and **Figure 4.9**). The inset shows extrapolations of the exponential and quadratic decay fits, which predict terminal thicknesses that far exceed the measured result. (T_s/T_p = 825/1040 °C). Reprinted with permission from *Applied Physics Letters* 2008, *92* (11), 113107. Copyright © 2008 American Institute of Physics.

The decay of growth rate with time has previously been attributed to several factors, which may not be mutually exclusive, including: diffusion-limitation, where activate precursors are restricted from the metal catalysts by the increasing height of the forest;[43, 44] decaying catalytic activity as growth proceeds;[45] and/or carbon over-coating or sooting on the surface of the metal catalyst from excessive gas-phase decomposition.[46, 47] Reaction-limited kinetics models have also been proposed to describe the growth, but these fail to predict growth deceleration and suggest rate remains linear indefinitely.[43, 48]

As real-time measurement of the forest height enables a precise measurement of the termination kinetics, I find that a piecewise curve-fit (**Figure 4.11**) is more appropriate than the single quadratic decay[49] (diffusion-limited) or exponential decay[45]

kinetics that have previously been proposed to fit the entire growth curve. In my experiments, the initial transient is captured by a power-law fit

$$h = mt^n, \ \ 1 < n < 2,$$
<div align="right">Eq. 4.3</div>

where h is the height of the forest, and m and n are fit parameter relating to the rate of height increase (curve slope). This transitions to a second region that is captured by a quadratic decay limitation[49]

$$h = 0.5\sqrt{A^2 + 4Bt} - 0.5A$$
<div align="right">Eq. 4.4</div>

or exponential decay[45]

$$h = \beta\tau_0\left(1 - e^{-t/\tau_0}\right),$$
<div align="right">Eq. 4.5</div>

which is then truncated by the termination event. In Eq. 4.4, $A = 2D/k_s$ and $B = 4DC_0/M$, where D is the diffusion coefficient, k_s is the first-order rate constant, is the C_2H_4 concentration at the top of the CNT forest, and M is the number of molecules of incorporated into a unit volume of the resulting forest. In Eq. 4.5, β is the initial growth rate, and τ_0 is the catalyst lifetime.

The parabolic and exponential decay models almost identically fit the second region of the curve, yet greatly overestimate the terminal forest height. In this case, the exponential decay model predicts relatively slow termination at 2.9 mm after approximately 25 min, and the diffusion-limited model predicts continued growth past 6 mm height after 30 min. Futaba *et al.*[45] propose that the exponential decay model captures termination of forest growth in their H_2O-assisted process; however, it appears

that their technique of sampling forest height at discrete intervals of several minutes in this particularly study does not adequately capture the termination kinetics.

The highly disordered morphology of the forest base suggests that the CNTs at this location are highly defective, and/or are mechanically strained or buckled. As the catalyst activity decays or the supply of active precursor to the catalyst is restricted, the catalyst particles may suddenly transition to a state where growth is no longer energetically favorable and therefore terminates abruptly. Simulations of CNT nucleation from individual Fe particles suggest that a critical carbon concentration in the catalyst is needed for nucleation and growth,[50] and in principle growth may stop when this condition is no longer satisfied. Further, while these fluctuations may be localized, the CNTs within a forest are mechanically coupled by entanglement and van der Waals forces,[4] and local fluctuations in growth rate can be spatially distributed by this coupling.[51, 52]

For discussion, I reproduce data in **Figure 4.12** from Bedewy, Meshot *et al.*,[1] which shows how CNT number density and alignment evolve during growth. A correlation between the two emerges after density reaches a maximum and begins decaying (blue squares), which suggests that alignment and density are directly related. Precisely the same way CNT alignment is induced by increasing density at the beginning of growth (Section 4.2.1), the decreasing number of physical interactions among neighboring CNTs leads to the loss of order observed at the base of the forest. Abrupt termination of CNT forest growth is caused by this loss of the self-supporting structure, and this event is triggered by accumulating growth termination of individual CNTs. Based on a finite element model of post-buckling behavior of CNTs in contact, which was developed by collaborators Prof. Wei Lu and Haicheng Guo (University of Michigan),[2] we identify a critical threshold in number density ($\approx 10^9$ cm^{-2}) required to maintain the self-aligned morphology. Below this value, the CNTs are severely disordered. **Figure 4.12b** shows that the distinct drop in alignment at the end of growth is nearly constant with density at approximately 2×10^9 cm^{-2}, which is near the defined threshold. Thus, the density saturates at this low
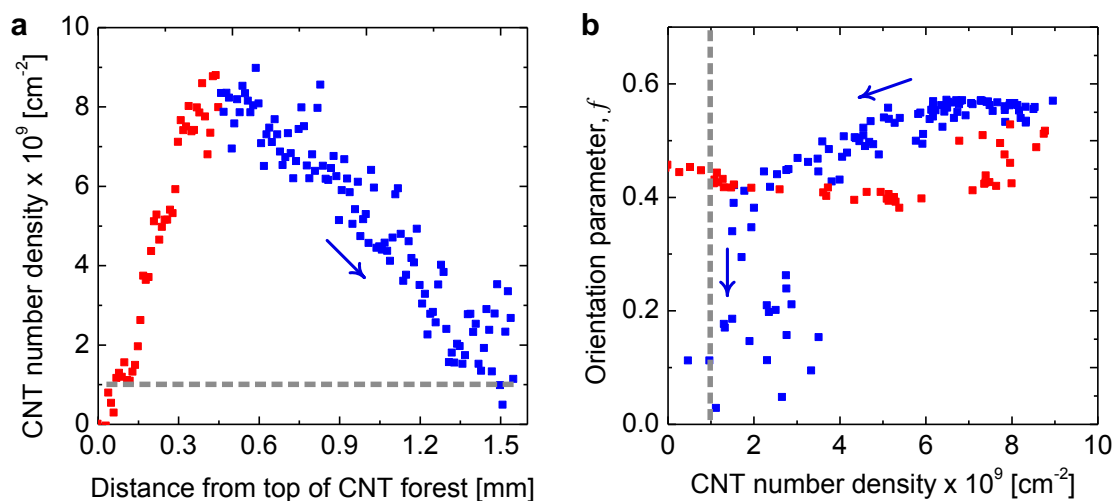
Figure 4.12 Evolution of CNT number density and alignment. (a) Number density versus CNT forest height (related to growth time) and (b) orientation parameter versus number density with blue and red color coding to denote corresponding data points between panels. Blue arrows indicate the direction of time evolution and dashed grey lines indicate the threshold for self-supporting forest structure. Data adapted from Bedewy, Meshot *et al.*[1]

critical value, at which point CNTs become increasingly more disordered until $f = 0$ upon self-termination of the height kinetics, indicating morphological isotropy. This interpretation of CNT growth termination also is supported by *in situ* TEM studies that show catalyst particles ripening and diffusing into the support layer during CNT growth,[53, 54] as well as *ex situ* XPS studies of Fe films after annealing.[1]

4.2.3 Correcting CNT forest height kinetics for tortuosity

Due to the inherently tortuous nature of CNTs, measurement of forest height is only an estimate of the true lengths of the constituent CNTs. As discussed previously, the average orientation of CNTs varies throughout the height of a forest. Thus, to accurately examine the *reaction* kinetics of CNT ensembles, I resolve the real lengthening kinetics of the CNTs by correlating the average alignment, as measured by SAXS mapping, with forest height. The following content derives primarily from a journal publication co-authored by Mostafa Bedewy and myself, who made equal
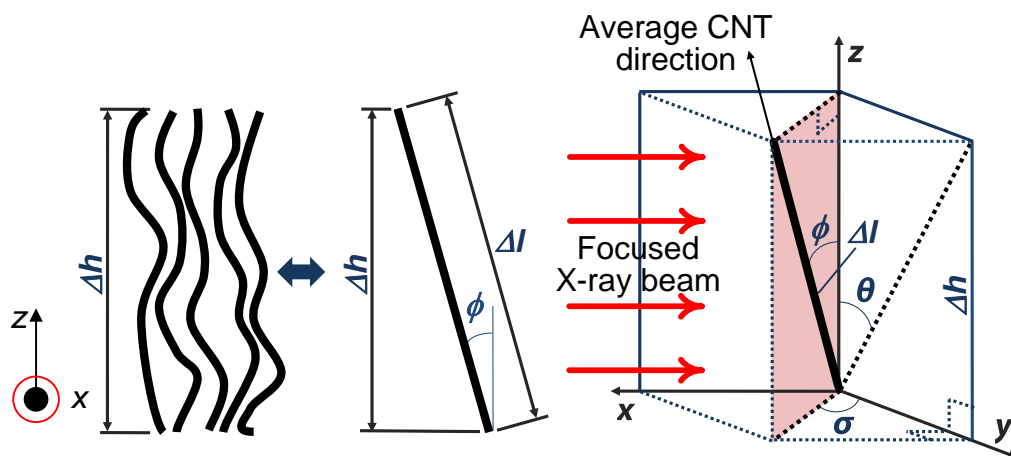
Figure 4.13 Schematic of a representative volume element in the X-ray beam path during SAXS mapping of CNT forests. It shows how we approximate an ensemble of tortuous CNTs as a singular straight element with an average direction by calculating integrated intensity distributions about ϕ (see **Figure 4.2**).

contributions to the work.[55] Adapted with permission from *Nanoscale* 2010, 896-900. Copyright © 2010 Royal Society of Chemistry.

A single-bounce monocapillary (**Figure 4.1**), fabricated at CHESS, is used to focus the beam down to ≈ 40 μm in diameter as it passes through the CNT sample, which is placed on a motorized stage at the focal length of the optics. The small size of the beam provides for high-resolution spatial mapping to reveal changes in CNT alignment over small displacements in height. Only a small portion, 0.1×0.2 mm^2, of the capillary is illuminated in order to limit the divergence at the sample position to approximately 1 milliradian.[56]

As shown in **Figure 4.13**, we consider that the CNTs within a differential volume of the forest can be assigned an average direction, which is skewed from the vertical axis by ϕ. Thus, the average true length (Δl) is calculated knowing the measured apparent differential height (Δh) and the average angle of alignment (ϕ). Here, ϕ is extracted from $\langle \cos^2 \phi \rangle$, which is calculated from the SAXS pattern as described above. It is important to note that this model assumes the CNT forest is isotropic in the horizontal plane, which is accurate due to the large number of CNTs within the beampath. Thus, all values of the

angle σ are equally probable, *i.e.*, $\langle \cos^2 \sigma \rangle = 1/2$, when the X-ray beam is parallel to the horizontal plane.

Now, the average CNT length within the same differential volume can be calculated from the height and orientation measurements. From here on, we distinguish the calculated CNT length from the measured CNT height simply by the terms *height* and *length*, respectively. From Figure 11d, the length and height are thusly related by the direction cosine of the CNT direction with respect to the z-axis:

$$\Delta l = \frac{\Delta h}{\cos \phi} .$$

Eq. 4.3

In order to directly correlate this transformation with the conventional orientation parameter, we can also express the direction cosine, or secant, in terms of *f*,

$$\Lambda(f) = \frac{\Delta l}{\Delta h} = \left(\frac{3}{2f+1} \right)^{\frac{1}{2}} .$$

Eq. 4.4

The variation of Λ with orientation is plotted in **Figure 4.14** and quantifies the conversion from differential height to length, as related to the value of *f*. As mentioned before, *f* = 1 represents perfectly vertical and parallel alignment, where the height is equal to the length ($\Lambda = 1$). Similarly, $\Lambda \rightarrow \infty$ as $f \rightarrow -0.5$, corresponding to CNTs with a perfectly horizontal configuration. On the other hand, $f = 0$ represents isotropic scattering from CNTs that have no preferential orientation, giving $\Lambda = 1.73$. Importantly, for the case of randomly oriented CNTs, the average planar angle of alignment (θ) equals $\Lambda = \pi/4$, i.e. $\langle \cos^2 \theta \rangle = 1/2$, which from the geometry (**Figure 4.13**) corresponds to $\langle \cos^2 \phi \rangle = 1/3$.

The spatial variation of CNT alignment, as quantified by SAXS, indicates that height maps nonlinearly to CNT length; thus we must employ the function Λ to spatially map height to length. To derive length versus time, we calculate and sum the differential

length element Δl along the height of the forest (H), applying Λ to the measured $\Delta h / \Delta t$ at each point. This ratio describes the relationship between the beamspot incremental step Δh, and the corresponding differential growth time Δt, which is determined from the *in situ* height measurements. The resulting summation is

$$l(t) = \sum_{i=1}^{N} \left(\frac{\Delta l}{\Delta h} \right)_i \cdot \left(\frac{\Delta h}{\Delta t} \right)_i = \sum_{i=1}^{N} \Lambda_i \cdot \left(\frac{\Delta h}{\Delta t} \right)_i,$$

Eq. 4.5

where $l(t)$ is length as a function of time, and N is the total number of points ($N = H/\Delta h$). As the incremental differential height becomes small ($\Delta h \rightarrow 0$) and the number of points at which we sample becomes large ($N \rightarrow \infty$), a continuous function can be integrated to find $l(t)$.

Previously, we have defined the different stages of collective CNT forest growth[2] and discussed the evolution of f.[2, 17, 18, 55] **Figure 4.15** plots the calculated value of f for a forest grown at $T_s/T_p = 750/1000$ °C, and we observe a slight increase in f over the first $\approx$ 100 µm resulting from self-organization of the CNTs (stage I). After this initial transient, we observe an approximately constant f regime (stage II) correlating with a period of steady height increase shown in **Figure 4.16**, followed by a transition as f decays (stage III) to zero at growth termination (stage IV). The non-monotonic decay of f after the steady regime indicates collective morphological changes as the forest alignment degrades. These are corroborated by previous observations of tilting[57] and cracking[58] of the forest as termination approaches.

We use this precise spatial mapping of the alignment to correct the forest height measurements with the transformation function $\Lambda = \Delta l / \Delta h = 1/\cos\phi$. **Figure 4.15** also shows how the transformation (Λ) from forest *height* to CNT *length* evolves throughout growth. Toward the end of growth, when the CNTs are very tortuous, differential height measurements underestimate the differential CNT length by as much as a factor of 1.9.

After applying the transformation, it is apparent that the total CNT length at any particular instant is greater than the forest height and, more importantly, that the shape of the length kinetics is distinctly different than the height kinetics (**Figure 4.16**). The
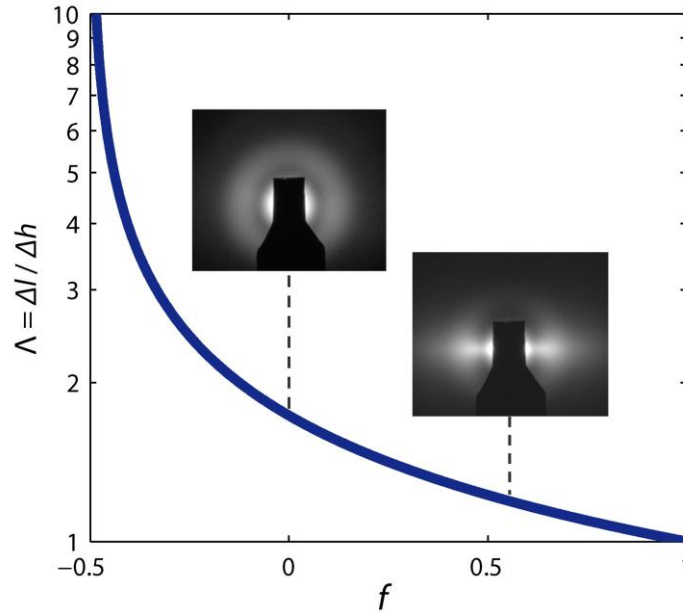
Figure 4.14 Variation of Λ (Eq. 4.4) as function of the orientation parameter f. Inset greyscale SAXS images show representative scattering patterns for typical unaligned and aligned CNT morphologies within a forest (i.e. $f = 0$ and $f = 0.55$).

transformation is most apparent in stages III and IV, where the alignment decreases with continued growth. Near termination, the tortuosity of the growing CNTs increases while the rate of forest height increase declines, so for the same individual CNT lengthening rate, there is less net displacement of the top of the forest. As a result of this feature, the length kinetics curve is linear until growth self-termination, even after the slope of the height kinetics begins to decrease. Finally, termination of CNT lengthening is more abrupt than that observed by forest height, suggesting the collective termination of CNT growth is of a sudden and catastrophic nature, which contradicts previous growth-rate decay models.

The shape of the kinetic curve denotes important information regarding the limiting mechanisms of the growth and termination processes, thus obtaining an accurate shape is vital in order to understand which model is correct. Notably, in my experiments, the length kinetics are linear, whereas the height kinetics are best described by the nonlinear quadratic/exponential decay curves as shown in **Figure 4.16**. The transformation in shape also suggests that the ubiquitous sub-linear shapes of forest

94
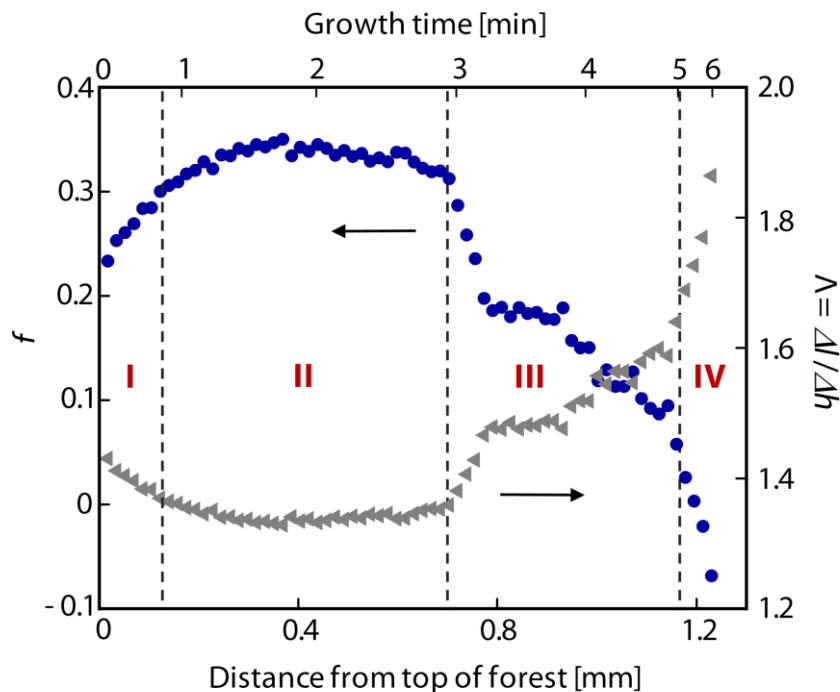
Figure 4.15 Plot of f (solid blue circles) and Λ (solid gray triangles) versus both CNT forest height and growth time. Growth stages I–IV (as described in the text) are labeled on the plot in red. Note that growth time scales nonlinearly with forest height.

height kinetics may be inaccurate portrayals of the real lengthening rate of individual CNTs. Specifically, a linear relationship between length and reaction time may indicate that growth is limited by the reaction rate at the catalyst surface,[43, 48] rather than by diffusion of the precursor to the base of the forest or by decay of catalyst activity, as has been suggested by curve fitting to the sub-linear kinetics curves. Likewise, it is important to note that kinetic models of the CNT growth typically represent growth behavior of an individual CNT, which does not necessarily capture the statistical distribution of CNTs within a forest. To this end, we found that CNT number density within a forest decays toward termination,[1, 2] and therefore the length kinetics presented here are a measure of the "longest-living" CNTs in the forest. Further, all these models fail to capture the abrupt nature of self-termination, which has been observed in our work and several other studies.[2, 18, 22, 57, 59-61]

The next phase of this work is aimed at investigating the rate of CNT lengthening under different reaction conditions as well as combining measurements of CNT length

95
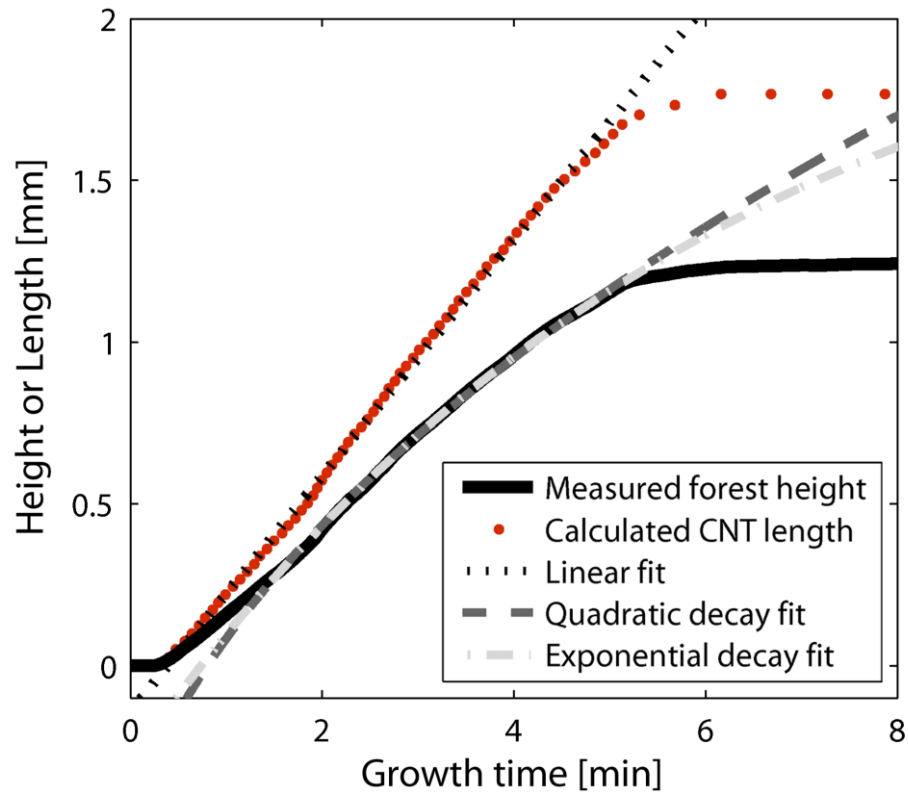
Figure 4.16 Corrected CNT lengthening kinetics as computed from *in situ* measurement of forest height (Eq. 4.5). Curve fitting demonstrates the transformation from a nonlinear to a linear characteristic. A linear, rate-limited kinetics model best fits the length kinetics, which quadratic decay and exponential decay best describe the steady growth regime of my height kinetics, although they over-predict terminal forest height as in **Figure 4.11**.

with forest mass.[1] Such a comprehensive approach truly reveals the population dynamics of CNT growth and hence determines how the growth rate and lifetime of individual CNTs depend statistically on their diameter, the growth conditions, and other important factors. We find that the mass-based kinetics of a CNT population are accurately represented by the S-shaped Gompertz model of population growth, although the CNT length kinetics are essentially linear.

4.3   Conclusions

The morphology of CNT forests evolves dynamically and is intimately related to the synthesis conditions. For instance, the initial self-organization of CNTs correlates to the average growth rate of the forest, suggesting that the formation of the aligned morphology is a function of the lengthening rate of CNTs. Further, using *in situ* measurements of forest height, I corroborate the onset of order in the forest with the start of vertical growth. CNTs remain well aligned during steady growth after the initial transient until order is lost upon self-termination of growth, which can be explained by catalyst migration. In order to truly overcome limiting mechanisms of CNT growth, I must understand how the lifetime of individual CNTs is determined by their particular multidimensional growth characteristics and by their collective interactions. Thus, the X-ray methodology presented in this chapter, which could readily be integrated as an *in situ* precision measurement system, could also advance our understanding of the fundamental physics and chemistry of growth of other filamentary structures.

4.4 References

1. Bedewy, M.; Meshot, E. R.; Reinker, M. J.; Hart, A. J., Population growth dynamics of carbon nanotubes. *ACS Nano* 2011, 5, 8974-8989.

2. Bedewy, M.; Meshot, E.; Guo, H.; Verploegen, E.; Lu, W.; Hart, A., Collective mechanism for the evolution and self-termination of vertically aligned carbon nanotube growth. *Journal of Physical Chemistry C* 2009, *113* (48), 20576-20582.

3. Lee, H. S.; Yun, C. H.; Kim, H. M.; Lee, C. J., Persistence length of multiwalled carbon nanotubes with static bending. *Journal of Physical Chemistry C* 2007, *111* (51), 18882-18887.

4. De Volder, M.; Vidaud, D.; Meshot, E.; Tawfick, S.; Hart, A., Self-similar organization of arrays of individual carbon nanotubes and carbon nanotube micropillars. *Microelectronic Engineering* 2010, 1233-1238.

5. Han, J. H.; Graff, R. A.; Welch, B.; Marsh, C. P.; Franks, R.; Strano, M. S., A mechanochemical model of growth termination in vertical carbon nanotube forests. *ACS Nano* 2008, *2* (1), 53-60.

6. Esconjauregui, S.; Fouquet, M.; Bayer, B.; Ducati, C.; Smajda, R.; Hofmann, S.; Robertson, J., Growth of ultrahigh density vertically aligned carbon nanotube forests for interconnects. *ACS Nano* 2010, *4* (12), 7431-7436.

7. Hart, A.; Slocum, A., Force output, control of film structure, and microscale shape transfer by carbon nanotube growth under mechanical pressure. *Nano Letters* 2006, *6* (6), 1254-1260.

8. Akoshima, M.; Hata, K.; Futaba, D.; Mizuno, K.; Baba, T.; Yumura, M., Thermal diffusivity of single-walled carbon nanotube forest measured by laser flash method. *Japanese Journal of Applied Physics* 2009, -.

9. Ivanov, I.; Puretzky, A.; Eres, G.; Wang, H.; Pan, Z.; Cui, H.; Jin, R.; Howe, J.; Geohegan, D. B., Fast and highly anisotropic thermal transport through vertically aligned carbon nanotube arrays. *Applied Physics Letters* 2006, *89* (22), 223110-3.

10. Yang, D.; Zhang, Q.; Chen, G.; Yoon, S.; Ahn, J.; Wang, S.; Zhou, Q.; Wang, Q.; Li, J., Thermal conductivity of multiwalled carbon nanotubes. *Physical Review B* 2002, -.

11. Panzer, M.; Zhang, G.; Mann, D.; Hu, X.; Pop, E.; Dai, H.; Goodson, K., Thermal properties of metal-coated vertically aligned single-wall nanotube arrays. *Journal of Heat Transfer-Transactions of the Asme* 2008.

12. Endo, M.; Hayashi, T.; Kim, Y.; Terrones, M.; Dresselhaus, M., Applications of carbon nanotubes in the twenty-first century. *Philosophical Transactions of the Royal Society of London Series A-Mathematical Physical and Engineering Sciences* 2004, *362* (1823), 2223-2238.

13. Garcia, E. J.; Wardle, B. L.; Hart, A. J., Joining prepreg composite interfaces with aligned carbon nanotubes. *Composites Part A-Applied Science and Manufacturing* 2008, *39* (6), 1065-1070.

14. Tong, T.; Zhao, Y.; Delzeit, L.; Kashani, A.; Meyyappan, M.; Majumdar, A., Dense, vertically aligned multiwalled carbon nanotube arrays as thermal interface materials. *IEEE Transactions on Components and Packaging Technologies* 2007, *30* (1), 92-100.

15. Baughman, R. H.; Zakhidov, A. A.; de Heer, W. A., Carbon nanotubes - the route toward applications. *Science* 2002, *297* (5582), 787-792.

16. Wang, H.; Xu, Z.; Eres, G., Order in vertically aligned carbon nanotube arrays. *Applied Physics Letters* 2006, *88* (21),.

17. Wang, B.; Bennett, R.; Verploegen, E.; Hart, A.; Cohen, R., Quantitative characterization of the morphology of multiwall carbon nanotube films by small-angle X-ray scattering. *Journal of Physical Chemistry C* 2007, *111* (16), 5859-5865.

18. Meshot, E.; Hart, A., Abrupt self-termination of vertically aligned carbon nanotube growth. *Applied Physics Letters* 2008, *92* (11), 113107.

19. Stadermann, M.; Sherlock, S. P.; In, J.-B.; Fornasiero, F.; Park, H. G.; Artyukhin, A. B.; Wang, Y.; De Yoreo, J. J.; Grigoropoulos, C. P.; Bakajin, O.; Chernov, A. A.; Noy, A., Mechanism and kinetics of growth termination in controlled chemical vapor deposition growth of multiwall carbon nanotube arrays. *Nano Letters* 2009, *9* (2), 738–744.

20. Shanov, V.; Mallik, N.; Chu, W.; Li, W.; Jayasinghe, C.; Yun, Y.; Schulz, M. J.; Yarmolenko, S.; Salunke, P.; Li, G., Advances in synthesis and application of carbon nanotube materials. Materials Science and Technology Conference, Pittsburgh, Pennsylvania, 2008.

21. Puretzky, A. A.; Eres, G.; Rouleau, C. M.; Ivanov, I. N.; Geohegan, D. B., Real-time imaging of vertically aligned carbon nanotube array growth kinetics. *Nanotechnology* 2008, *19* (5).

22. Mattevi, C.; Wirth, C. T.; Hofmann, S.; Blume, R.; Cantoro, M.; Ducati, C.; Cepek, C.; Knop-Gericke, A.; Milne, S.; Castellarin-Cudia, C.; Dolafi, S.; Goldoni, A.; Schloegl, R.; Robertson, J., In-situ X-ray photoelectron spectroscopy

study of catalyst-support interactions and growth of carbon nanotube forests. *Journal of Physical Chemistry C* 2008, *112* (32), 12207-12213.

23.   Patole, S. P.; Alegaonkar, P. S.; Lee, H. C.; Yoo, J. B., Optimization of water assisted chemical vapor deposition parameters for super growth of carbon nanotubes. *Carbon* 2008, *46* (14), 1987-1993.

24.   Wu, J.; Huang, Q. W.; Ma, Y. F.; Huang, Y.; Liu, Z. F.; Yang, X. Y.; Chen, Y. S.; Chen, D. P., Distortion of carbon nanotube array and its influence on carbon nanotube growth and termination. *Colloids and Surfaces a-Physicochemical and Engineering Aspects* 2008, *313*, 13-17.

25.   Hermans, P. H., *Contribution to the physics of cellulose fibres; a study in sorption, density, refractive power and orientation*. Elsevier Pub. Co.: Amsterdam, 1946.

26.   Ghosh, S., A model for the orientational order in liquid crystals. *Il Nuovo Cimento D* 1984, *4* (3), 229-244-244.

27.   Wang, B. N.; Bennett, R. D.; Verploegen, E.; Hart, A. J.; Cohen, R. E., Characterizing the morphologies of mechanically manipulated multiwall carbon nanotube films by small-angle X-ray scattering. *Journal of Physical Chemistry C* 2007, *111* (48), 17933-17940.

28.   Alexander, L. E., *X-ray diffraction methods in polymer science*. Wiley-Interscience: New York, 1969; p xv, 582 p.-xv, 582 p.

29.   Fan, S. S.; Chapline, M. G.; Franklin, N. R.; Tombler, T. W.; Cassell, A. M.; Dai, H. J., Self-oriented regular arrays of carbon nanotubes and their field emission properties. *Science* 1999, *283* (5401), 512-514.

30.   Esconjauregui, S.; Fouquet, M.; Bayer, B.; Robertson, J., Carbon nanotubes growth: from entanglement to vertical alignment. *Physica Status Solidi B-Basic Solid State Physics* 2010, *247* (11-12), 2656-2659.

31.   Ural, A.; Li, Y.; Dai, H., Electric-field-aligned growth of single-walled carbon nanotubes on surfaces. *Applied Physics Letters* 2002, *81* (18), 3464-3466.

32.   Bennett, R. D.; Hart, A. J.; Cohen, R. E., Controlling the morphology of carbon nanotnbe films by varying the areal density of catalyst nanoclusters using block-copolymer micellar thin films. *Advanced Materials* 2006, *18* (17), 2274.

33.   Haji-Akbari, A.; Engel, M.; Keys, A. S.; Zheng, X.; Petschek, R. G.; Palffy-Muhoray, P.; Glotzer, S. C., Disordered, quasicrystalline and crystalline phases of densely packed tetrahedra. *Nature* 2009, *462* (7274), 773-777.

34. Ulman, A., Formation and Structure of Self-Assembled Monolayers. *Chemical Reviews* 1996, *96* (4), 1533-1554.

35. Frenkel, D.; Lekkerkerker, H. N. W.; Stroobants, A., Thermodynamic stability of a smectic phase in a system of hard rods. *Nature* 1988, *332* (6167), 822-823.

36. Polson, J. M.; Frenkel, D., First-order nematic-smectic phase transition for hard spherocylinders in the limit of infinite aspect ratio. *Physical Review E* 1997, *56* (6), R6260-R6263.

37. Zhang, L.; Li, Z.; Tan, Y.; Lolli, G.; Sakulchaicharoen, N.; Requejo, F.; Mun, B.; Resasco, D., Influence of a top crust of entangled nanotubes on the structure of vertically aligned forests of single-walled carbon nanotubes. *Chemistry Of Materials* 2006, *18* (23), 5624-5629.

38. Levine, J. R.; Cohen, J. B.; Chung, Y. W.; Georgopoulos, P., Grazing-incidence small-angle X-ray scattering: new tool for studying thin film growth. *Journal of Applied Crystallography* 1989, *22* (6), 528-532.

39. Mane Mane, J.; Cojocaru, C. S.; Barbier, A.; Deville, J. P.; Thiodjio Sendja, B.; Le Normand, F., GISAXS study of the alignment of oriented carbon nanotubes grown on plain SiO_2/Si(100) substrates by a catalytically enhanced CVD process. *Physica Status Solidi A* 2007, *204* (12), 4209-4229.

40. Renaud, G.; Lazzari, R.; Leroy, F., Probing surface and interface morphology with Grazing Incidence Small Angle X-Ray Scattering. *Surface Science Reports* 2009, *64* (8), 255-380.

41. Koerner, L. J.; et al., X-ray tests of a Pixel Array Detector for coherent x-ray imaging at the Linac Coherent Light Source. *Journal of Instrumentation* 2009, *4* (03), P03001.

42. Plata, D.; Meshot, E.; Reddy, C.; Hart, A.; Gschwend, P., Multiple alkynes react with ethylene to enhance carbon nanotube synthesis, suggesting a polymerization-like formation mechanism. *ACS Nano* 2010, *4* (12), 7185-7192.

43. Zhu, L.; Xu, J.; Xiao, F.; Jiang, H.; Hess, D.; Wong, C., The growth of carbon nanotube stacks in the kinetics-controlled regime. *Carbon* 2007, *45* (2), 344-348.

44. Louchev, O.; Laude, T.; Sato, Y.; Kanda, H., Diffusion-controlled kinetics of carbon nanotube forest growth by chemical vapor deposition. *Journal of Chemical Physics* 2003, *118* (16), 7622-7634.

45. Futaba, D.; Hata, K.; Yamada, T.; Mizuno, K.; Yumura, M.; Iijima, S., Kinetics of water-assisted single-walled carbon nanotube synthesis revealed by a time-evolution analysis. *Physical Review Letters* 2005, *95* (5).

46.   Puretzky, A.; Geohegan, D.; Jesse, S.; Ivanov, I.; Eres, G., In situ measurements and modeling of carbon nanotube array growth kinetics during chemical vapor deposition. *Applied Physics A-Materials Science & Processing* 2005, *81* (2), 223-240.

47.   Wood, R. F.; Pannala, S.; Wells, J. C.; Puretzky, A. A.; Geohegan, D. B., Simple model of the interrelation between single- and multiwall carbon nanotube growth rates for the CVD process. *Physical Review B* 2007, *75* (23), 8.

48.   Xiang, R.; Yang, Z.; Zhang, Q.; Luo, G.; Qian, W.; Wei, F.; Kadowaki, M.; Einarsson, E.; Maruyama, S., Growth deceleration of vertically aligned carbon nanotube arrays: Catalyst deactivation or feedstock diffusion controlled? *Journal of Physical Chemistry C* 2008, *112* (13), 4892-4896.

49.   Zhu, L.; Hess, D.; Wong, C., Monitoring carbon nanotube growth by formation of nanotube stacks and investigation of the diffusion-controlled kinetics. *Journal of Physical Chemistry B* 2006, *110* (11), 5445-5449.

50.   Ding, F.; Bolton, K.; Rosén, A., Nucleation and growth of single-walled carbon nanotubes: a molecular dynamics study. *Journal of Physical Chemistry B* 2004, *108* (45), 17369-17377.

51.   Han, J.; Graff, R.; Welch, B.; Marsh, C.; Franks, R.; Strano, M., A mechanochemical model of growth termination in vertical carbon nanotube forests. *ACS Nano* 2008, *2* (1), 53-60.

52.   Zhang, Q.; Zhou, W.; Qian, W.; Xiang, R.; Huang, J.; Wang, D.; Wei, F., Synchronous growth of vertically aligned carbon nanotubes with pristine stress in the heterogeneous catalysis process. *Journal of Physical Chemistry C* 2007, *111* (40), 14638-14643.

53.   Amama, P.; Pint, C.; McJilton, L.; Kim, S.; Stach, E.; Murray, P.; Hauge, R.; Maruyama, B., Role of water in super growth of single-walled carbon nanotube carpets. *Nano Letters* 2009, *9* (1), 44-49.

54.   Kim, S. M.; Pint, C. L.; Amama, P. B.; Zakharov, D. N.; Hauge, R. H.; Maruyama, B.; Stach, E. A., Evolution in catalyst morphology leads to carbon nanotube growth termination. *Journal of Physical Chemistry Letters* 2010, *1* (6), 918-922.

55.   Meshot, E.; Bedewy, M.; Lyons, K.; Woll, A.; Juggernauth, K.; Tawfick, S.; Hart, A., Measuring the lengthening kinetics of aligned nanostructures by spatiotemporal correlation of height and orientation. *Nanoscale* 2010, 896-900.

56. Lamb, J. S.; Cornaby, S.; Andresen, K.; Kwok, L.; Park, H. Y.; Qiu, X.; Smilgies, D.-M.; Bilderback, D. H.; Pollack, L., Focusing capillary optics for use in solution small-angle X-ray scattering. *Journal of Applied Crystallography* 2007, *40* (1), 193-195.

57. Puretzky, A.; Eres, G.; Rouleau, C.; Ivanov, I.; Geohegan, D., Real-time imaging of vertically aligned carbon nanotube array growth kinetics. *Nanotechnology* 2008, *19* (5).

58. Hart, A. J.; van Laake, L.; Slocum, A. H., Desktop growth of carbon-nanotube monoliths with in situ optical imaging. *Small* 2007, *3* (5), 772-777.

59. Shanov, V.; Mallik, N.; Chu, W.; Jayasinghe, C.; Yun, Y.; Schulz, M. J.; Yarmolenko, S.; Salunke, P.; Li, G. In *Advances in synthesis and application of carbon nanotube materials.*, Materials Science and Technology Conference, Pittsburgh, Pennsylvania, Pittsburgh, Pennsylvania, 2008.

60. Wu, J.; Huang, Q.; Ma, Y.; Huang, Y.; Liu, Z.; Yang, X.; Chen, Y.; Chen, D., Distortion of carbon nanotube array and its influence on carbon nanotube growth and termination. *Colloids And Surfaces A-Physicochemical and Engineering Aspects* 2008, *313*, 13-17.

61. Patole, S. P.; Alegaonkar, P. S.; Lee, H.-C.; Yoo, J.-B., Optimization of water assisted chemical vapor deposition parameters for super growth of carbon nanotubes. *Carbon* 2008, *46* (14), 1987-1993.

Chapter 5
Engineering CNT forest growth by
decoupled thermal treatment of
precursor and catalyst

This chapter discusses the synthesis of vertically aligned carbon nanotube (CNT) "forests" by a decoupled method that facilitates control of the mean diameter and structural quality of the CNTs and enables tuning of the kinetics for efficient growth to forest heights of several millimeters. The growth substrate temperature (T_s) primarily determines the CNT diameter, whereas independent and rapid thermal treatment (T_p) of the C_2H_4/H_2 reactant mixture significantly changes the growth rate and terminal forest height but does not change the CNT diameter. Synchrotron X-ray scattering is utilized for precise, non-destructive measurement of CNT diameter in large numbers of samples, which reveals that diameter increases with T_s, regardless of the value of T_p tested in my experiments. CNT structural quality monotonically increases with T_s yet decreases with T_p, and forests grown by this decoupled method have significantly higher quality than those grown using a conventional single-zone tube furnace. Chemical analysis reveals that the thermal treatment generates a broad population of hydrocarbon species including volatile organic compounds (VOCs) and polycyclic aromatic hydrocarbons (PAHs). A non-monotonic relationship between catalyst lifetime and T_p suggests that certain carbon species either enhance or inhibit growth rate as well as crystallinity of CNTs. However, the forest height kinetics, as measured in real-time during growth, are self-similar thereby indicating that a common mechanism of growth termination may be present over a wide range of process conditions. The contents of this chapter originally appeared in various journal publications (*ACS Nano* 2010, 4, 7185-7192; *ACS Nano* 2009, 3, 2477-2486; *Carbon* 2011, 49, 804-810) and are reproduced here with permission from the respective

publishers. The current presentation of the work herein represents my contributions, principally, unless noted otherwise.

5.1   Introduction

Despite extensive study of CNT forest production,[1-16] including advances using water and oxygen as additives to increase reaction yield and catalyst lifetime, the limiting mechanisms of forest growth are not fully understood, and CNT forest heights are typically limited to several millimeters.

As described in previous chapters, the process of CNT film growth by CVD typically involves multiple stages: (1) the catalyst is prepared on a substrate, such as a silicon wafer; (2) the catalyst is heated and treated chemically, such as by exposure to a reducing atmosphere that causes a thin film to agglomerate into nanoparticles; (3) the catalyst is exposed to a carbon-containing atmosphere, which causes formation and "liftoff" of CNTs from the nanoparticles on the substrate; and (4) CNT growth continues by competing pathways between accumulation of "good" (graphitic) and "bad" (amorphous) carbon.[17] To engineer the functional properties of CNT materials such as forests, we must develop reaction processes that not only treat these stages independently, but that are also accompanied by characterization techniques that enable mapping of the forest characteristics for large sample sizes and populations.

I present a decoupled CVD method that enables precise tuning of CNT diameter, structural quality, and growth kinetics of vertically aligned CNT forests. While my study is restricted to a single catalyst composition and thickness, it demonstrates the importance of each process stage in determining the structural character of a CNT forest and the practical versatility that can be achieved by treating these process variables independently. Other methods of tuning CNT diameter include using porous templates such as anodic alumina,[18, 19] building metal nanoparticles within micelles defined by block copolymers,[20-23] by high-resolution lithography,[24] or by changing the starting thickness of the catalyst thin film.[25, 26] However, these approaches can be complicated and costly in mass production. The critical role of thermal decomposition of the reactant
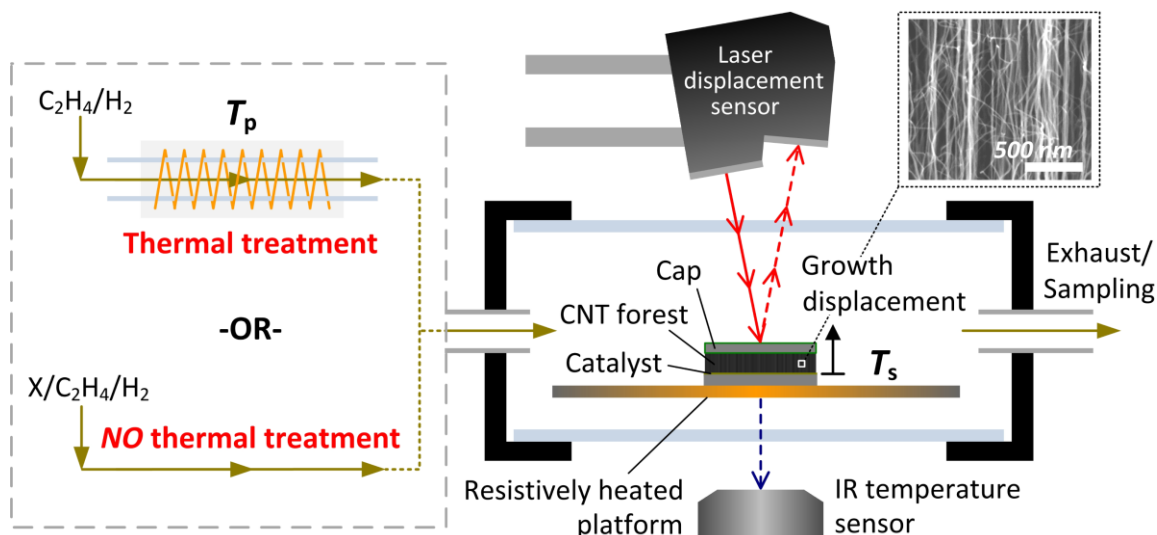
Figure 5.1 Schematic representation of atmospheric-pressure, cold-wall CVD reactor with decoupled thermal control over gaseous precursor and catalyst. Feedstock gases are delivered in one of two modes: (1) with thermal treatment (T_p= 900-1120 °C, C_2H_4 and H_2 only) or (2) without thermal treatment (C_2H_4 and H_2 and a test gas, "X"). The hydrocarbon precursors deposit at the growth substrate, maintained at T_s. CNT forest height is measured in real time by a laser displacement sensor. The inset SEM illustrates that CNTs synthesized by this method are vertically aligned. Reprinted with permission from *ACS Nano* 2010, 4, 7185-7192. Copyright © 2010 American Chemical Society.

is typically manipulated by changing the reactant composition and flow rate[27-30] or by plasma-enhanced methods,[27, 31] and to my knowledge has not been addressed systematically as in the present study.

5.1.1   Experimental methods

CNT forest growth is performed using a custom-built atmospheric-pressure CVD reactor (SabreTube, Absolute Nano) shown schematically in **Figure 5.1**, wherein the growth substrate rests on a resistively heated silicon platform, which is maintained at temperature T_s.[32] Due to its low thermal mass, the substrate heats at approximately 200 °C sec^{-1} when maximum power is applied. The forest height is measured in real time using a laser displacement sensor (Keyence LK-G152) mounted above the chamber. The gas mixture enters the chamber through a heated quartz pipe (4 mm ID) that is maintained at temperature T_p. The residence time of the reactant mixture in the heated

pipe is less than 0.1 sec, and the gas cools to ambient (room) temperature before entering the reaction chamber and reaching the growth substrate, where the quartz tube wall does not exceed 70 °C (as measured by surface-mounted thermocouples).

I explore CNT forest growth in a matrix of T_s and T_p conditions as schematically represented by the T_s-T_p map in **Figure 5.2**, where the growth substrate was 1/10 nm Fe/Al$_2$O$_3$, deposited by electron beam evaporation on a (100) silicon wafer coated with 100 nm thermally grown SiO$_2$.[15] All experiments are performed on 1 cm^2 catalyst substrates taken from the same Si wafer. For each experiment, the chamber is first flushed with He for 10 minutes, then flushed with 310/300 sccm H$_2$/He for 2 minutes. Then, the substrate is rapidly heated to T_s for 2 minutes before the atmosphere is adjusted to 120/310/180 sccm C$_2$H$_4$/H$_2$/He and held throughout the duration of growth. These flow rates are used throughout this chapter except in Section 5.2.4, where the use of trace gas additives is discussed. Reactions are performed at atmospheric pressure. Online quadrupole mass spectrometer residual gas analyzer (Pfeiffer OmniStar GSD 301) is plumbed into the exhaust port of the reaction chamber with a stainless steel capillary.

A dedicated LabVIEW interface monitors and controls the process variables: (1) T_s was measured using an infrared sensor (Exergen 2ACF-K-HIE) and controlled using a high speed controller (RKC Instruments, model HA400, 40Hz sampling rate); (2) T_p is measured using a K-type thermocouple and controlled using a PID controller (Omega CNi-series); (3) forest height is dynamically measured using a laser displacement sensor (Keyence LK-G152), and (4) gas flow rates are measured and controlled using digital mass flow controllers (Aalborg GFC 17, response time 2s). Experiments are fully automated by preloading programmed recipes, thus increasing throughput and reducing experimental error.

CNT diameters were measured non-destructively by transmission SAXS, which was performed at the X27C beamline at the National Synchrotron Light Source (NSLS) at Brookhaven National Laboratory. X-ray wavelength is 0.1371 nm with a spot size of approximately 0.3 mm in diameter. As described previously,[33] the integrated I-q taken from each SAXS image was fit using a form factor relationship for a lognormal distribution of hollow cylinders (see Chapter 3). This provides a non-destructive measurement of the mean CNT diameter and polydispersity within the X-ray beampath
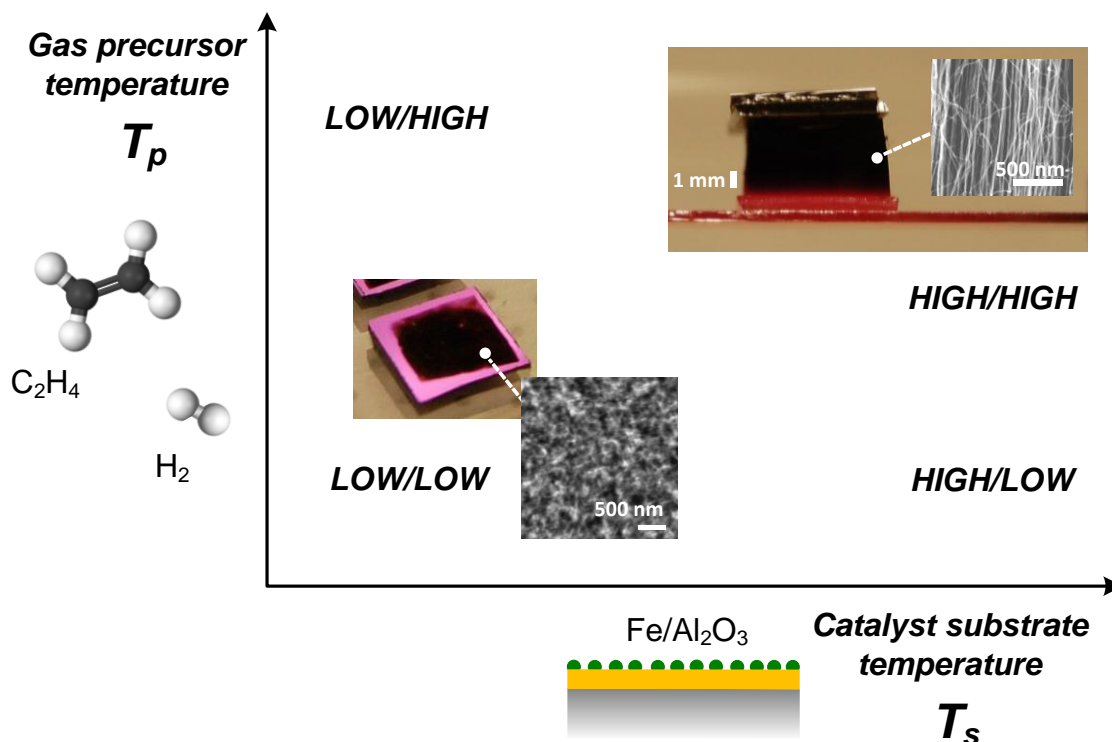
Figure 5.2 Schematic "map" spanning substrate and preheater temperatures (*i.e.*, T_s and T_p), where thermal decomposition and rearrangement is governed by Tp on the vertical axis, and catalyst particle formation and CNT templating (i.e., diameter) are governed by Ts on the horizontal axis. Short, disordered CNT films are achieved at low T_s and low T_p, and tall, vertically aligned CNTs at high T_s and high T_p, which is essentially the regime to which conventional tube furnaces are restricted because their thermal controls are coupled. On the other hand, it is interesting to access the other regimes by decoupling the thermal parameters for unique engineering of CNT film growth.

through each forest and agrees with diameter measurements based on TEM images for large numbers of individual CNTs. SEM (Philips XL30 FEG) and TEM (JEOL 3011 HREM) imaging was performed at the University of Michigan Electron Microbeam Analysis Laboratory (EMAL). TEM images were processed and analyzed with Infinity Analyze Version 4.5.

CNT structural quality is evaluated by Raman spectroscopy (Dimension P2, Lambda Solutions, $\lambda = 533$ nm), and several spectra per sample are acquired along the midpoint of the forest sidewall and subsequently averaged. For thermogravimetric analysis (TGA), forests are delaminated from the growth substrate and heated from room temperature to 1000°C at 10°C/minute in 20 sccm air flow (Perkin-Elmer Pyris 1 TGA). From Table 1, samples A, B, and C are synthesized by the decoupled method with specified T_s and T_p,

while samples TF1 and TF2 are synthesized in a commercial single-zone tube furnace, where the thermal conditions for gas decomposition are defined by the temperature profile along the heated path preceding the growth substrate.

The PAH, alkene, and alkane quantity of reactant gas mixtures are determined as described by Plata *et al.*[34] Briefly, polyurethane foam filters are used to concentrate PAHs over the entire course of the synthetic reaction. These filters are then extracted with organic solvents (dichloromethane and methanol), concentrated by rotary evaporation, and analyzed by gas chromatography- mass spectrometry (GC-MS). Gases that survived transit through the foam filter are collected in a stainless steel canister, cryogenically concentrated, and subsequently analyzed by GC-MS (hydrocarbon identification), GC-flame ionization detection (hydrocarbon identification and quantification), and GC-thermal conductivity detection (helium and hydrogen quantification).

5.1.2 Decoupled thermal control of CNT synthesis

We employ a complementary set of characterization techniques to precisely determine how these thermal conditions influence the key structural characteristics of CNT forests. Millimeter-tall forests are achieved at high T_s/T_p, which emulates single-zone tube furnace systems where gas and catalyst thermal treatments are inherently coupled. Low-temperature synthesis shows the limits of achieving tall forest growth as well as the critical role of T_p in making crystalline CNTs. By understanding the effects of precursor gas chemistry on CNT synthesis, I access unique areas of the T_s-T_p map for specialized tuning of CNT growth. For instance, increasing T_p at low T_s (toward CMOS compatibility) enables synthesis of films of higher-quality CNTs.[35] Also, identification and direct delivery of key hydrocarbon precursors to the reactor allow us to eliminate preheating altogether and thus perform synthesis at high T_s with room temperature T_p.[36]

While gas-phase reactions occur both in the preheater and in proximity of the substrate, T_p has a dominant effect in causing decomposition/rearrangement of C_2H_4/H_2, whereas the effect of T_s is negligible. For instance, I analyze the gas composition flowing out of the reactor during control experiments at three binary ON/OFF combinations

109
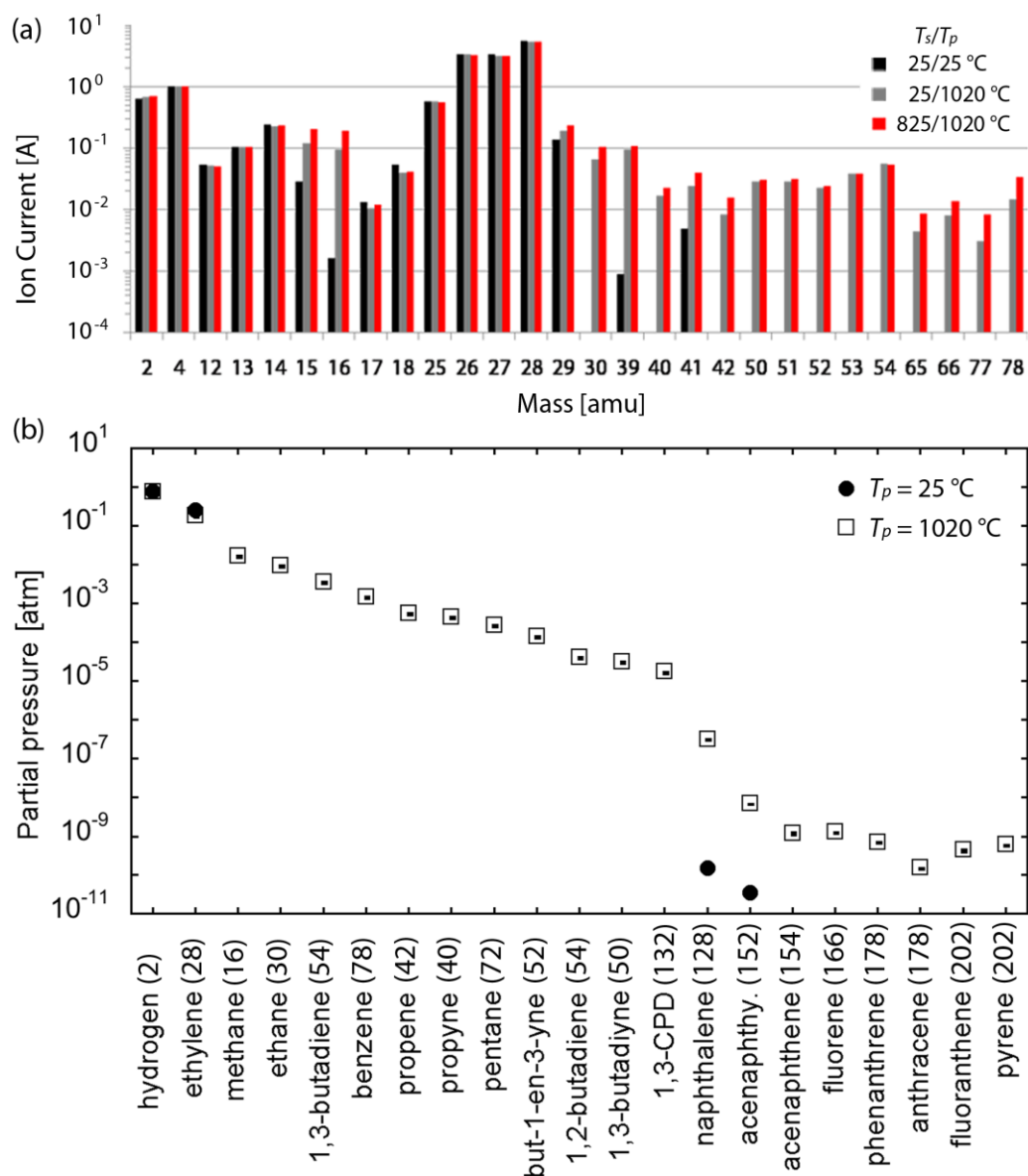
Figure 5.3 Population of gas species present in the growth atmosphere. (a) Mass spectra are collected *in situ* by a quadrupole mass spectrometer (MS) residual gas analyzer for thermal treatment of $C_2H_4/H_2 = 0.28/0.78$ atm, and I present relative changes in the abundance of select compounds where the ion current is normalized to the He signal. (b) The thermally treated gas mixture $C_2H_4/H_2 = 0.2/0.8$ atm is analyzed *ex situ* by GC-MS and GC-FID, which shows a broad range of compounds whose abundances vary by several orders of magnitude. The molecular weight of each species (in amu) is displayed with the name on the bottom axis. The error bars represent one standard deviation on triplicate analyses of the same sample. See Plata *et al.*[43] for a compound key and further details. 1,3-CPD = 1,3 cyclopentadiene; acenaphty.= acenaphthylene. Reprinted with permission from *ACS Nano* 2009, 3, 2477-2486. Copyright © 2009 American Chemical Society.

110

where T_s and T_p are set to typical values for this study. **Figure 5.3a** shows mass spectra generated under these conditions obtained by an online quadrapole mass spectrometer (QMS) that is plumbed into the reactor tube through the exhaust end cap (Supporting Information). These measurements reveal that the reactor contains a highly polydisperse atmosphere, and the composition is indifferent to T_s when the gas is thermally treated at T_p before entering the reactor.

Figure 5.3b displays the partial pressures of the compounds resulting from thermal treatment of C_2H_4/H_2 (0.2/0.8 atm) at approximately $T_p = 1020$ °C, as collected from the preheater output and analyzed *ex situ* by gas chromatography (GC)-MS and GC-flame ionization detection (FID). These spectra show a multitude of products including various alkanes, alkenes, and alkynes, as well as volatile organic compounds (VOCs) and polycyclic aromatic hydrocarbons (PAHs).[34] Incidentally, the untreated gas mixture ($T_s/T_p = 25/25$ °C) contains the expected compounds along with naphthalene and acenaphylene, which are ambient pollutants and derive from typical combustion processes. The variety of thermally generated products, as well as significant variations in relative abundances, demonstrate the complexity of the CVD process and suggest that one or more of the measured species is responsible for enhanced growth rates discussed later. Identifying and relating mechanistic understanding of the individual compounds that are responsible for enhanced growth is the focus of a study that followed this work[36] and exceeds the present scope of this chapter. However, identifying and quantifying the contents of the polydisperse hydrocarbon atmosphere provides a qualitative for interpreting the decoupled roles of T_s and T_p in determining CNT forest characteristics in the present study.

5.2   Results and discussion

5.2.1   Control of CNT diameter by catalyst substrate temperature

The first step in the CNT growth process is the formation of catalyst particles from the Fe thin film, which is natively an oxide when exposed to ambient air after
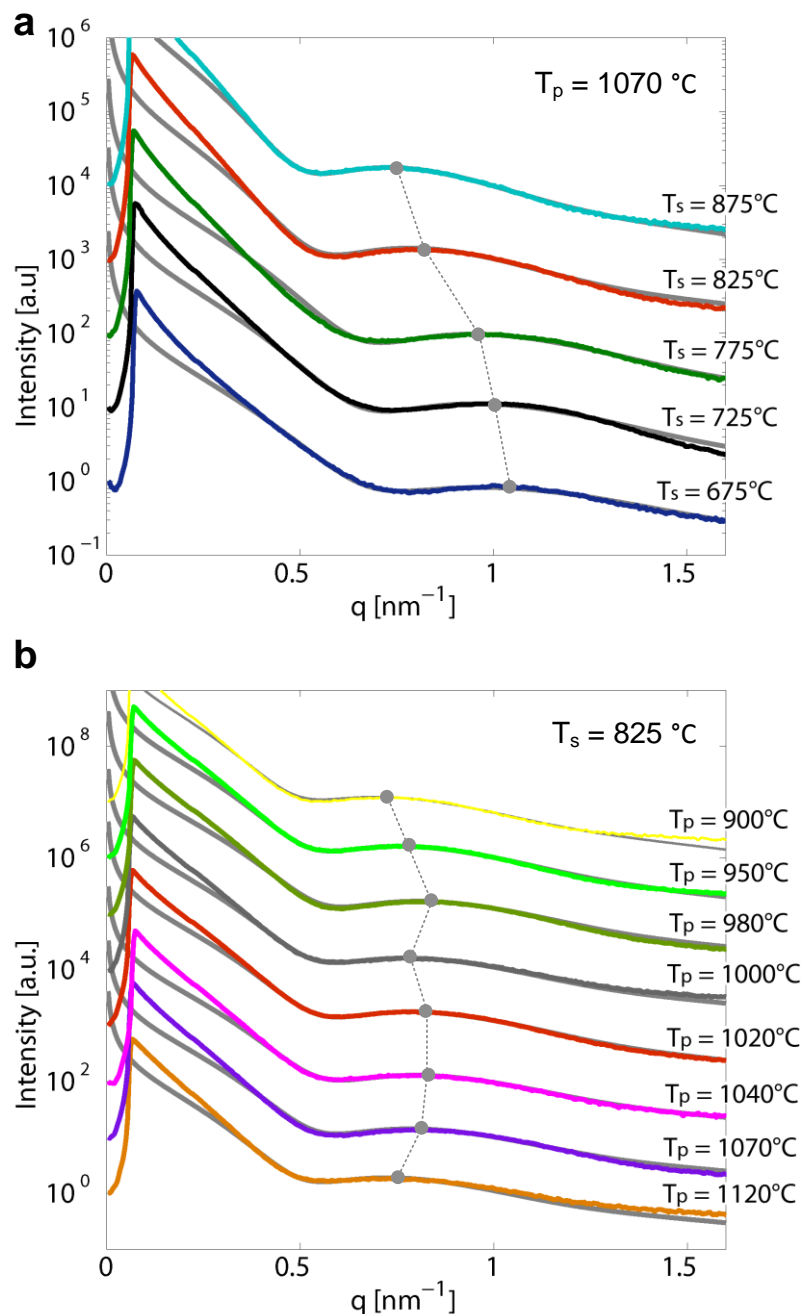
Figure 5.4 SAXS analysis of CNT forests synthesized by various thermal conditions. Plots of scattered intensity versus scattering vector (grey) taken at the vertical midpoint of forests and corresponding fits (color) that give information about the CNT population (*i.e.*, diameter, σ, number of walls) within the X-ray beampath. CNTs synthesized under various thermal conditions: (a) constant T_p = 1070 °C and (b) constant T_s = 825 °C. Grey circles denote SAXS peak locations in q (~ 1/diameter) and thus qualitatively demonstrate (a) a trend with constant T_p, variable T_s and (b) a lack thereof with constant T_s, variable T_p. Adapted with permission from *ACS Nano* 2009, 3, 2477-2486. Copyright © 2009 American Chemical Society.
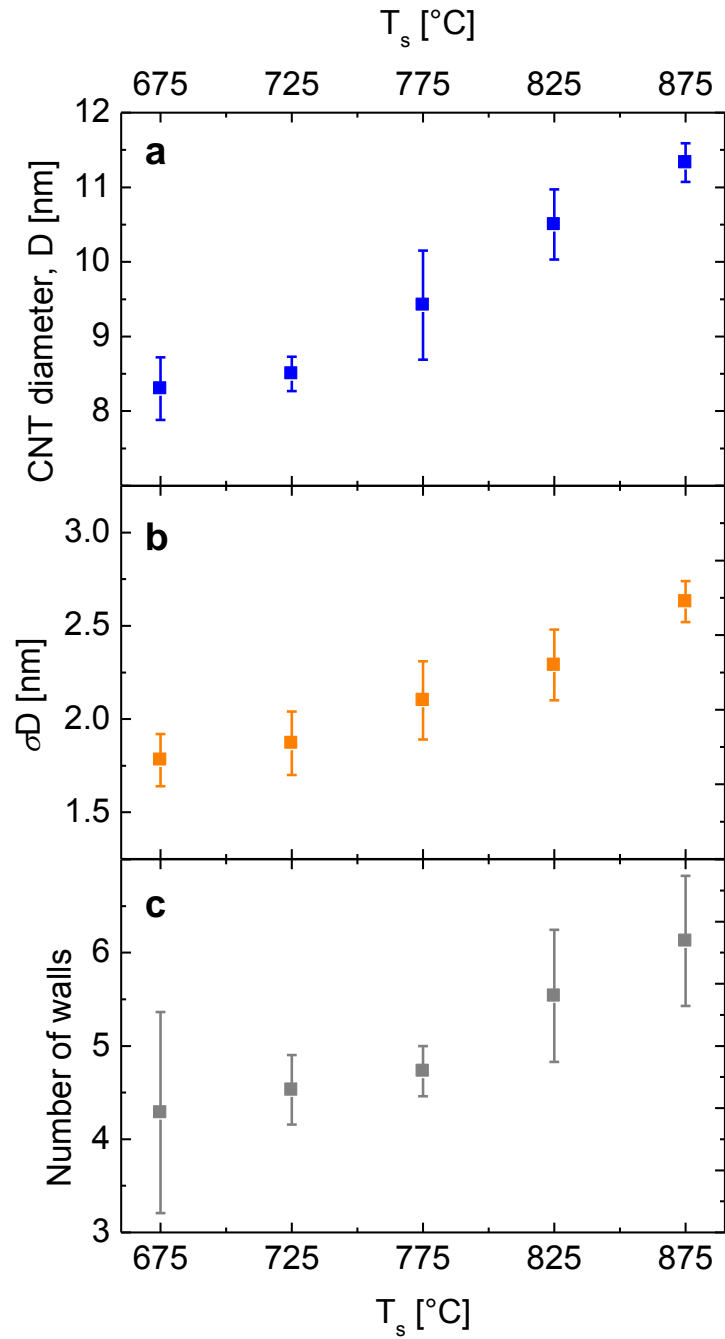
Figure 5.5 Summary of SAXS results from data fitting as in **Figure 5.4**: (a) CNT outer diameter, (b) standard deviation of CNT diameter population, and (c) number of walls. Each data point represents the mean value taken over a range of T_p values.

deposition but is reduced to its metallic state when heated in H_2/He.[30, 37] The process of film dewetting and particle formation is discussed at length in Chapter 3. The temperature of catalyst annealing by exposure to a reducing atmosphere before growth, which is equal to T_s during growth, is a principle means of controlling the CNT diameter. Conversely, the activity of the reactant mixture (determined by T_p) has a negligible effect on CNT diameter, which is further discussed later. Upon heating, the Fe film agglomerates almost instantaneously into well-defined nanoparticles, as verified by AFM imaging and *in situ* X-ray scattering (Chapter 3). In accordance with my AFM results, thin film theory predicts that the mean particle size will increase with higher T_s, so that the free energy of the particles decreases;[38-40] many previous studies have shown correlations between particle size and resultant CNT diameter.[41, 42] Upon introduction of C_2H_4, CNTs are formed at the catalyst nanoparticles, and after density surpasses a critical threshold,[23] CNTs crowd and form a vertically aligned configuration that accommodates continued upward growth as carbon is added at the base.

As in Chapter 3, I map the CNT forests by transmission small-angle X-ray scattering (SAXS)[33] and fit the resultant intensity scans to a mathematical model of a CNT forest as a population of hollow cylinders having a lognormal diameter distribution (**Figure 5.4**). This analysis reveals that the mean CNT diameter (D), mean standard deviation in diameter (σD), and the mean number of walls (N) are all directly related to T_s (**Figure 5.5**). TEM imaging verifies SAXS as a precise non-destructive measurement of CNT diameter. Using TEM, I measured mean diameters of 8.0 nm ($\sigma = 1.1$) and 10.5 nm ($\sigma = 2.0$) from approximately 60 CNTs grown at each set of thermal conditions $T_s/T_p = 675/1020 °C$ and $T_s/T_p = 875/1020 °C$. In comparison, the SAXS analysis determines 8.6 nm ($\sigma = 1.7$) and 11.1 nm ($\sigma = 2.6$) for the respective conditions; these values are within 10% of the TEM data. Note the skewed shape of the distributions in **Figure 5.6**, which corroborate my selection of the lognormal probability density function in the SAXS model. Further, while the diameter distribution broadens with increasing T_s, both SAXS and TEM data demonstrate that bimodal populations[43] do not evolve in my system. The explicit dependence of CNT diameter on T_s, which overlaps for a wide range of T_p, demonstrates that the diameter is not strongly influenced by the gas-phase rearrangement of C_2H_4 but rather is driven by the thermal treatment of the catalyst.

a T_s/T_p = 675/1020 °C
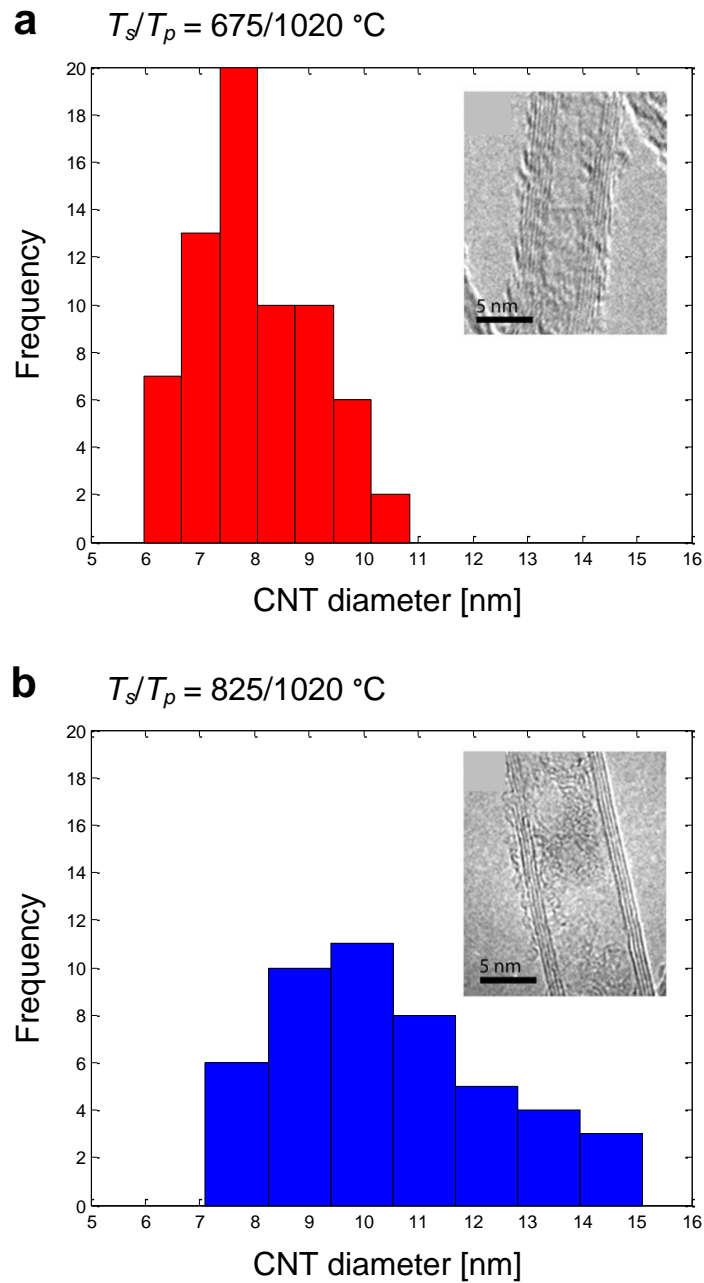
b T_s/T_p = 825/1020 °C

Figure 5.6 TEM analysis of CNT outer diameters for: (a) T_s/T_p = 675/1020 °C with D = 8.0 nm, σ = 1.1, N = 68 and (b) T_s/T_p = 825/1020 °C with D = 10.5 nm, σ = 2.0, N = 57. Inset TEMs show representative CNTs for respective thermal conditions.

5.2.2 Effects on structural quality of CNT forests

Next, I find that, while CNT diameter is independent of T_p, the CNT quality is affected strongly by both T_s and T_p. The Raman I_G/I_D peak intensity ratio is an ordinal measure of the amount of sp^2-hybridized carbon versus the amount of disordered carbon in the CNT material.[44] Accordingly, Raman spectra (**Figure 5.7**) demonstrate that the relative CNT structural quality monotonically increases with T_s. In contrast, I_G/I_D decreases with increasing T_p, suggesting that additional thermal rearrangement of the carbon source leads to lower-quality CNTs. At $T_s/T_p = 825/900$ °C $I_G/I_D = 2.3$, and in comparison, forests grown from the same catalyst composition in a single-zone tube furnace at 775 °C have $I_G/I_D = 1.2$. Further, I_G/I_D decreases slightly from the base to the top of the forest, verifying that amorphous carbon accumulates on the CNT walls after prolonged exposure to the growth environment (for base-growth mechanism), which is concurrent with other recent reports.[45] A previous study that synthesized CNTs from a C_{60} precursor showed that accumulation of graphite-like deposits on the CNT walls can result in a high I_G/I_D even though the CNT structure itself is poor; [42] however, TEM images (**Figure 5.6**) confirm that my CNTs are free of graphitic fragments.

However, Raman spectroscopy cannot quantitatively differentiate between structural defects in CNTs and amorphous carbon deposited on the CNT sidewalls. Thermogravimetric analysis (TGA) provides further insight into the independent roles of gas decomposition and catalyst heating in determining CNT material quality. Amorphous carbon accumulated on the CNT walls has a lower thermal stability than graphitic CNT carbon, and therefore the relative amounts of amorphous and graphitic carbon can be related by the relative mass losses at low (≈ 300 °C) and high (≈ 700 °C) temperatures. TGA reveals that the proportion of amorphous carbon depends on T_s and T_p, as well as on the growth time, which determines the amount of amorphous carbon deposition on the already grown sidewalls (**Figure 5.8**). CNTs grown by the decoupled method accumulate more amorphous carbon than those grown in a tube furnace; however, the ability to increase the catalyst temperature using the decoupled method can give CNTs with higher structural quality. This is inferred by the peak in mass loss rate at about 710 °C for CNTs grown at $T_s = 875$ °C, as compared to 670 °C for $T_s = 675$ °C.
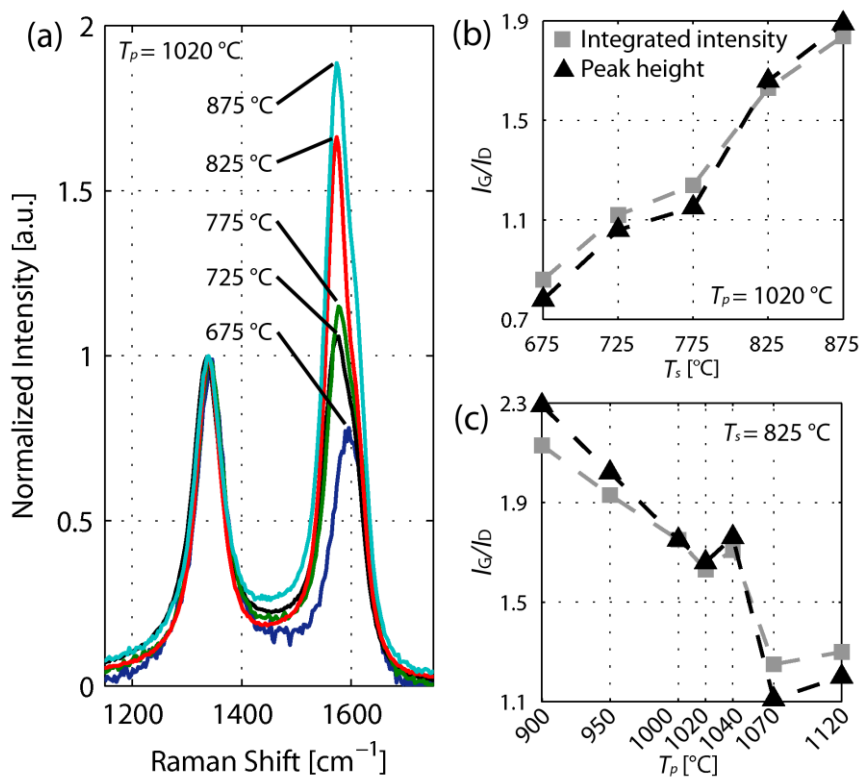
Figure 5.7 Raman spectroscopy analysis of CNT forests. (a) The averaged, normalized Raman spectra acquired for 5 CNT forests grown at different T_s (constant $T_p = 1020\ °C$) show that I_G/I_D monotonically increases with T_s, further emphasized in (b) with a linear fit. (c) The dependence of I_G/I_D on T_p with constant T_s (825 °C) also illustrates that CNT material quality degrades as T_p increases. I_G/I_D is calculated by both considering the peak heights (black triangles) and integrating the intensity curves (grey squares). Reprinted with permission from *ACS Nano* 2009, 3, 2477-2486. Copyright © 2009 American Chemical Society.

5.2.3 Kinetics trends and tradeoffs in CNT forest growth

Kinetics of CNT forest growth in our process, as measured in real time, feature three regimes (**Figure 5.9a**, **b**): (1) initial acceleration as the chamber reaches a steady-state reactant composition; (2) a prolonged period of a nearly constant yet gradually decreasing growth rate; and (3) abrupt termination when the growth rate rapidly drops to zero.[46] The decay of growth rate with time has previously been attributed to several factors, which may not be mutually exclusive, including: diffusion-limitation, where
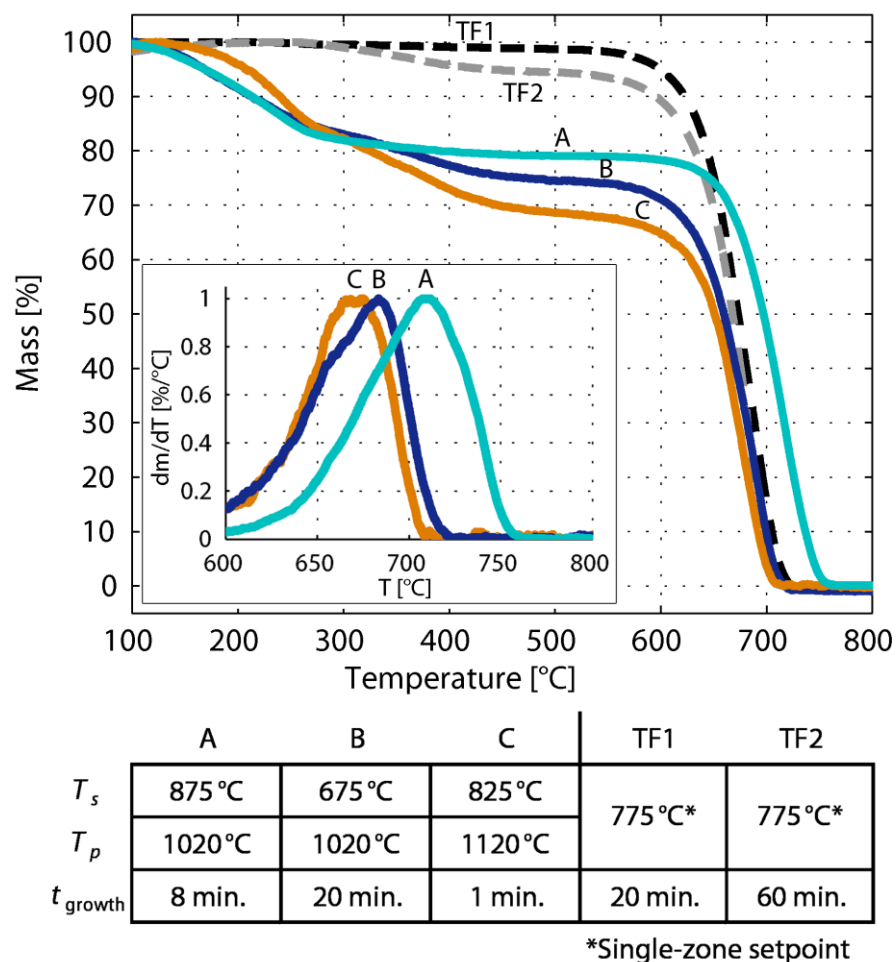
Figure 5.8 TGA of CNT forests synthesized under various conditions and reactors. The curves shows mass loss as a function of oxidation temperature, while the inset depicts normalized curves of the rate of mass loss. Synthesis conditions are detailed in the table below the plot. Reprinted with permission from *ACS Nano* 2009, 3, 2477-2486. Copyright © 2009 American Chemical Society.

activate precursors are restricted from the metal catalysts by the increasing height of the forest;[6, 9] decaying catalytic activity as growth proceeds;[3] and/or carbon over-coating or sooting on the surface of the metal catalyst from excessive gas-phase decomposition.[7, 16] Reaction-limited kinetics models have also been proposed to describe the growth, but these fail to predict growth deceleration and suggest the rate remains linear indefinitely.[8, 9] Although, our recent work in correcting the height kinetics for tortuosity within forests suggests that reaction kinetics could be more linear (see Section 4.2.3).[47] Growth rate,
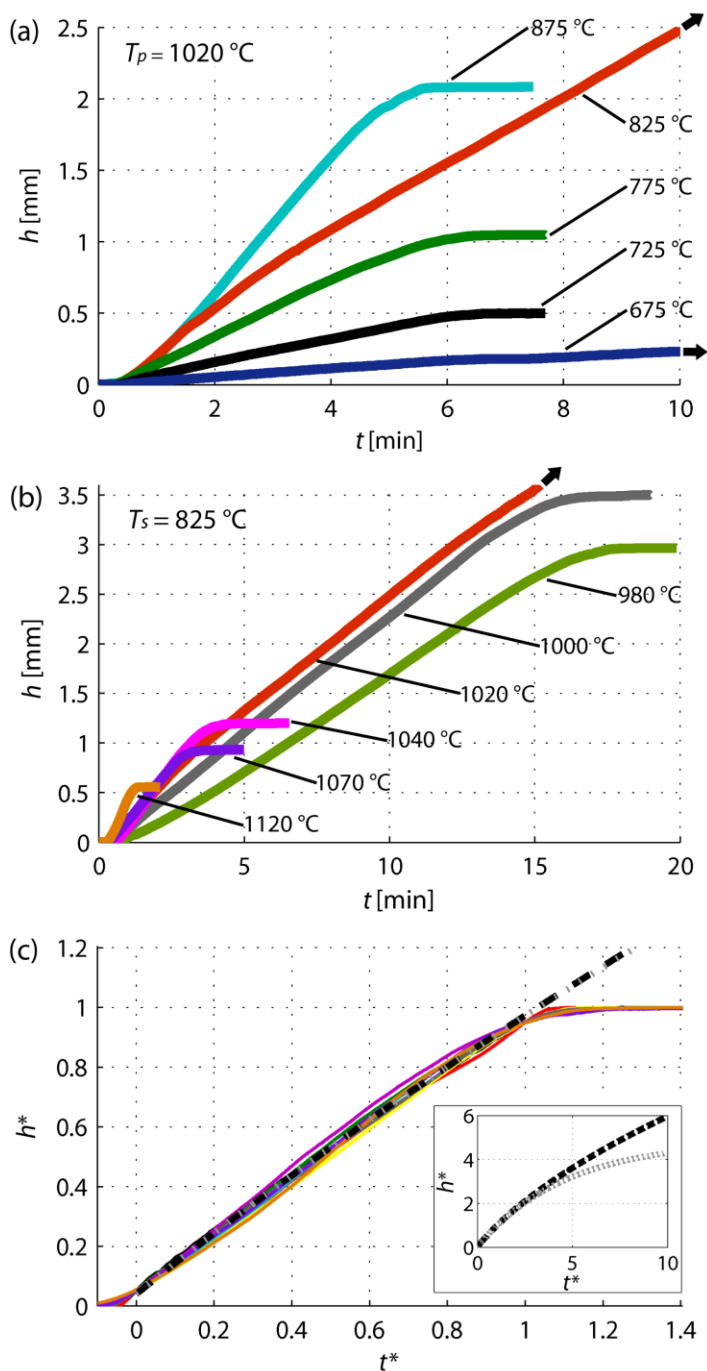
Figure 5.9 CNT forest height kinetics. (a) Height versus time for various T_s values (constant T_p = 1020 °C). The T_s = 825 °C curve terminates beyond 3.6 mm where the laser signal is lost, and the T_s = 675 °C curve reaches a terminal height of 400 μm after 20 minutes. (b) Height versus time for various T_p values (constant T_s = 825 °C), and the T_p = 1020 °C curve terminates beyond 3.6 mm. (c) Normalized kinetics from (a) and (b) with quadratic-decay and beta-decay fits of this self-similar curve (fits shown in black and grey dashed curves). The inset emphasizes that the catalyst decay and diffusion-limited models significantly overestimate the terminal CNT length. Reprinted with permission from *ACS Nano* 2009, 3, 2477-2486. Copyright © 2009 American Chemical Society.

catalyst lifetime, and terminal forest height all vary with T_s and T_p. However, when the kinetics curves are normalized (**Figure 5.9c**), self-similarity is apparent, amid slight deviations in the height measurements due to non-uniformities across the forest surface.

I non-dimensionalize the kinetics as height and time,

$$h^* = \frac{h}{h_{term}}$$
Eq. 5.1

and

$$t^* = \frac{(t - 0.05 \cdot t_{life})}{(0.95 \cdot t_{life} - 0.05 \cdot t_{life})},$$
Eq. 5.2

where h_{term} is the terminal height of the forest for a given reaction and t_{life} is the catalyst lifetime (defined as the elapsed time between 1% and 99% of h_{term}). Although forests reach various terminal heights at widely varying rates, growth terminates abruptly in all cases. Both diffusion limitation[10]

$$h = 0.5\sqrt{A^2 + 4Bt} - 0.5A$$
Eq. 5.3

and catalytic decay[3]

$$h = \beta \tau_0 \left(1 - e^{-t/\tau_0}\right)$$
Eq. 5.4

models fit the steady regime of the observed kinetics, but these models far overestimate the terminal forest height and fail to capture the abrupt termination event. In Eq. 5.3, $A = 2D/k_s$ and $B = 4DC_0/M$, where D is the diffusion coefficient, k_s is the first-order rate constant, is the C_2H_4 concentration at the top of the CNT forest, and M is the number of molecules of incorporated into a unit volume of the resulting forest. In Eq. 5.4, β is the initial growth rate, and τ_0 is the catalyst lifetime. This suggests a
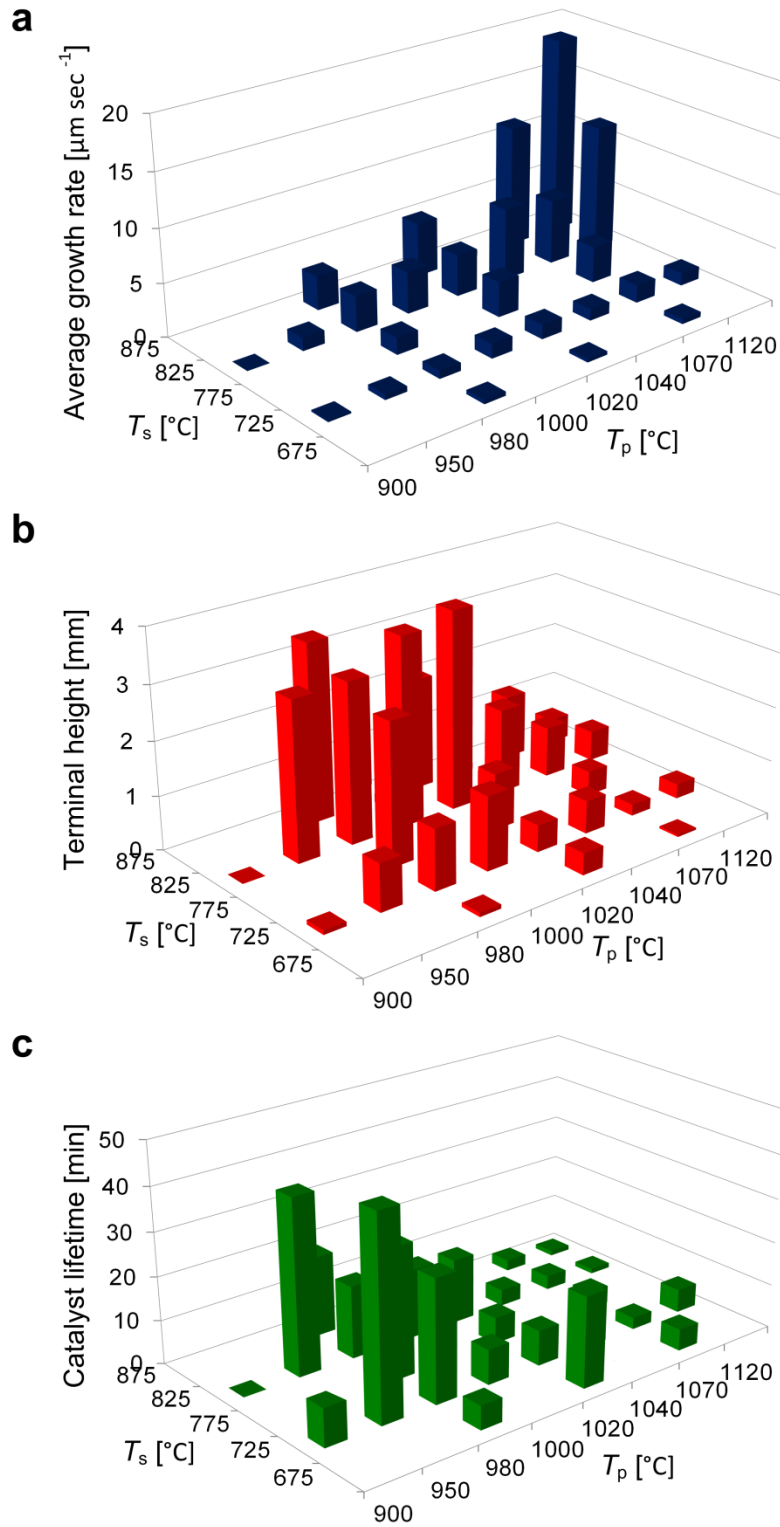
Figure 5.10 Kinetics trends for CNT forest growth under various temperature conditions (3-D): (a) average steady growth rate, (b) terminal forest height, and (c) lifetime of the catalyst.
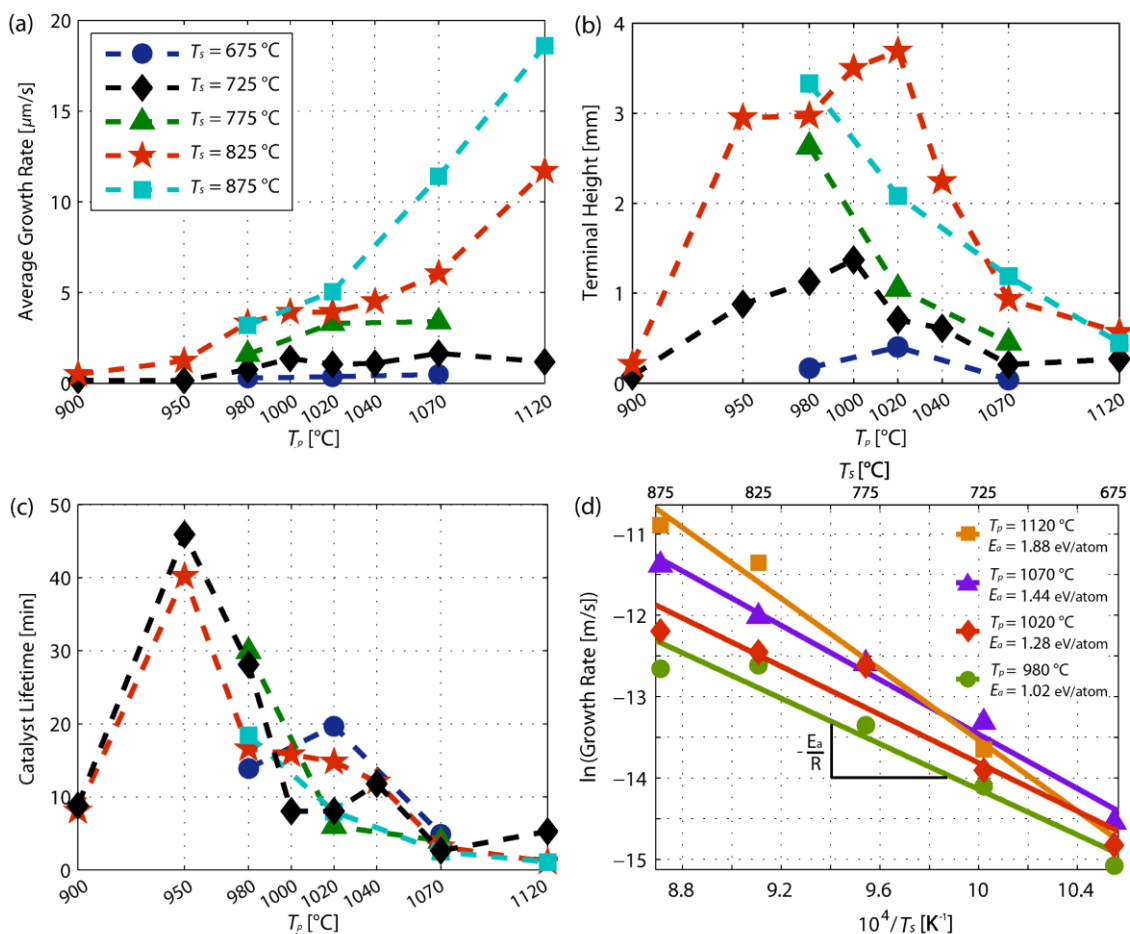
Figure 5.11 Kinetics trends for CNT forest growth under various temperature conditions (2-D): (a) average steady growth rate, (b) terminal forest height, (c) lifetime of the catalyst, and (d) Arrhenius plots with associated apparent activation energies (E_a). Reprinted with permission from *ACS Nano* 2009, 3, 2477-2486. Copyright © 2009 American Chemical Society.

sudden mechanism of CNT growth termination, which is not sufficiently described by either diffusion-limited precursor delivery or catalyst decay. Our recent work indicates that self-termination is a collective process, resulting from the accumulating termination of individual CNTs.[48, 49] This manifests in a clear decay in CNT number density that coincides with abrupt termination of forest height kinetics.

CNT forest growth kinetics are summarized for the test matrix in 3-D maps (**Figure 5.10**) as well as in distilled 2-D plots of the same data (**Figure 5.11**). The CNT forest growth rate during the steady period increases monotonically with both T_s and T_p (**Figure 5.11a**); however, there is a distinct exchange between steady growth rate and

catalyst lifetime (**Figure 5.11c**). I define the steady growth rate r_{avg} over the nearly linear portion of each growth curve, extending from 25% to 75% of h_{term}, such that

$$r_{avg} = \frac{(0.75 \cdot h_{term} - 0.25 \cdot h_{term})}{(0.75 \cdot t_{life} - 0.25 \cdot t_{life})} \; .$$

Eq. 5.5

Growth is fastest at both high T_s and T_p, but the catalyst lifetime is shortest under these conditions: r_{avg} = 18.5 μm sec^{-1} at T_s/T_p = 875/1120 °C. However, here the terminal height is only 0.5 mm compared to nearly 4 mm at T_s/T_p = 825/1020 °C (**Figure 5.11b**). Further, the slope of the relationship between r_{avg} and T_p increases with T_s. This is formally quantified by estimating the apparent activation energy E_a of the synthesis reaction using the Arrhenius relation,

$$\dot{h} \propto k = e^{-\frac{E_a}{RT_s}} \; .$$

Eq. 5.6

Here, R is the universal gas constant, and I assume the growth rate $\dot{h}$, which is proportional to the reaction rate k, is approximately equal to r_{avg}. By plotting $\ln(r_{avg})$ versus $1/T_s$, I extract E_a from the slope of the linear fits for various T_p values (**Figure 5.11d**); my values of E_a monotonically increase with T_p and are comparable to values previously reported for thermal CVD of CNTs.[50, 51] The dependence of E_a on T_p indicates that gas decomposition is a rate-determining step in CNT forest growth. Finally, the synergy between T_s and T_p appears to only be activated at T_s = 775 °C and above. This indicates a threshold beyond which interaction between the population of thermally generated hydrocarbon precursors and catalyst conditions nonlinearly enhances the rate of CNT growth from Fe on Al_2O_3.

The catalyst lifetime is primarily determined by the extent of thermal treatment of the feedstock gas (**Figure 5.11c**), *i.e.*, the preheater temperature T_p. Our further gas analysis, which is reported separately, shows that the relative abundance of certain hydrocarbon species increases by orders of magnitude with marginal increases in T_p.[34] While I show that varying T_p can enhance the growth process (*e.g.*, increased r_{avg} or

h_{term}), there is a corresponding drop in catalyst lifetime with higher T_p for all values of T_s. Further, while lowering T_p generally prolongs catalytic activity, there is a limit to this effect. That is, catalyst lifetime increases non-linearly as T_p decreases and reaches a maximum at $T_p = 950$ °C, but below this temperature it drops severely again, leading to relatively ineffective growth. This sharp transition suggests that some constituent parts of the decomposed gas mixture may be absent at low T_p (< 950 °C), whereas at high T_p, select compounds present considerable obstacles to one or more aspects of the growth process (*e.g.*, carbon deposition on the catalyst). Decaying trends in kinetic parameters have been previously discussed,[16] and while I show a persistent increase in growth rate for the temperature ranges tested, I do observe decays in lifetime and height at high temperatures.

Overall, to attain efficient growth of tall CNT forests, one must balance the reaction rate and catalyst lifetime, which is practically achieved by moderate T_p values. Thermal control at the catalyst is also critical, as forest height increases with T_s (**Figure 5.11b**); however, optimum heights are realized at $T_s = 825$ °C, not at the higher $T_s = 875$ °C as one might expect, which could be the result of compromised catalyst performance due to excessive heating. Independent tuning of characteristics can be achieved in many cases with the appropriate combination of thermal conditions, since diameter and lifetime are governed by only one thermal parameter.

5.2.4   Correlation between growth performance and precursor chemistry

As indicated in 5.2.3, thermal treatment of the feedstock (T_p) plays a critical role in determining the kinetics of the CNT synthesis process. For instance, measurements from our CVD apparatus, taken by Plata and Hart,[34, 36] show correlations between the relative abundance of select hydrocarbons and the forest growth rate (**Figure 5.12**). This corroborates our observations that there is a minimum value of T_p, above which forest growth is effective, presumably because key precursors are generated at sufficient partial pressures. Although growth rate monotonically increases for the partial pressures reported here (generated by increasing T_p), there is a clear tradeoff in the lifetime of the reaction (**Figure 5.10c** and **Figure 5.11c**). Therefore, I ascertain a window of critical T_p values for forest growth, with unique insight regarding the corresponding
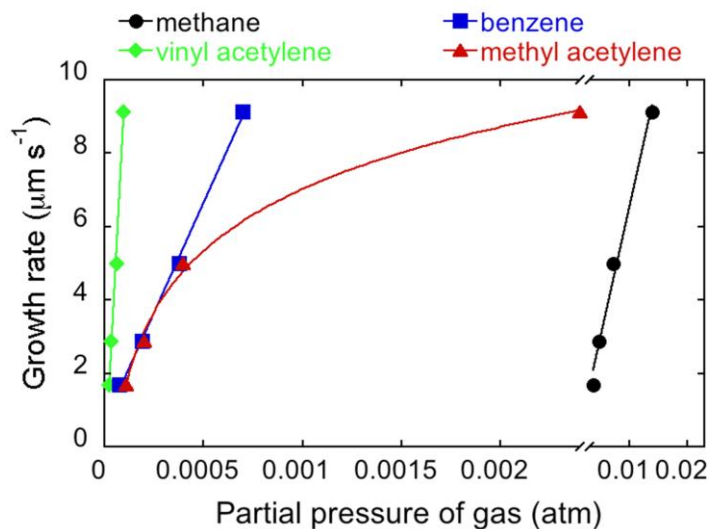
Figure 5.12 Thermally generated compounds correlate with CNT growth rate. Resultant concentrations (atm) from four different T_p (860, 920, 970, 1040 °C) are shown, and growth rate increases with T_p. The symbols are measured gas abundances just after the preheater tube and the lines are the best-fit curves. The abundances of methane, benzene, and vinyl acetylene were linearly related to the growth rate (all $R^2 = 0.99$, $n = 4$). The relationship between methyl acetylene and the CNT growth rate was fit by a hyperbola ($R^2 = 0.99$, $n = 4$). In all experiments, the gas flow during growth was $C_2H_4/H_2/He = 70/330/0$ sccm and the catalyst substrate temperature was 840 °C. Data collected and analyzed by Plata and Hart. Reprinted with permission from *ACS Nano* 2010, 4, 7185-7192. Copyright © 2010 American Chemical Society.
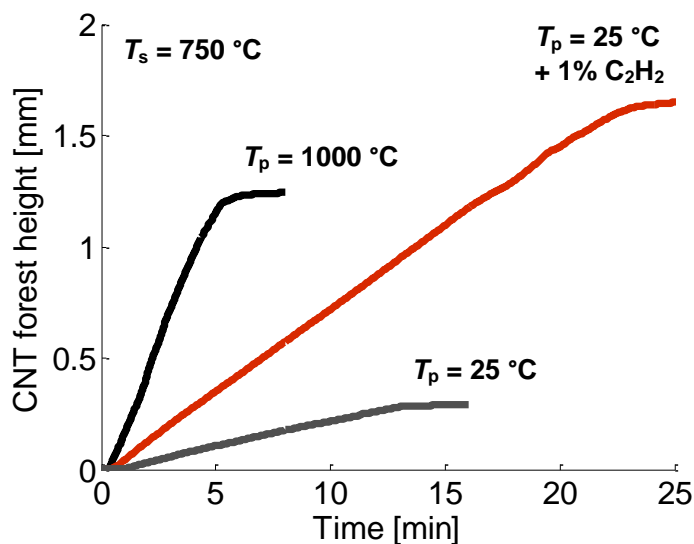
Figure 5.13 Effects of precursor chemistry on CNT growth kinetics. In all cases, standard growth gases ($C_2H_4/H_2 = 120/310$ sccm) were delivered with preheater ON ($T_p = 1000$ °C), preheater OFF ($T_p = 25$ °C), and preheater OFF with the addition of 1% C_2H_2 (*i.e.*, 6 sccm). Extensive study on the effects of precursor chemical structure are in Ref. 36. precursor partial pressures in this T_p range.[34, 52]

With these gas analyses as our guide, we select species to individually investigate their role in CNT formation. These experiments were performed in collaboration with Plata and colleagues.[36] In the absence of preheating, we deliver trace amounts of each hydrocarbon with typical quantities of C_2H_4/H_2, per the schematic in **Figure 5.1**, thus selectively simulating the growth atmosphere when C_2H_4/H_2 *is* thermally treated. Having a cold-wall apparatus with local heating at the catalyst is vital for these experiments in order to limit gas-phase reactions.

Briefly, we show that a particular class of alkynes ($C_{n \leq 4}$) are effective at enhancing both the growth rate and conversion efficiency, while other compounds previously thought to be important precursors (*i.e.*, methane, benzene) do not enhance growth. The fact that the abundances of methane and benzene track with forest growth rate indicates that correlation does not imply causation, which highlights the importance of our direct delivery method in determining which compounds are truly contributing to CNT formation.

While others have shown that acetylene is an effective precursor for CNT synthesis,[53, 54] we establish generality in identifying that the triple-bonded structure in small hydrocarbons is key to CNT formation. For instance, **Figure 5.13** demonstrates the growth enhancement achieved by adding a small amount (0.01 atm) of C_2H_2 to the reactor while $T_p = 25 \,°C$. Thus, as long as T_s is relatively high, we can achieve millimeter-tall CNT forests with low T_p, which enables energy saving and limits environmental harm due to toxic exhaust that is typical of high-T_p processes.[34] This type of enhancement is quantified for acetylene, methyl acetylene, ethyl acetylene, and vinyl acetylene, and we also show that C_2H_4 is still necessary to form our CNT product. Based on these findings, Plata proposed a mechanism in Ref. 36, whereby C_2H_4 acts in concert with C_2H_2 as a co-reactant at the catalyst's surface.

In addition to small hydrocarbons, we also show that larger polycyclic aromatic hydrocarbons (PAHs) are in the growth atmosphere. PAHs are potentially interesting because their structures typically resemble that of the aromatic lattice structure of CNTs, yet they are also known to lead to the formation of soot,[55] which is poisonous to CVD of CNTs. Preliminary direct delivery tests of a suite of PAHs that are commonly present during thermal CVD from C_2H_4/H_2 show that, unlike alkynes, PAHs do not enhance

forest growth rate. For instance, we test the PAHs we identify from the exhaust of the preheater **Figure 5.3** and achieve only short CNT films. Further, removal of PAHs from the thermally generated product of C_2H_4/H_2 by filtering with a polyurethane foam does not affect forest height kinetics. These observations demonstrate that PAHs are not necessarily vital in forest growth and that introducing PAHs to bare catalysts may actually inhibit forest growth. I attribute this to the propensity for these relatively stable chemical structures to adsorb to surfaces without being particularly reactive. For instance, PAHs may adhere to the surface of the catalyst and thus inhibit reaction with or uptake of carbon from other active species.

5.2.5 Low-temperature synthesis of CNT films

Although CNTs show great promise for future electronic applications,[56] it is challenging to synthesize high-quality CNTs on electrically conductive substrates at temperatures compatible with complementary metal-oxide-semiconductor (CMOS) processing, which is typically limited to 450 °C.[57, 58] Low-temperature growth is especially challenging because the decomposition temperature of most hydrocarbons used for CNT growth exceeds 500 °C. To meet this need, plasma-enhanced CVD has been used widely to achieve low-temperature CNT formation.[59, 60] However, plasma-enhanced methods can often generate undesirable defects in the CNT structure, particularly due to etching by ionized species.[61, 62]

I have established that T_p influences CNT growth kinetics, and understanding the limits of this parameter space is crucial for integration with electronic applications such as vertical vias,[63, 64] interconnects[65, 66] and CNT-based memory devices.[67] Further, **Figure 5.14** demonstrates the limits associated with CNT growth at low T_s without preheating. Below $T_s = 525$ °C, the CNTs do not form the self-aligned morphology characteristic of a forest (**Figure 5.15**), which indicates that either CNT number density is too low and/or CNTs are not long enough to form the self-supporting structure necessary for vertical growth.[48, 68] Chapter 4 describes the time evolution of the initial tangled layer in CNT forest growth. Another critical temperature is $T_s = 475$ °C,
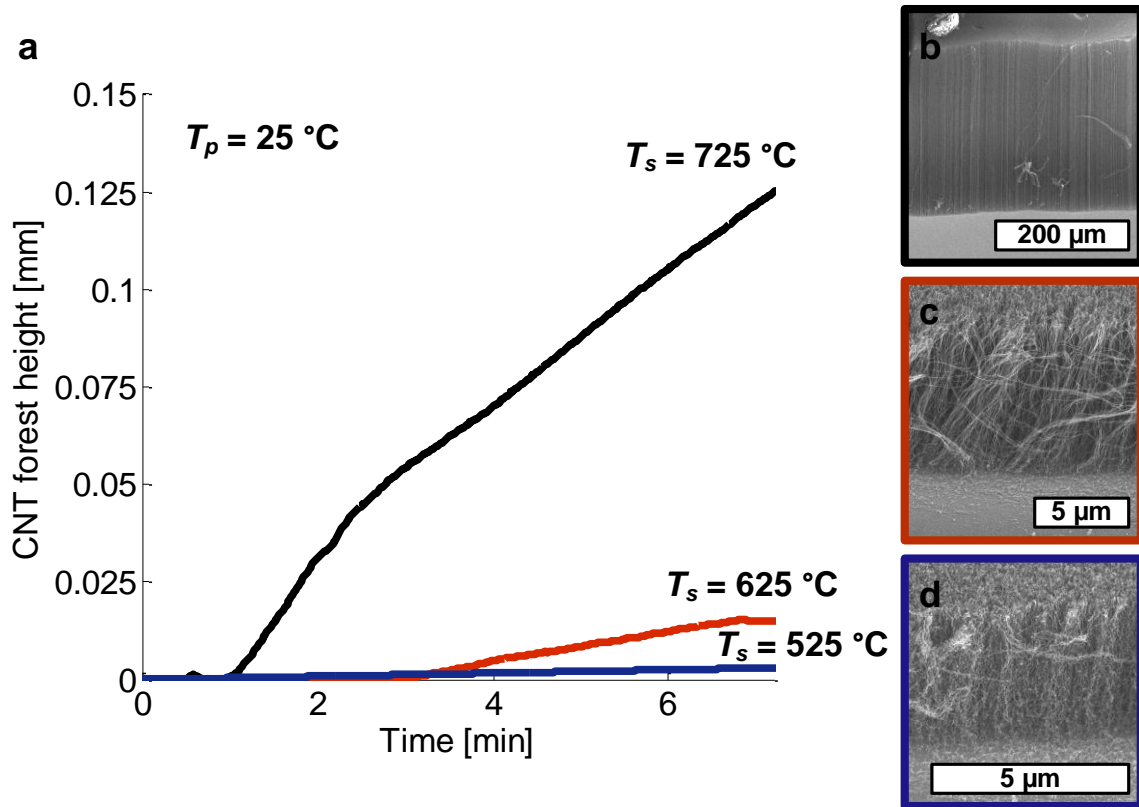
Figure 5.14 Kinetics of low-temperature synthesis *without* preheating, which show the limits of growing vertically aligned CNT forests (a). SEM images on the right-hand side are color coded to correspond to kinetics curves in (a), namely (b) $T_s = 725$ °C, (c) $T_s = 625$ °C, and (d) $T_s = 525$ °C. $T_p = 25$ °C in all cases shown.

below which the CNT film is no longer continuous, but rather is comprised of non-uniform bunches of CNTs with substantial areas of substrate exposed between them.

Another important characteristic in addition to the morphology of the CNT film is the structural quality of the CNTs. I observe that the crystal structure of the CNTs synthesized at low T_s is determined by the chemistry of the precursor gases.[35] For instance, the proportion of crystalline CNTs increases with T_p, as demonstrated by TEM images of representative structures in **Figure 5.16**. This suggests that thermal generation of precursor species is generally responsible for growth of crystalline CNTs at low T_s. Structures grown without preheating ($T_p = 25$ °C) have discontinuous walls and a poorly defined core as compared to the $T_p = 1000$ °C case, where the outer walls are continuous, crystalline, and both the walls and core appear to be well-defined. At $T_p = 900$ °C, the walls are discontinuous yet the core is more clearly defined, indicating a transition occurs
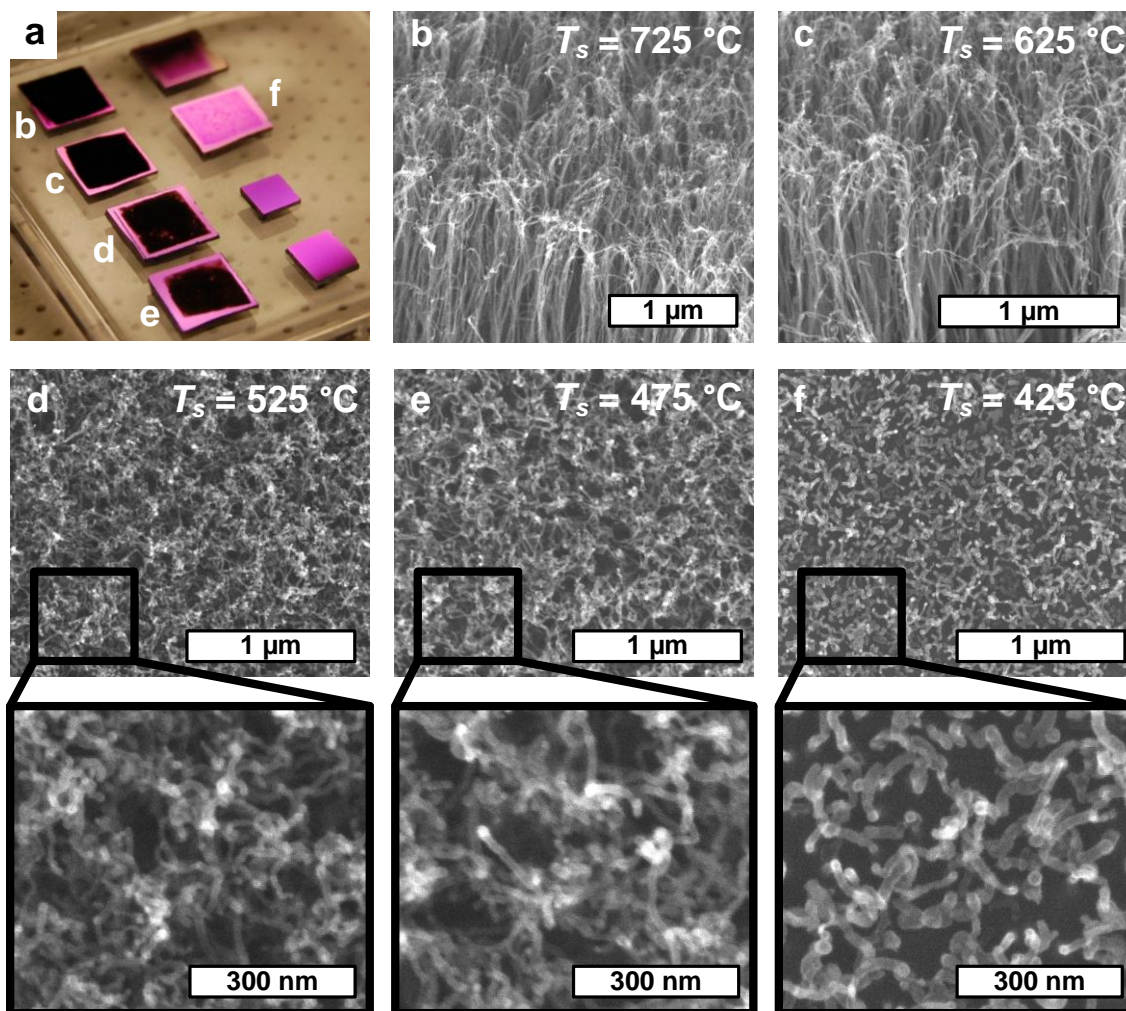
Figure 5.15 Low-temperature limits to vertically alignment and organization of CNT films. (a) Digital photograph of CNT films on Si substrates with labels corresponding to adjacent SEM images. Aligned CNT morphologies are observed for (b-d) T_s = 725-525 °C, with a decreasing trend in areal coverage and continuity for (d-f) T_s = 525-425 °C. T_p = 25 °C in all cases shown.

as I change the precursor chemistry *via* tuning T_p. This transition is also captured by Raman spectroscopy of the same CNT films (Figure 5.17), which shows an increase in structural quality for higher T_p, as indicated by the increase in I_G/I_D.

These results obtained using the decoupled cold-wall reactor are also corroborated by low-temperature synthesis performed in a hot-wall system on conductive substrates,[35] which supports the assertion that specifically critical gas compounds are generated within certain temperature windows, and these compounds can be responsible for structural transition in filamentous carbon nanostructures. Therefore, I suggest that the stated effect of precursor chemistry may be universal, although the particular conditions (*e.g.*,

T_p = 25 °C	T_p = 900 °C	T_p = 1000 °C
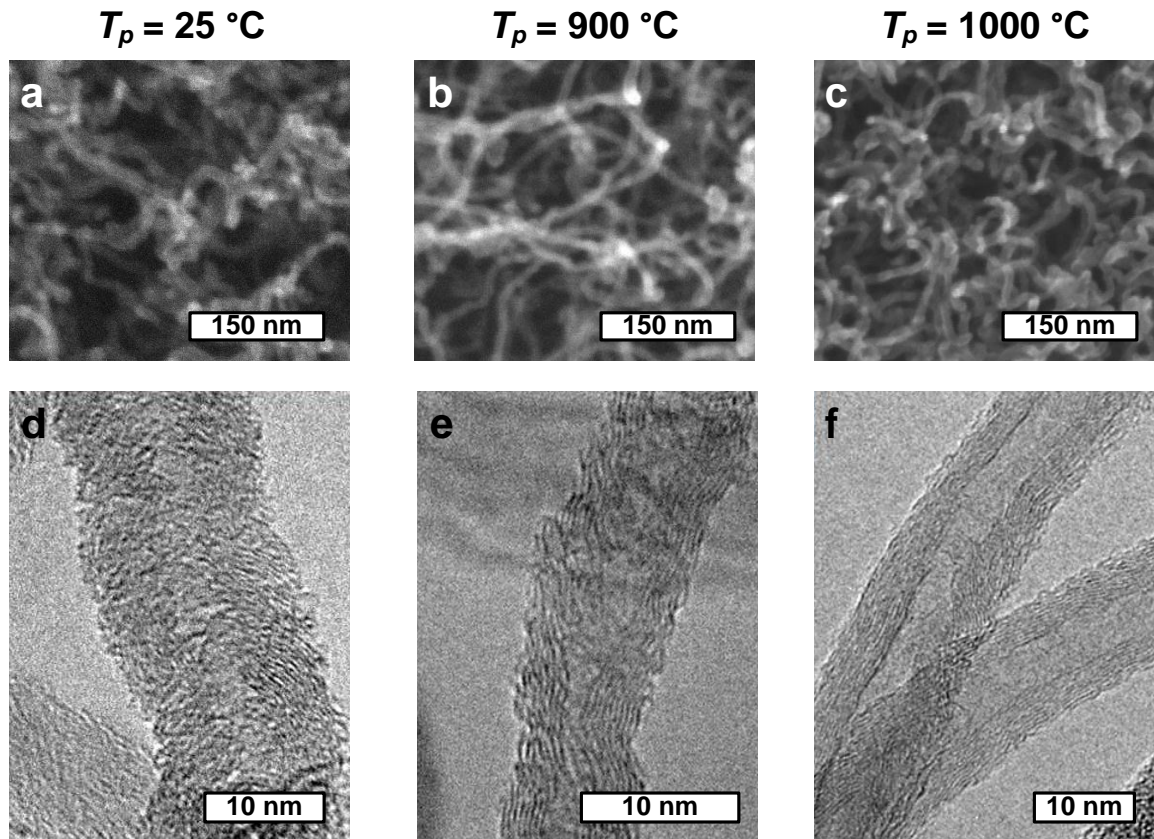
Figure 5.16 Film morphology and crystal structure of CNTs synthesized at low temperature. (a-c) SEM and (d-f) TEM imaging. Trend toward crystalline walls with well-defined core as T_p is increased from 25 °C to 1000 °C. T_s = 525 °C in all cases shown. Adapted with permission from *Carbon* 2011, 49, 804-810. Copyright © 2011 Elsevier.
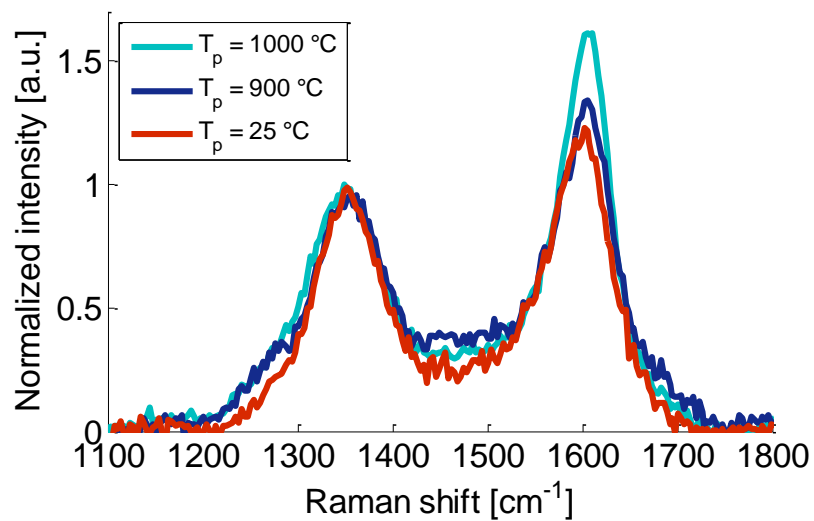
Figure 5.17 Raman spectroscopy for CNTs synthesized at low temperature (samples shown in **Figure 5.16**). I_G/I_D = 1.23, 1.34, 1.61 for T_p = 25 °C, 900 °C, 1000 °C, respectively.

T_p, T_s, flow rates) will be different based on the choices of the feedstock and catalyst and the nature of gas-catalyst interactions.

Considering the plurality and diversity of species formed by thermal treatment, it may be that a combination of gaseous precursor molecules is necessary to form crystalline CNTs by CVD. These findings also suggest that future studies of CNT growth mechanism must consider gas-catalyst interactions. In particular, the vapor-liquid-solid (VLS) model,[69] and/or models of carbon incorporation by surface or bulk diffusion[70, 71] may require modification to consider the effect of multiple precursor structures, rather than a single precursor. Many studies[72, 73] and *ab initio* molecular simulations[71] support the role of both small and large hydrocarbon compounds in the catalytic formation of carbon nanostructures. Further studies with other catalysts will also be insightful, in light of recent findings that CNTs can be grown from noble metal (*e.g.*, Au) and oxide[74] nanoparticles.

5.3 Conclusions

Decoupling thermal treatment of the precursor and catalyst enables new understanding of the mechanisms determining diameter, quality, and kinetics of CNT growth in a vertically aligned forest. High temperatures (T_s T_p) enhance the growth rate, yet terminal forest height, catalyst lifetime, and CNT quality suffer from excessive gas decomposition and/or catalyst deactivation at these conditions. Self-similarity of CNT forest growth kinetics suggests the existence of a universal and sudden termination mechanism that may limit indefinite growth of CNTs. Further, the decoupled processing method, supported by closed-loop automated control of the growth reactor, enables rapid mapping of a broad parameter space. There is a minimum temperature necessary to achieve vertical growth and make crystalline CNTs. This suggests the existence of competing pathways between graphitic and amorphous carbon deposited during synthesis and highlights a deficiency of CVD processes in which these thermal control parameters are coupled. My approach and findings provide an opportunity to make more efficient CVD methods by understanding how to deliver the right precursors without having to

thermally generate the entire spectrum of species.[34] To this extent, we demonstrate the generation a broad population of PAHs and VOCs in the CVD atmosphere, suggesting a role of select carbon species in either enhancing or inhibiting efficient and/or prolonged forest growth.

The precise mechanism of CNT forest growth termination remains unclear; however, it is reasonable to conclude that the large population of hydrocarbons resulting from thermal decomposition introduces constituent species that promote efficient forest growth, while others drive the catalyst into a state unfavorable for continuous deposition of graphitic carbon. By exploiting the interplay between T_s and T_p, I enhance the resultant I_G/I_D to generate as-grown, high-quality forests without implementing post-treatment purification steps,[75-79] which are often energy and time consumptive as well as destructive to the aligned structure of a forest. Extension of this study to other catalyst film thicknesses (*e.g.*, thinner catalyst films, which would be expected to give smaller diameter CNTs) and compositions could help establish application-oriented structure-property maps for CNT forest manufacturing.

5.4 References

1. Dell'Acqua-Bellavitis, L.; Ballard, J.; Ajayan, P.; Siegel, R., Kinetics for the synthesis reaction of aligned carbon nanotubes: A study based on in situ diffractography. *Nano Letters* 2004, 4, 1613-1620.

2. Einarsson, E.; Murakami, Y.; Kadowaki, M.; Maruyama, S., Growth dynamics of vertically aligned single-walled carbon nanotubes from in situ measurements. *Carbon* 2008, 46, 923-930.

3. Futaba, D.; Hata, K.; Yamada, T.; Mizuno, K.; Yumura, M.; Iijima, S., Kinetics of water-assisted single-walled carbon nanotube synthesis revealed by a time-evolution analysis. *Physical Review Letters* 2005, 95, -.

4. Han, J.; Graff, R.; Welch, B.; Marsh, C.; Franks, R.; Strano, M., A mechanochemical model of growth termination in vertical carbon nanotube forests. *ACS Nano* 2008, 2, 53-60.

5. Liu, K.; Jiang, K.; Feng, C.; Chen, Z.; Fan, S., A growth mark method for studying growth mechanism of carbon nanotube arrays. *Carbon* 2005, 43, 2850-2856.

6. Louchev, O.; Laude, T.; Sato, Y.; Kanda, H., Diffusion-controlled kinetics of carbon nanotube forest growth by chemical vapor deposition. *Journal of Chemical Physics* 2003, 118, 7622-7634.

7. Puretzky, A.; Geohegan, D.; Jesse, S.; Ivanov, I.; Eres, G., In situ measurements and modeling of carbon nanotube array growth kinetics during chemical vapor deposition. *Applied Physics A-Materials Science & Processing* 2005, 81, 223-240.

8. Xiang, R.; Yang, Z.; Zhang, Q.; Luo, G.; Qian, W.; Wei, F.; Kadowaki, M.; Einarsson, E.; Maruyama, S., Growth deceleration of vertically aligned carbon nanotube arrays: Catalyst deactivation or feedstock diffusion controlled? *Journal of Physical Chemistry C* 2008, 112, 4892-4896.

9. Zhu, L.; Xu, J.; Xiao, F.; Jiang, H.; Hess, D.; Wong, C., The growth of carbon nanotube stacks in the kinetics-controlled regime. *Carbon* 2007, 45, 344-348.

10. Zhu, L.; Hess, D.; Wong, C., Monitoring carbon nanotube growth by formation of nanotube stacks and investigation of the diffusion-controlled kinetics. *Journal of Physical Chemistry B* 2006, 110, 5445-5449.

11. Zhang, G. Y.; Mann, D.; Zhang, L.; Javey, A.; Li, Y. M.; Yenilmez, E.; Wang, Q.; McVittie, J. P.; Nishi, Y.; Gibbons, J.; Dai, H. J., Ultra-high-yield growth of vertical single-walled carbon nanotubes: Hidden roles of hydrogen and oxygen. *Proceedings of the National Academy of Sciences of the United States of America* 2005, 102, 16141-16145.

12. Hata, K.; Futaba, D. N.; Mizuno, K.; Namai, T.; Yumura, M.; Iijima, S., Water-assisted highly efficient synthesis of impurity-free single-waited carbon nanotubes. *Science* 2004, 306, 1362-1364.

13. Fan, S. S.; Chapline, M. G.; Franklin, N. R.; Tombler, T. W.; Cassell, A. M.; Dai, H. J., Self-oriented regular arrays of carbon nanotubes and their field emission properties. *Science* 1999, 283, 512-514.

14. Delzeit, L.; Nguyen, C. V.; Chen, B.; Stevens, R.; Cassell, A.; Han, J.; Meyyappan, M., Multiwalled carbon nanotubes by chemical vapor deposition using multilayered metal catalysts. *Journal of Physical Chemistry B* 2002, 106, 5629-5635.

15. Hart, A.; Slocum, A., Rapid growth and flow-mediated nucleation of millimeter-scale aligned carbon nanotube structures from a thin-film catalyst. *Journal of Physical Chemistry B* 2006, 110, 8250-8257.

16. Wood, R. F.; Pannala, S.; Wells, J. C.; Puretzky, A. A.; Geohegan, D. B., Simple model of the interrelation between single- and multiwall carbon nanotube growth rates for the CVD process. *Physical Review B* 2007, 75, 8.

17. Lacava, A. I.; Bernardo, C. A.; Trimm, D. L., Studies Of Deactivation Of Metals By Carbon Deposition. *Carbon* 1982, 20, 219-223.

18. Kaatz, F.; Siegal, M.; Overmyer, D.; Provencio, P.; Jackson, J., Diameter control and emission properties of carbon nanotubes grown using chemical vapor deposition. *Materials Science & Engineering C-Biomimetic and Supramolecular Systems* 2003, 23, 141-144.

19. Yuan, Z.; Huang, H.; Liu, L.; Fan, S., Controlled growth of carbon nanotubes in diameter and shape using template-synthesis method. *Chemical Physics Letters* 2001, 345, 39-43.

20. Fu, Q.; Huang, S.; Liu, J., Chemical vapor depositions of single-walled carbon nanotubes catalyzed by uniform Fe2O3 nanoclusters synthesized using diblock copolymer micelles. *Journal of Physical Chemistry B* 2004, 108, 6124-6129.

21.   Lu, J.; Kopley, T.; Moll, N.; Roitman, D.; Chamberlin, D.; Fu, Q.; Liu, J.; Russell, T.; Rider, D.; Manners, I.; Winnik, M., High-quality single-walled carbon nanotubes with small diameter, controlled density, and ordered locations using a polyferrocenylsilane block copolymer catalyst precursor. *Chemistry of Materials* 2005, 17, 2227.

22.   Bennett, R. D.; Xiong, G. Y.; Ren, Z. F.; Cohen, R. E., Using block copolymer micellar thin films as templates for the production of catalysts for carbon nanotube growth. *Chemistry of Materials* 2004, 16, 5589-5595.

23.   Bennett, R. D.; Hart, A. J.; Cohen, R. E., Controlling the morphology of carbon nanotnbe films by varying the areal density of catalyst nanoclusters using block-copolymer micellar thin films. *Advanced Materials* 2006, 18, 2274-+.

24.   Ishida, M.; Hongo, H.; Nihey, F.; Ochiai, Y., Diameter-controlled carbon nanotubes grown from lithographically defined nanoparticles. *Japanese Journal of Applied Physics Part 2* 2004, 43, L1356-L1358.

25.   Wei, Y.; Eres, G.; Merkulov, V.; Lowndes, D., Effect of catalyst film thickness on carbon nanotube growth by selective area chemical vapor deposition. *Applied Physics Letters* 2001, 78, 1394-1396.

26.   Zhao, B.; Futaba, D. N.; Yasuda, S.; Akoshima, M.; Yamada, T.; Hata, K., Exploring advantages of diverse carbon nanotube forests with tailored structures synthesized by supergrowth from engineered catalysts. *ACS Nano* 2009, 3, 108-114.

27.   Chhowalla, M.; Teo, K.; Ducati, C.; Rupesinghe, N.; Amaratunga, G.; Ferrari, A.; Roy, D.; Robertson, J.; Milne, W., Growth process conditions of vertically aligned carbon nanotubes using plasma enhanced chemical vapor deposition. *Journal of Applied Physics* 2001, 90, 5308-5317.

28.   Ho, G.; Wee, A.; Lin, J.; Tjiu, W., Synthesis of well-aligned multiwalled carbon nanotubes on Ni catalyst using radio frequency plasma-enhanced chemical vapor deposition. *Thin Solid Films* 2001, 388, 73-77.

29.   Lee, C.; Lyu, S.; Cho, Y.; Lee, J.; Cho, K., Diameter-controlled growth of carbon nanotubes using thermal chemical vapor deposition. *Chemical Physics Letters* 2001, 341, 245-249.

30.   Nessim, G. D.; Hart, A. J.; Kim, J. S.; Acquaviva, D.; Oh, J.; Morgan, C. D.; Seita, M.; Leib, J. S.; Thompson, C. V., Tuning of Vertically-Aligned Carbon Nanotube Diameter and Areal Density through Catalyst Pre-Treatment. *Nano Letters* 2008, 8, 3587-3593.

31. Choi, Y.; Shin, Y.; Lee, Y.; Lee, B.; Park, G.; Choi, W.; Lee, N.; Kim, J., Controlling the diameter, growth rate, and density of vertically aligned carbon nanotubes synthesized by microwave plasma-enhanced chemical vapor deposition. *Applied Physics Letters* 2000, 76, 2367-2369.

32. van Laake, L.; Hart, A. J.; Slocum, A. H., Suspended heated silicon platform for rapid thermal control of surface reactions with application to carbon nanotube synthesis. *Review of Scientific Instruments* 2007, 78.

33. Wang, B.; Bennett, R.; Verploegen, E.; Hart, A.; Cohen, R., Quantitative characterization of the morphology of multiwall carbon nanotube films by small-angle X-ray scattering. *Journal of Physical Chemistry C* 2007, 111, 5859-5865.

34. Plata, D. e. L.; Hart, A. J.; Reddy, C. M.; Gschwend, P. M., Early Evaluation of Potential Environmental Impacts of Carbon Nanotube Synthesis by Chemical Vapor Deposition. *Environmental Science & Technology* 2009, 43, 8367-8373.

35. Nessim, G.; Seita, M.; Plata, D.; O'Brien, K.; Hart, A.; Meshot, E.; Reddy, C.; Gschwend, P.; Thompson, C., Precursor gas chemistry determines the crystallinity of carbon nanotubes synthesized at low temperature. *Carbon* 2011, 49, 804-810.

36. Plata, D.; Meshot, E.; Reddy, C.; Hart, A.; Gschwend, P., Multiple alkynes react with ethylene to enhance carbon nanotube synthesis, suggesting a polymerization-like formation mechanism. *ACS Nano* 2010, 4, 7185-7192.

37. Hofmann, S.; Blume, R.; Wirth, C. T.; Cantoro, M.; Sharma, R.; Ducati, C.; Havecker, M.; Zafeiratos, S.; Schnoerch, P.; Oestereich, A.; Teschner, D.; Albrecht, M.; Knop-Gericke, A.; Schlogl, R.; Robertson, J., State of transition metal catalysts during carbon nanotube growth. *Journal of Physical Chemistry C* 2009, 113, 1648-1656.

38. Ardell, A. J. In *Experimental confirmation of the Lifshitz-Wagner theory of particle coarsening*, The Mechanism of Phase Transformations in Crystalline Solids, University of Manchester, University of Manchester, 1968.

39. Atwater, H. A.; Yang, C. M., Island growth and coarsening in thin-films - conservative and nonconservative systems. *Journal of Applied Physics* 1990, 67, 6202-6213.

40. Thompson, C. V., Coarsening of particles on a planar substrate - interface energy anisotropy and application to grain-growth in thin films. *Acta Metallurgica* 1988, 36, 2929-2934.

41. Kukovitsky, E. F.; L'Vov, S. G.; Sainov, N. A.; Shustov, V. A.; Chernozatonskii, L. A., Correlation between metal catalyst particle size and carbon nanotube growth. 2002, 355, 497-503.

42. Nerushev, O. A.; Dittmar, S.; Morjan, R. E.; Rohmund, F.; Campbell, E. E. B., Particle size dependence and model for iron-catalyzed growth of carbon nanotubes by thermal chemical vapor deposition. *Journal of Applied Physics* 2003, 93, 4185-4190.

43. Nerushev, O. A.; Morjan, R. E.; Ostrovskii, D. I.; Sveningsson, M.; Jönsson, M.; Rohmund, F.; Campbell, E. E. B., The temperature dependence of Fe-catalysed growth of carbon nanotubes on silicon substrates. *Proceedings of the Tsukuba Symposium on Carbon Nanotube in Commemoration of the 10th Anniversary of its Discovery* 2002, 323, 51-59.

44. Dresselhaus, M. S.; Dresselhaus, G.; Saito, R.; Jorio, A., Raman spectroscopy of carbon nanotubes. 2005, 409, 47-99.

45. Yasuda, S.; Hiraoka, T.; Futaba, D. N.; Yamada, T.; Yumura, M.; Hata, K., Existence and Kinetics of Graphitic Carbonaceous Impurities in Carbon Nanotube Forests to Assess the Absolute Purity. *Nano Letters* 2009, 9, 769-773.

46. Meshot, E.; Hart, A., Abrupt self-termination of vertically aligned carbon nanotube growth. *Applied Physics Letters* 2008, 113107.

47. Meshot, E.; Bedewy, M.; Lyons, K.; Woll, A.; Juggernauth, K.; Tawfick, S.; Hart, A., Measuring the lengthening kinetics of aligned nanostructures by spatiotemporal correlation of height and orientation. *Nanoscale* 2010, 896-900.

48. Bedewy, M.; Meshot, E.; Guo, H.; Verploegen, E.; Lu, W.; Hart, A., Collective Mechanism for the Evolution and Self-Termination of Vertically Aligned Carbon Nanotube Growth. *Journal of Physical Chemistry C* 2009, 113, 20576-20582.

49. Bedewy, M.; Meshot, E. R.; Reinker, M. J.; Hart, A. J., Population growth dynamics of carbon nanotubes. *ACS Nano* 2011, 5, 8974-8989.

50. Hofmann, S.; Kleinsorge, B.; Ducati, C.; Ferrari, A. C.; Robertson, J., Low-temperature plasma enhanced chemical vapour deposition of carbon nanotubes. *14th European Conference on Diamond, Diamond-Like Materials, Carbon Nanotubes, Nitrides and Silicon Carbide* 2004, 13, 1171-1176.

51. Hofmann, S.; Csanyi, G.; Ferrari, A.; Payne, M.; Robertson, J., Surface diffusion: The low activation energy path for nanotube growth. *Physical Review Letters* 2005, 95.

52. Meshot, E.; Plata, D.; Tawfick, S.; Zhang, Y.; Verploegen, E.; Hart, A., Engineering vertically aligned carbon nanotube growth by decoupled thermal treatment of precursor and catalyst. *ACS Nano* 2009, 3, 2477-2486.

53. Zhong, G.; Hofmann, S.; Yan, F.; Telg, H.; Warner, J. H.; Eder, D.; Thomsen, C.; Milne, W. I.; Robertson, J., Acetylene: A Key Growth Precursor for Single-Walled Carbon Nanotube Forests. *Journal of Physical Chemistry C* 2009, 113, 17321-17325.

54. Eres, G.; Kinkhabwala, A. A.; Cui, H.; Geohegan, D. B.; Puretzky, A. A.; Lowndes, D. H., Molecular Beam-Controlled Nucleation and Growth of Vertically Aligned Single-Wall Carbon Nanotube Arrays. *Journal of Physical Chemistry B* 2005, 109, 16684-16694.

55. Richter, H.; Howard, J. B., Formation of polycyclic aromatic hydrocarbons and their growth to soot - a review of chemical reaction pathways. *Progress in Energy and Combustion Science* 2000, 26, 565-608.

56. Baughman, R. H.; Zakhidov, A. A.; de Heer, W. A., Carbon Nanotubes--the Route Toward Applications. *Science* 2002, 297, 787-792.

57. Nessim, G. D.; Seita, M.; O'Brien, K. P.; Hart, A. J.; Bonaparte, R. K.; Mitchell, R. R.; Thompson, C. V., Low Temperature Synthesis of Vertically Aligned Carbon Nanotubes with Ohmic Contact to Metallic Substrates Enabled by Thermal Decomposition of the Carbon Feedstock. *Nano Letters* 2009, 9, 3398-3405.

58. Awano, Y.; Sato, S.; Kondo, D.; Ohfuti, M.; Kawabata, A.; Nihei, M.; Yokoyama, N., Carbon nanotube via interconnect technologies: size-classified catalyst nanoparticles and low-resistance ohmic contact formation. *Physica Status Solidi a-Applications and Materials Science* 2006, 203, 3611-3616.

59. Chhowalla, M.; Teo, K. B. K.; Ducati, C.; Rupesinghe, N. L.; Amaratunga, G. A. J.; Ferrari, A. C.; Roy, D.; Robertson, J.; Milne, W. I., Growth process conditions of vertically aligned carbon nanotubes using plasma enhanced chemical vapor deposition. *Journal of Applied Physics* 2001, 90, 5308-5317.

60. Zhong, G. F.; Iwasaki, T.; Honda, K.; Furukawa, Y.; Ohdomari, I.; Kawarada, H., Low temperature synthesis of extremely dense, and vertically aligned single-walled carbon nanotubes. *Japanese Journal of Applied Physics Part 1* 2005, 44, 1558-1561.

61. Lee, S.; Peng, J.-W.; Liu, C.-H., Probing plasma-induced defect formation and oxidation in carbon nanotubes by Raman dispersion spectroscopy. *Carbon* 2009, 47, 3488-3497.

62. Ren, Z. F.; Huang, Z. P.; Xu, J. W.; Wang, J. H.; Bush, P.; Siegal, M. P.; Provencio, P. N., Synthesis of Large Arrays of Well-Aligned Carbon Nanotubes on Glass. *Science* 1998, 282, 1105-1107.

63. Chiodarelli, N.; Li, Y.; Cott, D. J.; Mertens, S.; Peys, N.; Heyns, M.; De Gendt, S.; Groeseneken, G.; Vereecken, P. M., Integration and electrical characterization of carbon nanotube via interconnects. *Microelectronic Engineering* 2011, 88, 837-843.

64. Esconjauregui, S.; Fouquet, M.; Bayer, B.; Ducati, C.; Smajda, R.; Hofmann, S.; Robertson, J., Growth of ultrahigh density vertically aligned carbon nanotube forests for interconnects. *ACS Nano* 2010, 4, 7431-7436.

65. Zhang, C.; Cott, D.; Chiodarelli, N.; Vereecken, P.; Robertson, J.; Whelan, C. M., Growth of carbon nanotubes as horizontal interconnects. *Physica Status Solidi B* 2008, 245, 2308-2310.

66. Graham, A.; Duesberg, G.; Seidel, R.; Liebau, M.; Unger, E.; Kreupl, F.; Honlein, W., Towards the integration of carbon nanotubes in microelectronics. *Diamond and Related Materials* 2004, 13, 1296-1300.

67. Rueckes, T.; Kim, K.; Joselevich, E.; Tseng, G. Y.; Cheung, C.-L.; Lieber, C. M., Carbon nanotube-based nonvolatile random access memory for molecular computing. *Science* 2000, 289, 94-97.

68. Zhang, L.; Li, Z.; Tan, Y.; Lolli, G.; Sakulchaicharoen, N.; Requejo, F.; Mun, B.; Resasco, D., Influence of a top crust of entangled nanotubes on the structure of vertically aligned forests of single-walled carbon nanotubes. *Chemistry of materials* 2006, 18, 5624-5629.

69. Baker, R. T. K.; Barber, M. A.; Waite, R. J.; Harris, P. S.; Feates, F. S., Nucleation and growth of carbon deposits from nickel catalyzed decomposition of acetylene. *J Catal* 1972, 26, 51-&.

70. Ding, F.; Bolton, K.; Rosen, A., Nucleation and growth of single-walled carbon nanotubes: A molecular dynamics study. *Journal of Physical Chemistry B* 2004, 108, 17369-17377.

71. Raty, J. Y.; Gygi, F.; Galli, G., Growth of carbon nanotubes on metal nanoparticles: a microscopic mechanism from ab initio molecular dynamics simulations. *Physical Review Letters* 2005, 95, -.

72. Pope, C. J.; Marr, J. A.; Howard, J. B., Chemistry of Fullerenes C_{60} and C_{70} Formation in Flames. *Journal of Physical Chemistry* 1993, 97, 11001-11013.

73. Eres, G.; Kinkhabwala, A. A.; Cui, H. T.; Geohegan, D. B.; Puretzky, A. A.; Lowndes, D. H., Molecular beam-controlled nucleation and growth of vertically aligned single-wall carbon nanotube arrays. *Journal of Physical Chemistry B* 2005, 109, 16684-16694.

74. Steiner, S. A.; Baumann, T. F.; Bayer, B. C.; Blume, R.; Worsley, M. A.; MoberlyChan, W. J.; Shaw, E. L.; Schlogl, R.; Hart, A. J.; Hofmann, S.; Wardle, B. L., Nanoscale Zirconia as a Nonmetallic Catalyst for Graphitization of Carbon and Growth of Single- and Multiwall Carbon Nanotubes. *Journal of the American Chemical Society* 2009, 131, 12144-12154.

75. Tohji, K.; Takahashi, H.; Shinoda, Y.; Shimizu, N.; Jeyadevan, B.; Matsuoka, I.; Saito, Y.; Kasuya, A.; Ito, S.; Nishina, Y., Purification procedure for single-walled nanotubes. *Journal of Physical Chemistry B* 1997, 101, 1974-1978.

76. Rinzler, A. G.; Liu, J.; Dai, H.; Nikolaev, P.; Huffman, C. B.; Rodríguez-Macías, F. J.; Boul, P. J.; Lu, A. H.; Heymann, D.; Colbert, D. T.; Lee, R. S.; Fischer, J. E.; Rao, A. M.; Eklund, P. C.; Smalley, R. E., Large-scale purification of single-wall carbon nanotubes: process, product, and characterization. *Applied Physics A: Materials Science & Processing* 1998, 67, 29-37.

77. Shelimov, K. B.; Esenaliev, R. O.; Rinzler, A. G.; Huffman, C. B.; Smalley, R. E., Purification of single-wall carbon nanotubes by ultrasonically assisted filtration. 1998, 282, 429-434.

78. Zimmerman, J. L.; Bradley, R. K.; Huffman, C. B.; Hauge, R. H.; Margrave, J. L., Gas-Phase Purification of Single-Wall Carbon Nanotubes. *Chemistry of Materials* 2000, 12, 1361-1366.

79. Yamada, T.; Namai, T.; Hata, K.; Futaba, D. N.; Mizuno, K.; Fan, J.; Yudasaka, M.; Yumura, M.; Iijima, S., Size-selective growth of double-walled carbon nanotube forests from engineered iron catalysts. *Nature Nanotechnology* 2006, 1, 131-136.

Chapter 6
Photoconductive hybrid films via directional self-assembly of C_{60} on aligned CNTs

While synthesis of indefinitely long CNTs remains a significant challenge, many applications still benefit from ensembles of shorter CNTs. In this chapter, we explore an application of aligned CNTs as a scaffold material for building microscale hybrid films. Hybrid nanostructured systems capitalize on synergy between materials, enabling improved properties beyond those of the constituent component. This allows decoupled engineering of energy conversion and transport functions for instance. We demonstrate that aligned CNT films direct the crystallization and orientation of C_{60} rods from solution, resulting in hybrid structures where the C_{60} rods are oriented parallel to the direction of the CNTs.   Aligned rods are observed on the CNT film surface and through the film thickness. High-resolution imaging shows that the crystals incorporate CNTs during growth, yet grazing-incidence X-ray diffraction (GIXD) shows that the crystal structure of the C_{60} rods is not perturbed by the CNTs.   Real-time video imaging reveals that rod growth kinetics are enhanced 8-fold on CNTs compared to bare Si, emphasizing the importance of the aligned, porous morphology of the CNT films. Finally, we show how the hybrid sheets can be integrated electrically and employed as UV sensors having high photoconductive gain with a responsivity as high as 10^5 A W^{-1} at low biases ($\pm$ 0.5 V). Our methods and findings may also have broader importance to the science and applications of crystal growth of other materials such as aromatic hydrocarbons, synthetic polymers, and biomolecules. This chapter originally appeared as a manuscript in *Advanced Functional Materials* (in press at the time the chapter was written), and the content is reprinted here with permission from the publisher (Copyright © 2011 John

Wiley & Sons, Inc.). The current presentation of this work represents my contributions, principally, unless noted otherwise.

6.1   Introduction

Fullerenes (C_{60}) are a uniquely monodisperse nanoscale building block and can be assembled into nano- and microscale crystals having diverse and controllable sizes and shapes using evaporation of dispersions.[1-9] Crystalline C_{60} is a direct-band gap semiconductor,[10] an excellent electron acceptor,[10, 11] and calculations show that contacts between C_{60} molecules in a closely packed crystal have very low thermal conductance.[12] These features make C_{60} attractive for applications including diodes,[11, 13] field-effect transistors,[14, 15] photoelectrics,[8, 16] and thermoelectrics.[12] C_{60} crystals are generally made in bulk or deposited randomly on substrates; however, directed placement, alignment, and
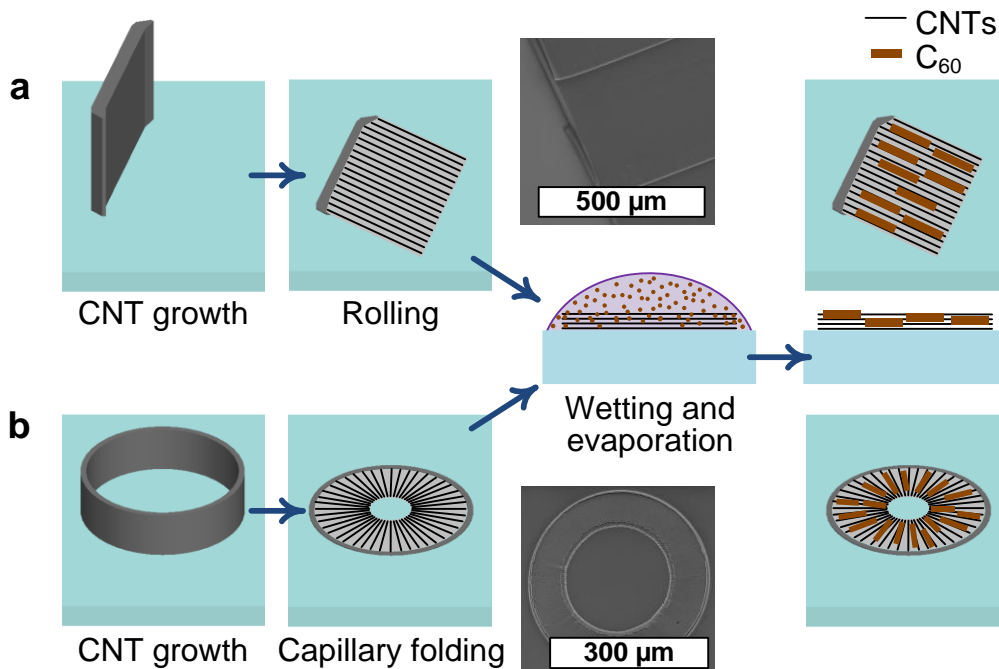
Figure 6.1 Fabrication of C_{60}-CNT hybrid films: (a) fabrication sequence involving rolling of vertical CNTs to produce laterally oriented (LO) films, followed by wetting and drying with C_{60} dispersion in *m*-xylene; and (b) fabrication of radially oriented (RO) CNT films by capillary folding, followed by synthesis of C_{60} crystals on the CNTs. Inset SEM images show CNT films before drop-casting of C_{60} dispersion. Solid models originally provided by Sameh Tawfick.

interconnection of C_{60} crystals is typically necessary for their utilization in devices.

We demonstrate that aligned carbon nanotube (CNT) films can spatially direct the crystallization of C_{60} from solution, therefore enabling integration of hybrid thin film devices by combining standard photolithography and two-step capillary self-assembly process. Uniquely, we find that C_{60} rods crystallize preferentially parallel to films of horizontally-aligned CNTs, thus creating a self-organized directional assembly wherein C_{60} crystals are pierced and interconnected by CNT conduits. We find that kinetics of crystallization are also significantly influenced in the presence of the CNT, with an enhancement factor greater than 8 in crystal growth rate compared to crystallization on bare silicon. The resultant hierarchical organization is advantageous for energy devices, especially considering that C_{60} crystals alone are poor electrical conductors. For instance, we demonstrate that the C_{60}-CNT hybrid films have high photoconductive gain under UV irradiation with a responsivity as high as 10^5 A W^{-1} at low biases ($\pm$ 0.5 V). Overall, the rational design and fabrication of templates that induce ordered crystallization, and the understanding of how nanostructured surfaces affect crystallization kinetics, are important topics for applications including organic electronics,[17] composite materials, and protein science. [18-21]

6.2   Results and discussion

6.2.1   Synthesis of C_{60}-CNT hybrid films

Directed crystallization of C_{60} on CNTs is achieved as shown in **Figure 6.1**. First, vertically aligned CNT "forests" are grown from lithographically patterned catalyst on silicon wafers using a standard catalytic chemical vapor deposition (CVD) process.[22-24] The forests comprise multi-wall CNTs with a mean diameter of 11 ± 2.8 nm.[25] Next, the vertical CNTs are transformed to a horizontal orientation via capillary folding by condensation of acetone onto the substrate.[26-30]   Because the direction of capillary folding depends on the geometry of the CNT microstructures,[27-30] capillary folding enables fabrication of not only unidirectional films (**Figure 6.2**) but also multi-directional CNT patterns, such as radially oriented and adjacently perpendicular CNT films that

overlap during capillary folding (**Figure 6.3**). This method results in uniform-thickness CNT films with high packing fraction (≈ 0.2)[26] and high in-plane anisotropy. Further, the CNT films can be folded such that they bridge a set of pre-patterned electrodes (in this case TiN). This provides a straight-forward and robust method for electrical integration of the C_{60}-CNT hybrids into sensors or other devices requiring electrical read-out. The in-plane anisotropy of the folded CNT sheets was previously quantified by X-ray scattering[26] and electrical resistance measurements. Finally, C_{60} dispersed in *m*-xylene (without surfactants)[1, 6, 9] is deposited by drop-casting onto the CNT films. The solution infiltrates the CNT film by capillary action and then is allowed to evaporate under ambient conditions. C_{60} rods crystallize on and within the CNT film during wetting and evaporation. Additional experimental details are in Section 6.3.

6.2.2   Characterization of alignment and structure

We observe that the major axis (length) of each C_{60} rod is oriented along the direction of CNTs within the film, in both unidirectional and multidirectional sheets. This is shown in **Figure 6.2** and **Figure 6.3**. In comparison, alignment is not observed in a control experiment where C_{60} crystallization is performed on the polished side of a bare (100) silicon wafer (**Figure 6.2a**). We quantify the average orientation of the C_{60} rods by the mean square cosine $\langle\cos^2\theta\rangle$, where θ is the orientation angle of each rod relative to a reference axis (red dashed line). This parameter has been used to quantify the order of other anisotropic structures including polymer chains,[31] liquid crystals,[32] and CNTs.[33] Note that $\langle\cos^2\theta\rangle = 1$ corresponds to perfect parallel alignment of the rods with the CNTs, while $\langle\cos^2\theta\rangle = 1/2$ represents random order. The C_{60} rods are randomly oriented when crystallized on bare silicon ($\langle\cos^2\theta\rangle = 0.54$), while those crystallized on CNTs are strongly correlated to the direction of CNT alignment ($\langle\cos^2\theta\rangle > 0.8$). On bare silicon, we occasionally observe areas where the solvent droplet becomes pinned to the substrate during evaporation. This causes a locally higher density of rods to form in arrangements that resemble drying rings, as in the "coffee stain" phenomenon (**Figure 6.4**).[34] At these locations, the pinned meniscus does slightly influence local rod orientation, resulting in $\langle\cos^2\theta\rangle < 0.7$. This likely occurs due to capillary forces that orient the rods as well as fluid flow and solute concentration gradients near the
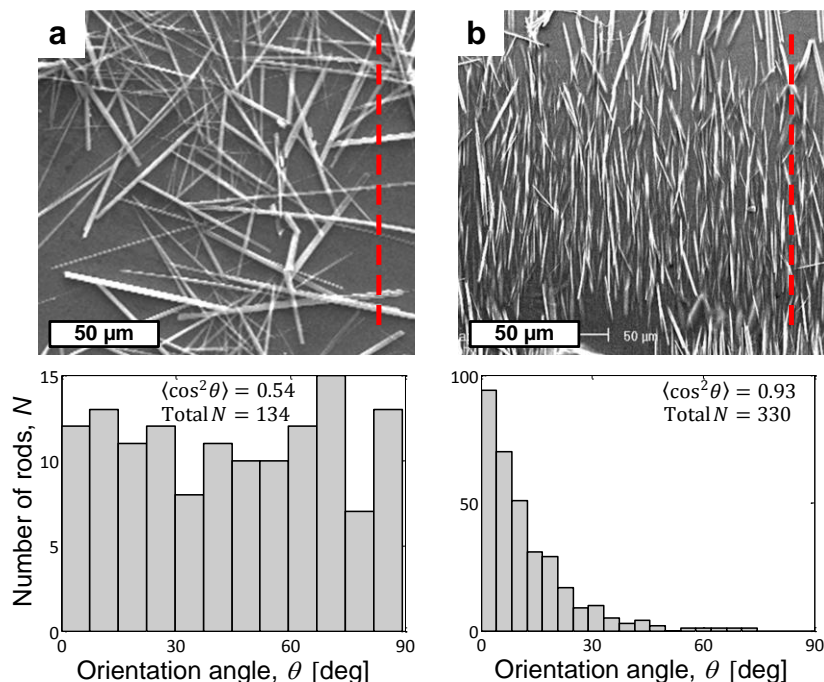
Figure 6.2 SEM images after synthesis of C_{60} rods on bare silicon and unidirectional CNT film, (a) and (b) respectively. Accompanying histograms are below each SEM, showing distribution of rod orientation relative to axis indicated by red dashed lines.
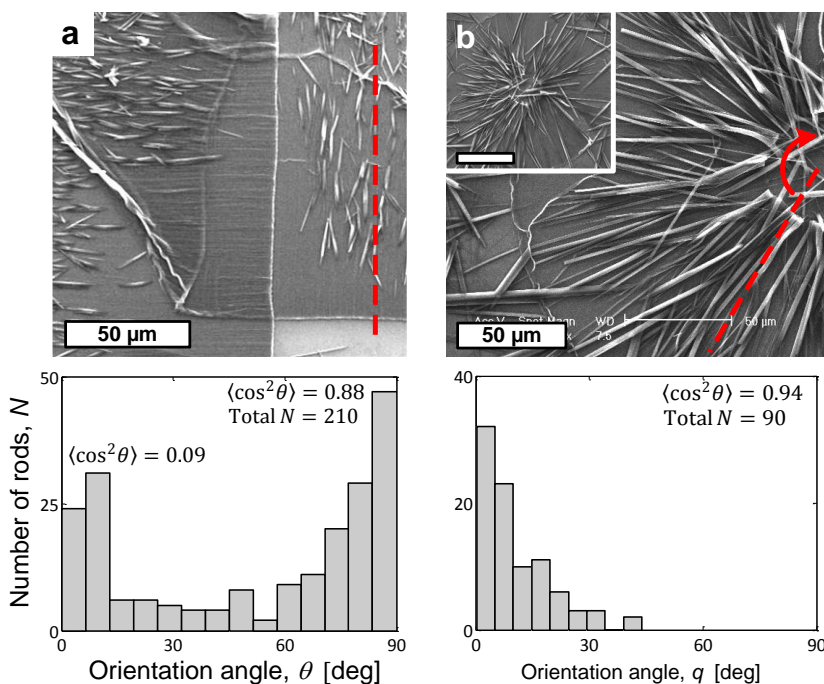
Figure 6.3 SEM images after synthesis of C_{60} rods on multi-directional pattern (perpendicular unidirectional films) and radially oriented (RO) CNT film, (a) and (b) respectively. Scale bar in inset of (b) is 100 µm. Accompanying histograms are below each SEM, showing distribution of rod orientation relative to axis indicated by red dashed lines.
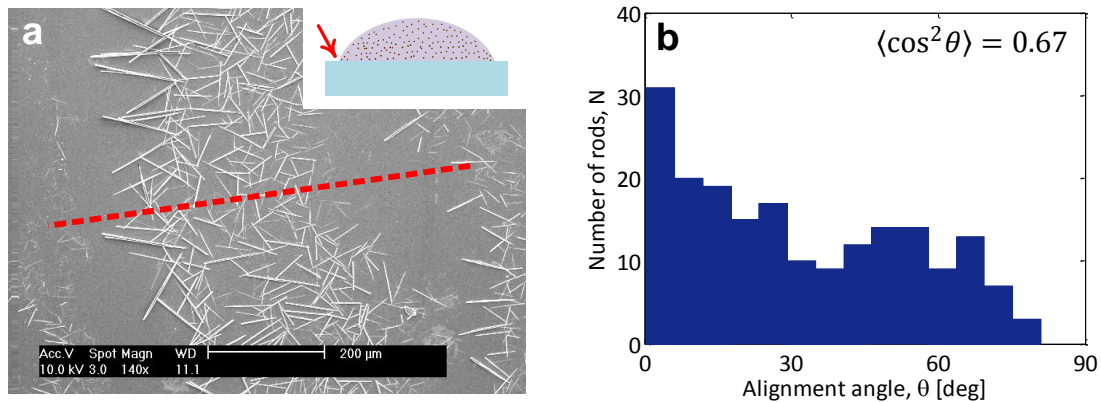
Figure 6.4 C_{60} crystals grown by drop-casting C_{60}/*m*-xylene on bare Si. (a) SEM taken in a region where the solvent pinned to the substrate during drying. Inset schematic shows the location where the droplet pinned to the Si. The red dashed line represents the estimated radial direction of this drying ring and serves as the axis from which we measure the orientation angle of the C_{60} rods. The results of these measurements are in the histogram (b).

meniscus,[34, 35] Thus, pinning of the meniscus on a flat substrate is not as uniformly effective in aligning the rods as compared to the CNT templates, albeit by a different mechanism.

Further investigation by electron microscopy shows that the C_{60} rods penetrate beneath the surface of the CNT films and that CNTs pierce through the C_{60} crystals. A magnified view of the hierarchical, aligned morphology of the CNTs and CNT bundles is shown in **Figure 6.5a** and **Figure 6.5b**. The existence of rods both on top and beneath the CNTs (**Figure 6.5**) suggests that C_{60} rods can nucleate and grow on the surface of the CNT film and/or within the film. In both cases the rod growth direction is influenced by the CNTs. As seen here and in **Figure 6.5d**, the CNT are laced through the C_{60} rods, forming a true hybrid material, where up to ~10^3 CNTs may be incorporated into a single crystal (~1 μm width), based on the packing density of the CNT film. TEM confirms that individual CNTs are connected to the side facet of the C_{60} rod (**Figure 6.5e**) and that the crystal structure of the rod is not disrupted by the CNTs (**Figure 6.5f**), which we later substantiate by X-ray diffraction.

Characteristic Raman spectroscopy peaks of C_{60} and CNTs allow for their identification within the hybrid film. We profile a single C_{60} rod that is partially embedded in the CNT film, and has one end exposed (**Figure 6.6a**) with a focused beam
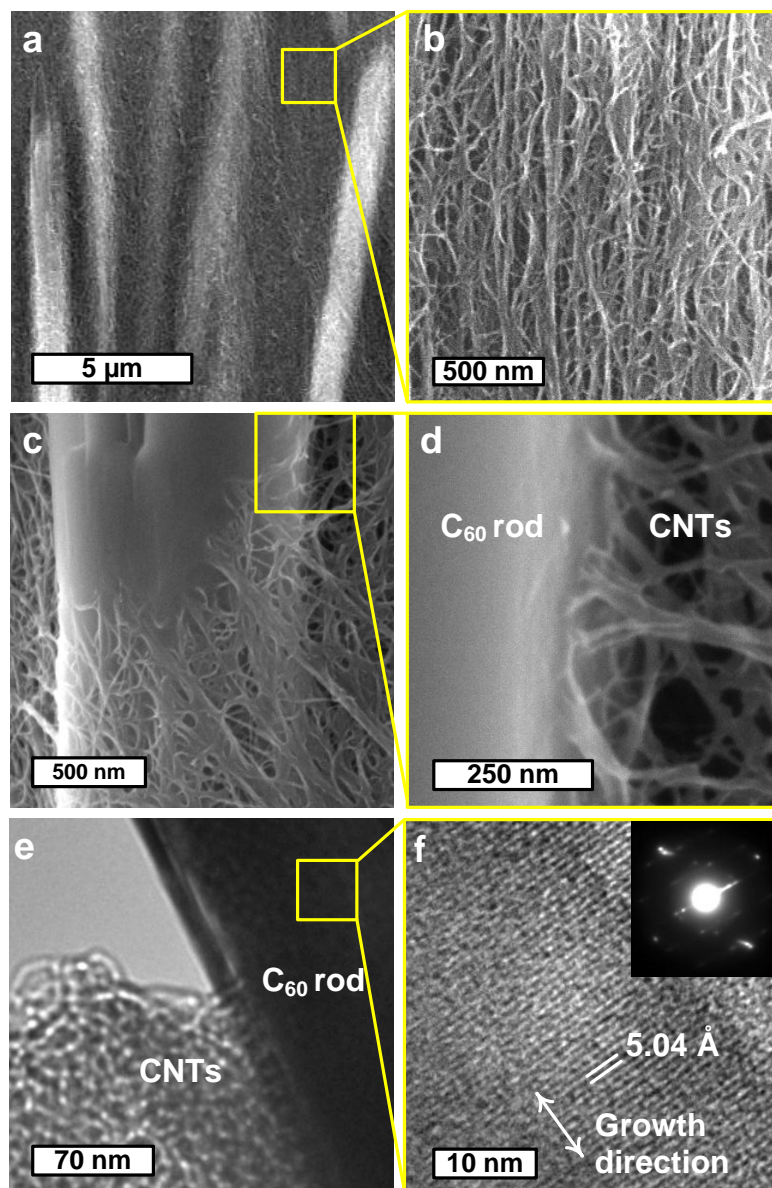
Figure 6.5 High-resolution electron microscopy of C_{60}-CNT hybrid film. (a) SEM image of C_{60} rods aligned to the CNTs; (b) Higher magnification of area between C_{60} crystals, showing aligned CNTs and CNT bundles; (c) a single C_{60} rod that pierces through the CNT film, showing a smooth transition between CNTs and the C_{60} crystal and interconnection with further magnification in (d). of (c), showing CNT bundles penetrating the side of the C_{60} rod. (e) TEM of the interface between CNTs and C_{60} crystal with higher magnification in (f) and inset selected-area electron diffraction (SAED) image.

of less than 1 μm at the sample. Initially at (1), where the C_{60} rod is fully exposed, the characteristic C_{60} peak at ~1468 cm^{-1}[36] is strong and discernible in the presence of the weaker CNT peaks near 1350 cm^{-1} and 1580 cm^{-1} (D- and G-bands, respectively).[37] The
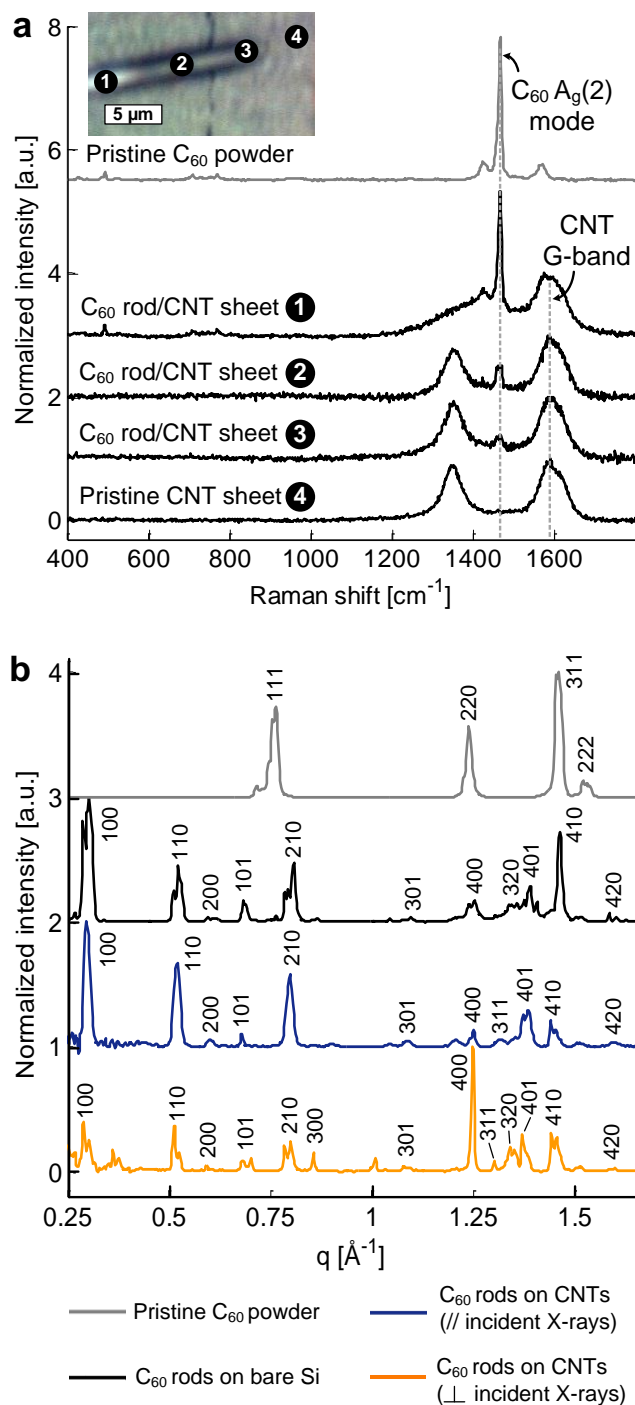
Figure 6.6 Structural characterization of a C_{60}-CNT hybrid film. (a) Micro-Raman spectroscopy ($\lambda = 514$ nm) profile of a C_{60} rod that is partially embedded in a CNT film is compared to a spectrum taken from as-received C_{60} powder. The ratio of $I_G/I_D \approx 1.2$ observed here is typical for multi-wall CNTs synthesized by our thermal CVD process. (b) GIXD data showing scattering intensity as a function of scattering vector q (where $q = 4\pi/\lambda \sin \psi$, and ψ is the scattering angle). The C_{60} crystals synthesized on CNTs are indexed as hexagonal lattice (a = 22.4 Å, c = 10.3 Å). See **Figure 6.7** for an example 2-D scattering image and further analysis.
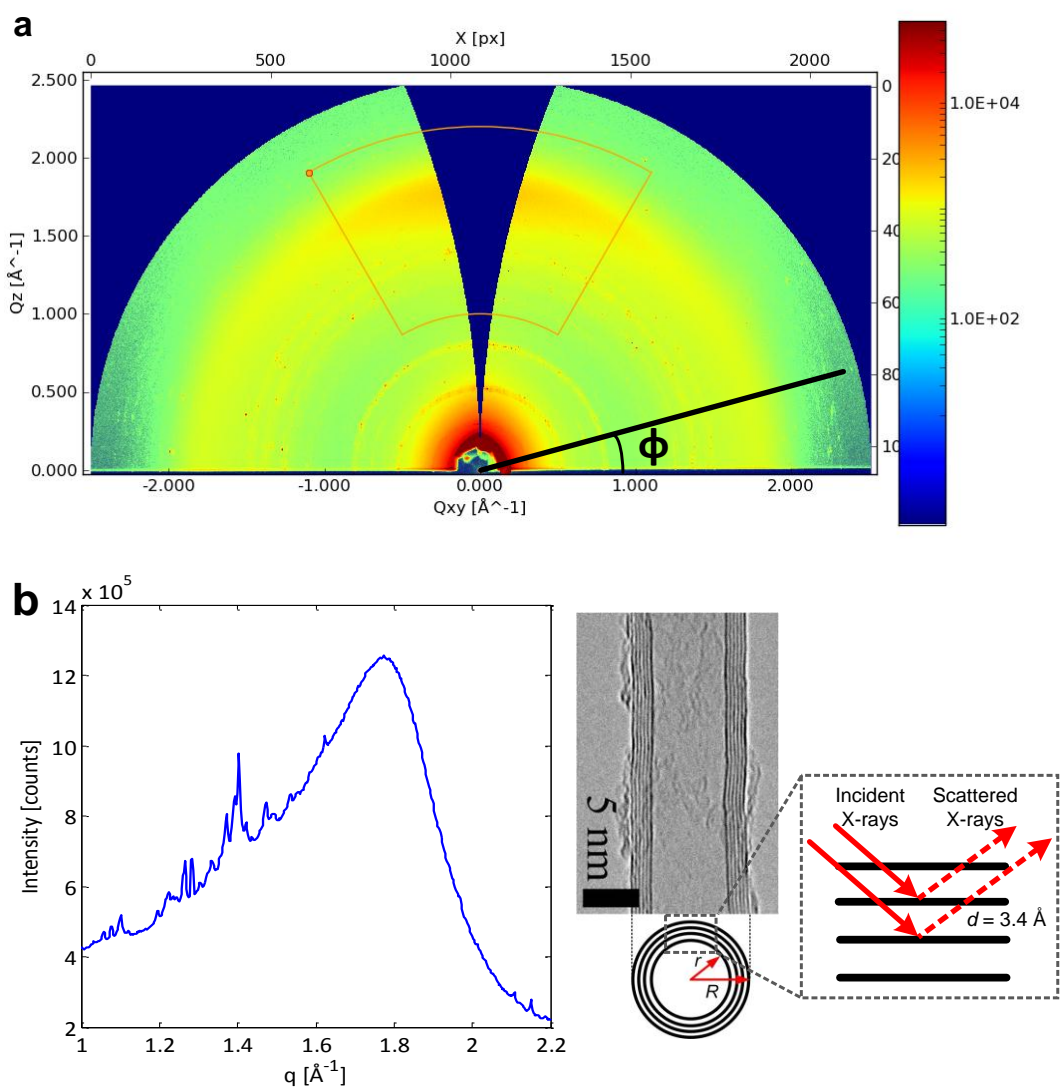
Figure 6.7 Representative 2-D GIXD image for C_{60} crystals on laterally oriented CNTs (X-ray beam parallel to CNT direction). The plots of intensity versus scattering vector q in **Figure 6.6** were obtained by integrating the intensity in the (a) 2-D image above about the azimuthal angle ϕ [1°,179°]. (b) Azimuthally integrated intensity of the sector outlined in (a) showing the diffraction peak from the CNT wall spacing (peak at 1.78 Å^{-1} corresponds to d-spacing of 3.53 Å, which agrees with the interplanar spacing of graphite 3.4 Å). GIXD data collected by Eric Verploegen at the Stanford Synchrotron Radiation Lightsource.

intensity of the C_{60} peak declines relative to the CNT G-band as the beam is scanned along the length of the rod [(2),(3)], matching with the transition of the rod into the CNT film. The peak position does not shift in frequency over the length of the rod, indicating that no chemical modification of the C_{60} molecules takes place before or during crystallization (*e.g.*, via polymerization[38]). No spectroscopic features of the C_{60} are observed away from the rod at (4), confirming that the synthesis process leaves C_{60} highly localized around the crystals.

We determine the crystal structure of the C_{60} rods by grazing incidence X-ray diffraction (GIXD) measurements (**Figure 6.6b**) using synchrotron radiation and a 2-D area detector (**Figure 6.7a**). These measurements show the as-received C_{60} powder has a face-centered cubic (FCC) crystal structure with the lattice parameter $a = 14.3$ Å,[6, 39] whereas the C_{60} rods grown on bare silicon and on CNT films both have a hexagonal structure ($a = 23.4$ Å, $c = 10.3$ Å), which is consistent with previous studies of C_{60} synthesized from *m*-xylene.[1, 6, 40] This change in packing from the higher-density FCC phase is due to the incorporation of trace solvent molecules at interstices,[6, 9, 40-42] where the C_{60}:*m*-xylene composition is 3:2.[40] Solvent is incorporated with the crystal partially due to the strong association between the its aromatic structure and the electron-rich hexagonal faces of C_{60},[43] as well as kinetics of the crystallization process, both of which are discussed later. A large difference in the scattered X-ray intensity is observed when the beam is aligned parallel versus perpendicular to the CNTs, emphasizing the crystallographic anisotropy of the hybrid material. C_{60} rods synthesized from *m*-xylene are known to crystallize along the *c*-axis (001),[5, 9] and the crystal lattice spacing we measure from TEM (5.04 Å) in **Figure 6.5f** is approximately half of *c* because there are two crystal planes per unit cell. The inset selected-area electron diffraction (SAED) image also shows six-fold symmetry with a spacing near that measured in TEM (4.88 Å).

6.2.3   Enhanced kinetics of C_{60} crystallization

Although the presence of CNTs does not alter the structure of the C_{60} crystals, C_{60} crystal growth on CNT films is significantly faster than on bare silicon. We use *in situ* optical microscopy to measure rod length versus time shown in **Figure 6.8**. The lengthening kinetics of C_{60} rods on CNTs are 8.6 times faster than on bare silicon
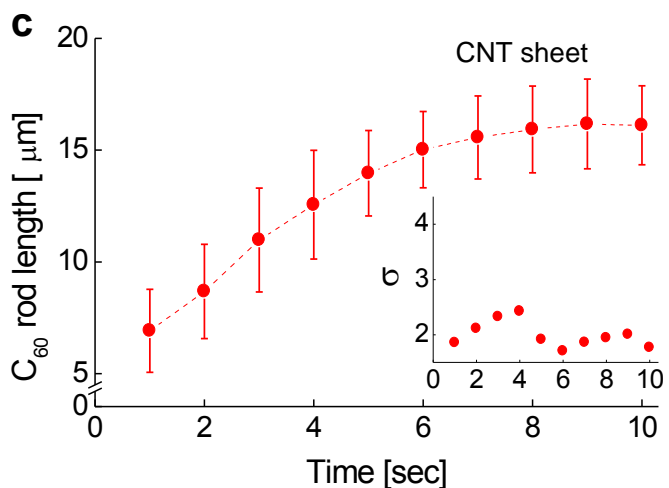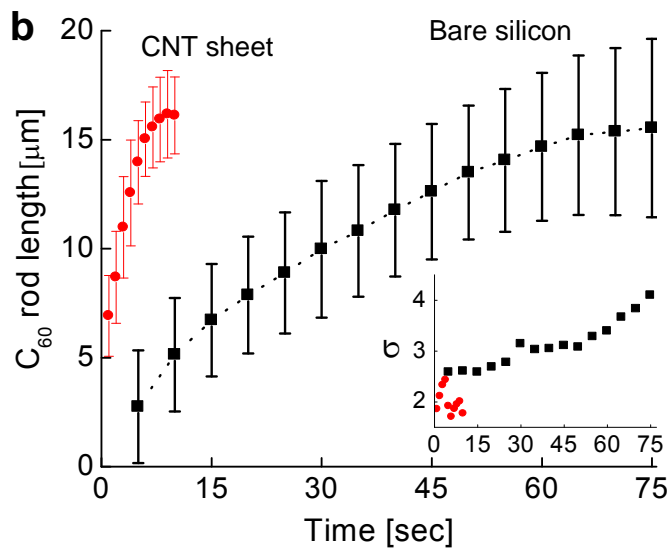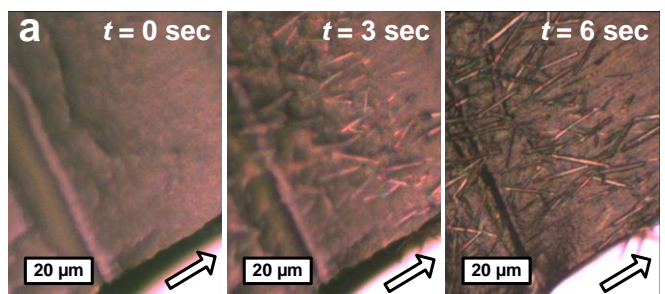
Figure 6.8 Lengthening kinetics of C_{60} rods on CNTs and bare silicon. (a) Snapshots of real-time recording of the C_{60} crystal growth on a CNT film. (b) Measurements of rod length versus time, comparing growth on CNTs (red circles) and on Si (black squares), with the length versus time curve for growth on CNTs is replicated in (c) with the x-axis rescaled to show similarity in shape and emphasize the difference in timescales. Each point and error bar represent the mean and standard deviation, respectively, for measurements taken from ten rods, while the inset plots show the standard deviation alone versus time for each case. $t = 0$ corresponds to the time at which a rod is first observed.

(average rates $\approx$ 1.8 and 0.2 µm sec^{-1}, respectively), and growth terminates when the solvent fully evaporates from the substrate. After this occurs, the average length of the crystals is nearly identical on both substrates (16.1 and 15.5 µm, respectively), yet the standard deviation of length is smaller on CNTs (1.8 and 4.1 µm, respectively). The average width of the C_{60} rods in both cases is 1.3 ± 0.4 µm when growth terminates. The length distribution broadens with time on Si, yet narrows with time on CNTs, suggesting that the CNT substrate also enables a more uniform delivery of C_{60} to the growth sites. We also note that the rods do not move or rotate during observable stages of growth on CNT films, yet they remain straight and predominantly follow the CNT direction as growth proceeds.

Additional control experiments reinforce that both the physical and chemical characteristics of CNTs influence the rapid, directed crystallization of C_{60}. First, we observe a very low density of rods on highly ordered pyrolytic graphite (HOPG), which presents similar chemical compatibility to C_{60} as CNTs. This is due to the smooth surface of HOPG and the strong wetting of *m*-xylene on HOPG, which accelerate evaporation and inhibit prolonged crystal growth. Therefore, the topography of the CNT film is important for a high nucleation density. Second, to preserve the physical texture and porosity of the CNT film while changing the surface chemistry, we conformally coated CNTs with alumina by atomic-layer deposition (ALD). On alumina-coated CNT films, rods form at low densities and are not aligned with the CNTs (**Figure 6.9a**). This demonstrates that both the native surface chemistry and texture of the aligned CNT films are needed for directional crystallization. Third, instead of crystallizing C_{60} directly on CNTs, we alternatively prepared C_{60} rods in solution by liquid-liquid interface precipitation (LLIP)[44, 45] and then drop-cast these rods onto CNT films. Even though the CNTs influence the motion of the meniscus during evaporation, the rods made by LLIP are not oriented with the same fidelity as those crystallized directly on the CNT films ($\langle\cos^2\theta\rangle = 0.72$ versus 0.93), and they do not penetrate into the CNT film (**Figure 6.9b**). Therefore, *in situ* crystallization on CNT templates is necessary to direct the rod orientation. This finding also emphasizes how the present work is different than previous approaches to align pre-made nanostructures by directional wetting.[35, 46, 47]
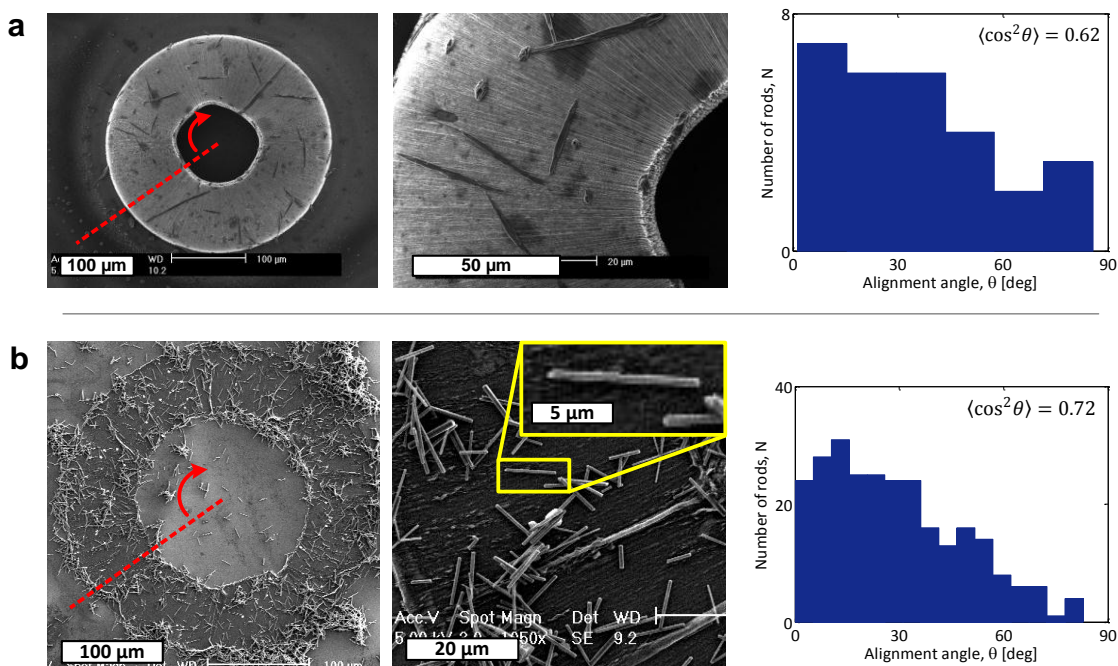
Figure 6.9 Control experiments for testing alignment mechanisms of C_{60} rods on CNTs. (a) SEM images of C_{60} crystals grown on RO- CNT films coated with ≈ 10 nm Al_2O_3 by atomic layer deposition. Note the low density of C_{60} rods and poor alignment to the coated CNTs (as measured from panel d, N = 28). (b) C_{60} rods that are first synthesized by liquid-liquid interface precipitation (LLIP) and then cast on RO-CNTs show poor alignment with the CNTs. Inset shows a rod on top of the CNTs rather than integrated. Accompanying histograms tabulate the orientation angle of the rods shown in low-magnification views in (a) (N = 265) and (b). Red dashed line represents the radial axis against which the rod angle is referenced.

We interpret these findings based on the anisotropic morphology of the CNT films as well as the physical interactions and known compatibility of CNTs, C_{60}, and the solvent. The CNT film is porous and is strongly wet by *m*-xylene; therefore, the solvent rapidly infiltrates the film upon drop-casting. Although the CNT packing fraction increases by as much as a factor of two during evaporation of the solvent,[26] the solvent and C_{60} clusters can still penetrate the CNT film because the size of the C_{60} clusters in solution (14.1 ± 2.9 nm, measured by dynamic light scattering, **Figure 6.10**) is less than the mean CNT-CNT nearest-neighbor spacing (*i.e.*, pore size), which is approximately 20 nm for a packing fraction of 0.2. Also, the carbon atoms in both CNTs and C_{60} are sp^2-hybridized, although they differ in aromaticity due to the presence of pentagonal faces in addition to hexagonal ones in C_{60}. Calculations show that the binding energy between a

153
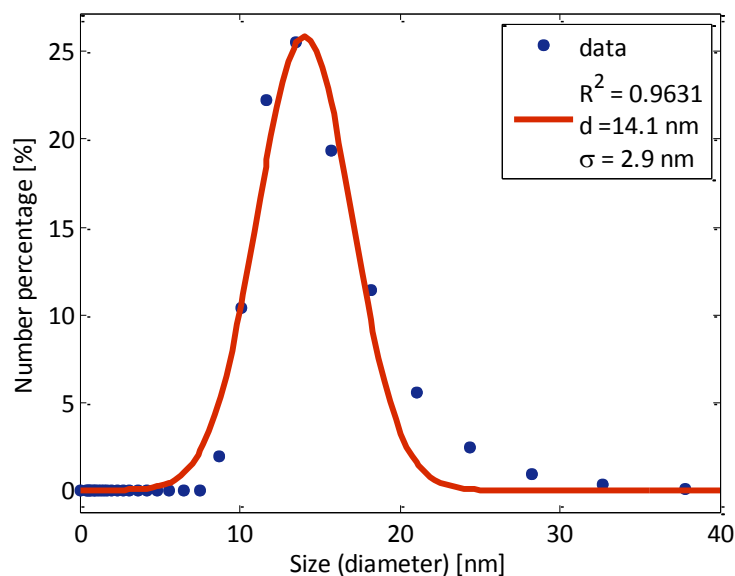
Figure 6.10 Dynamic light scattering (DLS) measurement of C_{60} dispersed in *m*-xylene (1 mg mL^{-1}) after 30 minutes of ultrasonication. The number of C_{60} in each cluster in solution is calculated from the measured average cluster size and by assuming hexagonal packing with unit cell dimensions that were measured by X-ray diffraction. The mean cluster diameter is equal to 14.1 ± 2.9 nm, representing $\approx 300\text{-}1100$ C_{60} per cluster.

single C_{60} molecule and the outer wall of a CNT (0.537 eV)[48, 49] exceeds that for either C_{60}-C_{60} (0.277 eV)[50] or solvent-CNT interactions (0.232 eV);[51] therefore, C_{60} in solution should be strongly attracted to the surface of CNTs.

Precedence in literature indicates that nanoscale roughness and porosity promote nucleation of C_{60} crystals[52] as well as other materials.[19-21, 53, 54] Thus, favorable crystallization of C_{60} on CNTs is a specific case of a more general behavior whereby nanostructured templates can assist crystallization via both fluidic and surface effects. Considering the strong C_{60}-CNT interaction, we hypothesize that rods nucleate when C_{60} clusters adhere to the CNTs while in solution, and then the crystal continues grows along CNTs by precipitation of the solute in a similar templating fashion previously observed in crystallization of polymers on CNTs.[55, 56] This may be aided by adsorption and migration of C_{60} clusters along the CNTs and the strong capillary action within the CNT film.[57] Surface defects are well known to act as favorable nucleation sites by restricting the mobility of adsorbed precursors, such as in vapor-solid growth of nanowires,[58-60] including formation of oxide nanostructures on CNT forests.[61, 62] Thus, we expect the

defect density of CNTs influences C_{60} crystal nucleation, and experiments with CNTs of different diameters (*i.e.*, single-wall CNTs which can have fewer defects) will be insightful. Likewise, the micro- and nanoscale surface texture of the CNT film (determined by the waviness and bundling of the CNTs) and the pore size (CNT spacing) within the film depend on the diameters and packing configuration of the CNTs, so controlling these characteristics may be a route to achieve enhanced control of selective crystal growth. For instance, previous studies found that bundles of CNTs selectively aid crystallization of organic molecules,[17] which Pan *et al*. suggest is due at least in part to favorable adsorption sites created by interstitial pores between CNT bundles.[63]

6.2.4 Device integration and photocurrent measurements

Finally, we electrically integrate CNT films as two-terminal devices to characterize the photoresponse of our material in the UV range. Our fabrication method is scalable because it employs standard photolithography of TiN electrodes that are compatible with high-temperature CVD of CNTs and because capillary folding and drop-casting of C_{60} are straightforward solvent processes. **Figure 6.11a** demonstrates that the photocurrent of the hybrid C_{60}-CNT device is substantially greater than either CNTs alone or C_{60} rods alone. The linear I-V characteristics indicate that the hybrid device is a photoconductor, and for instance, the resistance at 400 nm decreases by more than 20 times after integrating C_{60} rods with the CNT device. The responsivity of the hybrid device is 10^3-10^5 A W^{-1} in the range of 400-200 nm irradiation (**Figure 6.11b**), respectively. This exceeds recent benchmarks for nanostructured photodetectors (*e.g.*, ZnO or PbS quantum dots),[64] while our bias remains relatively low (0.5V). Although the CNT device has an appreciable responsivity in this wavelength range (likely due to heat-induced changes in resistivity resulting from absorption of light[65, 66]), the addition of C_{60} enhances the responsivity by approximately an order of magnitude.

The high photoconductivity of the hybrid film is the result of the interplay between the electronic structures of C_{60} and CNTs, as well as their hierarchical organization. We expect C_{60} crystals to generate excitons when illuminated by light with energy greater than the band gap of solid C_{60}, which is about 2.3 eV (540 nm).[67] Others have shown that individual C_{60} crystals with[68] or without[8] interstitial solvent molecules
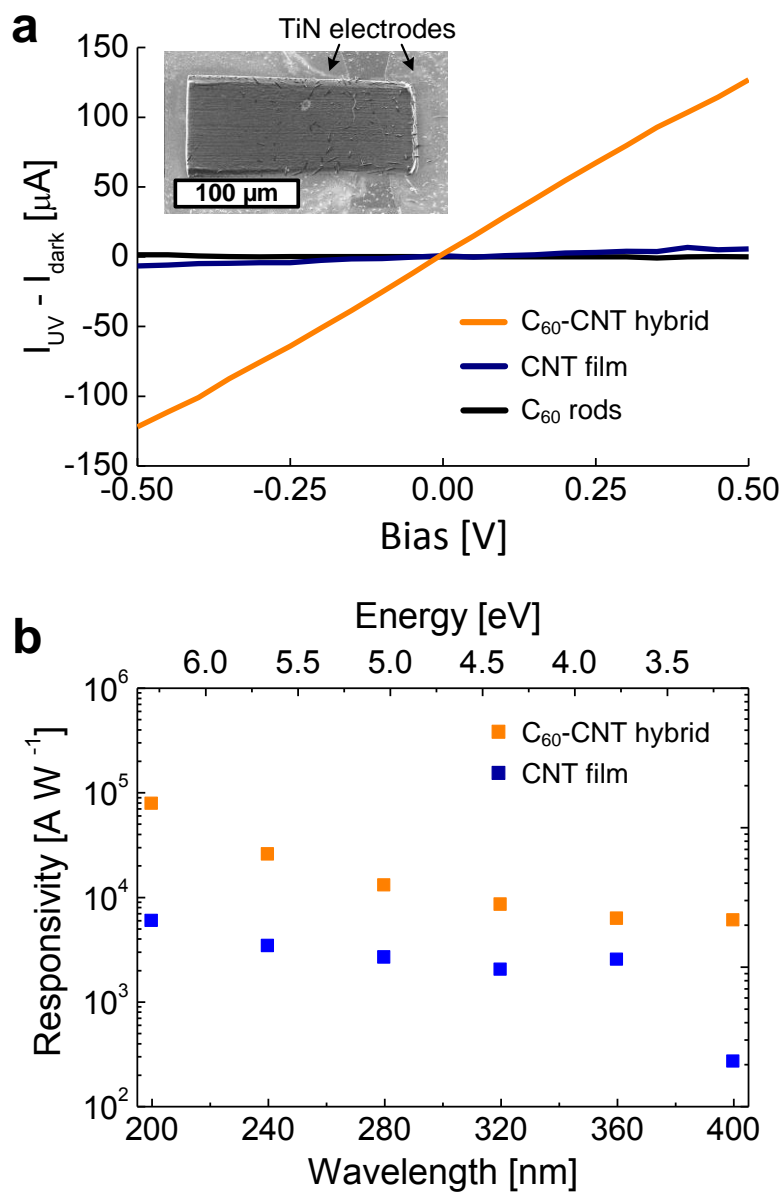
Figure 6.11 Photoresponse of CNT/C_{60} hybrid film devices. (a) Photocurrent measurement (applied bias $\pm$ 0.5 V) of device as shown in the inset SEM, where photocurrent is defined as the change in current measured with UV illumination on and off. (b) Responsivity (photocurrent divided by incident power) for range of UV wavelengths showing enhancement due to the addition of C_{60} to the CNT film. Each point represents the mean value taken from at least three measurements of the same device. Device integration and UV measurements performed by Michaël De Volder.

can generate photocurrent. The hierarchical structure of our hybrid film allows charge carriers to be injected into the multi-wall CNTs, which are metallic, and charge separation is also aided by C_{60}'s strong tendency to accept electrons.[10, 11] Thus, holes are likely the injected charge carrier and can pass through the circuit many times under the influence of the applied electric field (bias) before recombining with trapped electrons. While the absorption properties of C_{60}/m-xylene crystals in the tested wavelength range is relatively constant,[69] multi-wall CNTs show increased absorption toward 200 nm,[70] which explains the upward trend in responsivity we observe in both the CNT and C_{60}-CNT devices. The large surface-area-to-volume ratio of the hybrid films also plays a role in the large responsivity, increasing absorption and increasing the abundance of surfaces and interfaces, which can trap charge carriers, delay recombination, and thus increase the responsivity of the device.[64, 71, 72] Recent studies have also demonstrated the advantages of combining C_{60} with CNTs in various devices to enhance the performance of photodetectors[11] and photovoltaics.[73-75] While some of these examples also incorporate other materials, such as effective electron donors, the addition of C_{60} to these complexes is key, and our CNT template technology could be combined with these previously studied materials to achieve new device architectures.

6.2.5   3-D hybrids architectures

In the future, more complex multi-directional CNT architectures[76] may find use as scaffolds for spatially programmable 3-D self-assembly, where the formation and organization of crystals is predetermined by the nanoscale texture of the CNTs and their microscale form factor. For instance, the architectures shown in **Figure 6.12** demonstrate the use of aligned CNTs to form composite structures that not only are perpendicular to the substrate but may also have chirality, depending on the initial CNT microstructure. The formation of these composites is governed by the same mechanisms described herein, where the porous and aligned CNT ensemble acts as a scaffold to template and direct the crystallization of C_{60} as the solvent evaporates.
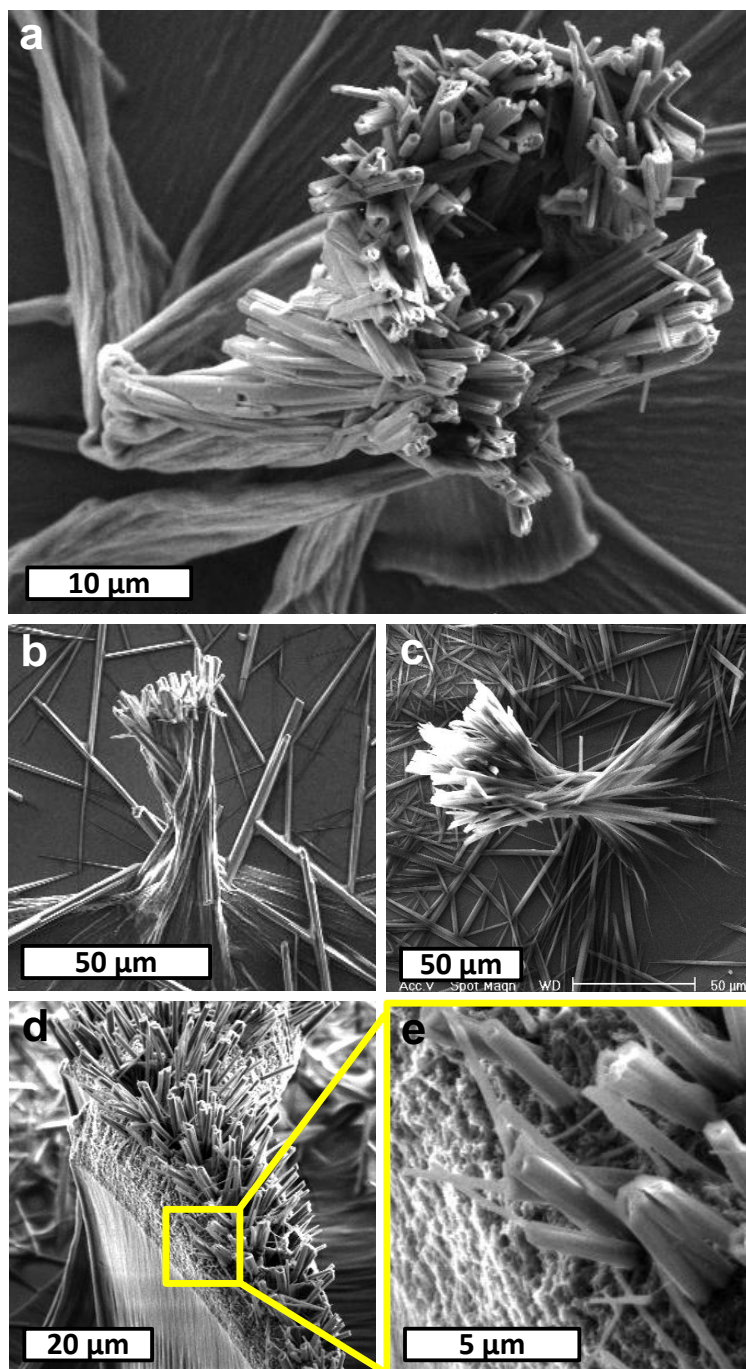
Figure 6.12 3-D hybrid architectures of C_{60} crystals and CNTs. C_{60} dispersion was drop-cast on various, vertical CNT microstructures before the CNTs were densified, and the dispersion infiltrated the microstructures, which enabled *in situ* crystallization of C_{60} rods as the CNTs densified. This produces vertical hybrid structures with rods aligning to the CNTs (a, b, c) and even penetrating the top surface of a pillar, forming an array of rods integrated with a CNT pillar (d, e). Whether the crystals grow along the surface of the CNT microstructure (a, b, c) or within (d, e) depends of the volume in the porous CNT structure that is available for wicking and infiltration of the dispersion.

6.3   Conclusions

We show that CNT films promote rapid crystallization of C_{60} from solution, and we harness the strong influence of the CNT direction to create multidirectional. The C_{60} crystals are interconnected by CNTs, where the CNTs provide a conducting pathway to the C_{60} crystals, making a unique hybrid material, which shows utility and promise as an organic UV photodetector with high responsivity. We assert that our methods and findings have general importance to the science and applications of crystal growth of other materials, including PAHs, synthetic polymers, and biomolecules.

6.4   Detailed methods

6.4.1   Fabrication of C_{60}-CNT hybrid films

CNT growth was performed using both a horizontal quartz tube furnace (Thermo-Fisher Mini-Mite, 22 mm inner diameter, 12 inch heated length). The catalyst substrate, which comprises of a 10 nm Al_2O_3 underlayer and 1 nm Fe, is deposited on (100) silicon wafers using e-beam evaporation and patterned by lithography and lift-off.[22] For lithography, we used SPR 220 - 3.0 photoresist. The lift-off was done by sonication in acetone followed by rinsing in isopropanol and evaporation using dry N_2. After installing the substrate and purging the reactor, the substrate was heated to the growth temperature in flowing H_2/He (100/400 sccm), and then C_2H_4 (100 sccm) was added for the growth duration. To prepare the laterally oriented (LO) CNTs, VA-CNTs are grown from parallel catalyst lines having 20 µm width and 200 µm spacing. The CNT line patterns are then mechanically rolled using a 300 µm diameter stainless steel roller in a custom-built force-controlled rolling machine.[26] To prepare radially oriented (RO) CNTs, acetone vapor is generated by boiling acetone in a flask and condensing the vapor onto vertically aligned CNT patterns (rings as shown in Fig. 1). The capillary forces exerted by the acetone during condensation from the CNTs mechanically fold the CNTs into RO CNT films.[28] Optionally, atomic layer deposition (ALD) of Al_2O_3 is done in an Oxford ALD system with trimethylaluminum (TMA) and water as precursors. A deposition

temperature of 200°C for 100 cycles results in ~10 nm of conformal coating of Al_2O_3 on the CNTs.

The C_{60} dispersion was prepared using *m*-xylene and C_{60} powder (99.5% purity; MTR, Ltd.) with a concentration of 1 mg mL^{-1}, which is below the solubility limit of C_{60} in *m*-xylene. The mixture was sonicated for 30 minutes immediately after the addition of the powder to the solvent. Droplets (<10 μL) of C_{60} dispersion were placed on the substrates using a micropipette. The solvent was allowed to completely evaporate from the substrate under ambient conditions. Real-time videos were recorded with a 3.1 megapixel CMOS color camera (Lumenera Infinity 1-3C) at 15 frames per second, and snapshots at specified time intervals were selected for processing and measurements.

6.4.2   Materials characterization

A Malvern Zetasizer Nanoseries was used to perform dynamic light scattering for estimation of the C_{60} cluster size in *m*-xylene. SEM was performed using a Philips XL30-FEG and a FEI Nova Nanolab, and TEM was performed on a JEOL 3011 HREM. Micro-Raman spectroscopy was performed using a Renishaw inVia Raman microscope equipped with a Leica microscope, RenCam CCD detector, 514 nm He-Ne laser. The spot size was <1 μm. In Figure 4a, peaks in the C_{60} powder spectrum at approximately 470 cm^{-1} and 1468 cm^{-1} represent the radial breathing and pentagonal-pinch vibrational modes of C_{60}, respectively.[36] Characteristic peaks of multi-wall CNTs appear near 1350 cm^{-1} and 1580 cm^{-1},[37] corresponding to the D- and G-bands, respectively.

Grazing incidence X-ray diffraction (GIXD) measurements were performed at the Stanford Synchrotron Radiation Lightsource (SSRL) using beamline 11–3 with a photon wavelength of 0.09758 nm. The scattering intensity was detected on a 2-D image plate (MAR-345) with a pixel size of 150 μm (2300 × 2300 pixels) and analyzed using the software package WxDiff, provided by Dr. Stefan Mannsfeld. The detector was located at a distance of 400.9 mm from the sample center. The incidence angle was chosen in the range of 0.10°-0.12° to optimize the signal to-background ratio. The beam size was 50 μm x 150 μm, which resulted in a beam footprint on sample 150 μm wide over the entire length of the 5-10 mm long sample. The data were distortion-corrected (θ-dependent image distortion introduced by planar detector surface) before performing quantitative

analysis on the images. The overall resolution in the GIXD experiments, dominated by the sample size, was about 0.08 Å^{-1}.

The samples are loaded into a probe station measuring the I-V characteristics of the material as it was illuminated at wavelengths ranging from 200 to 400 nm using a Sutter Instruments Co. Lambda 10-2 source. We measure the difference in current in dark conditions and during UV exposure for C_{60} rods, CNT sheets and the C_{60}-CNT hybrids with an applied bias of $\pm$ 0.5V at an illumination power range of 8.4-131 $\mu W/cm^2$ for 200-400 nm, respectively. Normalizing the change in current ($I_{UV}-I_{dark}/I_{dark}$) shows an increase in current of 5% in the case C_{60}-CNT hybrids, while this is more than 10 fold of pure CNT sheets or pure C_{60} in our setup.

6.5 References

1.   Park, C.; Song, H. J.; Choi, H. C., The critical effect of solvent geometry on the determination of fullerene (C_{60}) self-assembly into dot, wire and disk structures. *Chemical Communications* 2009, (32), 4803-4805.

2.   Gan, H. Y.; Liu, H. B.; Li, Y. L.; Gan, L. B.; Jiang, L.; Jiu, T. G.; Wang, N.; He, X. R.; Zhu, D. B., Fabrication of fullerene nanotube arrays using a template technique. *Carbon* 2005, *43* (1), 205-208.

3.   Miyazawa, K.; Minato, J.; Yoshii, T.; Fujino, M.; Suga, T., Structural characterization of the fullerene nanotubes prepared by the liquid-liquid interfacial precipitation method. *Journal of Materials Research* 2005, *20* (3), 688-695.

4.   Minato, J.; Miyazawa, K., Solvated structure of C_{60} nanowhiskers. *Carbon* 2005, *43* (14), 2837-2841.

5.   Ji, H. X.; Hu, J. S.; Wan, L. J.; Tang, Q. X.; Hu, W. P., Controllable crystalline structure of fullerene nanorods and transport properties of an individual nanorod. *Journal of Materials Chemistry* 2008, *18* (3), 328-332.

6.   Wang, L.; Liu, B. B.; Liu, D.; Yao, M. G.; Hou, Y. Y.; Yu, S. D.; Cui, T.; Li, D. M.; Zou, G. T.; Iwasiewicz, A.; Sundqvist, B., Synthesis of thin, rectangular C-60 nanorods using m-xylene as a shape controller. *Advanced Materials* 2006, *18* (14), 1883-1188.

7.   Sathish, M.; Miyazawa, K., Size-tunable hexagonal fullerene (C_{60}) nanosheets at the liquid-liquid interface. *Journal of the American Chemical Society* 2007, *129* (45), 13816-13817.

8.   Shin, H. S.; Yoon, S. M.; Tang, Q.; Chon, B.; Joo, T.; Choi, H. C., Highly selective synthesis of C-60 disks on graphite substrate by a vapor-solid process. *Angewandte Chemie-International Edition* 2008, *47* (4), 693-696.

9.   Yao, M. G.; Andersson, B. M.; Stenmark, P.; Sundqvist, B.; Liu, B. B.; Wagberg, T., Synthesis and growth mechanism of differently shaped C_{60} nano/microcrystals produced by evaporation of various aromatic C_{60} solutions. *Carbon* 2009, *47* (4), 1181-1188.

10.   Saito, S.; Oshiyama, A., Cohesive mechanism and energy-bands of solid C_{60}. *Physical Review Letters* 1991, *66* (20), 2637-2640.

11.   Arnold, M. S.; Zimmerman, J. D.; Renshaw, C. K.; Xu, X.; Lunt, R. R.; Austin, C. M.; Forrest, S. R., Broad Spectral Response Using Carbon Nanotube/Organic Semiconductor/C_{60} Photodetectors. *Nano Letters* 2009, *9* (9), 3354-3358.

12.   Esfarjani, K.; Zebarjadi, M.; Kawazoe, Y., Thermoelectric properties of a nanocontact made of two-capped single-wall carbon nanotubes calculated within the tight-binding approximation. *Physical Review B* 2006, *73*, 085406.

13.   Ma, L.; Ouyang, J.; Yang, Y., High-speed and high-current density C_{60} diodes. *Applied Physics Letters* 2004, *84* (23), 4786-4788.

14.   Doi, T.; Koyama, K.; Chiba, Y.; Tsuji, H.; Ueno, K.; Chen, S.-R.; Aoki, N.; Bird, J. P.; Ochiai, Y., Electron transport properties in photo and supersonic wave irradiated C_{60} fullerene nano-whisker field-effect transistors. *Japanese Journal of Applied Physics* 2010, *49*.

15.   Anthopoulos, T. D.; Singh, B.; Marjanovic, N.; Sariciftci, N. S.; Ramil, A. M.; Sitter, H.; Colle, M.; de Leeuw, D. M., High performance n-channel organic field-effect transistors and ring oscillators based on C_{60} fullerene films. *Applied Physics Letters* 2006, *89* (21), 213504-3.

16.   Jin, Y. Z.; Curry, R. J.; Sloan, J.; Hatton, R. A.; Chong, L. C.; Blanchard, N.; Stolojan, V.; Kroto, H. W.; Silva, S. R. P., Structural and optoelectronic properties of C_{60} rods obtained via a rapid synthesis route. *Journal of Materials Chemistry* 2006, *16* (37), 3715-3720.

17.   Liu, S.; Briseno, A. L.; Mannsfeld, S. C. B.; You, W.; Locklin, J.; Lee, H. W.; Xia, Y.; Bao, Z., Selective Crystallization of Organic Semiconductors on Patterned Templates of Carbon Nanotubes. *Advanced Functional Materials* 2007, *17* (15), 2891-2896.

18.   Chayen, N. E., Turning protein crystallisation from an art into a science. *Current Opinion in Structural Biology* 2004, *14* (5), 577-583.

19.   van Meel, J. A.; Sear, R. P.; Frenkel, D., Design principles for broad-spectrum protein-crystal nucleants with nanoscale pits. *Physical Review Letters* 2010, *105* (20), 205501.

20.   Curcio, E.; Curcio, V.; Profio, G. D.; Fontananova, E.; Drioli, E., Energetics of protein nucleation on rough polymeric surfaces. *Journal of Physical Chemistry B* 2010, *114* (43), 13650-13655.

21.   Chayen, N. E.; Saridakis, E.; Sear, R. P., Experiment and theory for heterogeneous nucleation of protein crystals in a porous medium. *Proceedings of the National Academy of Sciences of the United States of America* 2006, *103* (3), 597-601.

22.   Hart, A.; Slocum, A., Rapid growth and flow-mediated nucleation of millimeter-scale aligned carbon nanotube structures from a thin-film catalyst. *Journal of Physical Chemistry B* 2006, *110* (16), 8250-8257.

23.   Hata, K.; Futaba, D. N.; Mizuno, K.; Namai, T.; Yumura, M.; Iijima, S., Water-assisted highly efficient synthesis of impurity-free single-waited carbon nanotubes. *Science* 2004, *306* (5700), 1362-1364.

24.   De Volder, M. F. L.; Vidaud, D. O.; Meshot, E. R.; Tawfick, S.; Hart, A. J., Self-similar organization of arrays of individual carbon nanotubes and carbon nanotube micropillars. *Microelectronic Engineering* 2010, *87* (5-8), 1233-1238.

25.   Bedewy, M.; Meshot, E.; Guo, H.; Verploegen, E.; Lu, W.; Hart, A., Collective mechanism for the evolution and self-termination of vertically aligned carbon nanotube growth. *Journal of Physical Chemistry C* 2009, *113* (48), 20576-20582.

26.   Tawfick, S.; O'Brien, K.; Hart, A., Flexible high-conductivity carbon-nanotube interconnects made by rolling and printing. *Small* 2009, *5* (21), 2467-2473.

27.   Tawfick, S.; De Volder, M.; Hart, A. J., Structurally programmed capillary folding of carbon nanotube assemblies. *Langmuir* 2011, *27* (10), 6389-6394.

28.   De Volder, M.; Tawfick, S. H.; Park, S. J.; Copic, D.; Zhao, Z. Z.; Lu, W.; Hart, A. J., Diverse 3D Microarchitectures made by capillary forming of carbon nanotubes. *Advanced Materials* 2010, *22* (39), 4384-4389.

29.   Zhao, Z. Z.; Tawfick, S. H.; Park, S. J.; De Volder, M.; Hart, A. J.; Lu, W., Bending of nanoscale filament assemblies by elastocapillary densification. *Physical Review E* 2010, *82* (4).

30.   Michael, D. V.; Sameh, T.; Jin, P. S.; John, H. A., Corrugated carbon nanotube microstructures with geometrically tunable compliance. *ACS Nano* 2011, *5* (9), 7310–7317.

31.   Hermans, P. H., *Contribution to the physics of cellulose fibres; a study in sorption, density, refractive power and orientation*. Elsevier Pub. Co.: Amsterdam, 1946.

32.   Ghosh, S., A model for the orientational order in liquid crystals. *Il Nuovo Cimento D* 1984, *4* (3), 229-244-244.

33.   Wang, B.; Bennett, R.; Verploegen, E.; Hart, A.; Cohen, R., Quantitative characterization of the morphology of multiwall carbon nanotube films by small-angle X-ray scattering. *Journal of Physical Chemistry C* 2007, *111* (16), 5859-5865.

34.   Deegan, R. D.; Bakajin, O.; Dupont, T. F.; Huber, G.; Nagel, S. R.; Witten, T. A., Capillary flow as the cause of ring stains from dried liquid drops. *Nature* 1997, *389* (6653), 827-829.

35.   Sharma, R.; Lee, C. Y.; Choi, J. H.; Chen, K.; Strano, M. S., Nanometer positioning, parallel alignment, and placement of single anisotropic nanoparticles using hydrodynamic forces in cylindrical droplets. *Nano Letters* 2007, *7* (9), 2693-2700.

36.   Bethune, D. S.; Meijer, G.; Tang, W. C.; Rosen, H. J.; Golden, W. G.; Seki, H.; Brown, C. A.; Devries, M. S., Vibrational raman and infrared-spectra of chromatographically separated C_{60} and C_{70} fullerene clusters. *Chemical Physics Letters* 1991, *179* (1-2), 181-186.

37.   Dresselhaus, M. S.; Dresselhaus, G.; Saito, R.; Jorio, A., Raman spectroscopy of carbon nanotubes. 2005, *409* (2), 47-99.

38.   Rao, A. M.; Zhou, P.; Wang, K. A.; Hager, G. T.; Holden, J. M.; Wang, Y.; Lee, W. T.; Bi, X. X.; Eklund, P. C.; Cornett, D. S.; Duncan, M. A.; Amster, I. J., Photoinduced polymerization of solid C_{60} films. *Science* 1993, *259* (5097), 955-957.

39.   Guo, Y. J.; Karasawa, N.; Goddard, W. A., Prediction of fullerene packing in c60 and c70 crystals. *Nature* 1991, *351* (6326), 464-467.

40.   Korobov, M. V.; Stukalin, E. B.; Mirakyan, A. L.; Neretin, I. S.; Slovokhotov, Y. L.; Dzyabchenko, A. V.; Ancharov, A. I.; Tolochko, B. P., New solid solvates of C60 and C70 fullerenes: The relationship between structures and lattice energies. *Carbon* 2003, *41* (14), 2743-2755.

41.   Skokan, E. V.; Privalov, V. I.; Arkhangel'skii, I. V.; Davydov, V. Y.; Tamm, N. B., Solvent molecules in crystalline C_{60}. *Journal of Physical Chemistry B* 1999, *103* (12), 2050-2053.

42.   Masuhara, A.; Tan, Z. Q.; Kasai, H.; Nakanishi, H.; Oikawa, H., Fullerene Fine Crystals with Unique Shapes and Controlled Size. *Japanese Journal of Applied Physics* 2009, *48* (5), 3.

43.   Alargova, R. G.; Deguchi, S.; Tsujii, K., Stable colloidal dispersions of fullerenes in polar organic solvents. *Journal of the American Chemical Society* 2001, *123* (43), 10460-10467.

44.   Ji, H. X.; Hu, J. S.; Tang, Q. X.; Song, W. G.; Wang, C. R.; Hu, W. P.; Wan, L. J.; Lee, S. T., Controllable preparation of submicrometer single-crystal C_{60} rods

and tubes trough concentration depletion at the surfaces of seeds. *Journal of Physical Chemistry C* 2007, *111* (28), 10498-10502.

45.   Miyazawa, K.; Kuwasaki, Y.; Obayashi, A.; Kuwabara, M., C_{60} nanowhiskers formed by the liquid-liquid interfacial precipitation-method. *Journal of Materials Research* 2002, *17* (1), 83-88.

46.   Lim, J. K.; Lee, B. Y.; Pedano, M. L.; Senesi, A. J.; Jang, J.-W.; Shim, W.; Hong, S.; Mirkin, C. A., Alignment strategies for the assembly of nanowires with submicron diameters. *Small* 2010, *6* (16), 1736-1740.

47.   Liu, S.; Tok, J. B. H.; Locklin, J.; Bao, Z., Assembly and alignment of metallic nanorods on surfaces with patterned wettability. *Small* 2006, *2* (12), 1448-1453.

48.   Girifalco, L. A.; Hodak, M.; Lee, R. S., Carbon nanotubes, buckyballs, ropes, and a universal graphitic potential. *Physical Review B* 2000, *62* (19), 13104.

49.   Ruoff, R. S.; Hickman, A. P., Van der Waals binding to fullerenes to a graphite plane. *Journal of Physical Chemistry* 1993, *97* (11), 2494-2496.

50.   Girifalco, L. A.; Hodak, M., Van der Waals binding energies in graphitic structures. *Physical Review B* 2002, *65* (12), 125404.

51.   Woods, L. M.; Babrevedescu, S. C.; Reinecke, T. L., Adsorption of simple benzene derivatives on carbon nanotubes. *Physical Review B* 2007, *75* (15), 155415.

52.   Briseno, A. L.; Mannsfeld, S. C. B.; Ling, M. M.; Liu, S.; Tseng, R. J.; Reese, C.; Roberts, M. E.; Yang, Y.; Wudl, F.; Bao, Z., Patterning organic single-crystal transistor arrays. *Nature* 2006, *444* (7121), 913-917.

53.   Diao, Y.; Harada, T.; Myerson, A. S.; Alan Hatton, T.; Trout, B. L., The role of nanopore shape in surface-induced crystallization. *Nature Materials* 2011, *10*, 867-871.

54.   Diao, Y.; Myerson, A. S.; Hatton, T. A.; Trout, B. L., Surface design for controlled crystallization: the role of surface chemistry and nanoscale pores in heterogeneous nucleation. *Langmuir* 2011, *27* (9), 5324-5334.

55.   Li, C. Y.; Li, L.; Cai, W.; Kodjie, S. L.; Tenneti, K. K., Nanohybrid shish-kebabs: periodically functionalized carbon nanotubes. *Advanced Materials* 2005, *17* (9), 1198-1202.

56.   Li, B.; Li, L.; Wang, B.; Li, C. Y., Alternating patterns on single-walled carbon nanotubes. *Nature Nanotechnology* 2009, *4* (6), 358-362.

57.	Sugimoto, T., Preparation of monodispersed colloidal particles. *Advances in Colloid and Interface Science* 1987, *28*, 65-108.

58.	Heyer, H., Kinetics of crystal growth. *Angewandte Chemie-International Edition* 1966, *5* (1), 67-&.

59.	Sears, G. W., A growth mechanism for mercury whiskers. *Acta Metallurgica* 1955, *3* (4), 361-366.

60.	Bierman, M. J.; Lau, Y. K. A.; Kvit, A. V.; Schmitt, A. L.; Jin, S., Dislocation-driven nanowire growth and Eshelby twist. *Science* 2008, *320* (5879), 1060-1063.

61.	Ok, J. G.; Tawfick, S. H.; Juggernauth, K. A.; Sun, K.; Zhang, Y.; Hart, A. J., Electrically addressable hybrid architectures of zinc oxide nanowires grown on aligned carbon nanotubes. *Advanced Functional Materials* 2010, *20* (15), 2470-2480.

62.	Eder, D., Carbon nanotube−inorganic hybrids. *Chemical Reviews* 2010, *110* (3), 1348-1385.

63.	Pan, B.; Xing, B., Adsorption mechanisms of organic chemicals on carbon nanotubes. *Environmental Science & Technology* 2008, *42* (24), 9005-9013.

64.	Konstantatos, G.; Sargent, E. H., Nanostructured materials for photon detection. *Nat Nano* 2010, *5* (6), 391-400.

65.	Itkis, M. E.; Borondics, F.; Yu, A.; Haddon, R. C., Bolometric infrared photoresponse of suspended single-walled carbon nanotube films. *Science* 2006, *312* (5772), 413-416.

66.	Vera-Reveles, G.; Simmons, T. J.; Bravo-Sánchez, M.; Vidal, M. A.; Navarro-Contreras, H.; González, F. J., High-sensitivity bolometers from self-oriented single-walled carbon nanotube composites. *ACS Applied Materials & Interfaces* 2011, *3* (8), 3200-3204.

67.	Lof, R. W.; Vanveenendaal, M. A.; Koopmans, B.; Jonkman, H. T.; Sawatzky, G. A., Band-gap, excitons, and coulomb interaction in solid C_{60}. *Physical Review Letters* 1992, *68* (26), 3924-3927.

68.	Zhang, Y.; Liu, W.; Jiang, L.; Fan, L. Z.; Wang, C. R.; Hu, W. P.; Zhong, H. Z.; Li, Y. F.; Yang, S. H., Template-free solution growth of highly regular, crystal orientation-ordered C_{60} nanorod bundles. *Journal of Materials Chemistry* 2010, *20* (5), 953-956.

69.	Wang, L.; Liu, B. B.; Yu, S. D.; Yao, M. G.; Liu, D. D.; Hou, Y. Y.; Cui, T.; Zou, G. T.; Sundqvist, B.; You, H.; Zhang, D. K.; Ma, D. G., Highly enhanced

luminescence from single-crystalline C_{60} center dot 1m-xylene nanorods. *Chemistry of Materials* 2006, *18* (17), 4190-4194.

70.   Banerjee, S.; Wong, S. S., Synthesis and characterization of carbon nanotube−nanocrystal heterostructures. *Nano Letters* 2002, *2* (3), 195-200.

71.   Konstantatos, G.; Levina, L.; Fischer, A.; Sargent, E. H., Engineering the temporal response of photoconductive photodetectors via selective introduction of surface trap states. *Nano Letters* 2008, *8* (5), 1446-1450.

72.   Liu, J. S., High responsivity ultraviolet photodetector realized via a carrier-trapping process. *Applied Physics Letter* 2010, *97* (25), 251102.

73.   Bindl, D. J.; Wu, M.-Y.; Prehn, F. C.; Arnold, M. S., Efficiently harvesting excitons from electronic type-controlled semiconducting carbon nanotube films. *Nano Letters* 2010, *11* (2), 455-460.

74.   Tung, V. C.; Huang, J.-H.; Tevis, I.; Kim, F.; Kim, J.; Chu, C.-W.; Stupp, S. I.; Huang, J., Surfactant-free water-processable photoconductive all-carbon composite. *Journal of the American Chemical Society* 2011, *133* (13), 4940-4947.

75.   Li, C.; Chen, Y.; Ntim, S. A.; Mitra, S., Fullerene-multiwalled carbon nanotube complexes for bulk heterojunction photovoltaic cells. *Applied Physics Letters* 2010, *96* (14), 143303.

Chapter 7
Contributions and outlook

To summarize the contributions of my dissertation work: I have developed a complementary set of novel diagnostic tools for probing CNT synthesis, which has thus enabled new understanding of the so-called "birth, life, and death" of CNT forest growth.[1-9] Importantly, the *methodologies* described herein can be adapted and employed by others to continue improving upon CNT synthesis, as well as synthesis of other nanomaterials.

7.1 Contributions

The major contributions are divided into three categories: (1) characterization methods for nanomaterials; (2) chemical and physical insights into CNT forest growth; and (3) advances in CNT materials processing.

7.1.1 Novel characterization methods

- Created custom AFM image processing that enables automatic particle identification (even for clustered particles), thus accurately quantifying particle height and spacing. This uniquely validated the use of a truncated-sphere form factor model to describe X-ray scattering from Fe particles on Al_2O_3 support.Implemented *in situ* grazing-incidence small-angle X-ray scattering (GISAXS) for non-destructive monitoring of the dewetting of thin films.

- Improved previously published SAXS form factor model to describe CNTs as a log-normal distribution of core-shell cylinders as validated by TEM.[3]

- Combined *in situ* SAXS technique with modeling to monitor and quantify statistically significant *populations* of catalyst particles and CNTs (~10^9) at atmospheric pressure.

- Co-developed (with Mostafa Bedewy) a spatiotemporal correlation technique for measuring the lengthening kinetics of CNTs within a forest.[4] Here, we combined SAXS mapping and real-time forest height measurements to correct height kinetics for the inherent tortuosity of CNTs.

- Achieved X-ray beam spotsize < 20 µm in collaboration with Mostafa Bedewy and Arthur Woll (initially by using capillary focusing optics), which was an important development in high-resolution spatial mapping of forests by SAXS.

7.1.2 Insights into CNT forest growth

- Directly demonstrated that CNT forest growth by CVD is a multi-step process and identified the relevant time scales of each step: catalyst film dewetting and particle formation are rapid (~0.1-10 sec); coarsening of particles is slow (~100-1000 sec); CNT nucleation is rapid (~0.1-1 sec); forest self-organization (~10 sec) and the population of CNT diameters (~10-1000 sec) evolve slowly; and self-termination is abrupt (~1-10 sec).

- Used *in situ* and *ex situ* SAXS CNT alignment analysis to probe forest self-organization, steady growth, and termination.

- Showed that catalyst film dewetting and particle formation rates and morphologies depend on annealing conditions (*i.e.*, temperature ramp rate, hold time, gas environment)

- Elucidated the role of rapid heating of the catalyst in the growth gases. This induces rapid formation of particles and instantaneous nucleation of small-diameter CNTs.

- Connected specific annealing conditions with the evolution of the resultant population of CNTs, with implications for termination (*i.e.*, rapid heating in growth gases gives rapid, short-lived growth).

- Resolved the kinetics of self-organization in CNT forest growth and the limits of making well aligned films as a function of annealing and temperature conditions.

- Discovered that the time required to established well aligned CNTs during self-organization is coincident with the onset of vertical growth (*i.e.*, liftoff).
- Identified a potentially critical time regime in the *in situ* GISAXS image sequence during which CNTs and Fe particles "co-exist", signifying CNT nucleation.
- Discovered that abrupt self-termination in forest height kinetics is concomitant with loss of order at the end of growth.[1]
- Revealed that CNT height kinetics are self-similar over a wide range of thermal conditions, which suggests that governing mechanisms may be universal.[3]
- Proved quantitatively that preheating the gaseous precursors is a rate-limiting step in thermal CVD, demonstrating that decomposition and rearrangement of C_2H_4/H_2 due to thermal treatment is vital for growth in our system.[3]
- Confirmed that excessive heating of gaseous precursors decelerates CNT growth and results in degraded structural quality in CNT forests.

7.1.3 Advances in CNT materials processing

- Developed fully automated temperature and gas flow controls for the SabreTube CVD reactor (with Sameh Tawfick), which was vital for parametric studies and *in situ* X-ray and gas analysis investigations.
- Advanced the decoupled CVD approach (first design by John Hart; SabreTube, Absolute Nano, LLC)[1, 10] by developing T_s-T_p map of thermal parameters for tunable CNT forest growth and properties.[3]
- Introduced novel method for templating dewetting of the catalyst film to form ordered particles using porous anodic alumina (AAO).
- Directly showed that CNT diameter within forests is dictated by particle size and can be tuned from a single starting catalyst film thickness—CNT diameter is, to first order, indifferent to changes in gas chemistry.[3, 5]
- Co-developed direct delivery method for probing key gaseous precursors for CVD of CNTs (increased efficiency of growth, reduced harmful emissions), which resulted in filing a patent application as a co-inventor with Desirée Plata *et al*. ("Alkyne-assisted nanostructure growth").[5]

- Developed templated synthesis technique for assembling C_{60} on multidirectional CNT microstructures for self-assembly of C_{60}-CNT hybrid high photoconductive gain (responsivity of 10^5 A/W at 0.5 V bias).

7.2   Future directions

7.2.1   Next steps

This work has drawn many exciting conclusions and answered crucial questions in terms of CNT forest growth. However, there remain several grand challenges in the manufacture of CNTs (Chapter 2), and based on these challenges, I have listed the most important next phases of this research:

- Further development of templated dewetting of catalyst films into ordered particles via an AAO support (Section 3.2.5 of Chapter 3). To confirm the mechanism by which the particles self-organize, it is crucial to verify whether or not the particles are docking in the pores and also that catalyst material is not being lost in the pores. It will be important to explore a matrix of Fe thicknesses and AAO pore density to determine the limits of achieving predetermined particle size and spacing. Testing long annealing times is relevant considering recent results showing that catalyst evolution and migration is a governing factor in CNT growth. Exploring other materials beyond Fe (*i.e.*, Au, Pt, Pd, etc.) will make this work more broadly appealing and potentially higher impact, such as for fabrication of monodisperse catalyst nanoparticle arrays for other heterogenous catalysis studies, and growth of highly ordered semiconductor nanowire arrays.
- Building on the library of *in situ* X-ray techniques will continue to provide new insights into CNT growth. Continuing to foster collaborations at Cornell High-Energy Synchrotron Source (CHESS) is a vital component of this work. To this end, Sol Gruner and coworkers are currently developing the detector technology to collect small-angle and wide-angle X-ray scattering (WAXS) simultaneously, which would enable quantitative correlation of the number of CNT walls with the

outer diameter. This essentially eliminates a variable from the "growth equation", so we can precisely quantify mass kinetics during CNT growth.

- More immediately, *ex situ* WAXS mapping of CNT forests using synchrotron radiation will itself be an important improvement upon recent work.[11] Building a model of WAXS from CNT walls will complement experimental data and enable important parameters to be extracted and compared across processing conditions.

- Other break-through developments in our X-ray techniques will be *in situ* WAXS of the catalyst in grazing incidence, which will give a time-resolved powder diffraction pattern from which we decipher the crystal structure, and thus the chemical state, of the catalyst. This is an advancement beyond state-of-the-art *in situ* XPS and TEM techniques, which require low pressures and typically probe fewer particles than is possible with X-ray scattering. Similarly, employing some form of X-ray absorption spectroscopy (XAS) would give an indication of the electronic (*i.e.*, catalytic) behavior of the particles. Executing any of these techniques *during growth* will prove to be an excellent engineering feat because CNTs mask any signal from the catalyst by scattering the X-rays, but it will answer many important questions regarding the state of the catalyst during "birth, life, and death" (over a large sample population).

- Elucidating the correlation between CNT alignment and packing fraction is immediately possible, and it is crucial for understanding the interactions among CNTs during growth as well as engineering forests of CNTs with low defect density. This is particularly interesting in the early stages of self-organization. The results presented herein are promising, but quantifying the number density and length of CNTs during self-organization will reveal what mechanisms drive the transition from tangled films to vertically aligned growth. It will also be insightful and help guide experiments to model the CNT ensemble as a population of hard rods—much like models used to describe liquid crystal packing—but with varying number of rods and/or varying length with time (*i.e.*, aspect ratio $\rightarrow \infty$[12]).

- Deeper investigations into the role of hydrocarbons and hydrogen as well as the mechanisms of carbon inclusion at the growing lattice. It will be important to continue collaborative projects with Desirée Plata and capitalize on our collective

knowledge basis and investigative tools. Based on the results of our recent work,[5] there are natural questions regarding the interplay of ethylene, the alkyne, and the catalyst surface, especially how exactly the carbon-containing molecules incorporate into the growing lattice. There is precedence for a carbon-dimer inclusion mechanism,[13, 14] and by combining isotope labeling and our direct delivery method, we can feasibly answer the question of whether or not this occurs during CNT synthesis. Other questions involving the role, or lack thereof, of polycyclic aromatic hydrocarbons (PAHs) should also be investigated.

- Given the dramatic variations in alignment, density, and growth rates through the forest, researchers have begun to converge on the notion that mechanical forces are playing a significant role in forest growth,[7, 15-17] and I anticipate that the number of publications that discuss forces in growth will increase dramatically based on recent discussions at CNT workshops. Therefore, it will be of high impact to not only further quantify how forces influence self-organization and termination, but also how *applied* forces may be used to *direct* CNT growth and alter CNT structure.

7.3   References

1.   Meshot, E.; Hart, A., Abrupt self-termination of vertically aligned carbon nanotube growth. *Applied Physics Letters* 2008, 92, 113107.

2.   Bedewy, M.; Meshot, E.; Guo, H.; Verploegen, E.; Lu, W.; Hart, A., Collective mechanism for the evolution and self-termination of vertically aligned carbon nanotube growth. *Journal of Physical Chemistry C* 2009, 113, 20576-20582.

3.   Meshot, E.; Plata, D.; Tawfick, S.; Zhang, Y.; Verploegen, E.; Hart, A., Engineering vertically aligned carbon nanotube growth by decoupled thermal treatment of precursor and catalyst. *ACS Nano* 2009, 3, 2477-2486.

4.   Meshot, E.; Bedewy, M.; Lyons, K.; Woll, A.; Juggernauth, K.; Tawfick, S.; Hart, A., Measuring the lengthening kinetics of aligned nanostructures by spatiotemporal correlation of height and orientation. *Nanoscale* 2010, 896-900.

5.   Plata, D.; Meshot, E.; Reddy, C.; Hart, A.; Gschwend, P., Multiple alkynes react with ethylene to enhance carbon nanotube synthesis, suggesting a polymerization-like formation mechanism. *ACS Nano* 2010, 4, 7185-7192.

6.   Nessim, G.; Seita, M.; Plata, D.; O'Brien, K.; Hart, A.; Meshot, E.; Reddy, C.; Gschwend, P.; Thompson, C., Precursor gas chemistry determines the crystallinity of carbon nanotubes synthesized at low temperature. *Carbon* 2011, 49, 804-810.

7.   De Volder, M.; Vidaud, D.; Meshot, E.; Tawfick, S.; Hart, A., Self-similar organization of arrays of individual carbon nanotubes and carbon nanotube micropillars. *Microelectronic Engineering* 2010, 1233-1238.

8.   Bedewy, M.; Meshot, E. R.; Reinker, M. J.; Hart, A. J., Population growth dynamics of carbon nanotubes. *ACS Nano* 2011, 5, 8974-8989.

9.   Meshot, E. R.; Patel, K. D.; Tawfick, S.; Juggernauth, K. A.; Bedewy, M.; Verploegen, E. A.; De Volder, M. F. L.; Hart, A. J., Photoconductive hybrid films via directional self-assembly of C_{60} on aligned carbon nanotubes. *Advanced Functional Materials* 2011 (in press).

10.   van Laake, L.; Hart, A. J.; Slocum, A. H., Suspended heated silicon platform for rapid thermal control of surface reactions with application to carbon nanotube synthesis. *Review of Scientific Instruments* 2007, 78.

11.   Furuta, H.; Kawaharamura, T.; Furuta, M.; Kawabata, K.; Hirao, T.; Komukai, T.; Yoshihara, K.; Shimomoto, Y.; Oguchi, T., Crystal structure analysis of multiwalled carbon nanotube forests by newly developed cross-sectional x-ray diffraction measurement. *Applied Physics Express* 2010, 3.

12. Polson, J. M.; Frenkel, D., First-order nematic-smectic phase transition for hard spherocylinders in the limit of infinite aspect ratio. *Physical Review E* 1997, 56, R6260-R6263.

13. Ding, F.; Harutyunyan, A. R.; Yakobson, B. I., Dislocation theory of chirality-controlled nanotube growth. *Proceedings of the National Academy of Sciences* 2009, 106, 2506-2509.

14. Eres, G.; Rouleau, C. M.; Yoon, M.; Puretzky, A. A.; Jackson, J. J.; Geohegan, D. B., Model for self-assembly of carbon nanotubes from acetylene based on real-time studies of vertically aligned growth kinetics. *The Journal of Physical Chemistry C* 2009, 113, 15484-15491.

15. Han, J. H.; Graff, R. A.; Welch, B.; Marsh, C. P.; Franks, R.; Strano, M. S., A mechanochemical model of growth termination in vertical carbon nanotube forests. *ACS Nano* 2008, 2, 53-60.

16. Zhang, Q.; Zhou, W.; Qian, W.; Xiang, R.; Huang, J.; Wang, D.; Wei, F., Synchronous growth of vertically aligned carbon nanotubes with pristine stress in the heterogeneous catalysis process. *Journal of Physical Chemistry C* 2007, 111, 14638-14643.

17. Hart, A.; Slocum, A., Force output, control of film structure, and microscale shape transfer by carbon nanotube growth under mechanical pressure. *Nano Letters* 2006, 6, 1254-1260.